

Neutron Scattering Studies on Magnetic Excitations in Complex Ordered Manganites

Daniel Senff



Neutron Scattering Studies on Magnetic Excitations in Complex Ordered Manganites

Inaugural Dissertation

zur

Erlangung des Doktorgrades
der Mathematisch-Naturwissenschaftlichen Fakultät
der Universität zu Köln

vorgelegt von

Daniel Senff

aus Köln

Köln, September 2007

Berichterstatter:

Prof. Dr. M. Braden
Prof. Dr. M. Vojta
Prof. Dr. B. Büchner

Vorsitzender
der Prüfungskommission:

Prof. Dr. L. Bohatý

Tag der letzten mündlichen Prüfung:

29. Oktober 2007

*"Ordnung ist das halbe Leben,
woraus mag die andere Hälfte bestehen ?"*

Heinrich Böll

Contents

1	Introduction	3
2	Magnetic neutron scattering	5
2.1	Neutron scattering formulas	5
2.1.1	Nuclear neutron scattering	6
2.1.2	Magnetic neutron scattering	8
2.2	The triple-axis spectrometer	14
2.2.1	Basic principles of a TAS spectrometer	15
2.2.2	The resolution function	18
3	Magnetic excitation spectrum of single-layered LaSrMnO₄	21
3.1	Basic properties of single-layered LaSrMnO ₄	22
3.1.1	Magnetic order in undoped LaSrMnO ₄	25
3.2	Revision of the magnetic excitation spectrum in LaSrMnO ₄	29
3.2.1	Polarization analysis of the magnetic excitations	30
3.2.2	Field dependence of the magnetic excitations	33
3.3	Conclusions	38
4	Spin-wave excitations in charge-ordered manganites	41
4.1	Basic properties of the ordered state	42
4.1.1	The classic CE-type ordering	42
4.1.2	The Zener polaron model	45
4.1.3	Charge and orbital ordering in La _{1/2} Sr _{3/2} MnO ₄	46
4.1.4	The CE-type ordering in neutron scattering experiments	49
4.2	Spin-wave excitations and magnetic correlations in La _{1/2} Sr _{3/2} MnO ₄	51
4.2.1	Magnon dispersion in the COO state	54
4.2.2	Diffuse magnetic scattering	62
4.2.3	Thermal evolution of the magnetic fluctuations	77
4.3	Doping dependence of the COO order in La _{1-x} Sr _{1+x} MnO ₄	82
4.3.1	CE-type correlations in electron-doped La _{0.6} Sr _{1.4} MnO ₄	84
4.3.2	Magnetic correlations in hole-doped La _{0.4} Sr _{1.6} MnO ₄	101
4.3.3	Magneto-orbital phase diagram	111
4.4	Conclusions	112

5	Magnetic excitations in multiferroic TbMnO₃	115
5.1	Basic properties and multiferroicity in TbMnO ₃	117
5.1.1	Magnetoelectric effect in TbMnO ₃	119
5.1.2	Spiral ordering in TbMnO ₃	120
5.2	Spin-wave spectrum at the magnetic zone center	124
5.2.1	Tb crystal-field excitations and data treatment	125
5.2.2	Spin-wave spectrum in the spiral phase	126
5.2.3	Spin-wave spectrum in the spin-density wave phase	136
5.2.4	Thermal evolution of the spin-wave spectrum	143
5.2.5	Field dependence of the spin-wave spectrum	146
5.3	Spin-wave dispersion in TbMnO ₃	154
5.3.1	Dispersion along <i>a</i> and <i>c</i> : nearest-neighbor exchange	155
5.3.2	Dispersion along <i>b</i> : magnetic frustration	163
5.4	Conclusions	169
6	Summary	171
	List of Figures	175
	Glossary of Symbols	177
	Bibliography	181
	List of Publications	203
	Danksagung	207
	Offizielle Erklärung	211
	Zusammenfassung	213
	Abstract	215

1 Introduction

An entity might be considered as complex if it is “consisting of many different and connected parts” [1]. In light of this definition, transition-metal oxides are of special complexity, as their physical behavior arises from the sophisticated interplay between many different degrees of freedom including spin, charge, orbital, and the crystal lattice [2]. The electronic correlations often result in a competition or even coexistence of states with very different characteristics, and small external perturbations can lead to a giant response and novel behavior, as e. g. high-temperature superconductivity in cuprates [3] and the colossal change of the electric resistivity in a magnetic field in perovskite manganites, known as CMR-effect [4].

In manganites, a slight change of parameters tunes between ground states with contrasting properties, and the competition between various interactions results in a very rich – one might as well call it complex – phase diagram containing a variety of phases. In the neighborhood of two distinct states, the balance between the different degrees of freedom is often very subtle and can easily be manipulated. The most popular consequence is the CMR-effect, which today is considered as the switching between a ferromagnetic metallic and an antiferromagnetic charge-ordered state [4, 5]. A second remarkable feature, appearing at the border of two different antiferromagnetic states, is a gigantic magnetoelectric coupling, which has recently been discovered in multiferroic manganites [6] and which, due to its possible technical applications, immediately attracted a lot of interest.

The present thesis analyzes the magnetic excitation spectrum of three different manganese oxides related to these effects, undoped LaSrMnO_4 , charge-ordered $\text{La}_{1/2}\text{Sr}_{3/2}\text{MnO}_4$ and multiferroic TbMnO_3 , which were studied by means of inelastic neutron scattering. Common to all three systems is a complex magnetic ordering, and the magnetic state is strongly influenced by the interplay with other degrees of freedom. Conversely, understanding the static and dynamic magnetic properties does not yield insight only into the magnetic, but also e. g. into the orbital correlations.

LaSrMnO_4 is the two-dimensional analog of the parent compound of manganese oxides, LaMnO_3 . Although considered as a simple antiferromagnet in the recent literature [7], the spin-wave spectrum is not consistent with this simple approach, and the present results provide significant evidence for a heterogenous magnetic ground state driven by a close correlation of magnetic and orbital degrees of freedom.

Structurally similar to LaSrMnO_4 , the hole-doped system $\text{La}_{1/2}\text{Sr}_{3/2}\text{MnO}_4$ ex-

hibits the typical cooperative ordering of charges, orbitals, and spins, generic for manganites with a rational fraction of charge carriers. Although the ordered state has attracted a lot of interest since its prediction half a century ago [8], and despite the great importance for the understanding of the CMR-effect, even the ground-state properties of the ordered state are not well established and different concepts are still controversially discussed [9]. Analyzing the spin-wave dispersion allows to distinguish between the different proposals, unambiguously confirms the predictions of the classical model, and reveals certain similarities between the anti-ferromagnetic charge-ordered and the ferromagnetic state, which seem to compete in a wide parameter range resulting in the famous metal-insulator transition in perovskite manganites.

The orthorhombic manganite TbMnO_3 is one of the pivoting materials in the fascinating class of multiferroic oxides [10]. The dynamics of systems with simultaneous magnetic and ferroelectric order is predicted to be controlled by new collective excitations regarded as hybridized magnon-phonon vibrations [11], and the strong magnetoelectric coupling in TbMnO_3 allows, for the first time, the experimental observation of such excitations. The physical properties of TbMnO_3 are well understood by the momentum, temperature, and field dependence of the hybridized fluctuations, and the experimental results are in excellent agreement with recent theories connecting the observed ferroelectricity with complex magnetic ground states [12, 13].

The present thesis is divided into six chapters, which are arranged according to ascending physical complexity. These introductory remarks are followed by a brief introduction into the technique of inelastic neutron scattering in chapter 2. Subsequently, chapter 3, the first of three experimental chapters, discusses the magnetic and orbital correlations of the single-layered manganite LaSrMnO_4 . Chapter 4 is the longest section of this thesis and is dedicated to the charge- and orbital-ordered state in half-doped $\text{La}_{1/2}\text{Sr}_{3/2}\text{MnO}_4$, including the analysis of the excitation spectrum in $\text{La}_{1/2}\text{Sr}_{3/2}\text{MnO}_4$, as well as the thermal evolution and the doping dependence of the ordered state. The last experimental chapter 5 deals with the characterization of the excitation spectrum of multiferroic TbMnO_3 , and the thesis is finally closed by a summary of the most relevant results in chapter 6.

2 Magnetic neutron scattering

Only four years after the discovery of the neutron by J. Chadwick in 1932 it has been demonstrated that neutrons can be diffracted by condensed matter. Moreover, due to its magnetic moment neutrons are not only diffracted by crystalline, but also by magnetic lattices, as first has been suggested by Bloch in 1936 and fifteen years later has been verified in the pioneering work of Shull, Wollan and Strauser [14, 15]. Since then, and especially with today's advanced reactor sites and modern spallation sources neutron scattering has become one of the most powerful and versatile experimental techniques for probing condensed matter.

The fundamental physical properties of the neutron provide insight into the static and dynamical correlations of modern materials, which mostly are hardly accessible with alternative techniques. In elastic neutron studies one takes advantage of the short-range nature of the nuclear interaction potential, which yields a high visibility of light elements and a sizable contrast even between different isotopes, and of the neutron's magnetic moment, which interacts with the magnetization density of unpaired electrons and offers a unique method to study magnetic correlations on a microscopic scale. In the field of dynamic correlations neutron scattering is today by far the most important experimental tool, since only neutrons allow a sizeable momentum transfer at energy scales valid for collective excitations like phonons and magnons. Due to its rest mass $m_n = 1.674928 \times 10^{-24}$ g a thermal neutron with wavelength $\lambda = 2.4 \text{ \AA}$ possesses an energy $E \approx 14 \text{ meV}$, which is of the order of typical collective excitations. In contrast, the energy of a photon with similar wavelength is 7 – 8 orders of magnitude larger and an excellent energy resolution and thus a huge experimental effort is required to resolve a meV-change in the photon energy, which is available only since a few years at the most brilliant x-ray sources. Indeed, the recent developments in the wide field of spin and lattice dynamics are founded on experimental results achieved with inelastic neutron scattering.

2.1 Neutron scattering formulas

In a neutron scattering experiment the count rate C of neutrons with energy E in the interval E' and $E' + dE'$ scattered into a given solid angle $d\Omega$ normalized to the incident neutron flux I_0 is given by the differential cross section $\frac{d^2\sigma}{d\Omega dE'}$. In this section we recall briefly the basic expressions for the cross section of elastic and

inelastic scattering and connect the cross sections with the physical properties of the system under investigation. For an extended derivation and a detailed discussion of the various cross sections we refer, however, to the classical review articles and textbooks on neutron scattering [16–20].

Let \mathbf{k}_i be the wave vector and $\boldsymbol{\sigma}_i$ the spin state of the incident neutron. If we label the initial and final states of the scattering system by quantum numbers λ_i and λ_f the differential cross section for a scattered neutron with final wave vector \mathbf{k}_f and final spin state $\boldsymbol{\sigma}_f$ is given by Fermis Golden Rule:

$$\begin{aligned} & \left(\frac{d^2\sigma}{d\Omega dE'} \right)_{\mathbf{k}_i \rightarrow \mathbf{k}_f} \\ &= \frac{1}{N} \frac{k_f}{k_i} \left(\frac{m}{2\pi\hbar} \right)^2 \sum_{\lambda_i \boldsymbol{\sigma}_i} p_{\lambda_i} p_{\boldsymbol{\sigma}_i} \sum_{\lambda_f \boldsymbol{\sigma}_f} |\langle \mathbf{k}_f \boldsymbol{\sigma}_f \lambda_f | V | \mathbf{k}_i \boldsymbol{\sigma}_i \lambda_i \rangle|^2 \delta(\hbar\omega + E_{\lambda_i} - E_{\lambda_f}) \end{aligned} \quad (2.1)$$

with the energy of the incident and scattered neutrons E_i and E_f , the energy change of the scattering system $\hbar\omega$, the probability p_j to find the system or the neutron in the state j and the interaction potential V . This *masterformula of neutron scattering* is a very general result as no assumption about the interaction potential $V(\mathbf{r})$ is made, and the determination of the cross sections for the various magnetic and nuclear scattering processes has reduced to the elaboration of the matrix elements of the interaction potential $V(\mathbf{r})$.

The interaction of neutrons with matter can be divided into two parts – a nuclear part due to the scattering of the neutron at the nucleus and a magnetic part due to the magnetic dipole interaction between the magnetic moment of the neutron and the electrons of an atom. Since the focus of this thesis is on magnetic correlations, we will state the scattering formulas for the nuclear interaction briefly and discuss afterwards the magnetic interaction in some more detail.

2.1.1 Nuclear neutron scattering

The nuclear forces which cause the nuclear scattering act on a scale much smaller than the typical wavelength of a neutron. The scattering potential of an assembly of N atoms at positions \mathbf{R}_j of, for simplicity, a single element can therefore be modeled as

$$V_N(\mathbf{r}) = \frac{2\pi\hbar^2}{m} \sum_j b\delta(\mathbf{r} - \mathbf{R}_j) \quad (2.2)$$

with a single parameter b describing the scattering power of the atom j . The scattering length b is not only element specific, but does also depend on the variation of isotopes and on the total spin of the nucleus-neutron system. Defining the scattering vector $\mathbf{Q} = \mathbf{k}_f - \mathbf{k}_i$ the differential cross section for coherent and

incoherent nuclear scattering reads as:

$$\left(\frac{d^2\sigma}{d\Omega dE'}\right)_{\text{coh}} = \frac{1}{N} \frac{\sigma_{\text{coh}}}{4\pi} \frac{1}{2\pi\hbar} \frac{k_f}{k_i} \sum_{jj'} \int_{-\infty}^{\infty} \langle e^{-i\mathbf{Q}\mathbf{R}_j(0)} e^{i\mathbf{Q}\mathbf{R}_{j'}(t)} \rangle e^{i\omega t} dt \quad (2.3)$$

$$\left(\frac{d^2\sigma}{d\Omega dE'}\right)_{\text{inc}} = \frac{1}{N} \frac{\sigma_{\text{inc}}}{4\pi} \frac{1}{2\pi\hbar} \frac{k_f}{k_i} \sum_j \int_{-\infty}^{\infty} \langle e^{-i\mathbf{Q}\mathbf{R}_j(0)} e^{i\mathbf{Q}\mathbf{R}_j(t)} \rangle e^{-i\omega t} dt \quad (2.4)$$

where $\sigma_{\text{coh}} = 4\pi\bar{b}^2$ and $\sigma_{\text{inc}} = 4\pi(\bar{b}^2 - \bar{b}^2)$. We will focus only on the coherent part in the following, as the incoherent part does not give interference effects between different atoms j and j' .

It is useful and common practice to express the cross section eq. 2.3 in terms of correlation functions: If we define the *coherent scattering function* $S(\mathbf{Q}, \omega)$ as

$$S(\mathbf{Q}, \omega) = \frac{1}{N} \frac{1}{2\pi\hbar} \int_{-\infty}^{\infty} \sum_{jj'} \langle e^{-i\mathbf{Q}\mathbf{R}_j(0)} e^{i\mathbf{Q}\mathbf{R}_{j'}(t)} \rangle e^{-i\omega t} dt \quad (2.5)$$

the cross section for coherent scattering reduces to

$$\left(\frac{d^2\sigma}{d\Omega dE'}\right)_{\text{coh}} = \frac{\sigma_{\text{coh}}}{4\pi} \frac{k_f}{k_i} S(\mathbf{Q}, \omega). \quad (2.6)$$

The scattering function $S(\mathbf{Q}, \omega)$ describes the correlations in space and time between an atom j at time $t = 0$ at site \mathbf{R}_j and a second atom j' at a finite time t at site $\mathbf{R}_{j'}$. Obviously, the scattering function contains all desired informations about the static and dynamic behavior of the system under investigation.

Elastic nuclear Bragg scattering Consider a crystal with translation invariance \mathbf{j} and d atoms in the unit cell. Because of thermal motion each atom will oscillate around its equilibrium position \mathbf{d} and the position of atom d is

$$\mathbf{R}_{jd} = \mathbf{j} + \mathbf{d} + \mathbf{u}_d(j, t), \quad (2.7)$$

where $\mathbf{u}_d(j, t)$ is the displacement from the equilibrium. The translation invariance of the crystal reduces the double sum in eq. 2.5 to a single summation over the distances $\mathbf{j} - \mathbf{j}'$ and for elastic scattering ($\omega = 0$) the differential cross section transforms to

$$\left(\frac{d\sigma}{d\Omega}\right)_{\text{coh}}^{\text{el}} = \frac{(2\pi)^3}{v_0} \sum_{\boldsymbol{\tau}} |F_N(\mathbf{Q})|^2 \times \delta(\mathbf{Q} - \boldsymbol{\tau}) \quad (2.8)$$

with a reciprocal lattice vector $\boldsymbol{\tau}$, the unit cell volume v_0 and the nuclear structure factor $F_N(\mathbf{Q})$ defined by

$$F_N(\mathbf{Q}) = \sum_d \bar{b}_d e^{i\mathbf{Q}d} e^{-W_d(\mathbf{Q})}. \quad (2.9)$$

The Debye-Waller factor $\exp(-W_d(\mathbf{Q})) = \exp(-\langle (\mathbf{Q}\mathbf{u}(j, d))^2 \rangle)$ takes into account the mean square displacement of each atom and decreases the observed intensity of a Bragg peak with increasing $|\mathbf{Q}|$.

One phonon cross section The coherent one phonon cross section is derived from the expansion of the displacement correlation functions $\langle \mathbf{Q}\mathbf{u}_d(j, 0)\mathbf{Q}\mathbf{u}_d(j', t) \rangle$ and can shown to be:

$$\begin{aligned} \left(\frac{d^2\sigma}{d\Omega dE'} \right)_{\text{coh}}^{\text{inel}} &= \frac{k_f}{k_i} \frac{(2\pi)^3}{2v_0} \sum_{\boldsymbol{\tau}} \sum_{\nu, \mathbf{q}} \frac{1}{\omega_{\nu}(\mathbf{q})} \left| \sum_d \bar{b}_d e^{-W_d(\mathbf{Q})} e^{i\mathbf{Q}d} \cdot \frac{\mathbf{Q}\mathbf{e}_d(\mathbf{q}, \nu)}{\sqrt{M_d}} \right|^2 \\ &\times \left([n_{\nu}(\mathbf{q}) \delta(E_i - E_f + \hbar\omega_{\nu}(\mathbf{q})) \delta(\mathbf{Q} + \mathbf{q} - \boldsymbol{\tau})] \right. \\ &\quad \left. + [(n_{\nu}(\mathbf{q}) + 1) \delta(E_i - E_f - \hbar\omega_{\nu}(\mathbf{q})) \delta(\mathbf{Q} - \mathbf{q} - \boldsymbol{\tau})] \right) \end{aligned} \quad (2.10)$$

with the mass M_d of atom d , the thermal population factor for Bose particles $n_{\nu}(\mathbf{q})$ and the polarization vector $\mathbf{e}_d(\mathbf{q}, \nu)$ and the frequency $\omega_{\nu}(\mathbf{q})$ of the phonon ν [17]. The coherent one phonon cross section can be divided into two parts: The δ -functions in eq. 2.10 give the conservation of both energy and momentum in the scattering process and it is easily seen that the second line in eq. 2.10 describes the annihilation of a phonon and thus an increase of the neutron's energy in the scattering process, while the third line defines the creation of a phonon and an energy loss of the neutron. The contribution of these two processes to the cross section is asymmetric with respect to the principle of detailed balance: The annihilation of a phonon with frequency ω is counted with the single population function $n_{\nu}(\mathbf{q})$, while the creation of a phonon contributes with a prefactor $n_{\nu}(\mathbf{q}) + 1$ to the summation.

2.1.2 Magnetic neutron scattering

In the case of magnetic neutron scattering the interaction potential between a neutron in spin state $\boldsymbol{\sigma}$ and a moving electron of momentum \mathbf{p} and spin \mathbf{s} is

$$\mathbf{V}_M(\mathbf{r}) = -\gamma\mu_N 2\mu_B \boldsymbol{\sigma} \cdot \left[\text{curl} \left(\frac{\mathbf{s} \times \hat{\mathbf{R}}}{R^2} \right) + \frac{1}{\hbar} \frac{\mathbf{p} \times \hat{\mathbf{R}}}{R^2} \right] \quad (2.11)$$

where $\gamma = 1.9132$ is the gyromagnetic ratio, μ_n and μ_B are the nuclear and the Bohr magneton and \mathbf{R} is the distance vector between the electron and the

neutron. Restricting ourselves for the moment to an unpolarized beam of neutrons, inserting the potential \mathbf{V}_M into the masterformula eq. 2.1 results after some more sophisticated algebra in the differential cross section for pure magnetic scattering

$$\left(\frac{d^2\sigma}{d\Omega dE'}\right)_{\text{mag}} = \frac{(\gamma r_0)^2 k_f}{\hbar k_i} \sum_{\alpha,\beta} \left(\delta_{\alpha,\beta} - \frac{Q_\alpha Q_\beta}{Q^2}\right) S^{\alpha\beta}(\mathbf{Q}, \omega) \quad (2.12)$$

with the classic radius of the electron r_0 and the summation over the spatial coordinates $\alpha, \beta \in [x, y, z]$. The magnetic scattering function $\mathbf{S}(\mathbf{Q}, \omega)$ is defined by the spin-spin correlations

$$S^{\alpha\beta}(\mathbf{Q}, \omega) = \frac{1}{2\pi} \int_{-\infty}^{\infty} \sum_{j,d} \frac{1}{2} g_d f_d(\mathbf{Q}) e^{-W_d(\mathbf{q})} e^{i\mathbf{Q}(j+\mathbf{d})} \langle S_0^\alpha(0) S_{j+\mathbf{d}}^\beta(t) \rangle e^{-i\omega t} dt \quad (2.13)$$

where g is the Landé factor, \mathbf{S} describes the local magnetic moment and $f_d(\mathbf{Q})$ the atomic form factor of atom d in unit cell j .

The magnetic interaction leads in addition to magneto-vibrational scattering which is not included in the above cross section [17].

Elastic magnetic scattering For elastic magnetic scattering we have to evaluate the scattering function $\mathbf{S}(\mathbf{Q}, \omega = 0)$. Defining in analogy with the elastic structural scattering the magnetic structure factor

$$\mathbf{F}_M(\mathbf{Q}) = \gamma r_0 \sum_d \frac{1}{2} g_d f_d(\mathbf{Q}) \langle \mathbf{S}_d \rangle e^{i\mathbf{Q}\mathbf{d}} e^{-W_d(\mathbf{Q})} \quad (2.14)$$

and $\mathbf{F}_{M\perp} = \hat{\mathbf{Q}} \times \mathbf{F}_M \times \hat{\mathbf{Q}}$ with $\hat{\mathbf{Q}} = \mathbf{Q}/Q$, the cross section for elastic magnetic scattering reads

$$\left(\frac{d\sigma}{d\Omega}\right)_{\text{mag}}^{\text{el}} = \frac{2\pi^3}{v_0} \sum_{\tau_M} |\mathbf{F}_{M,\perp}(\tau_M)|^2 \times \delta(\mathbf{Q} - \tau_M), \quad (2.15)$$

and the form of the elastic magnetic cross section looks very similar to the one for nuclear scattering. However, there are some very crucial differences which turn out to be fruitful and will later on allow us to easily separate magnetic from nuclear scattering: In the magnetic structure factor the scattering power of each spin is determined by the prefactor $p = \frac{1}{2} \gamma r_0 g f_d(\mathbf{Q})$,¹ which due to the atomic form factor $f_d(\mathbf{Q})$ rapidly decreases with increasing $|\mathbf{Q}|$ and thus exhibits a contrary $|\mathbf{Q}|$ -dependence as in the nuclear case, where the scattering length b is

¹Notice that p has the dimension of a length; for $\mathbf{Q} = 0$ the magnetic scattering length $p_0 = \frac{1}{2} \gamma r_0 = 0.2695 \times 10^{-12}$ cm is of the same order as a typical nuclear scattering length b .

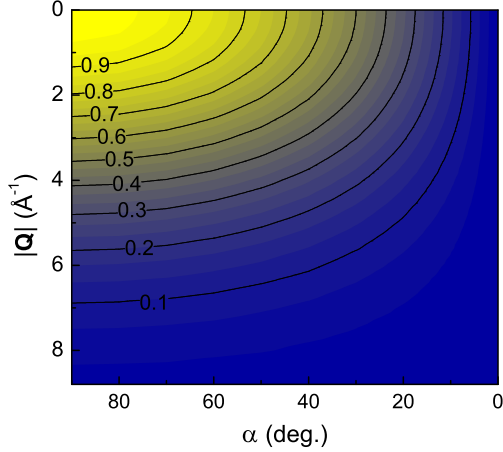


Figure 2.1: $|\mathbf{Q}|$ -dependence of magnetic scattering Simulation of the $|\mathbf{Q}|$ -dependence of the effective magnetic scattering length $f_{\text{Mn}^{3+}}(\mathbf{Q}) \sin(\alpha)$ of a Mn^{3+} -ion for various angles α between the scattering vector \mathbf{Q} and the magnetic moment \mathbf{S} [21].

\mathbf{Q} -independent. This behavior is superimposed by the general scattering law for magnetic scattering, that only the magnetization perpendicular to the scattering vector \mathbf{Q} contributes to the cross section.

To resume, magnetic scattering always exposes a characteristic decrease with $|\mathbf{Q}|$, which furthermore depends sensitively on the angle α between the scattering vector \mathbf{Q} and the magnetic moment \mathbf{S} , see Fig. 2.1.

Inelastic scattering by spin waves If we choose the quantization axis to be along z and if we assume the total z -component of the magnetization S^z to be a constant of motion (as is e.g. the case for the Heisenberg Model) only the terms $\alpha = \beta$ contribute in eq. 2.13 to the scattering function $\mathbf{S}(\mathbf{Q}, \omega)$ and we obtain for a Bravais lattice:

$$\begin{aligned} \left(\frac{d^2\sigma}{d\Omega dE'} \right)_{\text{mag}} &\propto \left(1 - \frac{Q_z^2}{Q^2} \right) \frac{1}{2\pi\hbar} \int_{-\infty}^{\infty} \sum_j e^{i\mathbf{Q}j} \langle S_0^z(0) S_j^z(t) \rangle e^{-i\omega t} dt \\ &+ \sum_{\alpha \in [x,y]} \left(1 - \frac{Q_\alpha^2}{Q^2} \right) \frac{1}{2\pi\hbar} \int_{-\infty}^{\infty} \sum_j e^{i\mathbf{Q}j} \langle S_0^\alpha(0) S_j^\alpha(t) \rangle e^{-i\omega t} dt. \end{aligned} \quad (2.16)$$

In linear approximation the first part of eq. 2.16 is time independent and reproduces the elastic magnetic scattering we have just discussed, and the inelastic scattering by spin waves is determined only by the transverse correlations $\langle S_0^{x,y}(0) S_j^{x,y}(t) \rangle$.

However, evaluating the transverse spin correlation terms for a given complex magnetic structure is in general a non-trivial task. To derive a semi-classical picture of the magnetic excitations in an ordered structure, which later on will be helpful in the interpretation of the observed spectra, we discuss here the simplest possible case – the Heisenberg FM with nearest-neighbor exchange only. The

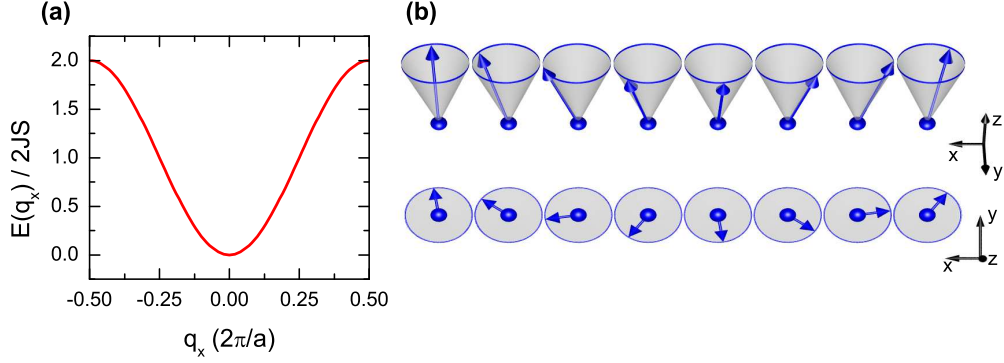


Figure 2.2: Spin waves in the FM Heisenberg model Magnon dispersion for the FM Heisenberg model calculated from eq. 2.18 (a), and snap shot of a spin wave as a precession of the transversal moment in the limit of large S (b)

Hamiltonian of a Heisenberg ferromagnet on a square lattice

$$\mathcal{H} = - \sum_{i,j} J_{i,j} \mathbf{S}_i \mathbf{S}_j = - \sum_{i,j} J_{i,j} \left(S_i^z S_j^z + \frac{1}{2} \left(S_i^+ S_j^- + S_i^- S_j^+ \right) \right) \quad (2.17)$$

is easily diagonalized using the Holstein-Primakoff transformation yielding the spin-wave dispersion, see Fig. 2.2:

$$\hbar\omega(\mathbf{q}) = 4S(J_{\mathbf{q}=0} - J(\mathbf{q})) = 4JS \cdot (2 - \cos(q_x a) - \cos(q_y a)). \quad (2.18)$$

The transverse cross section for the Heisenberg FM is finally given by

$$\begin{aligned} \left(\frac{d^2\sigma}{d\Omega dE'} \right)_{\text{mag}}^{\text{inel}} &= (\gamma r_0)^2 \frac{1}{2} S \left(\frac{1}{2} g f(\mathbf{Q}) \right)^2 \frac{k_f}{k_i} \left(1 + \frac{Q_z^2}{Q^2} \right) e^{-W(\mathbf{Q})} \\ &\times \sum_{\tau_M, \mathbf{q}} \left(n(\mathbf{q}) \delta(E_i - E_f + \hbar\omega_{\mathbf{q}}) \delta(\mathbf{Q} - \mathbf{q} - \tau_M) \right. \\ &\quad \left. + (n(\mathbf{q}) + 1) \delta(E_i - E_f - \hbar\omega_{\mathbf{q}}) \delta(\mathbf{Q} + \mathbf{q} - \tau_M) \right), \end{aligned} \quad (2.19)$$

and consists as for phonon scattering of two parts describing separately the annihilation and creation of a magnon with energy $\hbar\omega_{\mathbf{q}}$ by the neutron [17]. In the limit of large moments S_i the expectation values of the transverse correlations obey the equations

$$\langle S_0^x(0) S_j^x(t) \rangle \propto \cos(\mathbf{qj} - \omega t) \text{ and} \quad (2.20a)$$

$$\langle S_0^y(0) S_j^y(t) \rangle \propto \sin(\mathbf{qj} - \omega t), \quad (2.20b)$$

and a spin wave can be visualized as a precession of the spins around the z -axis, see Fig. 2.2.

Polarization analysis So far we have always integrated out the spin states of the neutron and the cross sections for nuclear and magnetic scattering did not depend explicitly on the neutron spin σ . However, with today's advanced spectrometers and polarization devices it is possible to manipulate very accurately the spin σ of the neutron and the technique of polarized neutron scattering yields additional, often very important details about the system under investigation.

A general treatment of the polarization analysis is quite complex [20]; here, we will restrict ourselves to the case of the *longitudinal polarization analysis* introduced first by Moon, Riste and Koehler [22], and analyze only the projection of the final polarization \mathbf{P}_f of the scattered neutrons on the direction of the initial polarization \mathbf{P}_i .

For the moment, we define a coordinate system (ζ, ς, ξ) for the spin space and take the spin-quantization axis to be along ξ . Treating the spin state of the neutron separately, each cross section using unpolarized neutrons will now give rise to two cross sections in which the spin state of the neutron changes from the $|\pm\rangle$ to the $|\mp\rangle$ state in the scattering process ("spin-flip scattering"), and two cross sections in which the spin state remains unchanged ("non spin-flip scattering"). Ignoring the incoherent scattering from the magnetic moments of the nuclei these cross sections are determined by the four transition amplitudes:

$$\left(\frac{d^2\sigma}{d\Omega dE'}\right)_{|\pm\rangle\rightarrow|\pm\rangle} \propto \left|N(\mathbf{Q}) \pm M_{\perp}^{\xi}(\mathbf{Q})\right|^2 \quad \text{and} \quad (2.21a)$$

$$\left(\frac{d^2\sigma}{d\Omega dE'}\right)_{|\pm\rangle\rightarrow|\mp\rangle} \propto \left|M_{\perp}^{\xi}(\mathbf{Q}) \pm iM_{\perp}^{\zeta}(\mathbf{Q})\right|^2 \quad (2.21b)$$

with the Fourier transform of the nuclear and magnetic density $N(\mathbf{Q})$ and $\mathbf{M}(\mathbf{Q})$ [22]. As aforementioned, in the magnetic channel only the component $\mathbf{M}_{\perp}(\mathbf{Q})$ of the magnetic density $\mathbf{M}(\mathbf{Q})$ perpendicular to the scattering vector \mathbf{Q} contributes to the cross section.

It is now intriguing to discuss the implications derived directly from eq. 2.21, rather than reciting the bulky expressions for the various cross sections.² Inspecting the cross sections eq. 2.21 the fundamental rules for the longitudinal polarization analysis are immediately derived:

- (i) Nuclear scattering does not flip the spin of the neutron.
- (ii) The components of $\mathbf{M}_{\perp}(\mathbf{Q})$ parallel to \mathbf{P}_i always contribute to the non spin-flip scattering.
- (iii) The magnetic components perpendicular to both \mathbf{P}_i and \mathbf{Q} are always detected in the spin-flip channel.

²A comprehensive discussion of this lengthy algebra is e.g. given in the classical textbook on neutron scattering by Marshall and Lovesey [17] and in the more modern review by Chatterij [20].

	NSF	SF
$\mathbf{P}_i \parallel \hat{\mathbf{x}}$	-	$(M_{\perp}^y)^2 + (M_{\perp}^z)^2$
$\mathbf{P}_i \parallel \hat{\mathbf{y}}$	$(M_{\perp}^y)^2$	$(M_{\perp}^z)^2$
$\mathbf{P}_i \parallel \hat{\mathbf{z}}$	$(M_{\perp}^z)^2$	$(M_{\perp}^y)^2$

Table 2.1: Contribution of the in-plane and out-of-plane effective magnetic moments M_{\perp}^y and M_{\perp}^z to the non spin-flip (NSF) and spin-flip (SF) channels for various choices of the incident polarization: parallel to the scattering vector \mathbf{Q} (x), perpendicular to \mathbf{Q} within (y), and perpendicular to both \mathbf{Q} and the scattering plane (z). For convenience, we neglect the influence of chiral terms and scattering due to nuclear-magnetic interference, which would give additional contributions in the SF- \mathbf{P}_x - and NSF- $\mathbf{P}_{y,z}$ -channels, see e. g. Ref. [20].

These simple rules exhibit their full beauty upon combining the cross sections for different choices of the incident polarization \mathbf{P}_i : We define the spatial coordinates (x, y, z) by $\hat{\mathbf{x}} \parallel \mathbf{Q}$, $\hat{\mathbf{y}} \perp \mathbf{Q}$ within and $\hat{\mathbf{z}} \perp \mathbf{Q}$ perpendicular to the scattering plane, as will always be the case for the polarized neutron data presented in this thesis. Now, if $\mathbf{P}_i \parallel \hat{\mathbf{x}}$, magnetic intensity is only observed in the SF-channel, while for $\mathbf{P}_i \parallel \hat{\mathbf{y}}$ only the vertical component $M_{\perp}^z(\mathbf{Q})$ of the magnetization density contributes to the SF-scattering, see Tab. 2.1.2. Taking the difference between the two observed intensities the common background cancels out and we obtain directly the in-plane component of the effective moment $M_{\perp}^y(\mathbf{Q})$:

$$\left(\frac{d^2\sigma}{d\Omega dE'} \right)_{\mathbf{P} \parallel \hat{\mathbf{x}}}^{|\pm\rangle \rightarrow |\mp\rangle} - \left(\frac{d^2\sigma}{d\Omega dE'} \right)_{\mathbf{P} \parallel \hat{\mathbf{y}}}^{|\pm\rangle \rightarrow |\mp\rangle} \propto |M_{\perp}^y(\mathbf{Q})|^2. \quad (2.22)$$

Measuring the various SF cross sections, respectively their differences provides thus the opportunity to define all three components of the magnetic density independently.

In conclusion, the longitudinal polarization analysis enables to recover the spatial details of the magnetic density distribution of a magnetically ordered structure, like e. g. in diffraction experiments the direction of the ordered moment, or, in the case of inelastic scattering, the eigenvectors of magnetic excitations in addition to their eigenfrequencies $\omega_{\mathbf{q}}$ [17, 22].

Crystal-field excitations So far, we have discussed the scattering of collective phenomena like e. g. spin waves. However, neutron scattering is also sensible to local excitations, which will concern us especially in the discussion of the excitation spectrum of the multiferroic compound TbMnO₃.

In a crystal, the surrounding electrostatic field as well as the spin-orbit coupling lifts the degeneracy of an unfilled $4f^n$ configuration of a rare-earth ion and gives

rise to J -multiplets. The neutron can excite the rare-earth ion from a lower to a higher state with a corresponding loss of the neutron energy or deexcite from a higher to a lower energy level. The obtained spectrum reflects the splitting of the J -multiplet and superimposes the scattering by collective excitations: If the different crystal-field states have eigenfunctions $|i\rangle$ with energies δ_i and thermal population n_i , the cross sections for a crystal-field excitation is determined by a series of delta functions:

$$\left(\frac{d^2\sigma}{d\Omega dE'}\right)_{\text{CEF}} \propto \frac{k_f}{k_i} f(\mathbf{Q})^2 \sum_{i,j} n_i |\langle i|J_\perp|j\rangle|^2 \delta(\delta_i - \delta_j - \hbar\omega), \quad (2.23)$$

and again only the component J_\perp of the momentum J perpendicular to \mathbf{Q} contributes to the cross section [23]. The best way to separate the different contributions is to study the \mathbf{Q} -dependence, since local excitations do not possess a characteristic dispersion.

2.2 The triple-axis spectrometer

The experimental realization for using neutrons as a spectroscopic tool for determining the dispersion of phononic and magnetic excitations is the triple-axis spectrometer (TAS) installed at a reactor neutron source. First build by Brockhouse in the late 1950s, a TAS spectrometer allows the full control over the entire (\mathbf{Q}, ω) -space within the borders set by the scattering kinematics in a wide energy and momentum transfer regime. In addition, today's spectrometers are very flexible and extreme sample environments as e.g. strong magnetic fields and advanced neutron techniques like polarization analysis can often be mounted onto these machines.

The TAS spectrometers used for the studies in this work are situated at the four major reactor sources in Germany and France – the “Hahn-Meitner Institut” (HMI) in Berlin, the “Forschungsneutronenquelle Heinz Maier-Leibnitz” (FRM II) in Munich, the “Laboratoire Léon Brillouin” (LLB) near Paris and the “Institut Laue Langevin” (ILL) in Grenoble. According to the energy spectrum of the incident neutrons from the reactor the various spectrometers are divided into three categories: cold, thermal and hot. At the cold spectrometers, like FLEX at the HMI, PANDA at the FRM II, 4F at the LLB and IN12 and IN14 at the ILL, the incoming neutrons are moderated inside the reactor to energies of ~ 25 K. These machines are well suited for high-resolution studies at low energies $\hbar\omega$ between 0 – 10 meV. Thermal spectrometers with incident energies around 300 K are dedicated to the energy regime $\hbar\omega = 10 - 100$ meV and are optimized to a high neutron flux at the sample with reduced energy and \mathbf{Q} resolution. Thermal spectrometers used in this thesis are the PUMA spectrometer installed at the FRM II, the 1T at the LLB and the IN22 at the ILL. Even higher energy transfers up

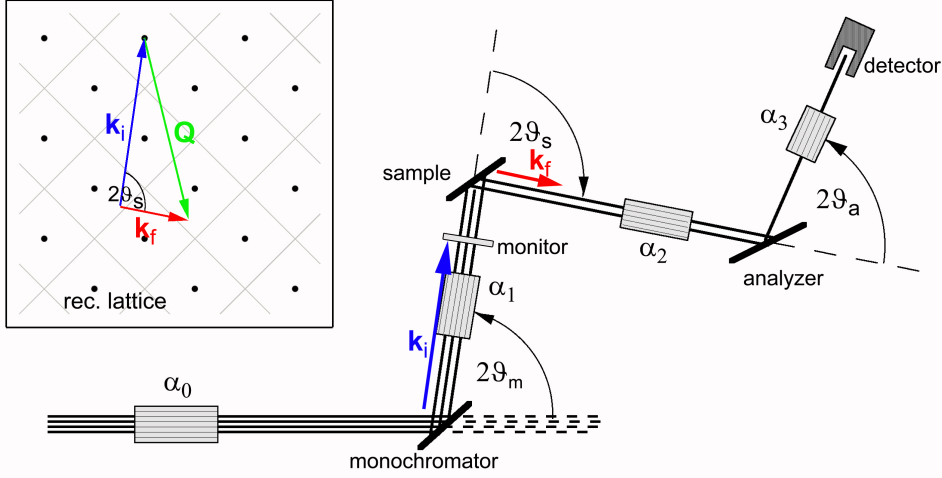


Figure 2.3: General layout of a TAS-spectrometer Classical “W”-configuration of a triple-axis spectrometer with the three movable axis, the horizontal collimation α_i and the trajectory of the neutron in real and reciprocal space.

to 500 meV can be achieved at hot sources, which are, however, not used in this work.

2.2.1 Basic principles of a TAS spectrometer

Although the characteristics of the various spectrometers are quite different, their general layout is very similar, see Fig. 2.3 and 2.4. In order to access a general point in the four-dimensional (\mathbf{Q}, ω) -space it is sufficient to control both the direction and the modulus of the wavevector of the neutron \mathbf{k}_i before and \mathbf{k}_f after the scattering process. The momentum transfer is then given by $\mathbf{Q} = \mathbf{k}_f - \mathbf{k}_i$ and the energy transfer by $\hbar\omega = \frac{\hbar^2}{2m_n}(k_i^2 - k_f^2)$. In a triple-axis spectrometer \mathbf{k}_i and \mathbf{k}_f are usually manipulated by applying Bragg’s law for reflection from a crystal. From the incident beam of neutrons with a continuous energy spectrum determined by the temperature of the moderator a specific energy k_i^2 is selected by elastic Bragg reflection from a monochromator crystal fixing \mathbf{k}_i in the reactor frame:

$$k_i = \frac{2\pi}{2d_M \sin 2\vartheta_M}, \quad (2.24)$$

with the distance d_M between a set of crystal planes and the associated grazing angle ϑ_M . After the scattering at the sample the beam of neutrons is again polychromatic due to inelastic processes and a defined energy k_f^2 in a given direction \mathbf{k}_f can be selected by a second Bragg reflection from an analyzing single crystal before the neutrons are counted in the detector unit. The spatial arrangement of

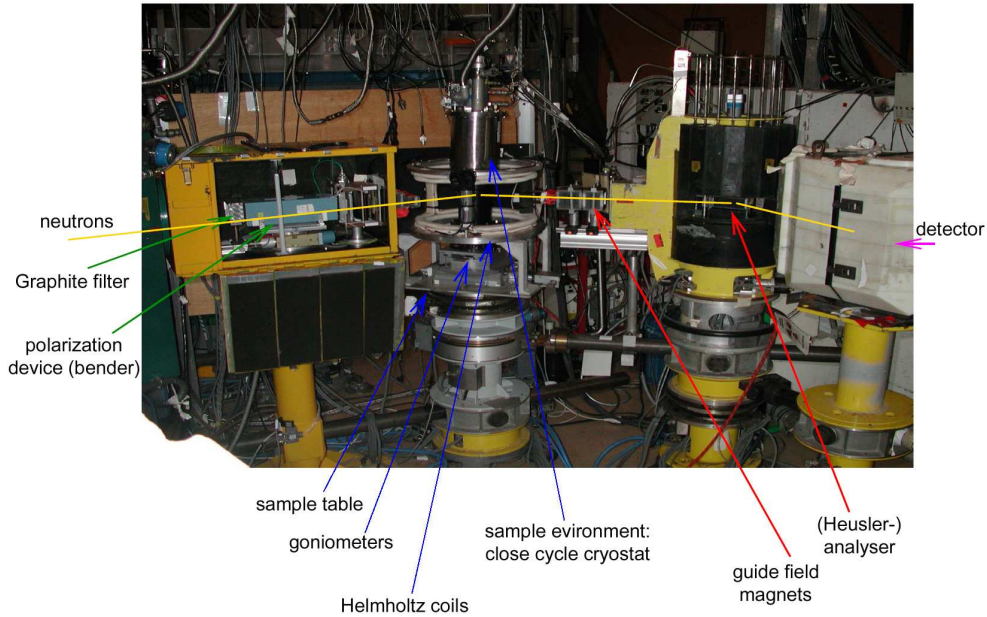


Figure 2.4: Cold triple-axis spectrometer 4F at the LLB The primary spectrometer with the monochromator unit is marked by green, the sample area equipped with a closed-cycle cryostat and the typical Helmholtz coils for longitudinal polarization analysis by blue, and the secondary spectrometer with the monochromator crystal by red annotations. The reactor core is situated in the left and the neutron's trajectory from left to right is marked in yellow.

the monochromator, the sample, the analyzer and the detector thereby defines a plane in the coordinate system of the reactor to which the possible choices for the set $(\mathbf{k}_i, \mathbf{k}_f)$ is restricted. The momentum transfer \mathbf{Q} is thus obviously limited to a single particular crystallographic plane, which has to be chosen properly at the beginning of each experiment!

Besides the reactor, the most important components which determine the performance of a spectrometer are the monochromator and the analyzer. Typically, for unpolarized studies the neutrons are analyzed using the (002)-reflection of pyrolytic Graphite (PG), and in the case of polarized experiments by the (111)-reflection of a Heusler alloy. At lower incident energies $E_i \lesssim 40$ meV the PG(002) reflection is also commonly used for monochromation, while the thermal spectrometers provide additionally a Cu(111) or Cu(220) monochromator for higher neutron energies. To increase the neutron intensity, the monochromator as well as the analyzer consists of several blades which can be curved vertically (and sometimes also horizontally) to focus the divergent neutron beam to the sample position.

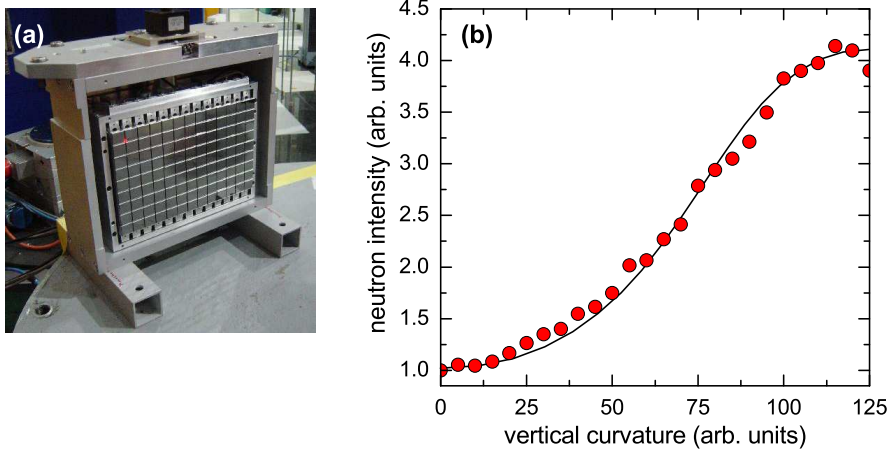


Figure 2.5: Double-focusing PG monochromator at the PANDA spectrometer Double-focusing PG(002) monochromator of the PANDA spectrometer consisting of 117 single blades mounted on the curvature mechanics (a). Measured elastic intensity from a Vanadium standard as a function of the vertical monochromator curvature with a neutron energy of $k_f=1.55 \text{ \AA}^{-1}$ (b).

With this type of curvature on both the monochromator and the analyzer side the measured intensity can easily gain more than a factor 10, see Fig. 2.5, which more than overcompensates the small decrease in resolution due to the focusing. All of the inelastic experiments presented in this thesis have been performed using fully focusing configurations.

The transfer of energy in the scattering process can be realized in two alternative ways – one may either fix the energy of the incident or of the final neutrons to a constant value and vary the other. If possible, we always choose the second alternative with k_f fixed, since in this configuration the spatial angles on the secondary spectrometer are held constant and the angular dependence of the reflectivity of the analyzer has not to be taken into account. Checking the flux of the neutrons behind the monochromator allows to easily correct for changes in the reflectivity of the monochromator and the intensity spectrum of the reactor source simply by normalization to the monitor countrate.

The actual value of the fixed final neutron energy depends decisively on the velocity spectrum of the incident neutron beam. The Maxwell distribution for thermal neutrons has a broad maximum centered at $\approx 50 \text{ meV}$, while on a cold spectrometer the incident flux is maximized around $\approx 5 \text{ meV}$. Therefore, thermal spectrometers perform best with $k_f = 3 - 4 \text{ \AA}^{-1}$, as on a cold machine the incident flux limits the final energy to $k_f < 2 \text{ \AA}^{-1}$. As the density of the reciprocal space increases with decreasing wavelengths, the resolution in both Q and ω is best on a cold source with small fixed final energies – the typical energy resolution determined by the width of the incoherent line of a Vanadium standard on a cold

TAS with k_f fixed to 1.5 \AA^{-1} of $\Delta E \approx 50 \mu\text{eV}$ is an order of magnitude better than on a thermal spectrometer with $\Delta E \approx 800 \mu\text{eV}$ for $k_f = 2.662 \text{ \AA}^{-1}$.

A major problem on a triple-axis spectrometer are higher-harmonic wavelengths, which also satisfy the Bragg condition at the monochromator and analyzer. To reduce the contamination by these parasitic wavelengths appropriate filter based once more on Bragg reflection are commonly used: The maximum wavelength for which Bragg scattering can occur is $\lambda_{\text{max}} = 2d_{\text{max}}$ with a maximum d -spacing d_{max} . For wavelengths greater than λ_{max} the filter is transparent, and choosing a material with an appropriate d_{max} allows to diminish contaminations by higher-order neutrons. In the low-energy regime we have always used polycrystalline Beryllium with an upper cut-off energy of $5.2 \text{ meV} (\approx 1.58 \text{ \AA}^{-1})$ as a band-pass filter. In the higher-energy regime at thermal spectrometers filters of pyrolytic Graphite are the best choice. However, PG-filters are restricted to certain energies with a high transmittance for λ and simultaneously low transmittance, of the order of 10^{-4} , for $\lambda/2$. These energies are well known to be at 13.70 meV , 14.68 meV , 30.6 meV and 34.8 meV , energies which appear in almost all publications on inelastic neutron scattering.

2.2.2 The resolution function

One of the most important aspects in the planning, realization and analysis of a TAS experiment concerns the resolution of the chosen instrument. As the proper manipulation of the resolution is of such immense importance in a TAS measurement, we will present the basic properties of the resolution function in the following paragraph. For further insights into this widespread problematic we, however, refer to the original literature [24–26] and to the excellent illustration in the practical textbook of the Brookhaven group [19].

In a TAS experiment a selected point (\mathbf{Q}_0, ω_0) of the four-dimensional (\mathbf{Q}, ω) -space is selected by the proper settings of the scattering angles at all three axis of the spectrometer, see Fig. 2.3. However, the finite collimation and the imperfect mosaicity of the monochromator crystals allows neutrons corresponding to the scattering event $(\mathbf{Q}_0 + \Delta\mathbf{Q}, \omega + \Delta\omega)$ to reach the detector as well, and the resolution function R of a TAS instrument is defined as the probability of detection of neutrons as a function of $\Delta\mathbf{Q}$ and $\Delta\omega$ when the instrument has been set to measure a scattering process corresponding to the point (\mathbf{Q}_0, ω_0) [24]. Quite obviously, for any given scattering function $S(\mathbf{Q}, \omega)$ the observed intensity in an experiment is determined by the convolution of the scattering function with the instrument's resolution function R ,

$$I(\mathbf{Q}_0, \omega_0) = \int R(\mathbf{Q} - \mathbf{Q}_0, \omega - \omega_0) S(\mathbf{Q}, \omega) d\mathbf{Q} d\omega. \quad (2.25)$$

It is very useful to visualize the resolution function as a four-dimensional ellip-

soid in (\mathbf{Q}, ω) space. The ellipsoid is centered at (\mathbf{Q}_0, ω_0) and the points at the borders of the ellipsoid possess a probability of 50% to reach the detector unit, see Fig. 2.6. The exact size and the spatial orientation of the ellipsoid depends, of course, sensitively on the neutron wavelength, the type of the monochromator crystals, or more precisely on the selected d-spacing, on the scattering sense at the three axis, and on the selected collimation restricting the divergence of the beam.

The control of the spatial orientation of the resolution ellipsoid is often of great importance in an experiment, especially when dealing with dispersive excitations. In Fig. 2.6a we show the low-energy part of the spin-wave dispersion of the charge and orbitally ordered compound $\text{La}_{1/2}\text{Sr}_{3/2}\text{MnO}_4$, which is analyzed in detail in chap. 4. Leaving a detailed discussion to one of the following chapters, for the moment the dispersion can well be understood by two equivalent magnon branches propagation outward from the magnetic zone center $\mathbf{Q} = (0.75 \ 0.75 \ 0)$, corresponding to the modes traveling in the $\pm[q_h - q_h 0]$ directions. Typically, such a dispersion is mapped experimentally by scanning the momentum transfer \mathbf{Q} at a constant energy E , as is indicated by the dotted red line in Fig. 2.6a. However, the experimental response depends decisively on the relative orientation of the resolution ellipsoid and the dispersion surface in the four-dimensional (\mathbf{Q}, ω) -space, and the experimentally observed signal for both (equivalent) branches will be different: For one of the two sides the slope of the dispersion is inclined to the long axes of the ellipsoid, and at this “focusing” side the convolution of the resolution function with the dispersion surface yields a sharp signal. On the other side, the long axes of the ellipsoid are, in the most extreme case, oriented perpendicular to the dispersion surface resulting in a very broad response, see Fig. 2.6b. Of course, in an experiment it is always preferable to choose an appropriate \mathbf{Q} -position allowing to work on the focusing side!

So far, the argumentation seems reversed, as usually the dispersion surface is not known *before* the experiment. Inverting however the above argumentation, the scattering function $S(\mathbf{Q}, \omega)$ has to be extracted by a “deconvolution” of the observed intensity and the experimental resolution. The resolution matrix of a TAS instrument can easily be calculated [24], we usually use the ResLib code implemented for Matlab [27]. An arbitrary scattering function $S(\mathbf{Q}, \omega)$ can then be convoluted with the resolution ellipsoid and subsequently be fitted to a set of data to extract the desired parameters, as e.g. the dispersion relation $\hbar\omega(\mathbf{q})$ of a magnon excitation. A typical example is shown in Fig. 2.6b, where the experimental data are fitted to a model dispersion convoluted with the experimental resolution. Note, that in addition to the physical parameters describing the properties of the scattering function $S(\mathbf{Q}, \omega)$ there is only one adjustable parameter for *all* data points scaling the neutron intensity in this procedure.

In principle, iterating the above algorithm allows a very accurate description of the experimental data yielding simultaneously all relevant physical parameters.

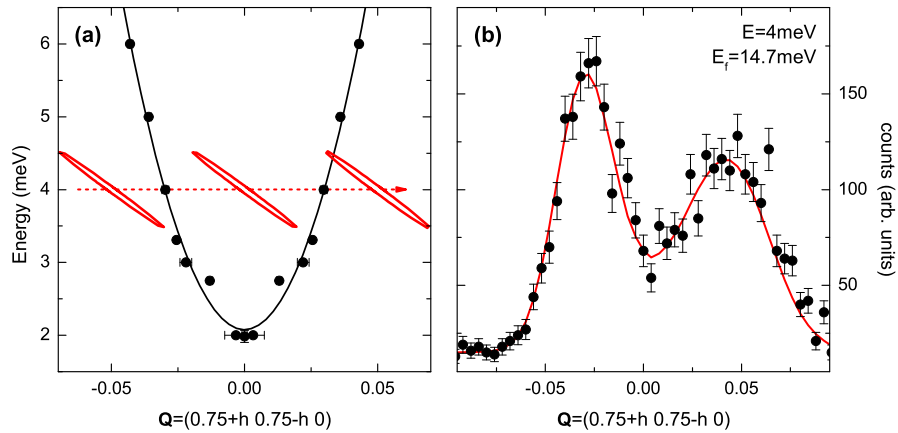


Figure 2.6: The resolution function of a TAS instrument. Low-energy part of the spin-wave dispersion in $\text{La}_{1/2}\text{Sr}_{3/2}\text{MnO}_4$, cf. chap. 4. Red ellipses denote the projection of the resolution ellipsoid onto the $([1\bar{1}0], \omega)$ -plane along a scan with constant energy $E = 4 \text{ meV}$ marked by the dotted line (a). Corresponding raw-data scan recorded at the spectrometer 1T.1 installed at the reactor Orphée in Saclay with the focusing side at negative q_h . The solid line denotes a fit of the scattering function $S(\mathbf{Q}, \omega)$ convoluted with the resolution function to the experimental data (b).

However, performing a triple-axis experiment is always a compromise between several, sometimes conflicting aspects, and the actual situation is often more complex, e. g. the experimental data might not be sufficient to determine all parameters of the scattering function $S(\mathbf{Q}, \omega)$, the resolution function of the spectrometer might not be properly known, as the spatial distances of the instrument had to be varied to optimize the experimental background or the neutron flux, or the experimental conditions are slightly imperfect due to a bad mosaicity of the used single crystal. Therefore, in most of the data presented in this thesis we neglect the, nevertheless, small influence of resolution effects in the analysis, and we obtain the excitation frequencies with a very good accuracy by fitting the data assuming simple Gaussian or Lorentzian line shapes. To acquire a satisfying and consistent description of the data, only in very few cases resolution effects have to be taken explicitly into account, and these exceptions will be considered separately whenever they occur within the following discussion.

3 Magnetic excitation spectrum of single-layered LaSrMnO_4

The parent compound of the perovskite CMR-manganites LaMnO_3 is surely one of the most intensively studied and best characterized compounds in the wide field of transition-metal oxides. The physical properties of pseudo-cubic LaMnO_3 are especially influenced by the orbital degree of freedom, and over the last 50 years experimental and theoretical studies of LaMnO_3 have revealed some very general concepts in the range of what today is called “orbital physics” [28–30]: The strong coupling of the orbital and magnetic degrees of freedom, summarized in the famous Goodenough-Kanamori-Anderson rules (GKA) determining the magnetic ground state of very different transition-metal oxides [31–33], the cooperative ordering of orbitals [34, 35] and the possibility of elementary excitations within this orbital lattice [36, 37] are all inspired by pioneering work on LaMnO_3 . However, besides the great success on the way towards a comprehensive understanding of the Mott-insulator LaMnO_3 in the last decades, some of the main physical properties are still discussed very controversially today, and the debate is remarkably vivid, see e. g. Refs. [38–40].

Closely related to the perovskite LaMnO_3 is its two-dimensional analog, single-layered LaSrMnO_4 . However, in light of the enormous amount of work on perovskite and even bilayer manganites, it appears very astonishing that the single-layered system is only little studied so far. The reduction of the electronic dimensionality together with the simple crystallographic structure in the $\text{La}_{1-x}\text{Sr}_{1+x}\text{MnO}_4$ -series offers the unique opportunity to study the complex interplay between orbital, spin and lattice degrees of freedom, typical for the physics of manganites, in a less complex environment, and opens the way to a systematic investigation of certain aspects related with the CMR-effect, namely charge and orbital order phenomena.

In this chapter we present our results of inelastic neutron-scattering experiments on the magnetic excitation spectrum in the parent compound of the family of single-layered manganites, LaSrMnO_4 . To introduce the properties of the $\text{La}_{1-x}\text{Sr}_{1+x}\text{MnO}_4$ -series more closely, we review in the beginning of this chapter the main features of the electronic phase diagram, focusing, however, on the orbital and magnetic ordering in the undoped compound LaSrMnO_4 . Subsequently, we continue with the discussion of the experimental results on the magnetic excitation spectrum, and, finally, we close the chapter with some concluding remarks.

3.1 Basic properties of single-layered LaSrMnO_4

The partial substitution of three-valent La by two-valent Sr in the series of single-layered manganites $\text{La}_{1-x}\text{Sr}_{1+x}\text{MnO}_4$ oxidizes the central Manganese sites, which possess a formal valence $\text{Mn}^{(3+x)+}$. In this sense, the composition LaSrMnO_4 corresponds to the perovskite LaMnO_3 , as all Mn-ions are three valent with a $3d^4$ electron configuration. Therefore, we frequently refer to LaSrMnO_4 as undoped. The main physical features of undoped LaSrMnO_4 and of the phase diagram of $\text{La}_{1-x}\text{Sr}_{1+x}\text{MnO}_4$ and $0 \leq x \leq 1$ have been elaborated by several groups, see Refs. [7, 41–45], as well as [46] and [senff05a], and we will shortly summarize the basic properties in the following introductory section.

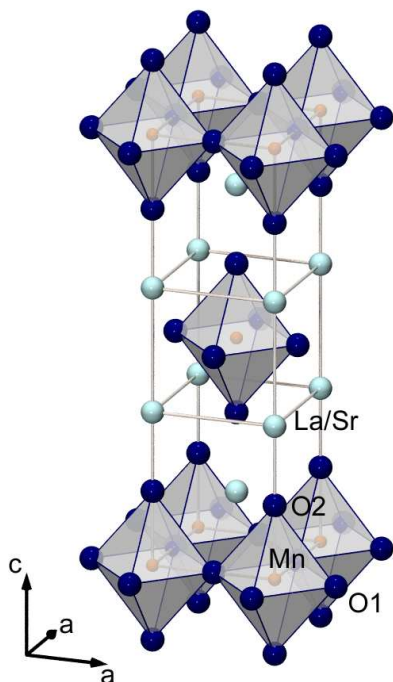


Figure 3.1: Tetragonal crystal structure of space-group symmetry $I4/mmm$ of the single-layered 214-manganites $\text{La}_{1-x}\text{Sr}_{1+x}\text{MnO}_4$.

structure adjacent planes are shifted by $[a/2 a/2 0]$ with respect to each other and separated by an intermediate rock-salt like La/Sr-O block along the tetragonal axis, reducing the electronic dimensionality from three down to two.

The electronic phase diagram of the $\text{La}_{1-x}\text{Sr}_{1+x}\text{MnO}_4$ -series as published in Ref. [7] is shown in Fig. 3.2. Similar to LaMnO_3 , the parent compound LaSrMnO_4 is a typical Mott-Hubbard system [47, 48], showing an insulating behavior with, due to the layered structure, very anisotropic transport properties [42]. Below $T_N \approx 128 \text{ K}$ the system orders magnetically with, contrary to the well-known

All known compounds of the series $\text{La}_{1-x}\text{Sr}_{1+x}\text{MnO}_4$ crystallize in the tetragonal K_2NiF_4 structure with space-group symmetry $I4/mmm$ [41, 43], see Fig. 3.1. In this high-symmetry structure the characteristic MnO_6 -octahedra are linked by common corners to form an array of perfect MnO_2 -square planes. These planes are topologically identical to those of the other known members of the Ruddlesden-Popper series of rare-earth manganites $\text{R}_{n+1}\text{Mn}_n\text{O}_{3n+1}$, such as the perovskite RMnO_3 ($n = \infty$, frequently referred to as 113-structure) and the double-layer compound $\text{R}_3\text{Mn}_2\text{O}_7$ with $n = 2$ (often labeled as 327-structure), and in this, as well as in the following chapter, we will mainly be concerned with the orbital and magnetic correlations within these layers. While in the perovskite structure neighboring planes are directly linked to form a three-dimensional network, in the 214-

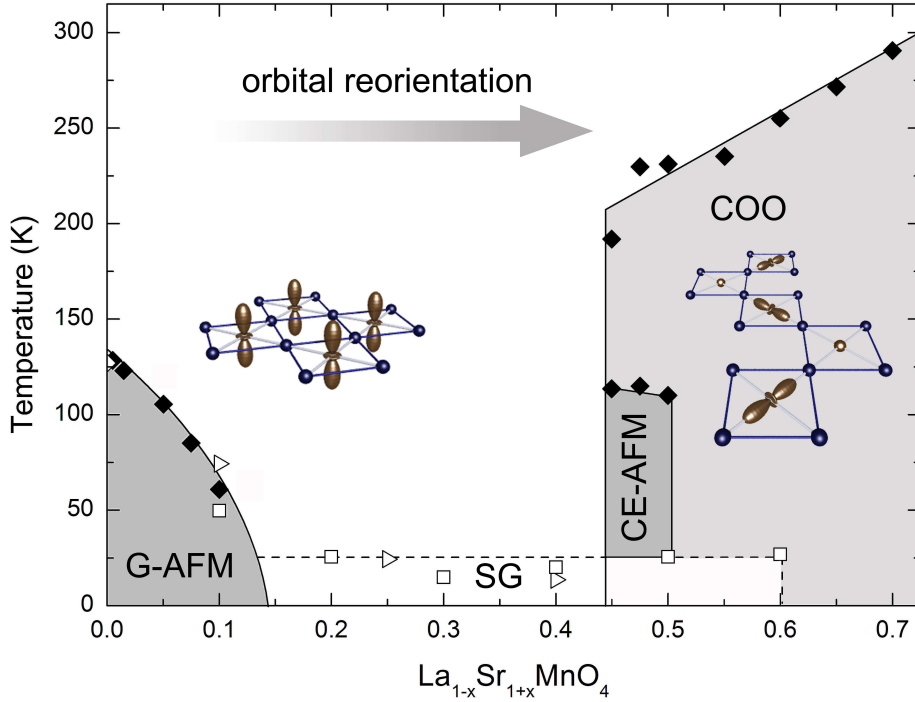


Figure 3.2: Electronic phase diagram of $\text{La}_{1-x}\text{Sr}_{1+x}\text{MnO}_4$ Phase diagram of single-layered manganites $\text{La}_{1-x}\text{Sr}_{1+x}\text{MnO}_4$ as published by Laroche et al. [7]. The abbreviations are G-type antiferromagnet, G-AFM; CE-type antiferromagnet, CE-AFM; spin glass, SG; charge/orbital order phase, COO; short-range charge and orbital order, SRO. Also included is the occupation of the e_g -orbitals; in the low doping regime the electrons occupy orbitals with $d_{3z^2-r^2}$ -symmetry aligned perpendicular to the planes, whereas for larger x the orbitals are oriented within the MnO_2 -layers. The phase diagram for $x > 0.75$ has been studied in Ref. [44] and the charge ordered state extends to $x \approx 0.9$.

A-type ordering in LaMnO_3 , an AFM coupling within the MnO_2 -layers [49, 50]. Next-nearest neighbor planes order ferromagnetically, and in analogy to the classification scheme of the perovskites the spin arrangement in LaSrMnO_4 is frequently referred to as a G-type ordering, see Fig. 3.3.¹

Upon doping, the room temperature resistivity decreases continuously, but all compounds remain insulating [42]. Simultaneously, hole doping suppresses the G-type ordering observed for $x = 0$: The Néel temperature rapidly decreases with increasing hole concentration and the G-type ordering finally disappears around $x \approx 0.15$ [7, 43]. For intermediate doping concentrations $0.15 < x < 0.4$ no long-range order exists, and spin-glass behavior is revealed by several experimental

¹However, as the classification scheme derived by Wollan and Kohler is ambiguous in the case of layered structures, the magnetic ordering in LaSrMnO_4 is referred to as C-type in some publications [51, 52].

techniques [7, 42, 53]. For larger values $x \geq 0.4$ magnetic ordering reappears, but the ordering scheme is more complex than the simple G-type. The region around half doping is characterized by a combined ordering of charge, orbital and lattice degrees of freedom [42, 54], which is discussed very controversially [8, 9], and seems to be intimately coupled to the observed huge drop of the electric resistivity at the metal-insulator transition in the perovskite manganites. However, this region of the phase diagram will be the issue of the following chapter, and for the moment we will restrict ourselves to the low-doping regime $x < 0.4$. Note, however, that our analysis of the magnetic correlations around half doping results in a critical revision of the present phase diagram shown in Fig. 3.2, see Fig. 4.34 in Chap. 4.

Orbital correlations in single-layered manganites La_{1-x}Sr_{1+x}MnO₄ The electronic phase diagram is significantly influenced by the orbital degree of freedom, which in the single-layered manganites is strongly correlated with the magnetic ordering via the GKA-rules.

In the undoped compound LaSrMnO₄ all Mn-ions are three valent with electronic configuration $3d^4$ and the doubly degenerate e_g -level of cubic symmetry is single occupied. The remaining degeneracy of the two e_g -levels can further be removed in a tetragonal symmetry, either by a tetragonal crystal field [55] or by the well-known Jahn-Teller effect [29], and it has been shown by band structure calculations and by Monte Carlo simulations that an intermediate crystal-field E_z stabilizes a dominant occupation of the out-of-plane $d_{3z^2-r^2}$ -orbitals against the in-plane $d_{x^2-y^2}$ -states in LaSrMnO₄ [56, 57].² Indeed, x-ray and neutron diffraction experiments reveal a negative thermal expansion of the tetragonal c -axis below $T_{JT} \approx 600$ K, which is shown to arise from a temperature-dependent elongation of the MnO₆-octahedra and which is interpreted as evidence for a ferro-orbital ordering of the $d_{3z^2-r^2}$ -states, see [43, 46] and [senff05a]. Later on, this argumentation has been confirmed by measurements of linear dichroism [58] and by results of x-ray absorption experiments [51, 52].

Slightly substituting La by Sr removes electrons from the e_g -band forming isolated Mn⁴⁺-ions with local electron configuration $3d^3$ and *empty* e_g -states, thereby affecting also the orbital occupation on the neighboring sites. The subtle balance of the crystal-field energy E_z and the orbital ordering is decisively influenced even by small changes in the e_g -electron density n_e [57], and it has been shown that a localized hole attracts the surrounding orbitals to form a composite object involving several Mn-sites, which frequently is referred to as “orbital polaron” [59, 60]. Consequently, even slight hole doping changes the orbital occupation considerably, and the out-of-plane occupation in LaSrMnO₄ flops into the MnO₂-layers for in-

²The crystal field parameter E_z is usually understood as an effective parameter parameterizing the splitting of the e_g -level due to the tetragonal crystal field E_{tetra} and the Jahn-Teller energy E_{JT} .

intermediate doping levels $x \geq 0.25$, as is experimentally evidenced by the rapid suppression of the c -axis elongation with increasing x and recent results of x-ray absorption measurements [43, 52] and [senff05a].

The orbital structure is closely related with the observed magnetic correlations, and the AFM coupling of adjacent Mn-sites within the planes in the G-type ordering is fully consistent with the ferro-orbital ordering of the $d_{3z^2-r^2}$ -type [33]. The observed rapid suppression of the G-type ordering upon slight hole doping is the counterpart of the reorientation of orbital occupation in the magnetic sector: The appearance of the spin-glass phase for $x \approx 0.25$ might be attributed to the competition between the AFM superexchange and the FM Zener double exchange in a Mn^{3+} - Mn^{4+} cluster, mediated within the planes by the anisotropic orbital arrangement [57, 60].

3.1.1 Magnetic order in undoped LaSrMnO_4

So far, the magnetic and orbital ordering in the undoped compound seems well understood. However, as we will show below, this seems far from truth as certain experimental observations are inconsistent with the simple G-type ordering.

The G-type magnetic ordering in undoped LaSrMnO_4 has been investigated in detail by several groups [7, 42, 43, 46, 49, 50]. Below $T_N \approx 128\text{K}$ the compound orders antiferromagnetically as evidenced by the appearance of superstructure reflections with propagation vector $\mathbf{Q} = (1/2\ 1/2\ 0)$ in neutron scattering experiments. The magnetic moments are aligned along the tetragonal c -axis, and at low temperatures the ordering is three dimensional and long range. Due to the antiferromagnetic ordering within the planes, the coupling between neighboring planes is frustrated in the body-centered K_2NiF_4 structure, and two different twin do-

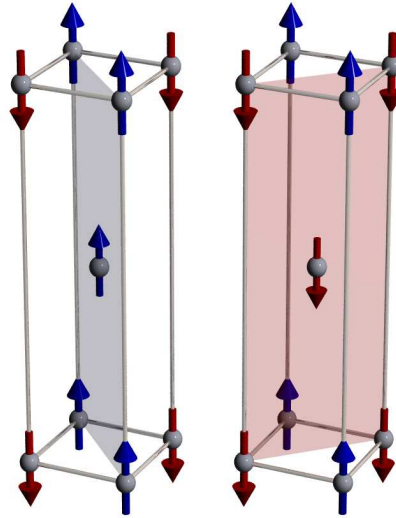


Figure 3.3: Magnetic G-type ordering in LaSrMnO_4 showing the two different magnetic domains.

domains corresponding to the two ordering schemes shown in Fig. 3.3 contribute in diffraction experiments. Next-nearest neighbor planes are coupled ferromagnetically via a weak higher-order process yielding the three-dimensional G-type arrangement. At low temperatures, the ordered moment is quite large, $3.21\ \mu_B$, but still lower than $4.0\ \mu_B$ expected for a Mn^{3+} -ion without an orbital contribution, and the reduction of the ordered moment can only partially be explained by the

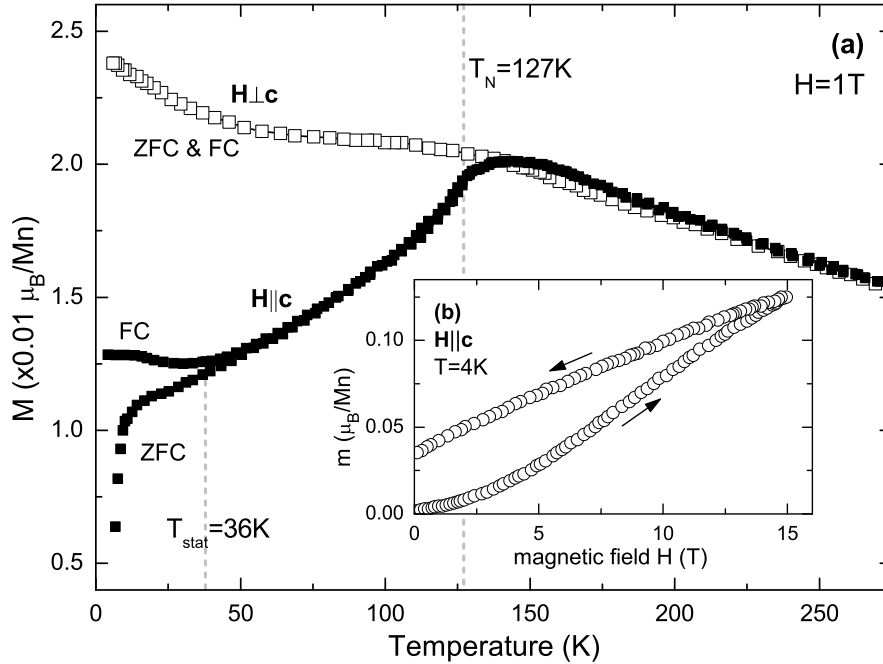


Figure 3.4: Macroscopic magnetization of LaSrMnO_4 Temperature dependence of the macroscopic magnetization $M(T)$ in LaSrMnO_4 for a field $H = 1 \text{ T}$ applied parallel and perpendicular to the c -axis. Upon field cooling (FC), a finite magnetization is visible for $H \parallel c$, while in the zero-field run (ZFC) the magnetization vanishes for $T \rightarrow 0 \text{ K}$ (a). Field dependence of the magnetization $M(H)$ at $T = 4 \text{ K}$ for the field H applied along c revealing a finite remanent magnetization of $\approx 0.05 \mu_B/\text{Mn}$ (b). All data were digitized from Ref. [43].

influence of magnetic fluctuations in the two-dimensional structure. The critical behavior close to the phase transition at T_N has been shown to resemble the characteristic behavior of a two-dimensional antiferromagnet with a strong Ising-like anisotropy, which furthermore is supported by a large anisotropy-gap in the magnetic excitation spectrum, and LaSrMnO_4 is treated as a simple two-dimensional Heisenberg antiferromagnet in the recent literature [7]. However, although the above picture seems consistent and agrees nicely with the proposed orbital ordering in LaSrMnO_4 , a careful analysis of the macroscopic magnetization and of the magnetic excitation spectrum are contrasting this simple approach and the actual situation is more complex [43, 46].

Macroscopic magnetization of LaSrMnO_4 In Fig. 3.4 we show the temperature and field dependence of the macroscopic magnetization $M(T, H)$ as reported by P. Reutler [43]. In a wide temperature regime the magnetization $M(T)$ exhibits the typical behavior of a conventional antiferromagnet with the moment aligned along c – above $T_N = 128 \text{ K}$ $M(T)$ shows a Curie-like increase and below

the Néel transition the parallel magnetization $M_{\parallel}(T)$ with the field \mathbf{H} applied parallel to the ordered moment decreases, while the perpendicular magnetization $M_{\perp}(T)$ is only slightly affected due to the induced canting of the spins. However, at low temperatures $T < 40$ K the progression of $M_{\parallel}(T)$ significantly deviates from the expected behavior of a simple antiferromagnet: While $M_{\parallel}(T)$ vanishes for $T \rightarrow 0$ K in the zero-field cooled (ZFC) cycle, the field-cooled (FC) signal shows a pronounced cusp at $T_{\text{stat}} \approx 36$ K and the magnetization remains at a finite value of $\approx 0.015 \mu_{\text{B}}/\text{Mn}$ for $T \rightarrow 0$ K. A similar behavior is absent in the perpendicular magnetization and the low-temperature properties of the magnetization $M(T)$ point to the existence of *ferromagnetic* domains, which can be aligned by a magnetic field applied along \mathbf{c} .

The field dependence of the magnetization $M(H)$ at $T = 4$ K further supports the existence of ferromagnetic correlations. Below T_{stat} , for small fields $\mathbf{H} \parallel \mathbf{c}$ $\frac{\partial^2 M}{\partial H^2} > 0$, and $M(H)$ is curved to the left, while $M(H)$ is right-curved for strong fields $H > 10$ T, somehow reminiscent of a metamagnetic transition [61]. Furthermore, with decreasing field a significant hysteresis and a finite remanent magnetization $\approx 0.05 \mu_{\text{B}}/\text{Mn}$ is observed, in strong contrast to the expected behavior of an antiferromagnet with vanishing macroscopic magnetization in zero field [43].

Magnon spectrum of LaSrMnO₄ The second experimental evidence against the simple Heisenberg ordering in LaSrMnO₄ comes from the analysis of the spin-wave excitation spectrum. The magnon dispersion in the ordered phase has been investigated using inelastic neutron scattering by Laroche et al. [7] and in the Diploma thesis of myself [46]. The \mathbf{q} -dependence of the magnetic excitations along the main symmetry directions as elaborated in Ref. [46] is shown in Fig. 3.5.

Using cold neutrons, the energy scan at the antiferromagnetic zone-center $\mathbf{Q} = (0.50.50)$ reveals three different contributions to the excitation spectrum at $\hbar\omega_{\text{cl},1} = 3.3$ meV, $\hbar\omega_{\text{cl},2} = 6.5$ meV, and $\hbar\omega_{\text{sw}} = 8.80$ meV [46],³ in contrast to the expectation of a single magnon branch in a two-dimensional Heisenberg model, see Fig. 3.5b. However, only the mode ω_{sw} possesses a pronounced \mathbf{q} -dependence within the MnO₂-planes, see Fig. 3.5a, which is well describable following linear spin-wave theory. With only a nearest-neighbor exchange J_{AFM} in the layers, the Heisenberg model on a two-dimensional square lattice yields in linear approximation the dispersion relation

$$\hbar\omega = 4J_{\text{AFM}}S\sqrt{(1 + \alpha)^2 - \frac{1}{4}(\cos(2\pi q_h) + \cos(2\pi q_k))^2}, \quad (3.1)$$

with $\alpha = \Lambda/2J_{\text{AFM}}$ and the single-ion anisotropy Λ [62]. The observed \mathbf{q} -dependence is excellently modeled using the parameter set $J_{\text{AFM}} = 3.07$ meV

³Note, that Laroche et al. only discuss a single magnon branch at 8.80 meV, although a second feature at 6.5 meV is clearly resolvable in the data shown in Fig. 4 of Ref. [7].

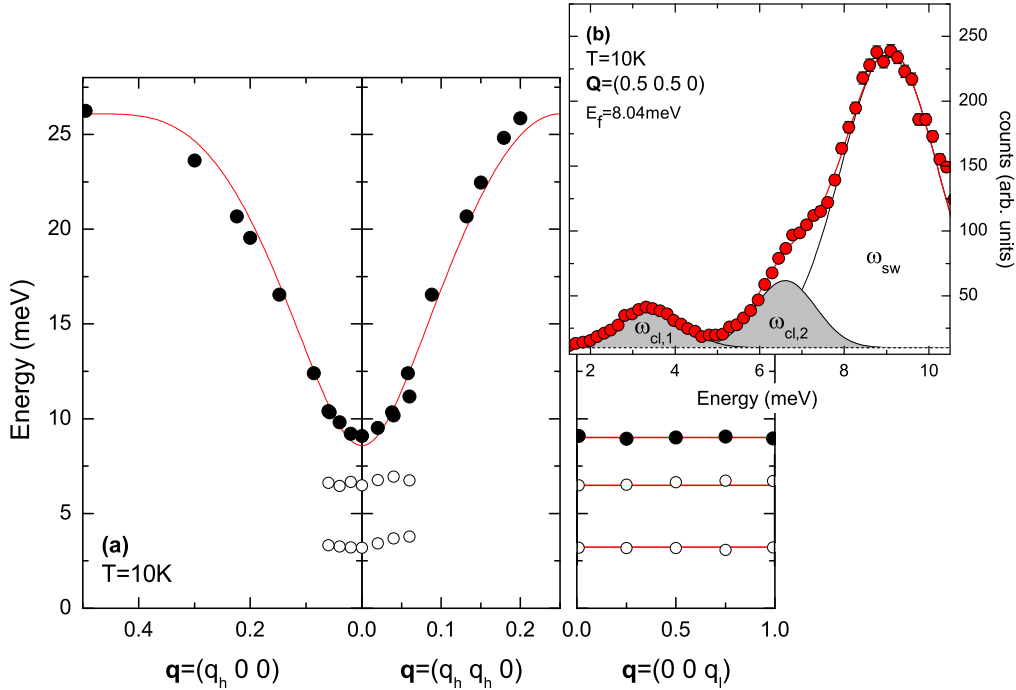


Figure 3.5: Spin-wave dispersion in LaSrMnO_4 Spin-wave dispersion of LaSrMnO_4 at $T = 10\text{ K}$ as determined in Ref. [46] (a). Energy scan at the antiferromagnetic zone center $\mathbf{Q} = (0.5\ 0.5\ 0)$ recorded at the cold TAS-instrument 4F.1 with $E_f = 8.04\text{ meV}$ revealing the three different contributions to the magnetic excitation spectrum at $\hbar\omega_{\text{cl},1} = 3.3\text{ meV}$, $\hbar\omega_{\text{cl},2} = 6.5\text{ meV}$, and $\hbar\omega_{\text{sw}} = 8.80\text{ meV}$ (b). In (a), solid lines denote the fit of the data using the dispersion relation eq. 3.1, while in (b) solid lines represent the fit of the raw data using Gaussian line shapes for the different components of the spectrum.

and $\Lambda = 0.38\text{ meV}$ [46], which is in good congruence with the results reported by Laroche et al. [7]. Along $[001]$ the frequency of the mode ω_{sw} does not change significantly, and the magnetic exchange along \mathbf{c} is considerably small – from the experimental resolution one may deduce $J_c < 0.02J_{\text{AFM}}$ – pointing to the two-dimensional character of the magnetic ordering in the layered structure.

As aforementioned, the two additional modes at 3.3 meV and 6.5 meV are not consistent with the simple G-type approach. In contrast to the branch ω_{sw} these modes do not possess a significant \mathbf{q} -dependence, and both are localized around $\mathbf{q} = 0$ in reciprocal space fading rather rapidly away upon increasing $|\mathbf{q}|$ [46]. The physical origin of the two modes ω_{cl} , and whether or not these two modes have to be connected with the ferromagnetic domains revealed in the analysis of the macroscopic magnetization is still an open question. First attempts to explain at least the unusual behavior of the magnetic susceptibility suggest a slight canting of the magnetic moments away from the tetragonal axis or even a *ferrimagnetic* ordering for LaSrMnO_4 , but remain somehow speculative [43].

Before we proceed with the presentation of our new results on the magnetic excitation spectrum in LaSrMnO_4 , we first want to comment on the generality of the above observations, which seems of certain relevance for the following discussion. Regarding the drastic changes of the magnetic properties upon slight changes in the nominal valency of the Mn-ions, see the phase diagram Fig. 3.2, a precise control of the stoichiometry of the used sample crystals is vital for the interpretation of the experimental data. In light of this aspect, it seems noteworthy that the experimental findings discussed above, the unusual behavior of the magnetic susceptibility and the unconventional magnetic excitation spectrum, have been obtained from experiments on the same specimen grown by P. Reutler at the University of Paris [43]. However, although not explicitly discussed in the literature, both features are visible in the published data, too – e.g. a non-vanishing macroscopic magnetization for $H||c$ is revealed in the data published by Moritomo et al. [42], while the neutron data of Laroche et al. exhibit an additional mode in the excitation spectrum around ≈ 6.5 meV [7].

To further cross-check these results, another sample crystal of nominal composition LaSrMnO_4 was grown by M. Benomar at the University of Cologne [63]. Although the Néel temperature was slightly higher in this crystal, pointing to an even better stoichiometry of this specimen, the same unconventional behavior with three different magnon branches and a finite macroscopic magnetization for $T \rightarrow 0$ K is observed [64, 65]. Furthermore, a recently grown crystal of nominal stoichiometry $\text{La}_{0.95}\text{Sr}_{1.05}\text{MnO}_4$, $x = 0.05$, does not show similar effect [66]. Hence, with at least four different sample crystals, two in our group and the crystals used in Refs. [42] and [7], showing similar results, the unconventional behavior is unique and can not be ascribed to the influence of a slight non-stoichiometry of the samples, but has to be attributed to the physics of undoped LaSrMnO_4 .

3.2 Revision of the magnetic excitation spectrum in LaSrMnO_4

In order to establish the magnetic character of the two additional modes in the magnetic excitation spectrum of LaSrMnO_4 and to further characterize the properties of these unusual features, we have extended our former neutron studies to a comprehensive investigation with polarized neutrons as well as with strong magnetic fields. Both experiments were performed at the thermal triple-axis spectrometer IN22 installed at the ILL in Grenoble. We used the same large single crystal grown by P. Reutler as in our previous studies [43, 67]. The sample was fixed in a special mount, which allowed to easily change the orientation of the sample, so that reflections of the kind $(h k 0)$ or $(h h l)$ were accessible in these experiments – however, in most of the cases we worked with the first orientation and the scatter-

ing plane defined by the directions $[1\ 0\ 0]$ and $[0\ 1\ 0]$ of the tetragonal structure. At the thermal beam, we typically fixed the energy of the scattered neutrons on the analyzer side to 14.7 meV (corresponding to $k_f = 2.662\ \text{\AA}^{-1}$), but to increase the experimental resolution selected scans were repeated with the final energy set to $E_f = 8.04\ \text{meV}$ ($\hat{=} 1.97\ \text{\AA}^{-1}$). In all cases a PG-filter was used to suppress spurious contributions by second-order neutrons. The field dependence of the excitations was studied using a 12 T superconducting vertical magnet, while the polarization analysis was performed using the Cryopad device mounted on IN22 [68]. In the first case, the energy of the initial and final neutrons was controlled using the $(0\ 0\ 2)$ -reflection of pyrolytic Graphite, whereas we used the $(1\ 1\ 1)$ -reflection of a Heusler alloy on both sides of the spectrometer to control both the neutron wave vector and spin in the polarization study.

3.2.1 Polarization analysis of the magnetic excitations

We start with the discussion of the polarization analysis of the magnetic excitation spectrum in LaSrMnO_4 . In Fig. 3.6 we show the spin-flip (SF) intensity of the energy scan at the antiferromagnetic zone center $\mathbf{Q} = (0.5\ 0.5\ 0)$ at $T = 1.5\ \text{K}$ for the spin quantization axis parallel to the scattering vector \mathbf{Q} . In the SF-channel nuclear scattering does not contribute and all observable scattering is magnetic. Also included in Fig. 3.6 is the similar scan recorded with unpolarized neutrons and enhanced experimental resolution, presented already in Fig. 3.5b: Although the polarized data appear slightly scattered around the unpolarized data due to a lower statistic,⁴ both data sets scale almost perfectly, proving unambiguously the magnetic character of all three features in the excitation spectrum.

Hence, as a first result we conclude that two additional modes $\omega_{\text{cl},1}$ and $\omega_{\text{cl},2}$ are indeed *magnetic* excitations. However, polarization analysis is much more powerful, and the combination of different choices of the neutron spin quantization axis allows to resolve not only the frequencies of the different modes, but also their polarization with respect to the ordered moment. In the classical longitudinal polarization analysis described in the introductory chapter, the projection \mathbf{P}_f of the neutron spin after the scattering process onto the direction of the spin quantization axis \mathbf{P}_i before the scattering process is analyzed for three different choices of \mathbf{P}_i : Parallel to the scattering vector \mathbf{Q} (x), perpendicular to the scattering vector \mathbf{Q} and parallel to the scattering plane defined by \mathbf{k}_i and \mathbf{k}_f (y), and perpendicular to both \mathbf{Q} and the scattering plane (z), as is illustrated in the inset

⁴Note that working with polarized neutrons significantly reduces the neutron flux as only one neutron spin state is selected and the experimental setup is more complex. Compared to a measurement with unpolarized neutrons the count rate is decreased by at least a factor 6 at the IN22 spectrometer, which due to the limited beam time available restricts the polarization analysis to some selected scans or points.

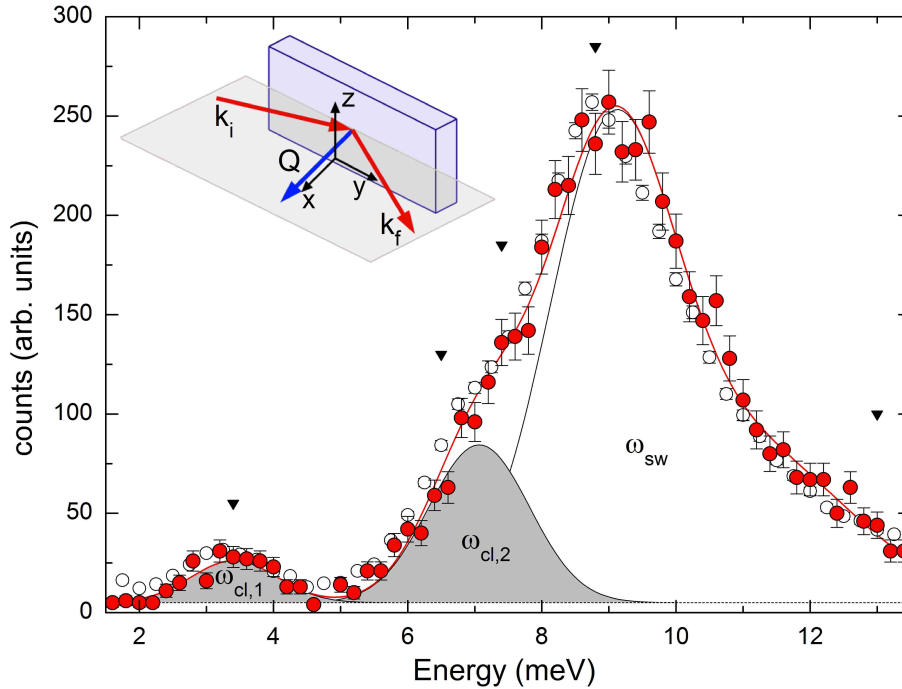


Figure 3.6: Polarization analysis of the magnetic excitation spectrum at $\mathbf{q}=0$ Spin-flip channel (SF) of the energy scan at the antiferromagnetic zone center $\mathbf{Q} = (0.5\ 0.5\ 0)$ at $T = 1.5\text{ K}$ recorded using polarized neutrons at the IN22 spectrometer with the spin quantization axis parallel to the scattering vector \mathbf{Q} and $E_f = 14.7\text{ meV}$ (a). Open symbols denote the corresponding scan with unpolarized neutrons already shown in Fig. 3.5b. Black triangles mark the energies which were investigated in more detail using different choices of the quantization axis, see text for details. The inset sketches the classical choice of the coordinate system for spin space in the longitudinal polarization analysis relative to the scattering vector \mathbf{Q} and to the scattering plane.

of Fig. 3.6.⁵ The combination of the different cross sections allows to reconstruct the components of the magnetization parallel and perpendicular to the scattering plane, see Tab. 2.1.2 in Chap. 2. As for the complete polarization analysis six different cross sections have to be measured – NSF- and SF-channel for each of the three different choices for \mathbf{P}_i – this analysis is very time consuming, and we have decided to study in detail five representative energies of the excitation spectrum with sufficient statistic, depicted by the black triangles in Fig. 3.6. A typical counting time for these measurement is 45 min for one of the six necessary

⁵Note, that the Cryopad device allows to go beyond this classical analysis and enables even to reconstruct the non-diagonal terms of the polarization matrix, which is frequently referred to as full or spherical polarization analysis [20, 68]. We will, however, restrict ourselves to the analysis of the longitudinal terms, as the transverse terms usually vanish in a collinear magnetic structure.

3 Magnetic excitation spectrum of single-layered LaSrMnO₄

Q	Energy		P_x	P_y	P_z	FR _{x}	FR _{y}	FR _{z}
(0.5 0.5 0)	0.0 meV	SF	256144	257032	10711			
		NSF	10651	10376	254484	0.042(1)	0.040(1)	23.8(2)
(0.5 1.5 0)	0.0 meV	SF	189503	189114	6719			
		NSF	6636	6729	190015	0.035(1)	0.036(1)	28.3(4)
(200)	0.0 meV	SF	5074	5185	5354			
		NSF	124427	127020	128507	24.5(4)	24.5(3)	24.0(3)
(0.5 0.5 0)	3.4 meV	SF	425	-14	460			
		NSF	23	455	10	0.054(9)	32(8)	0.021(7)
	6.5 meV	SF	612	19	604			
		NSF	13	577	12	0.021(6)	30(7)	0.020(6)
	7.4 meV	SF	598	22	621			
		NSF	30	631	25	0.050(9)	29(6)	0.040(8)
	8.8 meV	SF	1267	60	1212			
		NSF	70	1216	47	0.055(7)	20(2)	0.039(6)
	13.0 meV	SF	427	25	397			
		NSF	32	410	49	0.075(9)	16(4)	0.040(8)

Table 3.1: Summary of the results of the longitudinal polarization analysis in LaSrMnO₄ at T=1.5 K as determined at the spectrometer IN22. The spin quantization axis is given by P_j , where the subscripts x, y, z refer to $\mathbf{P} \parallel \mathbf{Q}$ (x), $\mathbf{P} \perp \mathbf{Q}$ within (y), and $\mathbf{P} \perp \mathbf{Q}$ perpendicular to the scattering plane (z). For each Q -position the spin-flip (SF) and the non spin-flip (NSF) intensity, as well as the corresponding flipping ratio $FR_j = (SF/NSF)_j$ is shown at various energies. A common background has been subtracted in all the data shown.

configurations, restricting the detailed analysis to selected points only. The results are summarized in Tab. 3.1.

However, before we proceed with the polarization analysis of the magnetic excitations, we first discuss the elastic response, and investigate in detail the exact orientation of the magnetic moments in the ordered phase of LaSrMnO₄. In the upper part of Tab. 3.1 we have included the results of the elastic polarization analysis for the two magnetic Bragg positions $\mathbf{Q}_1 = (0.5 0.5 0)$, $\mathbf{Q}_2 = (0.5 1.5 0)$, and for the structural Bragg position $\mathbf{Q}_{\text{tet}} = (200)$. At the integer-indexed position \mathbf{Q}_{tet} only structural scattering contributes, and the detected spin-flip intensity defines the experimental loss of polarization along the trajectory of the neutron – the observed large flipping ratio $FR = I_{SF}/I_{NSF} \approx 24$ for all three choices of \mathbf{P}_i , corresponding to a loss of polarization of 4%, demonstrates the high precision of our experimental setup. Regarding next the two magnetic Bragg positions \mathbf{Q}_1 and \mathbf{Q}_2 , strong intensity is observed in the spin-flip channels for $\mathbf{P}_i \parallel \mathbf{x}, \mathbf{y}$, and in the non spin-flip channel for $\mathbf{P}_i \parallel \mathbf{z}$, as is expected for a magnetic structure with the ordered moment aligned along \mathbf{c} (z). A static magnetic moment within the planes, as e.g. might be induced by a slight canting of the spin structure away

from the tetragonal axis, should be detectable as a reduction of the flipping ratios for $i = y, z$, and in a significant difference of the spin-flip intensities for $i = x, y$. However, the observed flipping ratios are comparable to those at the structural position \mathbf{Q}_{tet} , respectively to their inverse, and we do not find any evidence for a considerable canting of the spin structure away from the \mathbf{c} -axis as is suggested in Ref. [43]: Within the statistics of our data we can exclude any canting away from the \mathbf{c} -axis larger than 0.5° , and the ordered moment is perfectly aligned along the tetragonal \mathbf{c} -axis in the ordered phase of LaSrMnO₄.

Turning our attention now to the polarization analysis at finite energies, which is shown in the lower part of Tab. 3.1, we first focus on the two highest energy transfers available, $\hbar\omega = 8.8 \text{ meV}$ and $\hbar\omega = 13.0 \text{ meV}$. Regarding the energy scan in Fig. 3.6, these two points characterize the behavior of the dispersive mode ω_{sw} identified in Ref. [46]. Note at this point, that the asymmetric shape of the mode ω_{sw} in Fig. 3.5 has to be ascribed to the convolution of the resolution function with the dispersion surface as discussed at the end of Chap. 2. For both energies, the magnetic intensity revealed in the SF_{*x*}-channel is spin-flip scattering for $\mathbf{P}_z \parallel \mathbf{c}$ and non spin-flip scattering in the y -channel, just opposite to the response at the elastic position. Hence, the mode ω_{sw} is polarized within the MnO₂-layers, and this mode corresponds to the conventional transverse magnon described by linear spin-wave theory.

Interestingly, the polarization analysis at the three remaining energies, which characterize the two localized modes $\omega_{\text{cl},1}$ and $\omega_{\text{cl},2}$, reveals a similar behavior as for the spin-wave excitation ω_{sw} – for all energies investigated the magnetic scattering flips the spin in the z -channel, and is non spin-flip in the y -channel. We have no indication for a longitudinal magnetic fluctuation along \mathbf{c} , the associated cross sections are all zero within the determined flipping ratio, and we may summarize the results of the polarization analysis of the magnetic excitation spectrum by stating that at the magnetic zone center $\mathbf{q} = 0$ three different contributions can be identified, which all correspond to magnetic fluctuations within the MnO₂-planes.

3.2.2 Field dependence of the magnetic excitations

The field dependence of the magnetic excitation spectrum for a maximum field of 11 T applied parallel to \mathbf{c} is shown in Fig. 3.7. As is obvious at first sight, the magnetic field induces drastic changes in the excitation spectrum, which, however, can only partially be explained by linear spin-wave theory.

Again, we start with the discussion of the properties of the dispersive mode with frequency $\hbar\omega_{\text{sw}} = 8.8 \text{ meV}$ in zero field. Upon increasing field, the high-energy branch seems to split into two distinct signals, and for $H = 11 \text{ T}$ two well-separated modes are resolvable around $\approx 7.5 \text{ meV}$ and $\approx 10.5 \text{ meV}$. The observed splitting of the mode ω_{sw} is consistent with the predictions of linear spin-wave

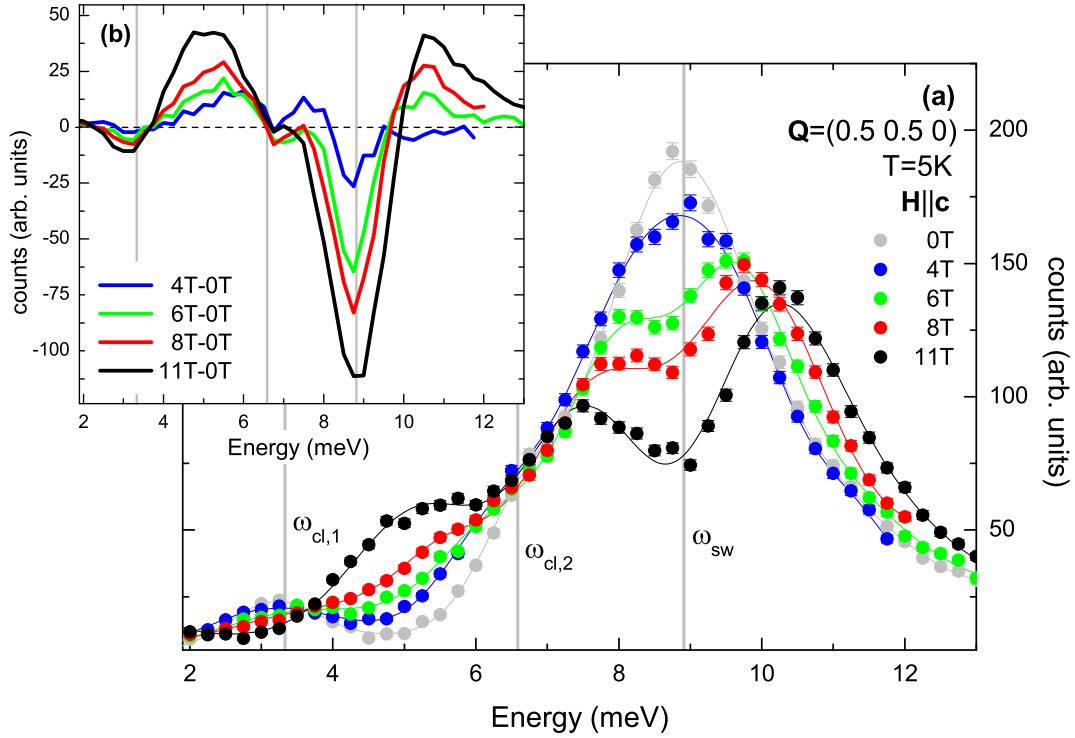
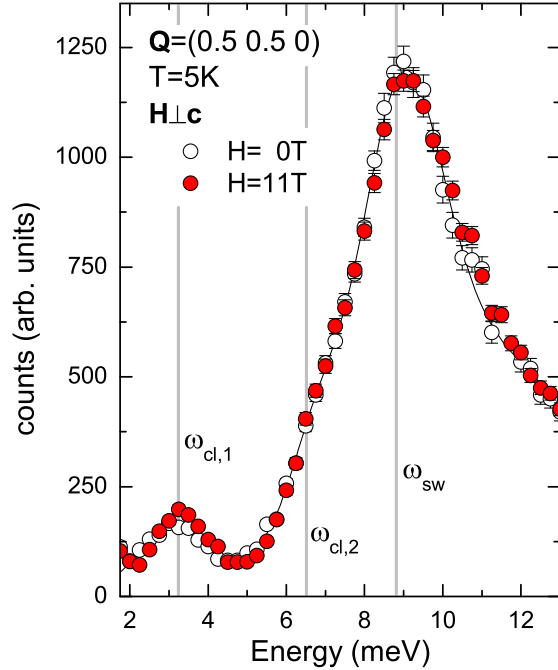


Figure 3.7: Field dependence of the magnetic excitations in LaSrMnO_4 (I.) Energy scan at the magnetic zone center $\mathbf{Q} = (0.5\ 0.5\ 0)$ at $T = 5\text{ K}$ for different magnetic fields $\mathbf{H} \parallel \mathbf{c}$ recorded at the thermal spectrometer IN22 with $E_f = 14.7\text{ meV}$. Solid lines denote fits to the data assuming Gaussian profiles for the different contributions (a). Difference spectra between the data in finite and zero field calculated from the data presented in (a) (b). Vertical gray bars mark the frequencies of the different magnetic excitations in zero field.

theory for the Heisenberg model, as a magnetic field parallel to the easy axis is expected to remove the degeneracy of the two antiferromagnetic magnon branches [62, 69]. The splitting is proportional to the magnetic field H and assuming a linear change of the magnon frequencies with H , $\omega_{\text{sw}}(H) = \omega_{\text{sw}}^{H=0} \pm \lambda H$, results in a satisfying description of the experimental data above $\approx 6\text{ meV}$ yielding the spin-wave frequencies $\hbar\omega_{\text{sw}}^- = 7.49(3)\text{ meV}$ and $\hbar\omega_{\text{sw}}^+ = 10.11(3)\text{ meV}$ for $H = 11\text{ T}$, see Fig. 3.7.

The field dependence of the two localized modes ω_{cl} is, in contrast, more subtle, and the evolution of the inelastic intensity below $\approx 6\text{ meV}$ is less obvious. With increasing field the mode $\omega_{\text{cl},1}$ is shifted to higher energies and the spectral weight around 3.0 meV is nearly completely suppressed in the spectrum at 11 T . Simultaneously, the mode $\omega_{\text{cl},2}$ seems to soften with the increase of the field, and both modes merge into a single, rather intense excitation ω_{cl} centered at $\hbar\omega = 5.15(5)\text{ meV}$ for $H = 11\text{ T}$, which dominates the energy region below

Figure 3.8: Field dependence of the magnetic excitations in LaSrMnO_4 (II.) Energy scan at $\mathbf{Q} = (0.5\ 0.5\ 0)$ at $T = 5\text{ K}$ in zero field and for a magnetic field $H = 11\text{ T}$ applied perpendicular to \mathbf{c} recorded at the spectrometer IN22 with $E_f = 14.7\text{ meV}$. Vertical gray bars mark the positions of the three different modes in zero magnetic field.



$\approx 6\text{ meV}$ in the high-field data. However, as the low-energy branch of the spin-wave ω_{sw} partially overlaps with mode $\omega_{\text{cl},2}$ for strong fields, we can not exclude a more complex behavior for $\omega_{\text{cl},2}$ – one might expect a splitting of this mode as well.

In contrast to the drastic influence of a magnetic field applied parallel to \mathbf{c} , a magnetic field \mathbf{H}_{ab} in the perpendicular direction has nearly no impact on the magnetic excitation spectrum. In Fig. 3.8 we show similar scans as presented before, however, this time measured in a rotated orientation and the magnetic field \mathbf{H} applied perpendicular to \mathbf{c} – up to the maximum available field of 11 T we can not resolve any changes in the excitation spectrum. For the dispersive mode ω_{sw} this behavior is again consistent with conventional spin-wave theory, whereas the response of the modes ω_{cl} seems quite interesting in light of the origin of the additional branches: Similar to the response of the ferromagnetic domains in the macroscopic magnetization, the additional modes in the excitation spectrum are “active” only for the magnetic field applied along the tetragonal axis. Therefore, it seems very intriguing to associated the two magnetic excitations ω_{cl} with the dynamic properties of the ferromagnetic clusters.

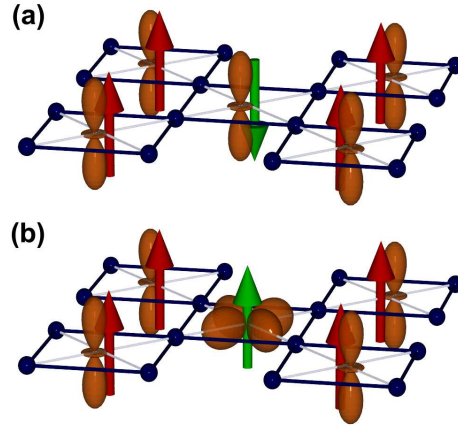
In conclusion, combining all results of the magnetic excitation spectrum, including the polarization analysis as well as the field dependence, with the analysis of the macroscopic magnetization yields a complete experimental characterization of the magnetic ordering in LaSrMnO_4 , which obviously can not be interpreted on the basis of a simple G-type antiferromagnet:

- The analysis of the macroscopic magnetization in Ref. [43] reveals the existence of ferromagnetic domains with an ordered moment of $\approx 0.05 \mu_B/\text{Mn}$, which can be aligned only by a magnetic field applied along \mathbf{c} .
- The analysis of the magnetic excitation spectrum reveals three different branches. One of these three modes, ω_{sw} , is polarized transversely, splits linearly in a magnetic field parallel to the magnetic easy axis, and exhibits a pronounced dispersion. This mode is the conventional transversal magnon of the G-type structure predicted by linear spin-wave theory.
- The additional modes with $\hbar\omega_{\text{cl},1} = 3.3 \text{ meV}$ and $\hbar\omega_{\text{cl},2} = 6.5 \text{ meV}$ are associated with the ferromagnetic clusters. These modes are localized around the AFM zone-center, correspond to magnetic fluctuations perpendicular to \mathbf{c} , and exhibit an unusual behavior in a magnetic field parallel to the tetragonal axis.

Considering the physical origin of this unconventional properties, an explanation based on a homogenous magnetic state seems very unlikely to us – a possible canting of the spins against the tetragonal axis suggested in Ref. [43] to explain the finite remanent magnetization is excluded by the polarization analysis of the magnetic Bragg scattering, proving that the ordered moment is almost perfectly aligned along \mathbf{c} . Instead, we propose a scenario in which the finite magnetization is associated with small two-dimensional FM clusters with a net magnetic moment along \mathbf{c} , embedded in the AFM matrix. The two localized branches identified in the excitation spectrum correspond to the possible excitations within these clusters.

This idea is supported by theoretical investigations of spin-wave excitations in finite-size clusters [70], and by observations of confined spin-waves in slightly doped perovskite manganites [71, 72]. Hendriksen et al. have shown, that in a magnetic cluster of finite dimensions the associated excitation spectrum consists of discrete energy levels, which are considerably broadened in momentum space. In the case of small clusters, the possible excitations can be viewed as standing waves with wavelength commensurate with the cluster dimensions [70]. Experimentally, confined spin-waves are recently reported to exist in perovskite manganites close to the metallic state, and the observations resemble much of the properties of the localized modes in LaSrMnO₄. The spin-wave dispersion in La_{7/8}Sr_{1/8}MnO₃ consists of one dispersive branch and several dispersionless energy levels with constant distance ΔE localized around the FM zone boundary in reciprocal space, which are interpreted as an evidence for a clustered magnetic state. The discrete energy levels are associated with confined spin excitations within the clusters [71, 72], and the similarities with the properties of the modes ω_{cl} might suggest a similar mechanism in LaSrMnO₄, too: The modes $\omega_{\text{cl},1}$ and $\omega_{\text{cl},2}$ are both observed around the position $\mathbf{Q} = (0.5\ 0.5\ 0)$ in reciprocal space, which is a zone center

Figure 3.9: Orbital polaron in LaSrMnO_4 Sketch of the majority spin and orbital correlations in the ordered state of LaSrMnO_4 with the occupied orbitals pointing out of the plane and an antiferromagnetic spin alignment (a). A minority of the e_g -electrons occupy the in-plane $d_{x^2-y^2}$ -states forming an orbital polaron with the surrounding Mn-sites with ferromagnetic correlations (b).



of the antiferromagnetic lattice, and, simultaneously, a *zone boundary* for the ferromagnetic unit cell.⁶

However, what might be the reason for finite-size ferromagnetic clusters in undoped LaSrMnO_4 , as in an electronically homogenous system a heterogenous magnetic state appears very unusual? Although the orbital state in LaSrMnO_4 seems to be well defined with a predominant occupation of the out-of-plane states with $d_{3z^2-r^2}$ -symmetry, the orbital polarization is not perfect and experimental results suggest a slight, but non-vanishing occupation of the in-plane states [51, 52], which is supported by theoretical investigations demonstrating that the orbital state depends sensitively on small changes in the local crystallographic environment [57, 73]. Recently, it has been shown that the quenched disordered σ associated with the solid solution of the A-site cations substantially influences the ground-state properties of single-layered manganites around half doping [74, 75], and it seems very likely that in LaSrMnO_4 with a maximal mixing of Lanthanum and Strontium ions the enhancement of the A-site disorder effects the orbital arrangement as well: In the surrounding of Sr-rich regions the crystal field E_z might be slightly modulated, which leads to a local “flop” of the orbital and to the stabilization of the in-plane $d_{x^2-y^2}$ -state, resulting in the formation of orbital polarons with, as we will show below, ferromagnetic correlations embedded in the AFM matrix [59, 60], see Fig. 3.9.

The flop of a single e_g -electron from an out-of plane $d_{3z^2-r^2}$ -state into a $d_{x^2-y^2}$ -state oriented within the plane affects the magnetic exchange interactions in the cluster, and locally the situation is well comparable with the perovskite LaMnO_3 , as the central e_g -orbital points to empty orbitals on neighboring sites [34, 35]. Hence, the magnetic coupling in the orbital polaron will be ferromagnetic with a net magnetic moment along the tetragonal axis, see Fig. 3.9b.

⁶Following the argumentation in Refs. [71, 72], the same excitations should be visible around $\mathbf{Q} = (0.500)$, which has, unfortunately, not been checked so far.

The formation of ferromagnetic polarons furthermore provides a natural interpretation for the two localized modes in the magnetic excitation spectrum. One of the two modes, probably the one with lower energy, corresponds to the vibration of the central spin of the polaron in phase opposition to its neighbors – which corresponds to the zone-boundary mode in a conventional ferromagnet – and tests essentially the ferromagnetic coupling J_{FM} within the cluster. The second mode can be ascribed to the in-phase fluctuations of the cluster with respect to the surrounding AFM matrix. This mode basically senses the magnetic anisotropy at the boundaries of the cluster, which should be reduced compared to the anisotropy Λ in the core of the AFM matrix by $\approx 25\%$.

What remains somehow puzzling is the observed response to an applied magnetic field. Clearly, a moderate field applied perpendicular to the ordered moment should not disturb the clusters, which agrees with the experimental results. However, for the field along \mathbf{c} the situation is more complex as the moment of the cluster can either be parallel or antiparallel to the external field. In the first case, a sufficient field should flip the central spin of the cluster. Due to the strong coupling the orbital follows and the polaron is completely “annealed” into the AFM ordered structure. In contrast, the clusters with parallel moments are stabilized and might even grow in the external field, and the different response of the two types of clusters can qualitatively explain the observed behavior of the macroscopic magnetization $M(H)$.

Obviously, for the analysis of the field dependence of the magnetic excitations we only have to consider the clusters with parallel moment. As the clusters are stabilized by the field, the low-energy mode corresponding to the out-of phase fluctuation should harden, as it perceives the additional anisotropy of the external field. For a ferromagnet linear spin-wave theory predicts an increase of the magnon frequencies by $g\mu_{\text{B}}H \approx 0.12 \text{ meV/T}$ for the field applied along the easy axis [62], which is in good agreement with the observation, as we find $\hbar\omega_{H>0} - \hbar\omega_{H=0} = 1.6 \text{ meV}$ at $H = 11 \text{ T}$ for the low-energy mode $\omega_{\text{cl},1}$. Since the second mode $\omega_{\text{cl},2}$ should be related to the anisotropy of the antiferromagnetic phase, one might expect this mode to split in the external field, similar to the dispersive mode ω_{sw} . The data do not exclude such a scenario, however we can only observe the lower-energy branch $\omega_{\text{cl},2}^-$ since the higher energy branch strongly overlaps with the lower branch ω_{sw}^- of the spin-wave mode. Nevertheless, it is interesting to note that the mode $\omega_{\text{cl},2}^-$ softens by 1.53 meV , which again is in good agreement with the expected value for a field $H = 11 \text{ T}$.

3.3 Conclusions

In this chapter we presented an extensive revision of the magnetic excitation spectrum of the parent compound LaSrMnO₄ of single-layered manganites using po-

larized neutrons as well as strong external magnetic fields.

The basic properties of LaSrMnO_4 can well be understood by a ferro-orbital ordering with the e_g -electrons occupying out-of-plane $d_{3z^2-r^2}$ -states associated with an antiferromagnetic ordering of neighboring spins in the MnO_2 -layers, and the system is referred to as a simple G-type antiferromagnet in the recent literature [7], which is widely accepted. However, the actual situation is more complex, and the macroscopic magnetization [43], as well as the magnetic excitation spectrum are inconsistent with this simple approach. In particular, our previous neutron scattering study revealed three different contributions to the magnetic excitation spectrum [46], which were investigated in further detail in this chapter.

One of the three modes corresponds to the classical spin-wave excitation associated with the antiferromagnetic G-type ordering. The polarization analysis confirms its transversal character, and the mode splits in an external magnetic field, which together with the observed dispersion is fully consistent with linear spin-wave theory for a two-dimensional antiferromagnet. The two other modes can not be described within the G-type arrangement, but the polarization analysis unambiguously establishes their magnetic character, and both modes correspond to magnetic fluctuations within the MnO_2 -layers. The unconventional character of these modes is furthermore demonstrated by an unusual field dependence – for a strong field along c both modes merge into a single excitation at intermediate energies.

To explain the observed unusual behavior we suggest the existence of ferromagnetically correlated orbital polarons arising from a slight modulation of the crystal field due to quenched disorder in the crystal structure, which are embedded in the antiferromagnetic matrix. The observed additional modes in the spin-wave spectrum are associated with the magnetic excitations within the cluster, and the unusual field dependence of the magnetization and of the excitation spectrum is related to the response of the orbital polarons to the external field.

4 Spin-wave excitations in charge-ordered manganites

The strong correlations between different degrees of freedom in manganese oxides result in complex phase diagrams characterized by the close competition of various ground states with very different properties. The most famous consequence of this interplay is the colossal magnetoresistance effect (CMR) in perovskite manganites, the field-induced metal-insulator transition with a change of the electric resistivity by more than ten orders of magnitude in a narrow temperature interval, which is in the focus of interest since its discovery in the 1990's [4, 76]. Qualitatively, the CMR-effect can be understood on the basis of the double exchange mechanism connecting the kinetic energy of the charge carriers with ferromagnetic correlations between the localized Mn spins [77–79]. However, a quantitative analysis has to go beyond this simple picture [80], and today more sophisticated models are discussed [2].

A second regime of strong interest in the phase diagrams of manganites is the insulating phase at half band filling with a cooperative ordering of orbitals, charges and spins [30]. Besides the intrinsic fascination of a collective ordering of several degrees of freedom this charge- and orbital-ordered state (COO) is intimately coupled to the CMR-regime as it competes with the FM metallic state, which seems to be crucial for the huge drop of resistivity at the metal-insulator transition. Indeed, recent experimental [81–84] and theoretical [5, 85–87] studies on the CMR-effect focus on phase separation scenarios between the FM metallic and the COO insulating phases, and electronically soft states with the CMR-effect appearing as a percolative phenomenon.

In light of its relevance for the colossal magnetoresistivity and the huge number of investigations on the CMR-effect in all kinds of perovskite manganites, it seems astonishing that some of the basic physical properties of the COO state are not yet fully established today. Even the exact nature of the COO ground state is still discussed controversially, as different experimental results favor different theoretical explanations: The classical CE-type picture with the charges centered on the Mn-sites introduced in the pioneering work of Wollan and Koehler [88] and Goodenough [8] has recently been challenged by a model consisting of closely coupled magnetic dimers with the charges localized on the bridging oxygen ions, usually referred to as Zener polaron ordering [9].

Particularly well suited for a systematic study of the COO state is the two-

dimensional single-layered 214-compound $\text{La}_{1-x}\text{Sr}_{1+x}\text{MnO}_4$ already introduced in the previous chapter, as the ordered state is exceptionally stable in this system. In this chapter, we report on a comprehensive analysis of the development of the ordered state in $\text{La}_{1-x}\text{Sr}_{1+x}\text{MnO}_4$: Starting with a brief introduction into the main physical ideas behind the two different concepts, the CE ordering on the one side and the Zener polaron on the other, we discuss the spin-wave dispersion of the optimally doped compound $\text{La}_{1/2}\text{Sr}_{3/2}\text{MnO}_4$ ($x=0.5$) and analyze the relevant magnetic interactions in light of those of the FM metallic manganites. Subsequently, we focus on the thermal evolution of the ordered state and study the critical magnetic scattering and the spin dynamics in the disordered state. Following the discussion of the half-doped compound we extend our analysis and focus on the doping dependence of the ordered state by investigating the electron-rich system $\text{La}_{0.6}\text{Sr}_{1.4}\text{MnO}_4$ revealing a tendency towards FM correlations, and the overdoped compound $\text{La}_{0.4}\text{Sr}_{1.6}\text{MnO}_4$ exhibiting an incommensurable ordering scheme. The chapter is finally closed by the revision of the magneto-orbital phase diagram of the single-layered manganites $\text{La}_{1-x}\text{Sr}_{1+x}\text{MnO}_4$ around half doping, summarizing all results obtained in this chapter.

Some of the results presented in this chapter are included in the publications [[senff06a](#)] and [[senff07c](#)].

4.1 Basic properties of the ordered state

In the 113-perovskite manganites $\text{Re}_{1-x}\text{A}_x\text{MnO}_3$ the doping level x controls the formal valence of the Mn-sites. At rational values, as e. g. $x = \frac{1}{8}, \frac{1}{2}, \frac{2}{3} \dots$, the ratio of three- and four-valent Mn-sites is commensurable and these systems are often unstable against the real-space localization of the doped charge carriers [[89–92](#)].

Especially around half doping, $x = \frac{1}{2}$, with the Mn-ions possessing a formal valence close to 3.5+, charge ordering appears as a generic feature in the phase diagrams of the three dimensional CMR-perovskites $\text{Re}_{1-x}\text{A}_x\text{MnO}_3$, as well as in the related two-dimensional single- and double-layered compounds $\text{La}_{1-x}\text{Sr}_{1+x}\text{MnO}_4$ and $\text{La}_{2-2x}\text{Sr}_{1+2x}\text{Mn}_2\text{O}_7$, manifesting itself by a sharp increase of the electric resistivity and the simultaneous appearance of characteristic superstructure reflections in diffraction experiments [[30, 42, 93, 94](#)].

4.1.1 The classic CE-type ordering

The first interpretation of a charge- and orbital-ordered state in the half-doped manganite $\text{La}_{1/2}\text{Ca}_{1/2}\text{MnO}_3$ has been given by Goodenough in the 1950's basing on the results of one of the first neutron scattering experiments on magnetic structures

by Wollan and Koehler [8, 88].¹

To explain the observed quarter-indexed magnetic superstructure reflections Goodenough predicted a checkerboard-like ordering of Mn^{3+} and Mn^{4+} sites with each three-valent cation always surrounded by four-valent ions within the *ab*-planes of the pseudo-cubic structure and vice versa. As a Mn^{3+} -ion has an electronic configuration $3d^4$ with a single electron occupying the e_g -level, which is absent in the $3d^3$ configuration of a four-valent Mn-site, this charge ordering is accompanied by the ordering of the orbital occupation: To minimize the elastic strain the single e_g -electron alternately occupies a $d_{3x^2-r^2}$ - or $d_{3y^2-r^2}$ -orbital along the Mn-Mn bonds, resulting in a stripy ordering of orbitals along the face diagonals of the pseudo-cubic structure, see Fig. 4.1a.

Since the Goodenough-Kanamori-Anderson rules (GKA) closely couple the magnetic correlations between transition-metal ions to the orbital degrees of freedom [31–33], the combined ordering of charges and orbitals sets strict conditions for the magnetic ground state. If the occupied e_g -orbital points along the bond of a Mn^{3+} - Mn^{4+} pair the magnetic coupling between these two will be ferromagnetic, and it will be antiferromagnetic if the orbital is oriented perpendicular to the bond. Hence, the underlying orbital lattice of the COO structure results in a complex magnetic structure consisting of an AFM stacking of FM ordered zig-zag chains; the corner sites of the chains are always constituted by four-valent ions, which are ferromagnetically coupled via a bridging Mn^{3+} -site, see Fig. 4.1b.

In the following, we will refer to this combined ordering of charges, orbitals and spins as the CE-type ordering or the Goodenough model of the COO state.² Experimentally the CE-type ordering has conventionally been tested by x-ray and neutron diffraction experiments. Although neither of the two techniques is directly sensitive to the ordering of charges or orbitals, both superstructures result in a characteristic structural distortion of the MnO_6 -octahedra detectable in conventional diffraction experiments: A smaller Mn^{4+} ion compresses the octahedron with respect to an average 3.5-valent site, whereas a Mn^{3+} ion expands it. In addition, due to the half-filled e_g -level the three-valent ions are Jahn-Teller active leading to a characteristic shear-type distortion of the octahedra with an elongation in the direction of the occupied orbital, see Fig. 4.1a.

Based on powder diffraction, the first structural refinement of the charge- and orbital-ordered state has been reported by Radaelli et al. for the 113-compound

¹To be more precise, the experiment of Wollan and Koehler first established the CE-type magnetic order in $\text{La}_{1/2}\text{Ca}_{1/2}\text{MnO}_3$, which then has been explained by Goodenough on the basis of a charge- and orbital-ordered state.

²According to the original classification scheme set up by Wollan and Koehler the CE-type ordering denotes only the magnetic part of the structure. However, today it is common use in the literature to include the charge and orbital part as well, and the cooperative ordering of charges, orbitals and spins as described by the Goodenough model depicted in Fig. 4.1 is frequently referred to as CE ordering.

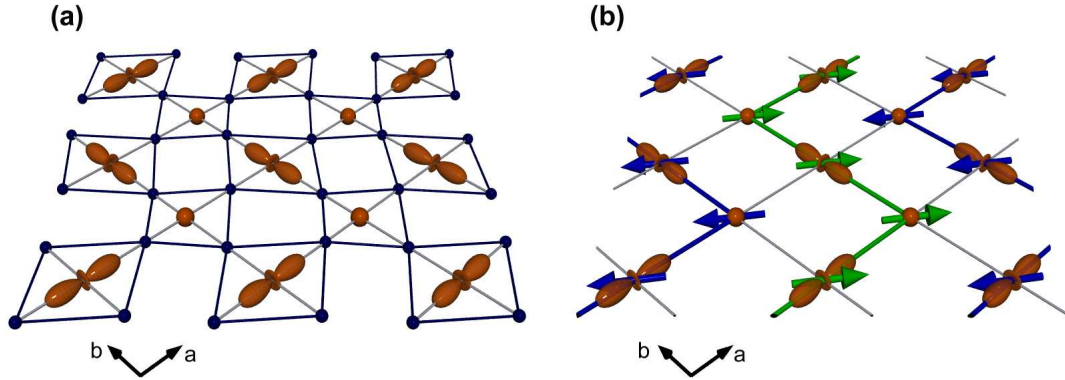


Figure 4.1: Goodenough model of the COO state Sketch of the CE-type ordering in the ab -planes of half-doped manganites after Goodenough [8]. The checkerboard ordering of charges with Mn^{3+} and Mn^{4+} -sites alternating along the cubic axis is accompanied by a stripe ordering of occupied $d_{3x^2-r^2}/d_{3y^2-r^2}$ -orbitals along the diagonal. Both charge and orbital order imply characteristic distortions of the MnO_6 -octahedra with the same modulation wavelength (a). The magnetic ground state consists of an AFM ordering of FM zig-zag chains reflecting the anisotropic exchange pathways set by the orbital order (b).

$\text{La}_{1/2}\text{Ca}_{1/2}\text{MnO}_3$ [95], which was followed by a series of publications on different half-doped manganites yielding similar results [96–102]. In the pseudo-cubic perovskites the transition into the charge- and orbital-ordered phase coincides with a systematic reduction of the crystallographic symmetry from orthorhombic down to the monoclinic space group $P2_1/m$ and a quadrupling of the cubic unit cell in the ab -planes with three inequivalent Mn-sites, both fully consistent with the Goodenough model. However, the analysis of the different bond distances excludes a full segregation of the e_g -electron and the charge ordering has to be considered as incomplete resulting in formal valencies $\text{Mn}^{3.5\pm\delta}$ and $\delta \approx 0.12 - 0.25$ for the two distinct Mn-sites [99, 102, 103]. The identification as Mn^{3+} , respectively Mn^{4+} , seems nevertheless justified, as the crystallographic environment of both sites is distinct: One of the two species, labeled “ Mn^{3+} ”, exhibits a typical Jahn-Teller distortion of the surrounding oxygen polyhedra with two long and four short Mn-O bonds. In contrast, the sites referred to as “ Mn^{4+} ” expose an isotropic structural environment with six equal Mn-O distances.

Further support for an imperfect charge ordering is given by the refinement of the magnetic structure. Several authors observe two independent magnetic sublattices attributed to the different size of the localized moments at the distinct Mn-positions in the charge ordered structure, once more fully consistent with the proposed CE-type ordering. However, the refined moments amount to $\simeq 3.0 \mu_B$ for the “3+”-sites and $\simeq 2.7 \mu_B$ for the “4+”-sites [93, 96], which differ significantly from the values expected for a complete charge disproportionation.

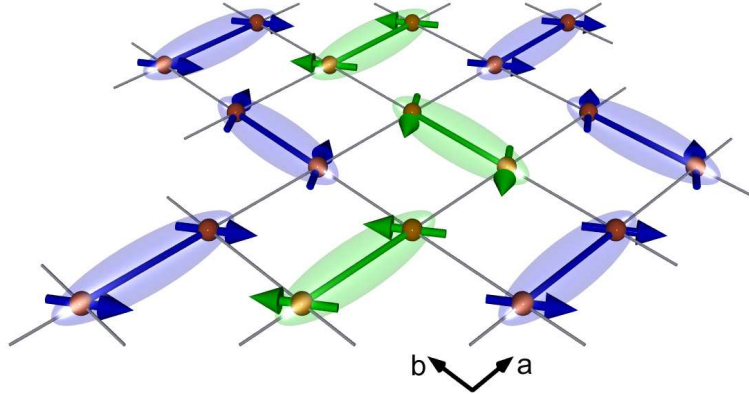


Figure 4.2: Zener polaron ordering Sketch of the Zener polaron model in the ab -planes of doped manganites with the magnetic dimers marked by thick lines. As the dimers are stacked diagonal to the Mn-Mn bonds and parallel aligned dimers are always coupled antiferromagnetically magnetic zig-zag chains are formed similar to the classical CE-type ordering.

The experimental results are supplemented by numerous theoretical investigations, and the CE ground state can be stabilized by electron-phonon coupling [104], as well as by pure magnetic [105] and electronic interactions [106]. However, all of these studies qualitatively reproduce basically the same charge- and orbital-ordered pattern as predicted almost 50 years ago.

4.1.2 The Zener polaron model

The classical Goodenough model described above for the COO state in half-doped manganites has recently been challenged by neutron diffraction experiments on a $\text{Pr}_{0.6}\text{Ca}_{0.4}\text{MnO}_3$ single crystal [9].³ Refining more than 700 COO superstructure reflections the data are not consistent with the monoclinic symmetry $P2_1/m$ and the $\text{Mn}^{3+}/\text{Mn}^{4+}$ checkerboard charge ordering. Instead, Daoud-Aladine et al. propose a coherent stacking of dimerized Mn-pairs along the face diagonals of the cubic lattice with the single e_g electron fully delocalized between the two sites of the dimer. Consequently, all Mn-sites are equally charged and possess a formal valence 3.5+, see Fig. 4.2. As the dimers are formed by the strong FM exchange mediated through the common e_g electron this alternative picture is frequently called Zener polaron (ZP) model. This interpretation is further supported by x-ray absorption experiments, which seem to exclude different manganese valencies at half doping [107, 108].

The magnetic structure induced by the Zener polaron ordering is less obvious

³Note that in the (Pr,Ca)-series the COO state extends down to doping levels $x=0.3$, implying the substitution of Mn^{3+} at the Mn^{4+} sites for $x \neq 0.5$.

than in the Goodenough model. Clearly, the intradimer exchange is strongly ferromagnetic, but the magnetic correlations between different dimers are less defined. Efremov et al. have proposed, that the coupling between adjacent dimers which are oriented parallel is always antiferromagnetic, while the magnetic moments of perpendicular dimers are orthogonal [109]. As the dimers are stacked diagonal to the Mn-Mn bonds, the magnetic ordering again gives rise to magnetic zig-zag chains with a modulation wavelength similar to the classical Goodenough model; however, in the ZP model the orientation of the magnetic moments within a single chain is not always collinear, see Fig. 4.2, and the magnetic structure appears as a special kind of spiral ordering [110].

With the publication of an alternative model for the COO state in half-doped manganites, the Zener polaron ordering immediately gained attention, and various theoretical groups stabilized the ZP state against the CE-type model [109, 111, 112], so that two contrary models for the COO state are discussed in the literature. As both contrasting models yield similar structural modulations – in both cases the charge and orbital ordering quadruples the cubic unit cell in the *ab*-plane, while the magnetic order octuplicates it – standard diffraction experiments can hardly differentiate between both concepts. In contrast, as the magnetic exchange interactions are supposed to be distinct, the dynamic spin correlations will be different and analyzing the spin-wave dispersion in the COO state might yield a clear indication for either of the two competing models [113].

However, due to the systematic reduction of symmetry from cubic down to monoclinic in the COO phase, $\text{Re}_{1-x}\text{A}_x\text{MnO}_3$ single crystals are always heavily twinned, and a sample crystal consists of up to 12 different domains in the charge-ordered phase, rendering the systematic analysis of inelastic neutron data nearly impossible. To escape these difficulties the single-layered compound $\text{La}_{1/2}\text{Sr}_{3/2}\text{MnO}_4$ has recently attracted a lot of interest, as it allows to study the properties of the COO phase in a less complex crystallographic environment.

4.1.3 Charge and orbital ordering in $\text{La}_{1/2}\text{Sr}_{3/2}\text{MnO}_4$

Like all members of the family of single-layered manganites $\text{La}_{1-x}\text{Sr}_{1+x}\text{MnO}_4$, the half-doped compound $\text{La}_{1/2}\text{Sr}_{3/2}\text{MnO}_4$ crystallizes in the tetragonal K_2MnF_4 -structure with space group symmetry $I4/mmm$ and room temperature lattice constants $a = 3.863 \text{ \AA}$ and $c = 12.421 \text{ \AA}$ [114], see Fig. 3.1 in Chap. 3. The confinement of the electrons to the separated MnO_2 sheets reduces significantly the one-electron bandwidth, thereby stabilizing the charge-ordered state against other ground states, and the COO state appears rather robust in the layered system rewarding $\text{La}_{1/2}\text{Sr}_{3/2}\text{MnO}_4$ a prototype-system for the investigations of the properties of the charge- and orbital-ordered state.

Charge and orbital ordering occurs in $\text{La}_{1/2}\text{Sr}_{3/2}\text{MnO}_4$ below $T_{\text{CO}} \approx 220 \text{ K}$, as is determined by the increase of the electric resistivity and the simultaneous appear-

ance of the typical half- and quarter-indexed superlattice reflections in diffraction experiments [41, 42, 54]. At lower temperatures, magnetic ordering of the CE type accompanies the COO ordering, and neutron diffraction reports the onset of long-range magnetic ordering below $T_N \approx 110$ K [54]. The ordered ground state appears very robust against applied magnetic fields, and only strong fields (of the order of 30 T) can melt the ordered state, thereby inducing sizable changes in the electric conductivity, reminiscent of the physics in the CMR-perovskite manganites [115].

In the last years, the ordered state in $\text{La}_{1/2}\text{Sr}_{3/2}\text{MnO}_4$ has been extensively studied using resonant diffraction techniques, both with hard x-rays probing the Jahn-Teller distortion of the oxygen octahedron [116–118], and with soft x-rays directly sensitive to the ordering of the $3d$ electrons [119–123]. The common intention of all these works is the observation of orbital ordering of the kind as proposed by Goodenough, but while the analysis of the data by some groups favors a “classical” ordering of alternating $d_{3x^2-r^2}/d_{3y^2-r^2}$ -orbitals [51, 120], other publications strengthen an alternative occupation of the $d_{x^2-z^2}/d_{y^2-z^2}$ -type for the e_g -electrons [121, 123]. Also the degree of charge ordering is discussed controversially, and the reported value of the disproportionation ranges continuously from a nearly complete segregation into Mn^{3+} and Mn^{4+} [116] to an almost intermediate valence state close to 3.5+ for both Mn-sites [124]. Nevertheless, besides these inconsistencies, the observed line shapes in the RXD-experiments always seem to support the site-centered CE-type model for the COO state in $\text{La}_{1/2}\text{Sr}_{3/2}\text{MnO}_4$. However, the experimental data are, best to our knowledge, never discussed on the basis of the alternative Zener polaron model, most likely due to theoretical difficulties in deriving a reasonable modeling of the expected spectra [125]. Therefore, the RXD-experiments can not (yet) give a clear statement either for or against the relevance of the Zener polaron approach.

The stable tetragonal symmetry of the single-layered compounds, however, opens the way to detailed crystallographic investigations of the COO state. The onset of the charge and orbital order in $\text{La}_{1/2}\text{Sr}_{3/2}\text{MnO}_4$ results in a small orthorhombic distortion inducing only a simple twofold twinning [7, 126], as the orbitals can be either stacked along the $[1\ 1\ 0]$ - or the $[1\ \bar{1}\ 0]$ -direction of the tetragonal structure.⁴ First results of x-ray diffraction experiments yield an orthorhombic unit cell $2\sqrt{2}a \times \sqrt{2}a$ rotated by 45° with respect to the crystallographic axis for the charge-ordered phase [126]. The symmetry of the ordered phase has been determined to belong to space group $Bbmm$ [7], which is compatible with the CE-type ordering, but not consistent with the Zener polaron model.

These preliminary results are strongly supported by a recent combined neutron and x-ray diffraction study on a high-quality single crystal [127]. The *unrestricted* refinement of a large set of superstructure reflections provides for the first time

⁴Note that in the pseudo-cubic perovskites any crystallographic investigation has to deal with up to 12 different twin domains in the COO phase.

a complete and unambiguous determination of the structural distortions of the ordered phase, and seems to finally terminate the long lasting debate on the nature of the charge-ordered ground state in doped manganites. The structure can indeed be refined within the symmetry of space group $Bbmm$ and two crystallographic inequivalent Mn-sites, fully consistent with the Goodenough picture on the one side, and excluding the Zener polaron approach on the other: One of the two Mn-sites exhibits a pronounced Jahn-Teller type distortion of the surrounding oxygen octahedron, resembling the behavior of a Mn^{3+} -ion, while the octahedron of the second Mn-site appears compressed and is hence labeled Mn^{4+} . From the analysis of the different Mn-O bond distances an incomplete charge segregation of $0.2e^-$ is derived, and the size of the charge separation as well as the determined structural distortions are in excellent agreement with theoretical predictions for the single-layered manganites [128]. Furthermore, a current LDA calculation based on the determined superstructure naturally produces an insulating and charge-ordered ground state with a predominant occupation of the bands associated with the $d_{3x^2-r^2}/d_{3y^2-r^2}$ -orbitals, once more resembling the basic properties of the classical CE model [129].

Actual results on half-doped 113-manganites assist this interpretation, as they also seem to exclude the Zener polaron ordering. At first, two high-resolution neutron powder diffraction studies on $\text{Pr}_{1/2}\text{Ca}_{1/2}\text{MnO}_3$ and $\text{La}_{1/2}\text{Ca}_{1/2}\text{MnO}_3$ are inconsistent with the Zener polaron description, but in agreement with the CE ordering and the initial observations by Radaelli [103, 130]. Finally, a NMR experiment on the (Pr,Ca)-system, sensing precisely the local environment of the oxygens in the ordered phase, also rejects the bond-centered model, as the number of observed NMR-active transitions contradicts the expectations derived from the ZP model, but is, once more, compatible with the classical model of the COO state [131].

To resume, the nature of the charge-ordered state observed in many manganites around half doping is still discussed controversially, and two contrasting models, the classical Goodenough site-centered type of ordering and the coherent ordering of closely coupled ferromagnetic dimers, have been proposed to explain the experimental observations. Recent results however, especially obtained from diffraction experiments on the single-layered compound $\text{La}_{1/2}\text{Sr}_{3/2}\text{MnO}_4$, seem to be in contradiction with the Zener polaron concept and strongly support the CE-type model for the COO state.

As we will show in the following, the analysis of the dynamical properties of the magnetic ground state and the doping dependence of the COO state in the single-layered compound is in perfect agreement with this interpretation.

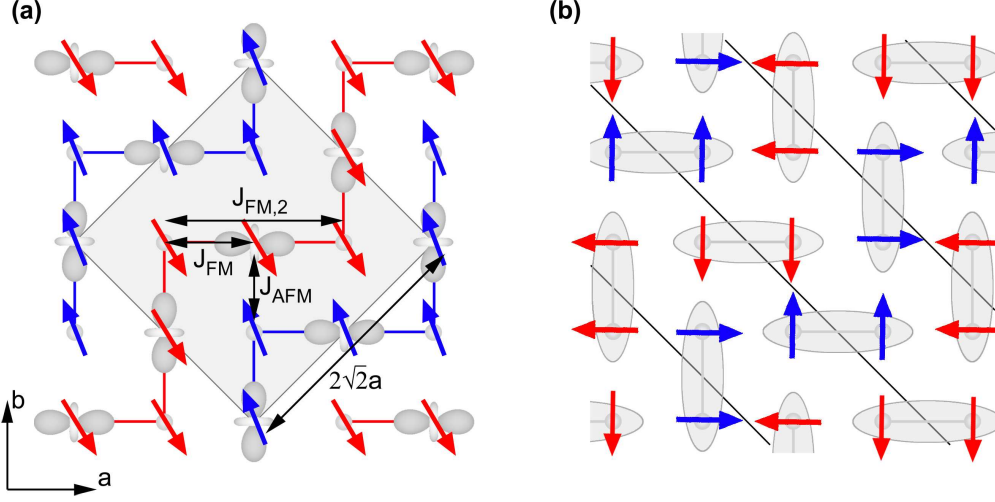


Figure 4.3: Analysis of the superstructures in the COO state Schematic representation of the ordered ground state in the ab -plane according to the classical Goodenough model (a) and to the Zener polaron picture (b). Note that in both sketches the orbitals, respectively dimers are stacked along the $[1\bar{1}0]$ direction and the FM zig-zag chains run along $[110]$. In (a) the three magnetic exchange pathways as described later in the text are also included.

4.1.4 The CE-type ordering in neutron scattering experiments

Before we can proceed with the presentation and analysis of our neutron data on the magnetic correlations in $\text{La}_{1-x}\text{Sr}_{1+x}\text{MnO}_4$ near half doping, we will first have to setup an unique frame for the discussion of the results.

For this purpose, let us illustrate the different propagation vectors associated with the two proposals with the aid of Fig. 4.3. We start with the Goodenough model, Fig. 4.3a. Below T_{CO} the checkerboard arrangement of charges with propagation vector $\mathbf{k}_{\text{CO}} = (\frac{1}{2} \frac{1}{2} 0)$ doubles the tetragonal unit cell and the charge-ordered cell has dimensions $\sqrt{2}a \times \sqrt{2}a$. The concomitant orbital ordering reduces the crystallographic symmetry and the nuclear lattice becomes orthorhombic with lattice constants $2\sqrt{2}a$ along $[110]$ and $\sqrt{2}a$ along $[1\bar{1}0]$. Orbital ordering is related to superstructure reflections with $\mathbf{k}_{\text{OO}} = \pm(\frac{1}{4} \frac{1}{4} 0)$. Considering the magnetic ordering, the CE structure has to be divided into two sublattices, as we have to distinguish between the two magnetic Mn-species. For the Mn^{3+} -sites the magnetic lattice is orthorhombic, too, and of the same size as the structural one, but rotated by 90° – $\sqrt{2}a$ along $[110]$ and $2\sqrt{2}a$ along $[1\bar{1}0]$. The Mn^{3+} spins therefore contribute to magnetic superstructure reflections with $\mathbf{k}_{\text{Mn}^{3+}} = \pm(\frac{1}{4} -\frac{1}{4} 0)$; for example there is a contribution at $\mathbf{Q} = (0.25 \ 0.75 \ 0) \hat{=} (0.25 \ -0.25 \ 0)$, but not

		T_C	fund. reflections	unit cell
charge order		$\simeq 220$ K	$\pm(\frac{1}{2} \frac{1}{2} 0)$	$\sqrt{2}a \times \sqrt{2}a$
orbital order		$\simeq 220$ K	$\pm(\frac{1}{4} \frac{1}{4} 0)$	$2\sqrt{2}a \times \sqrt{2}a$
magnetic order	Mn ³⁺	$\simeq 110$ K	$\pm(\frac{1}{4} \bar{1} \frac{1}{4} 0)$	$\sqrt{2}a \times 2\sqrt{2}a$
	Mn ⁴⁺	$\simeq 110$ K	$\pm(\frac{1}{2} 0 0)$	$2a \times 2a$

Table 4.1: Summary of the fundamental superlattice reflections and the size of the various unit cells in the COO state according to the Goodenough model together with the observed transition temperatures for $\text{La}_{1/2}\text{Sr}_{3/2}\text{MnO}_4$.

at $\mathbf{Q} = (0.25\ 0.25\ 0)$, where the orbital lattice contributes. The Mn⁴⁺ spins contribute to neither of these positions, but to positions with $\mathbf{k}_{\text{Mn}^{4+}} = \pm(\frac{1}{2}\ 0\ 0)$, where the Mn³⁺ spins do not contribute. The full magnetic cell has to be described in a pseudoquadratic lattice with constants $2\sqrt{2}a$ along $[1\ 1\ 0]$ and $[1\ \bar{1}\ 0]$, as is shown in Fig. 4.3a. For convenience, Tab. 4.1 summarizes the various unit cells and fundamental reflections associated with the CE-type ordering.

The formation of the magnetic dimers in the Zener polaron approach, Fig. 4.3b, can be visualized as the localization of the e_g -electrons on the bridging oxygens [111], and results in a doubling of the nuclear unit. With the coherent stacking of the dimers the symmetry is further reduced and the lattice gets orthorhombic with constants $2\sqrt{2}a$ along $[1\ 1\ 0]$ and $\sqrt{2}a$ along $[1\ \bar{1}\ 0]$, both similar to the Goodenough model. The magnetic structure proposed by Efremov et al. [109] has to be described in a quadratic supercell with lattice constant $2\sqrt{2}a$ rotated by 45° with respect to the nuclear lattice. However, due to extinction conditions the magnetic ordering only contributes to reflections with $\mathbf{k}_{\text{mag}} = \pm(\frac{1}{4} - \frac{1}{4} 0)$ and $\pm(\frac{1}{2} 0 0)$, but not to $\mathbf{k}_{\text{mag}} = \pm(\frac{1}{4} \frac{1}{4} 0)$, and the number, as well as the position of the structural and magnetic Bragg reflections in the ZP-picture equals those of the CE model.

As aforementioned, the orthorhombic distortion of the ordered state induces a simple twinning in all sample crystals, as the occupied orbitals or the magnetic dimers, respectively, can either be stacked along the $[1\ 1\ 0]$ - or the $[1\ \bar{1}\ 0]$ -direction of the tetragonal lattice, and the arrangement depicted in Fig. 4.3 (orientation I) is superimposed by the same rotated by 90° (orientation II) in scattering experiments. However, throughout this chapter we will always refer to orientation I in the analysis of our data.

4.2 Spin-wave excitations and magnetic correlations in $\text{La}_{1/2}\text{Sr}_{3/2}\text{MnO}_4$

The static and dynamic magnetic correlations in $\text{La}_{1/2}\text{Sr}_{3/2}\text{MnO}_4$ were studied in a series of neutron scattering experiments on various spectrometers: at the thermal spectrometers 1T and 3T.1 and at the cold spectrometers 4F.1 and G4.3, all installed at the Laboratoire Léon Brillouin (LLB) in Saclay, at the spectrometers PANDA and PUMA of the FRM II in Munich, at IN3 at the Institut Laue Langevin (ILL) in Grenoble and at the spectrometer FLEX at the Hahn-Meitner Institut in Berlin.

For our studies we coaligned two single crystals of equal size, each with a volume of 0.6 cm^3 , grown by M. Benomar and by O. J. Schumann at the University of Cologne using a mirror furnace [63, 127]. The high quality of both samples was checked by diffraction techniques and by macroscopic measurements, yielding transition temperatures in good agreement with published results, see below.

In most of our experiments the $[001]$ -direction was set vertical to the scattering plane, allowing momentum transfers of the kind $(hk0)$. Only for selected scans at the PANDA and the G4.3 spectrometer we used a third, smaller crystal with a different mounting, so that reflections of the kind (hhl) were accessible during these experiments. In all experiments the energy transfer was achieved by varying the wavelength of the incoming neutrons monochromized either by the (002) -reflection of pyrolytic Graphite (PG) or, at higher incident energies, by the (111) -reflection of Copper, while on the analyzer side the energy of the neutrons was kept fix to, depending on the desired resolution, $E_f = 4.66\text{ meV}$, 14.7 meV or 30.5 meV . Spurious contributions by higher-order neutrons were always suppressed by mounting an appropriate filter, either PG or cooled Beryllium, behind the sample in the neutron's trajectory. Experiments with polarized neutrons were performed at the FLEX spectrometer using the standard longitudinal polarization analysis as described in the introduction, cf. Chap. 2.

Phonons

As we will show below, the magnon frequencies in $\text{La}_{1/2}\text{Sr}_{3/2}\text{MnO}_4$ extend to an energy regime typical for phononic excitations. The experimental identification of the magnetic signal is, hence, significantly hampered by the phonon background, and a very careful analysis is needed to uncover the magnetic contributions in the scattered intensity. In light of this problematic, a detailed knowledge of the phonon dispersion seems advantageous. Furthermore, in systems with complex ordering phenomena and strong electron-phonon coupling the phonon dispersion provides by itself important insights into the physical properties, as the phonon modes associated with the ordering scheme often exhibit an unusual behavior across the phase transition [132–134]. In a series of experiments at the thermal

spectrometer 1T.1 we have investigated large parts of the phonon dispersion within the MnO_2 -layers of $\text{La}_{1/2}\text{Sr}_{3/2}\text{MnO}_4$. However, as the scope of this chapter is on the magnetic excitations in the charge- and orbital-ordered phase, we will not discuss the phonon dispersion. Nevertheless, for the purpose of documentation, we plot the phonon dispersion for $T = 10\text{ K}$ in Fig. 4.4 and comment briefly on some important aspects in the following.

Along the main symmetry directions $[100]$ (Δ) and $[110]$ (Σ) of the tetragonal structure, the modes are indexed according to three or four irreducible representations. Common to the notation in Ref. [135], the subscript 1 always refers to the representation the longitudinal acoustic mode belongs to, while the subscript 3 signifies the representation containing the transverse acoustic modes. As in our experiments the $[001]$ direction was always oriented perpendicular to the scattering plane, we could only measure phonon modes polarized within the MnO_2 -layers, transverse phonons polarized along \mathbf{c} , corresponding to the subscript 4 in Ref. [135], are hence not included in the presentation of Fig. 4.4.

In the phonon dispersion shown in Fig. 4.4 several phonon bands, indicated by the gray-shaded areas, can be distinguished: In the low-energy region below $\approx 20\text{ meV}$ the acoustic modes are observed. The band between 20 meV and 25 meV represents the La/Sr-Mn vibrations, whereas the modes between 25 meV and 50 meV can be associated with the different Mn and Mn-O bond-bending modes. Phonons with higher frequencies between 50 meV to 70 meV have to be ascribed to the vibrations including the apical oxygen [135]. Of special interest concerning the COO transition at T_{CO} are the bond-stretching phonons at high energies above 70 meV : The in-plane breathing mode of Σ_1 symmetry might well be related to the checkerboard charge ordering, whereas the orbital ordering with propagation vector $(0.25\ 0.25\ 0)$ is connected to the transverse bond-stretching phonons of Σ_3 character – for a detailed discussion of the different polarization patterns we refer the interested reader to the presentation in Ref. [136].

In Fig. 4.4 we have also included the results of a first, very tentative calculation using a shell model, derived from the analysis of the phonon frequencies in the parent-compound LaSrMnO_4 [137]. The calculation does not consider the reduction of the structural symmetry from tetragonal to orthorhombic at T_{CO} and is based on the tetragonal crystal structure at room temperature. However, besides the bond-stretching modes the phonon frequencies are qualitatively well reproduced. Quantitatively, the model underestimates especially the frequencies of the bond-bending modes, but for such a simple approach the overall agreement in the intermediate energy regime below 70 meV is surprisingly good. In contrast, the description of the bond-stretching modes above 70 meV is insufficient: The longitudinal bond-stretching branch with Δ_1 symmetry exhibits a very anomalous behavior and appears to be split into at least two different contributions, whereas one would expect only a single mode in a tetragonal environment. The frequency splitting between the two bond-stretching contributions of the order of $\approx 15\text{ meV}$

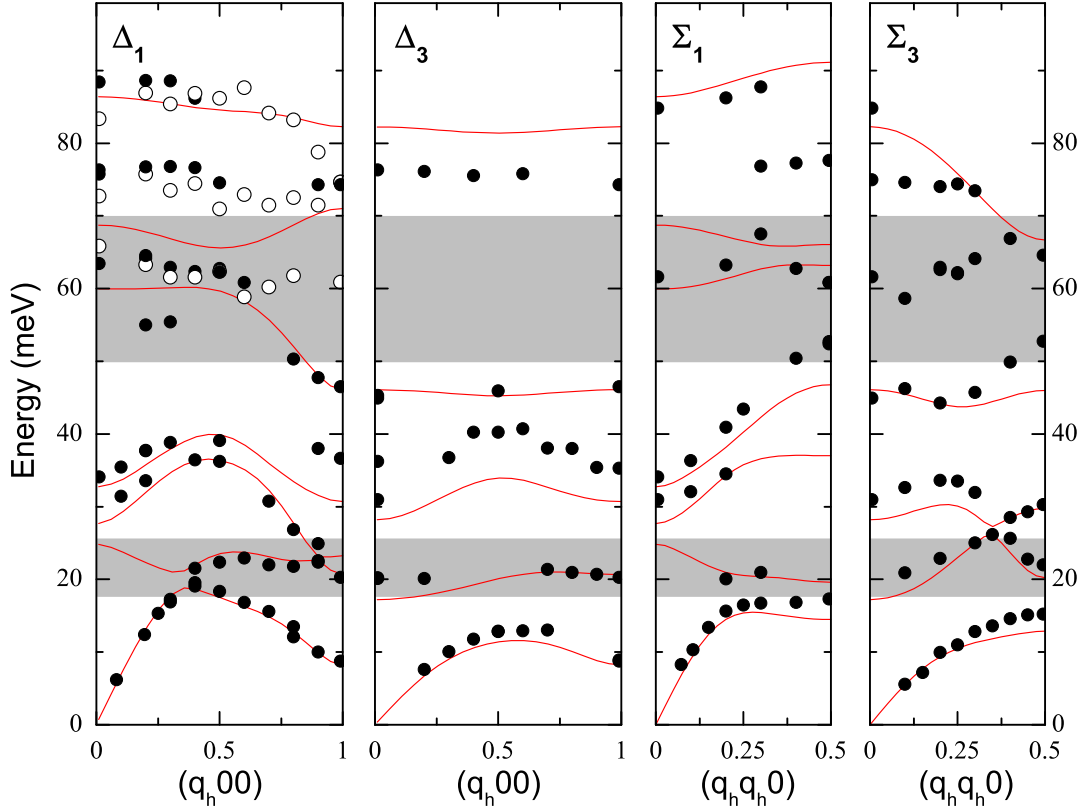


Figure 4.4: Phonon dispersion in $\text{La}_{1/2}\text{Sr}_{3/2}\text{MnO}_4$ Phonon dispersion of the in-plane modes at $T = 10$ K along the main symmetry directions $[100]$ (Δ) and $[110]$ (Σ). Full symbols denote data for the optimal doped compound $\text{La}_{1/2}\text{Sr}_{3/2}\text{MnO}_4$, whereas open symbols mark data obtained in the closely related, but slightly overdoped system $\text{La}_{0.4}\text{Sr}_{1.6}\text{MnO}_4$; solid red lines represent a semi-quantitative description using a shell model based on the tetragonal high-temperature structure derived from the parent compound LaSrMnO_4 . Gray-shaded areas mark the different phonon bands. See the text for more details.

is extraordinarily high. In the $[110]$ -direction there is again a splitting of the longitudinal modes, which furthermore both possess a much lower energy than the corresponding mode at 100 meV in the parent compound LaSrMnO_4 . Note at this point, that the planar breathing distortion of the charge ordered state is closely related to the polarization pattern of the bond-stretching modes with Σ_1 symmetry.

The structural distortions corresponding to the orbital ordering of the CE pattern correspond to the transversal bond-stretching modes along the $[110]$ -direction of Σ_3 symmetry. Following the branch Σ_3 from the zone center to the zone boundary we do not find any particularities at the ordering wave vector $(0.25, 0.25, 0)$, but similar to the longitudinal modes the bond-stretching frequen-

cies are split by several meV.

The observed splitting of the bond-stretching modes agrees nicely with recent results using Raman spectroscopy [138]: Yamamoto et al. report on the observation of Raman-active phonon modes at 64 meV, 79 meV and 86 meV in the ordered state, which disappear at the transition into the disordered phase at T_{CO} . These phonon frequencies agree very well with our neutron data, as we find 63.4 meV, 76.3 meV and 88.4 meV for the frequencies of the highest zone-center modes.

We finish the little excursion to the phonon scattering by concluding, that the observed splitting of the bond-stretching modes can not be explained within the tetragonal crystal structure of space group $I4/mmm$ – the frequencies of the bond-stretching modes are closely related to the local distortions in the COO state. However, a comprehensive understanding of the complex phonon dispersion in the course of a shell-model calculation based on the orthorhombic structure of the ordered state surely requires a better experimental characterization of the phonon frequencies both above and below T_{CO} , and more neutron beam-time is surely needed.

4.2.1 Magnon dispersion in the COO state

The spin-wave spectrum of $\text{La}_{1/2}\text{Sr}_{3/2}\text{MnO}_4$ at the magnetic zone-center $\mathbf{Q} = (\frac{3}{4} \frac{3}{4} 0)$ for $T=10$ K is shown in Fig. 4.5. Regarding first the left panel of Fig. 4.5, at $\mathbf{q} = 0$ the spectrum consists of two well distinguishable contributions centered at $\omega_1 = 1.0$ meV and $\omega_2 = 2.0$ meV. However, the splitting of the two modes is restricted to the region very close to the zone center, moving away from $\mathbf{q} = 0$ the two excitations immediately merge into a single feature and already at $|\mathbf{q}| = 3.9 \times 10^{-3} \text{ \AA}^{-1}$ away from the zone center no splitting in the magnon frequencies is resolved anymore, see Fig. 4.5b. As the magnetic moments are aligned within the \mathbf{ab} -planes of the layered structure [54, 122], the splitting of the modes at the zone center might be caused by the influence of the spin-orbit coupling resulting in a weak anisotropy in the superexchange interaction, which is rather typical for layered structures [62, 139]. In the two-dimensional isostructural cuprates, such a mechanism provokes a similar removal of the magnon degeneracy at the zone center, and the in-plane fluctuations appear lower in energy than the out-of plane oscillations [140, 141].

To test this interpretation, we measured the q_t -dependence of the spin-wave excitations at the PANDA spectrometer, see Fig. 4.5c. As only the component of the dynamic magnetization perpendicular to the scattering vector \mathbf{Q} contributes to the cross section, the fluctuations parallel and perpendicular to the \mathbf{ab} -planes are both expected to exhibit a characteristic behavior as the scattering vector is aligned parallel to the \mathbf{c} -axis. However, comparing the measured spectra at the same \mathbf{Q} -position ($\frac{3}{4} \frac{3}{4} 0$), the two magnon contributions appear hard to be resolvable in the spectra shown in Fig. 4.5c. With the different choice of the scattering

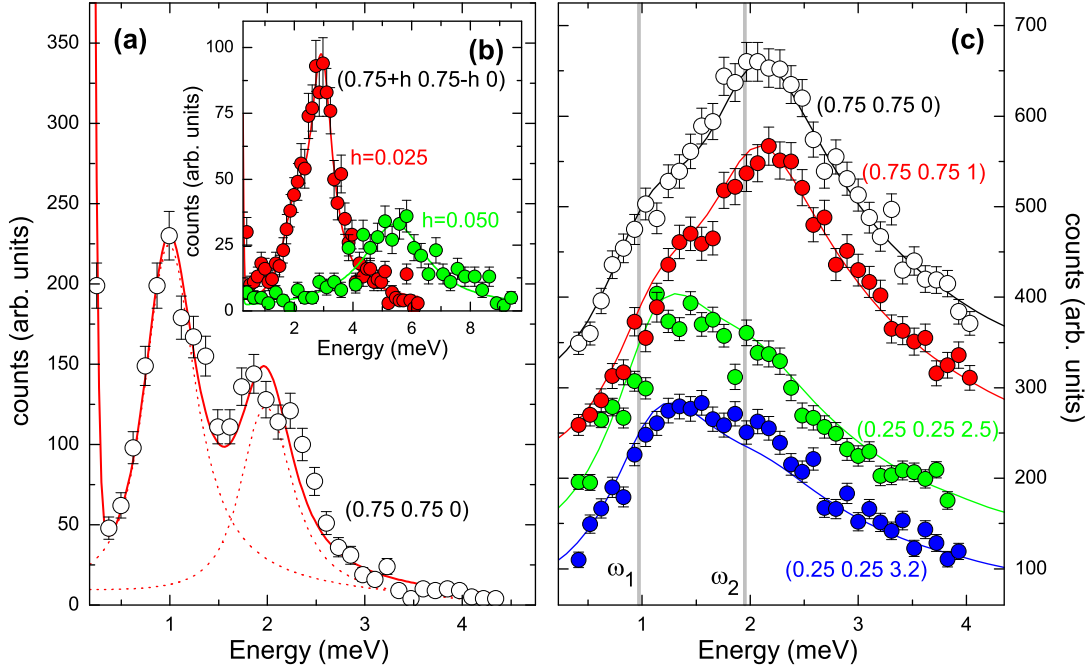


Figure 4.5: Anisotropy gap at the magnetic zone center Magnetic excitation spectrum of $\text{La}_{1/2}\text{Sr}_{3/2}\text{MnO}_4$ for $T=10\text{ K}$ at the magnetic zone-center $Q = (\frac{3}{4}, \frac{3}{4}, 0)$ measured at the cold spectrometer 4F.1 and the energy of the analyzed neutrons fixed to $E_f = 4.66\text{ meV}$ (a). q -dependence of the spectrum close to the zone center with $q \parallel [1 \bar{1} 0]$ determined using the same configuration (b). q_l -dependence of the spectrum recorded at the PANDA spectrometer, again with E_f fixed to 4.66 meV , but with a different scattering geometry, see text (c). For clarity, the spectra are successively shifted vertically in (c). Lines are fits to the data including the convolution of the spectrometer resolution function as described in the text, vertical gray lines mark the positions of the two excitations as determined in the 4F experiment.

plane – in the first experiment at the 4F the c -axis was vertical, whereas for the PANDA experiment the sample was aligned with the reflections $(110)/(001)$ defining the space of possible momentum transfers – the different line shapes have to be attributed to resolution effects due to the relaxed vertical resolution of a focusing TAS spectrometer: As in a two-dimensional system the magnon dispersion along c is negligible, see the discussion in Chap. 3, the first choice of the scattering plane ensures an efficient integration over large parts of the Brillouin zone without affecting the experimentally observed response, whereas in the second case the integration occurs along the steep part of the dispersion, which significantly broadens the observed signal, cf. Chap. 2.

To take the different experimental conditions into account, all spectra presented in Fig. 4.5 were modeled using the ResLib package [27], enabling a four-dimensional convolution of the resolution function with the dispersion surface. In

a first step, we fitted the spectra obtained with the \mathbf{c} -axis vertical, yielding the magnon energies $\hbar\omega_1 = 0.97(2)$ meV and $\hbar\omega_2 = 1.97(4)$ meV. These energies were then kept fixed for the refinement of the data obtained in the second scattering geometry.

Now, we can turn to the discussion of the q_l -dependence of the spectra shown in Fig. 4.5c. Apparently, all spectra can be reasonably well described assuming always the same frequencies for the two different contributions. Therefore, the magnon dispersion along the \mathbf{c} -axis is indeed negligible, and we will ignore it for the rest of the discussion in this chapter – in the layered structure the coupling of neighboring planes is at least one order of magnitude weaker than within the planes, see the dispersion of the undoped compound LaSrMnO₄ in Chap. 2. The increase of the q_l -component, however, affects essentially the distribution of spectral weight between the two modes. While the intensity of the mode ω_1 follows the magnetic form factor of Mn³⁺ [21], the mode ω_2 is additionally suppressed as the scattering vector \mathbf{Q} is rotated towards the \mathbf{c} -axis. This behavior already suggests a dominant component along \mathbf{c} for the mode ω_2 . Assuming in the fitting process the mode ω_1 to be polarized entirely within, and the mode ω_2 perpendicular to the \mathbf{ab} -plane, the observed distribution of spectral weight is described reasonably well for all recorded spectra. Hence, we conclude that at the magnetic zone center the degeneracy of the AFM spin-wave branches is removed due to different magnetic anisotropies; the fluctuations parallel to the \mathbf{ab} -plane have a lower frequency than those perpendicular.

In addition to the experiments at the cold instruments, the full magnon dispersion within the \mathbf{ab} -planes has been determined in several experiments at the thermal spectrometer 1T.1. Typical scans aiming at different parts of the dispersion are shown in Fig. 4.6. At higher energies, the magnetic scattering interferes with phonon signals, but the different $|\mathbf{Q}|$ -dependence separates between both contributions, see Fig. 4.6b and c. The counting times for these scans range from 30 sec./point at low energies and using the PG monochromator to 4 min./point for higher energies and using the Copper monochromator. As resolution effects are less pronounced in these scans, these data were always analyzed using simple Gaussian line shapes. More importantly, in spite of the twinning of the crystal structure in the COO phase, we are able to separate the magnon branches parallel and perpendicular to the zig-zag chains, as only one twin contributes to a quarter-indexed magnetic superstructure reflection: When going from the antiferromagnetic zone center $(\frac{3}{4} - \frac{3}{4} 0)$ along the $[110]$ -direction we determine the spin-wave dispersion parallel to the chains, see Fig. 4.6e, and, going along the $[1\bar{1}0]$ -direction, we measure the dispersion perpendicular to the chains, see Fig. 4.6d.

Already the raw-data scans shown in Fig. 4.6 unambiguously demonstrate that the dispersion along the zig-zag chains is much steeper than perpendicular to them. The magnetic structure has to be considered as a weak antiferromagnetic ordering

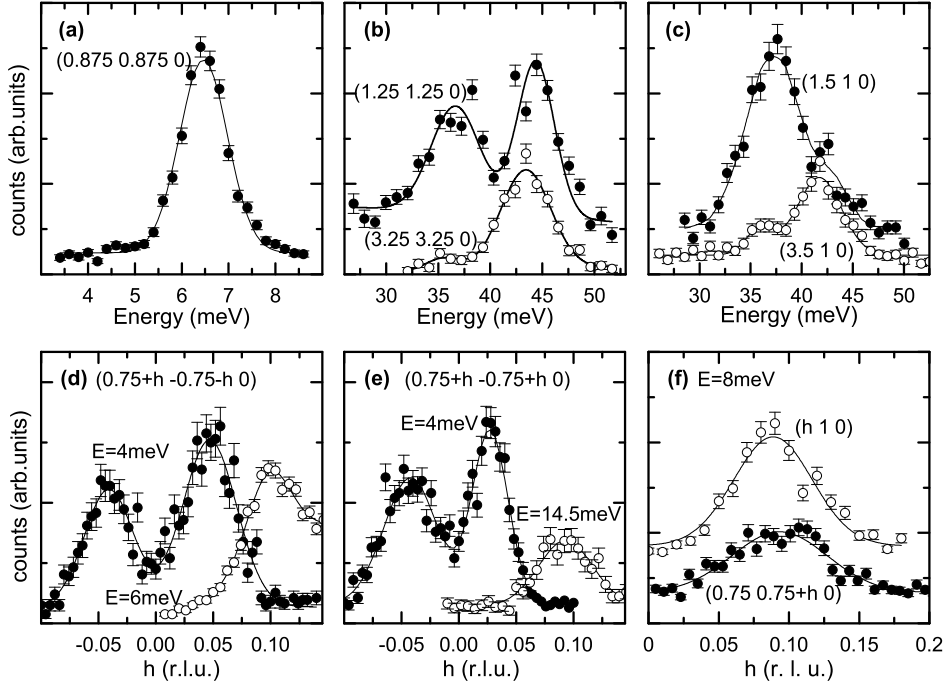


Figure 4.6: Raw-data scans to determine the magnon dispersion Scans aiming at various parts of the magnon dispersion in $\text{La}_{1/2}\text{Sr}_{3/2}\text{MnO}_4$; symbols denote the data and lines fits with Gaussians. Constant Q scans at the antiferromagnetic zone center and zone boundaries (a)-(c), and constant energy scans for different energies across $(0.75\text{-}0.75\ 0)$ in the $[1\ \bar{1}\ 0]$ -direction, i.e. perpendicular to the zig-zag chains, (d), in the $[1\ 1\ 0]$ -direction, i.e. parallel to the zig-zag chains, (e), and in the $[1\ 0\ 0]$ -direction, i.e. in a direction 45° to the chains, (f). All scans were measured at the thermal instrument 1T.1 at $T = 10\text{K}$, scans in (a) and (d)-(f) using the PG monochromator and the energy of the scattered neutrons fixed to $E_f = 14.7\text{meV}$, scans in (b) and (c) using the copper monochromator and $E_f = 30.5\text{meV}$. The different $|Q|$ -dependence separates magnetic from phononic scattering at higher energies in (b) and (c).

of strongly coupled ferromagnetic chains. The obtained magnon dispersion is presented in Fig. 4.7.⁵ The branch propagating along the chains, $\Gamma - C$, is much steeper than the branch propagating perpendicular to it, path $\Gamma - B$, and we find magnon energies at the zone boundaries C and B of 19meV and 6.5meV , respectively. At the point C where q is parallel to the chains, the end point of the acoustic branch coincides with that of the lowest optic branch, whereas there is a large gap between these branches along the path $\Gamma - B$. The magnon branch along the $[1\ 0\ 0]$ -direction, path $\Gamma - A$ at 45° to the chains, exhibits an

⁵The splitting of the magnon branches at the zone center discussed above is neglected, as it is limited to regions close to $q = 0$ and irrelevant for the overall dispersion. The value chosen for the figure is the average of the above results.

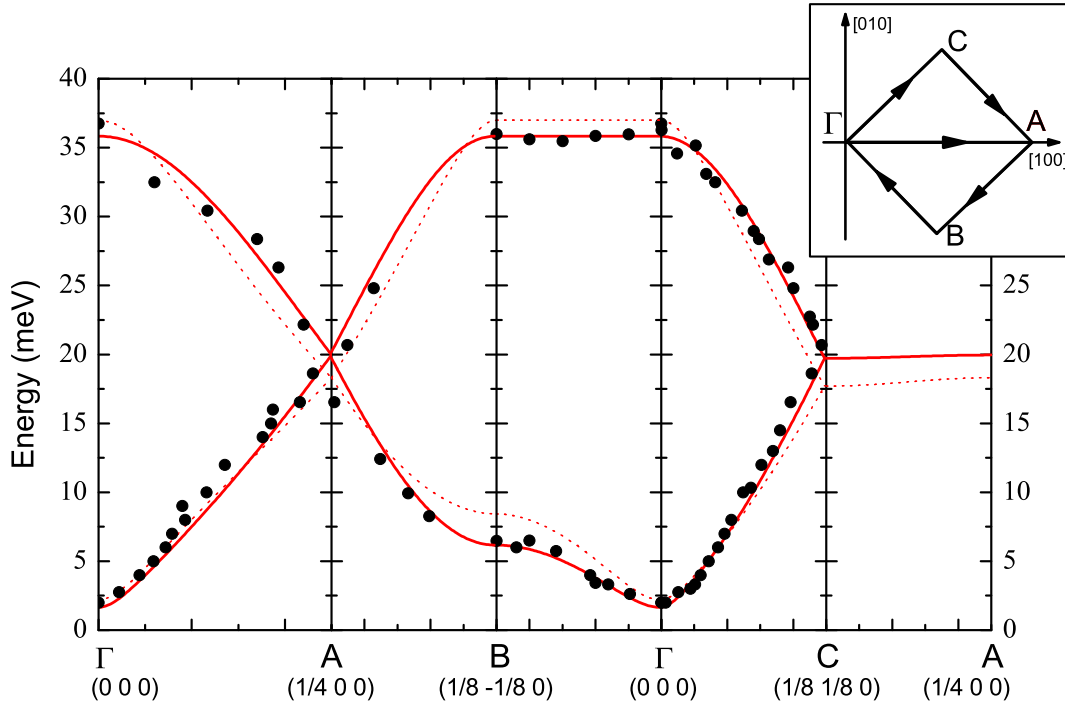


Figure 4.7: Magnon dispersion in $\text{La}_{1/2}\text{Sr}_{3/2}\text{MnO}_4$ Dispersion of the magnetic excitations in $\text{La}_{1/2}\text{Sr}_{3/2}\text{MnO}_4$ in a direction parallel to $[100]$, Γ to A , perpendicular to the zig-zag chains, Γ to B , and parallel to the zig-zag chains, Γ to C . The solid and the dashed lines give the spin-wave dispersion calculated with the two parameter sets discussed in the text. The inset sketches a part of the magnetic Brillouin zone, displaying the high symmetry points $\Gamma = (000)$, $A = (\frac{1}{4}00)$, $B = (\frac{1}{8}-\frac{1}{8}0)$, $C = (\frac{1}{8}\frac{1}{8}0)$, and the path of the calculated dispersion. Note, that the zig-zag chains run along the $[110]$ -direction.

intermediate dispersion. Finally, all zone-boundary modes connect when passing along the zone-boundary paths $A - B$ and $A - C$.

In addition to the scans around quarter-indexed magnetic reflections, we have performed measurements around half-indexed ones as well. As explained in the introductory section, in elastic scans at these Q -values one strictly measures the scattering contributions due to the Mn^{3+} and Mn^{4+} sites, respectively. This separation should hold for inelastic scattering at rather low energies as well. Around these Q -values we find exactly the same dispersion, as it is expected for collective magnons. At finite energies there is also a significant structure factor around the integer-indexed Q -values, like (100) ; again the dispersion of the modes fully agrees with the other zones. The dispersion shown in Fig. 4.7 was obtained finally by combining many scans in different magnetic zones. At energies significantly above the saturation of the acoustic magnon branch perpendicular to the zig-zag chains, i.e. 6.5 meV, the magnetic interaction perpendicular to the chains does

not play any role anymore and the magnon dispersion exhibits an one-dimensional character.

To analyze the observed spin-wave dispersion, the magnon spectrum of the classical CE-type ordering shown in Fig. 4.3a has been calculated using the Holstein-Primakoff transformation and a simple spin-only Hamiltonian,

$$\begin{aligned} \mathcal{H} = & - \sum_{(\text{Mn}^{3+}, \text{Mn}^{4+})_{\parallel}} J_{\text{FM}} \mathbf{S}_i \cdot \mathbf{S}_j \\ & + \sum_{(\text{Mn}^{3+}, \text{Mn}^{4+})_{\perp}} J_{\text{AFM}} \mathbf{S}_i \cdot \mathbf{S}_j \\ & - \sum_{(\text{Mn}^{4+}, \text{Mn}^{4+})_{\parallel}} J_{\text{FM},2} \mathbf{S}_i \cdot \mathbf{S}_j - \sum_{\text{Mn}} \Lambda S_z^2, \end{aligned} \quad (4.1)$$

as a part of the PhD-thesis of F. Krüger [142, 143]. The summations in eq. 4.1 extend over all Mn-Mn sites within a plane of the layered structure,⁶ the first sum includes the FM-interaction J_{FM} between adjacent Mn^{3+} and Mn^{4+} sites within the zig-zag chains, the second the AFM-interaction J_{AFM} of neighboring sites on different chains, and the third term incorporates a FM interaction $J_{\text{FM},2}$ between the cornering Mn^{4+} spins of the chains. For an illustration of the different magnetic interactions see the sketch in Fig. 4.3a. The last term in the Hamiltonian eq. 4.1 reflects a single-ion anisotropy Λ to account for the observed gap at the zone-center. As we are not aware of an unambiguous determination of the magnetic structure of the CE phase, the spin-values for the Mn^{3+} and Mn^{4+} -sites were fixed to $S = 2$ and $S = 1.5$ in the calculation, respectively.

Taking into account only the two nearest-neighbor interactions for a $\text{Mn}^{3+}/\text{Mn}^{4+}$ pair within and in-between the zig-zag chains, J_{FM} and J_{AFM} , we obtain a good description of the measured dispersion denoted in Fig. 4.7 by the dotted lines. However, significant discrepancies remain, and it is impossible to simultaneously describe the large initial slope of the spin-wave dispersion along the chains and the relatively lower zone-boundary frequencies. This behavior implies the relevance of an additional longer-distance interaction parameter acting along the ferromagnetic chains. Indeed, a fully satisfactory description is obtained by including the ferromagnetic interaction $J_{\text{FM},2}$ for Mn^{4+} - Mn^{4+} spin pairs connected via a Mn^{3+} within a zig-zag chain, see the solid lines in Fig. 4.7, and we obtain the parameters $J_{\text{FM}} = 4.99$ meV, $J_{\text{AFM}} = 0.92$ meV, $J_{\text{FM},2} = 1.85$ meV for the relevant magnetic exchange interactions and an anisotropy term of $\Lambda = 0.05$ meV.⁷

⁶The definition of the exchange integral J in the Heisenberg Hamiltonian $\mathcal{H} = \sum_{i,j} J_{ij} \mathbf{S}_i \cdot \mathbf{S}_j$ may easily evoke a “factor-2-problem”, as there is no consensus at this point in the literature. Throughout this thesis we follow the “common” convention set by the recent discussion on manganites, see e. g. Ref. [144], and define the summation over all lattice sites, i. e. each bond contributes twice to the total energy, in contrast to, for example, the classical work of Anderson on antiferromagnetic fluctuations [145].

⁷The magnon dispersion can be described nearly equally well when considering a long-range FM coupling between two Mn^{3+} -sites along the zig-zag chains, but this parameter appears less physical.

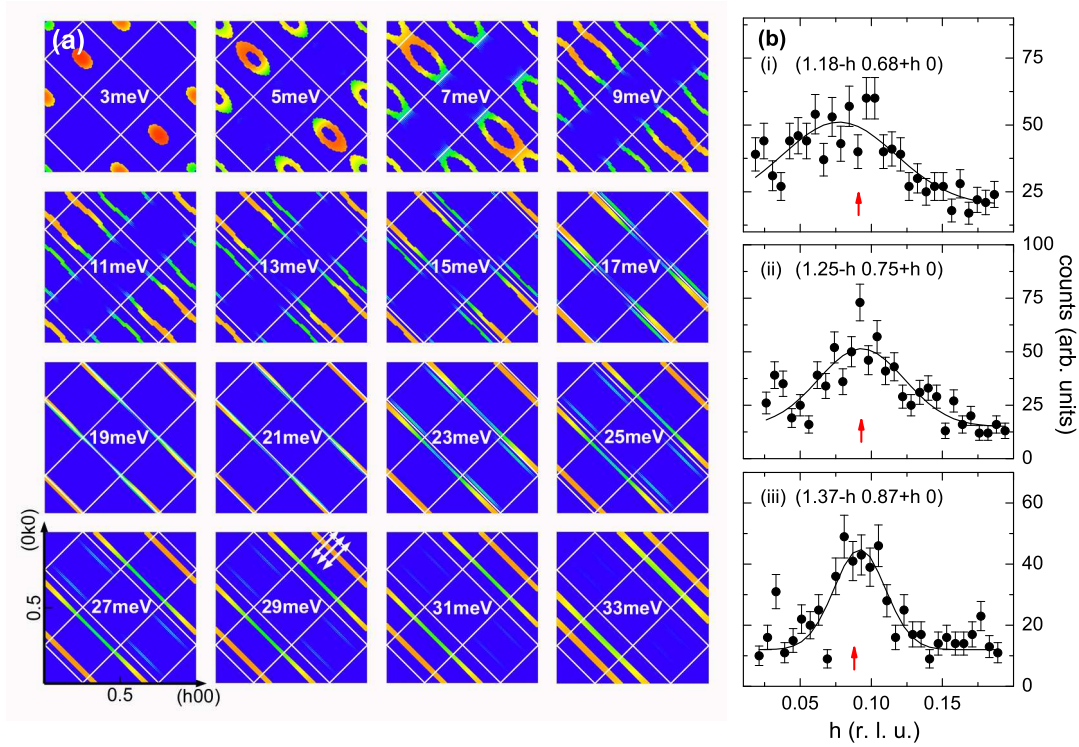


Figure 4.8: Simulated neutron intensity Constant energy cuts through the calculated spin-wave structure factor $S(\mathbf{Q}, \omega)$ with constant energy resolution of 2 meV within each plot and with energy steps of 2 meV between adjacent plots, showing the dispersion and intensity distribution of the lowest magnon bands within the tetragonal Brillouin zone. The magnetic zones are denoted by white squares (a). Constant energy scans at $E = 29$ meV along the direction indicated by the white arrows in (a) to experimentally verify the one-dimensional character of the high-energy magnetic scattering. The red arrows indicate the expected positions of the magnon as determined from the calculation (b).

In addition to the dispersion, the calculation also yields the inelastic structure factors and the neutron scattering intensities, which are presented in Fig. 4.8. Although a quantitative comparison with the experimental data is very difficult, the calculated and observed intensities agree qualitatively very well. Actually, the theoretical description has always been refined as soon as new experimental informations were available, and the neutron scattering experiments were always guided by the predictions of the current model, until a conclusive experimental and theoretical picture was finally achieved.⁸

⁸The calculation predicts the existence of a second, high-energy magnon band between 70 meV and 75 meV, which could not be confirmed so far by the experiment because of the strong phonon signal at these energies.

The contour plots of the calculated structure factors in Fig. 4.8 reveal how the anisotropic spin-wave cones develop around the magnetic Bragg peaks with finite structure factor. At intermediate energies also those magnetic Brillouin zones contribute where there is no elastic scattering. Fig. 4.8 further illustrates that well above the maximum of the acoustic magnon perpendicular to the zig-zag chains, the system looks like a magnetically one-dimensional system as the magnons disperse only along the zig-zag chains. To further confirm the one-dimensional character we have performed constant energy scans at $E = 29$ meV parallel to the chain direction at three different positions along the magnon streak. The observed magnon signals match almost perfectly with the predictions, see Fig. 4.8b.

In contrast to the excellent modeling of the magnon dispersion based on the Goodenough model, there is no straightforward description of the observed dispersion within the Zener polaron model. Ab initio calculations show, that the different exchange couplings in the Zener polaron picture are supposed to be very anisotropic. Clearly, the FM coupling within a dimer sets the magnetic energy scale within this approach, the interdimer interactions are shown to be at least one order of magnitude smaller [110, 112]. Hence, the steepest branch of the spin-wave dispersion is expected along the direction probing the intradimer exchange. However, in the herringbone pattern shown in Fig. 4.3b, the dimers are stacked *perpendicular* to the propagation of the zig-zag chains, and, consequently, the dispersive branch is expected along his direction – just opposite to the experimental result with the steep dispersion parallel to the zig-zag chains. This failure and the precise spin-wave description obtained within the CE-type model give strong support for the latter in $\text{La}_{1/2}\text{Sr}_{3/2}\text{MnO}_4$. In the following, we neglect the Zener polaron and focus only on the Goodenough model.

Analyzing the spin-wave dispersion in more detail, the ferromagnetic interactions along the zig-zag chains are remarkably large, the FM nearest neighbor exchange J_{FM} is about a factor of 5 stronger than the ferromagnetic coupling in LaMnO_3 acting on two Mn^{3+} sites with an antiferroorbital ordering [144, 146], whereas the antiferromagnetic interchain coupling J_{AFM} is only small, probably due to competing effects. J_{FM} is even significantly larger than the ferromagnetic interaction in the metallic ferromagnetic phases with the highest Curie temperatures [147, 148], pointing towards a sizable delocalization of the e_g -electrons along the zig-zag chains. Indeed, Furukawa has shown, how the double exchange model in the metallic manganite phases maps to a Heisenberg model description: with increasing electron localization the spin-spin interactions become more short range and vice versa [149]. Hence, the strong ferromagnetic interaction in $\text{La}_{1/2}\text{Sr}_{3/2}\text{MnO}_4$ being not restricted to nearest neighbors indicates that the electrons are not fully localized in the charge-ordered phase, suggesting an one-dimensional electronic structure. The insulating character of the zig-zag chains is, nevertheless, preserved by topological aspects [106].

A one-dimensional electronic structure of the ordered state is furthermore in good agreement with theoretical investigations [105] and recent experimental observations [150–152]. Using optical spectroscopy, it has been demonstrated that below T_{CO} the optical properties are anisotropic, and the electronic energy gap is smaller parallel than perpendicular to the chains. Hence, electron hopping is most effective along the chain direction [152], pointing towards a one-dimensional electronic structure comparable with the implications derived from the anisotropic spin-wave dispersion.

4.2.2 Diffuse magnetic scattering

The dominant character of the ferromagnetic exchange J_{FM} along the zig-zag chains revealed in the analysis of the spin-wave dispersion also results in a characteristic temperature dependence of the magnetic correlations: As the temperature is increased the long-range antiferromagnetic CE-type correlations are destroyed and short-range ferromagnetic correlations appear as the precursor of the zig-zag ordering above the Néel temperature in the neutron scattering data. In the following, we will discuss this diffuse magnetic scattering above T_N and the temperature dependence of the magnetic fluctuations.

To characterize the diffuse magnetic scattering in a wide temperature regime between 10 K and 250 K we have performed two experiments at the double-axis diffractometer 3T.1 and at the triple-axis spectrometer G4.3, both installed at the Orphée reactor at the LLB in Saclay. The 3T.1 diffractometer is a high-flux instrument, and the experiment was performed with at a fixed neutron energy of $E_i = 14.7$ meV and relaxed experimental resolution. The spectrometer G4.3 is installed at a neutron guide serving an excellent signal-to-noise ratio and a good experimental resolution with $E_f = 13.7$ meV. Typically, selected scans performed at the 3T.1 were repeated at the G4.3 to improve the experimental resolution and to estimate the contribution of slow magnetic fluctuations to the diffuse signal, as the diffractometer integrates over a sizable energy interval. However, the data taken on both instruments agree qualitatively and quantitatively very well, setting an upper cut-off energy of $\Delta E \approx 0.5$ meV, corresponding to a timescale for the magnetic fluctuations of 10^{-11} sec., for both experiments. Special care was always put on an efficient suppression of the contamination by second-order neutrons with PG-filters mounted in the neutron's pathway.

As aforementioned, the orbital ordering induces a single twinning as the chains can either propagate along the $[110]$ or the $[1\bar{1}0]$ direction. As before, for the analysis of the data we always refer to the first orientation (see Fig. 4.3a), but in an experiment both twins contribute equally to the scattered intensity. Hence, each quarter-indexed reflection measures the magnetic correlations of the first twin and, at the same time, the orbital superstructure of the second and vice versa. However, the different $|\mathbf{Q}|$ -dependence of magnetic and structural scattering allows

4.2 Spin-wave excitations and magnetic correlations in $\text{La}_{1/2}\text{Sr}_{3/2}\text{MnO}_4$

\mathbf{Q}		P_x	P_y	P_z	FR_x	FR_y	FR_z	$I_{\text{mag}}/I_{\text{struc}}$
(0.75 0.25 0)	SF	14511	1087	14619				
	NSF	796	14179	848	18.2(7)	0.077(2)	17.2(6)	1.00 / 0.00
(0.75 0.75 0)	SF	1625	161	1624				
	NSF	208	1659	264	7.8(6)	0.097(8)	6.2(4)	0.94 / 0.06
(1.25 0.25 0)	SF	3013	475	3194				
	NSF	486	3085	498	6.2(3)	0.154(8)	6.4(3)	0.91 / 0.09
(1.75 0.25 0)	SF	8550	4475	7508				
	NSF	72665	76331	72745	0.118(1)	0.059(1)	0.103(1)	0.05 / 0.95
(0.5 1 0)	SF	12999	1200	13091				
	NSF	797	12653	734	16.3(6)	0.095(3)	17.8(7)	1.00 / 0.00
(2 0 0)	SF	2486	1903	1800				
	NSF	30032	30846	31304	0.083(2)	0.062(1)	0.058(1)	0.00 / 1.00

Table 4.2: Polarization analysis of different superstructure reflections at $T=5$ K measured at the FLEX spectrometer. The spin quantization axis is given by P_j , where the subscripts x, y, z refer to $\mathbf{P} \parallel \mathbf{Q}$ (x), $\mathbf{P} \perp \mathbf{Q}$ within (y), and $\mathbf{P} \perp \mathbf{Q}$ perpendicular to the scattering plane (z). For each \mathbf{Q} -value, the columns give the observed intensities with the spin flipper on and $\mathbf{P}_i = -\mathbf{P}_f$ (SF), and off and $\mathbf{P}_i = \mathbf{P}_f$ (NSF), as well as the calculated flipping ratios $\text{FR}_j = (\text{SF}/\text{NSF})_j$ for the different choices of the neutron quantization axis. The last column states the calculated distribution of magnetic and nuclear scattering at the different \mathbf{Q} -positions.

to separate the different contributions, which will be important for the following discussion; for small $|\mathbf{Q}|$, as e. g. $\mathbf{Q}_{\text{mag}} = (0.75 \ 0.25 \ 0)$, the structural contribution is weak and the observed intensity is determined by the magnetic order parameter. In contrast, at large $|\mathbf{Q}|$, as e. g. $\mathbf{Q}_{\text{orb}} = (2.25 \ 0.25 \ 0)$, the magnetic part is suppressed following the magnetic form factor and, simultaneously, the structural structure factor is severely increased, as it scales with $|\mathbf{Q}|^2$. To further quantify these considerations, we have performed a longitudinal polarization analysis of the scattered intensity for different \mathbf{Q} -positions at the FLEX spectrometer at the HMI in Berlin, see table 4.2.

In the classical polarization analysis [22], spin-flip scattering (SF) is always magnetic, whereas non spin-flip scattering (NSF) can be either magnetic or structural: Magnetic moments aligned perpendicular to the neutron quantization axis contribute to the spin-flip channel, those aligned parallel to the non spin-flip channel. These selection rules are corroborated by the general rule, that only the component of the magnetization perpendicular to the scattering vector \mathbf{Q} contributes to the cross section (cf. Chap. 2). With the scattering plane defined by the \mathbf{ab} -plane and the usual choice of the neutron coordinate system – $\mathbf{P} \parallel \mathbf{Q}$, $\mathbf{P} \perp \mathbf{Q}$ within and $\mathbf{P} \perp \mathbf{Q}$ perpendicular to the scattering plane denoted as x, y, z , respectively – all magnetic scattering is spin-flip in the x -channel. With $\mathbf{P} \parallel \mathbf{y}$, the out-of-plane

magnetization is detected in the SF-channel and the in-plane component in the NSF-channel, and vice versa for $\mathbf{P} \parallel \mathbf{z}$.

In addition to the quarter-indexed reflections, table 4.2 includes the full polarization analysis for the entirely magnetic reflection $\mathbf{Q}=(0.5\ 1\ 0)$ and the $I4/mmm$ Bragg position $\mathbf{Q}=(2\ 0\ 0)$. These two reflections serve as a reference for the analysis of the quarter reflections and probe essentially the quality of the experimental setup. The imperfectness of the flipping ratios, $\text{FR} = I_{\text{SF}} : I_{\text{NSF}}$, at these \mathbf{Q} -values reflects the experimental loss of polarization along the neutron's trajectory. Inspecting the distribution of magnetic scattering in the various P_i -channels at the magnetic position $(0.5\ 1\ 0)$, it is immediately clear that the magnetic moments are confined within the \mathbf{ab} -planes, in agreement with the literature [54].

Turning to the quarter-indexed reflections, the comparison of the flipping ratios with those of the reference positions directly demonstrates how the character of the scattering changes with increasing $|\mathbf{Q}|$. For $\mathbf{Q}_{\text{mag}} = (0.75\ 0.25\ 0)$ the FR's are nearly identical to those of the magnetic reflection $\mathbf{Q} = (0.5\ 1\ 0)$, and only magnetic scattering contributes at \mathbf{Q}_{mag} . With increasing $|\mathbf{Q}|$ the structural scattering gets dominant and at $\mathbf{Q} = (1.75\ 0.25\ 0)$ the magnetic contribution is marginal as the FR's are comparable with those determined at $\mathbf{Q} = (2\ 0\ 0)$. A quantitative analysis of the data confirms this qualitative argumentation. Indeed, the scattering at $\mathbf{Q}_{\text{mag}} = (0.75\ 0.25\ 0)$ is entirely magnetic in character, whereas at $\mathbf{Q} = (1.75\ 0.25\ 0)$ only 5% of the scattering has a magnetic origin, while 95% must be associated with structural distortion induced by the orbital ordering. Therefore, in the following we will always attribute any scattering around the position $\mathbf{Q}_{\text{mag}} = (0.75\ 0.25\ 0)$ to magnetic correlations.

In order to analyze the magnetic correlations above the Néel ordering at $T_{\text{N}} \approx 110\ \text{K}$ [7, 54], we mapped the reciprocal space around the magnetic position \mathbf{Q}_{mag} at four different temperatures – well above the COO transition at 250 K, below the phase transition at T_{CO} but above T_{N} at 200 K and 150 K, and below the Néel transition at 100 K, see Fig. 4.9. All four mappings exhibit a significant magnetic response and the comparison of the different temperatures directly reveals drastic changes in the nature of the short-range magnetic correlations.

At $T = 250\ \text{K}$, i. e. in the disordered state well above the charge and orbital ordering, the magnetic scattering appears as a broad, structureless feature centered around $\mathbf{Q}_{\text{FM}} = (1\ 0\ 0)$, see Fig. 4.9a. In the body-centered structure of space group $I4/mmm$ the existence of a diffraction signal around this position always points to short-range ferromagnetic correlations, as the $(1\ 0\ 0)$ -reflection is forbidden for nuclear scattering due to the space-group extinction rules. From the width of the signal an isotropic correlation length $\xi_{\text{iso}} \approx 8\ \text{\AA}$ can be estimated for a pair of ferromagnetically aligned moments, see below. With the transition into the orbital-ordered phase the distribution of intensity changes remarkably and the magnetic scattering develops a distinct anisotropy. At $T = 200\ \text{K}$ the FM signal at $\mathbf{Q}_{\text{FM}} = (1\ 0\ 0)$ has lost a significant amount of spectral weight, and, simulta-

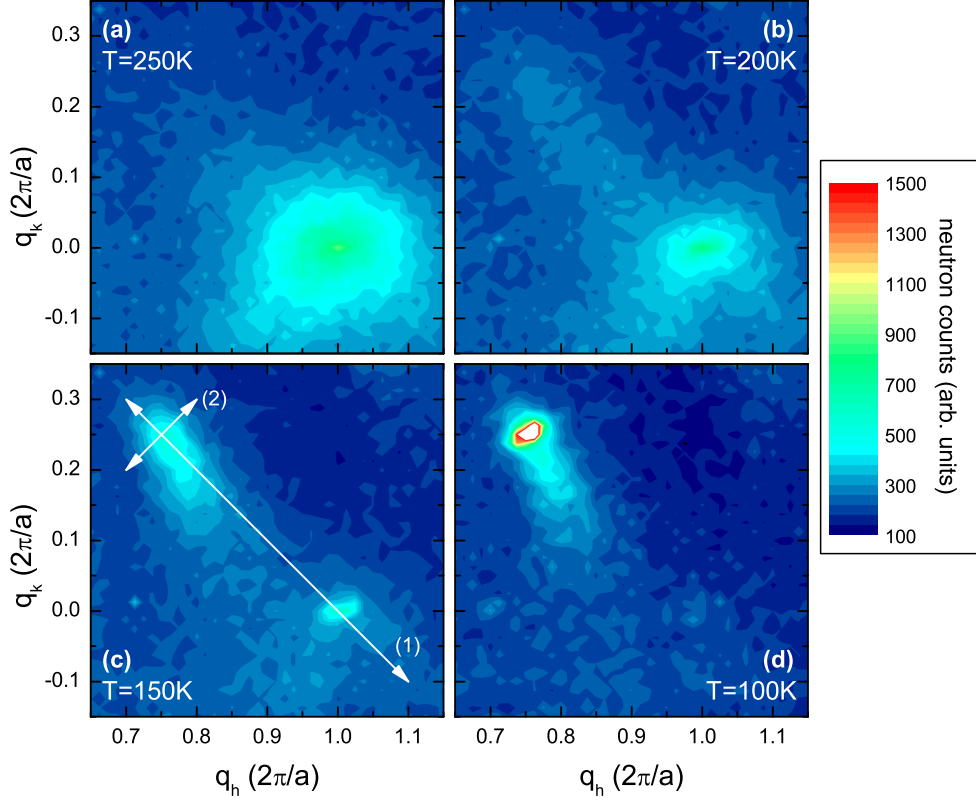


Figure 4.9: Diffuse magnetic scattering in $\text{La}_{1/2}\text{Sr}_{3/2}\text{MnO}_4$ Contour mappings of the diffuse magnetic scattering around the magnetic CE-type position $\mathbf{Q}_{\text{mag}} = (0.75\ 0.25\ 0)$ at various temperatures above the charge and orbital ordering at $T=250\text{ K}$ (a), below T_{CO} but above the Néel transition at $T=200\text{ K}$, (b), and 150 K (c), and below the AFM transition at $T=100\text{ K}$ (d). All maps were calculated from a grid of 41×41 data points with $\Delta q_h = \Delta q_k = 0.0125$, measured at the thermal diffractometer 3T.1. The two arrows in (c) denote the directions of the scans investigated in more detail, see text for more informations.

neously, the scattered intensity is increased along the path $(1\ 0\ 0) \rightarrow (0.75\ 0.25\ 0)$ in reciprocal space, see Fig. 4.9b. Upon further cooling this trend continues and for $T = 150\text{ K}$ two distinct features are resolvable. The FM signal at \mathbf{Q}_{FM} has further lost intensity, and a second peak has formed around $\mathbf{Q}_{\text{mag}} = (0.75\ 0.25\ 0)$, representing AFM correlations of the CE type. Still, both peaks are not resolution limited and along the line in reciprocal space connecting both positions the scattered intensity remains significantly enhanced above the background level, Fig. 4.9c. At $T = 100\text{ K}$, i.e. below T_{N} , the diffuse scattering around \mathbf{Q}_{FM} is completely suppressed and has entirely transformed into the sharp CE-type reflection at $\mathbf{Q}_{\text{mag}} = (0.75\ 0.25\ 0)$. However, the peak shape of this reflection is still asymmetric and the distribution of magnetic intensity around the commensurable

position is enhanced towards the FM position, reminiscent of the development of the diffuse magnetic scattering above T_N , see Fig. 4.9d.

Already at this stage of the discussion, the development of the diffuse magnetic scattering with anisotropic magnetic correlations appearing as a precursor for the AFM CE-type ordering below T_N nicely demonstrates the different character of the magnetic interactions along and perpendicular to the zig-zag chains, as is also found in the spin-wave dispersion, and emphasizes impressively the close correlation between the orbital ordering and the magnetic correlations. An equivalent observation has recently been reported by Ye et al. for the 113-compound $\text{Pr}_{0.55}(\text{Ca}_{0.8}\text{Sr}_{0.2})_{0.45}\text{MnO}_3$ [153], showing similar anisotropic correlations above T_N . To discuss their data, these authors introduced the concept of an one-dimensional, electronically smectic-like liquid crystal, based on the theory of anisotropic short-range double exchange interactions introduced by van den Brink et al. and Solovyev and Terakura [105, 106], very similar to our interpretation of the dominant magnetic interaction along the zig-zag chains.

To further analyze the thermal evolution of the magnetic correlations we studied the temperature dependence along two selected lines of reciprocal space, depicted in Fig. 4.9c by the two white lines, in more detail. Scan 1 runs parallel to the $[1\bar{1}0]$ -direction along the diffuse rod of magnetic intensity connecting the two CE-type reflections $(0.75\ 0.25\ 0)$ and $(1.25\ 0.25\ 0)$ and crossing the FM position (100) . Scan 2 is oriented perpendicular to the rod along the $[110]$ -direction, crossing the diffuse streak at the commensurable position \mathbf{Q}_{mag} . As only the magnetic twin with the chains running along the $[110]$ -direction contributes around $\mathbf{Q}_{\text{mag}} = (0.75\ 0.25\ 0)$, both scans measure essentially the magnetic correlations perpendicular (scan 1) and parallel (scan 2) to the zig-zag chains.

We start with the discussion of the thermal evolution of the magnetic correlations along the $[1\bar{1}0]$ -direction, i. e. perpendicular to the zig-zag chains (scan 1), shown in Fig. 4.10. At the highest temperature investigated, $T=250\text{ K}$, the magnetic intensity is dominated by a broad feature centered around $\mathbf{Q}_{\text{FM}} = (100)$, as has already been evidenced by the intensity mapping at this temperature. The line shape of this feature can be described by a Lorentzian, and taking the experimental resolution into account, the determined width σ of the peak corresponds to a correlation length $\xi_{\text{iso}} = 8\text{ \AA}$ for a pair of ferromagnetically aligned spins. Upon decreasing temperature, the intensity and shape of the feature stays roughly unaffected until charge and orbital ordering sets in at $T_{\text{CO}} \approx 220\text{ K}$. With the onset of the COO order, the FM signal at \mathbf{Q}_{FM} begins to die out and additional magnetic scattering emerges along the $[1\bar{1}0]$ -direction: Immediately below T_{CO} weak satellite reflections become apparent around $(1 \pm \varepsilon \mp \varepsilon\ 0)$, which upon further cooling rapidly gain intensity and move outward towards the commensurable CE positions $(1 \pm 0.25 \mp 0.25\ 0)$. Close to $T_N \approx 110\text{ K}$ the FM signal at \mathbf{Q}_{FM} is finally suppressed completely, and the AFM signal has evolved into two sharp, still slightly asymmetric reflections centered around the two quarter-indexed positions. Within the

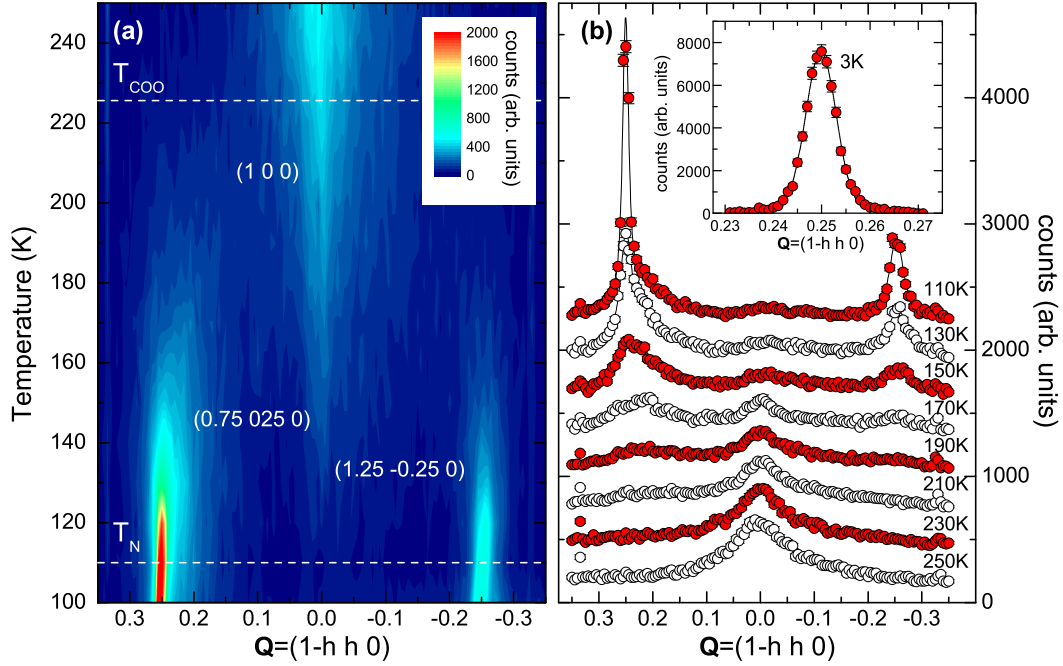


Figure 4.10: Thermal evolution of the magnetic correlations \perp chains Temperature dependence of the magnetic intensity along the scan depicted by line 1 in Fig. 4.9c. Data were collected between $T=100$ K and 250 K at temperature steps of 10 K at the diffractometer 3T.1 (a). Raw-data scans underlying the contour plot in (a) at temperature steps of 20 K. For clarity, the data are successively shifted vertically by 300 counts. The inset gives the profile of the magnetic Bragg reflection at low temperatures, $T=2.5$ K. Lines correspond to fits as described in the text (b). In all data a minor contamination by second-harmonic neutrons centered at $\mathbf{Q}_{\text{FM}} = (100)$ is subtracted.

AFM-ordered phase below T_N , the peak shape of the AFM satellites is no longer Lorentzian, but Gaussian and fully determined by the experimental resolution, pointing towards a long-range magnetic ordering, see the inset of Fig. 4.10b.

Scan 2, running along the perpendicular direction, is especially sensitive to the existence of CE-type correlations along the zig-zag chains. As can be seen in Fig. 4.11, no magnetic signal is observable well above the COO transition at $T = 250$ K. However, with the charge/orbital ordering a magnetic signal appears at $\mathbf{Q}_{\text{mag}} = (0.75\ 0.25\ 0)$, which is clearly distinguishable from the background already at $T = 220$ K, i. e. more than 100 K above the Néel transition. Note, that there is no structural contribution to the scattering intensity at this \mathbf{Q} -position, as is evidenced by the polarization analysis of the scattered intensity, see table 4.2. Upon cooling the Lorentzian-shaped signal rapidly sharpens and increases in intensity, reflecting the transfer of spectral weight along the one-dimensional streak as discussed above. The transition into the magnetically ordered phase at $T_N = 110$ K is evidenced by the change in the line shape of the observed

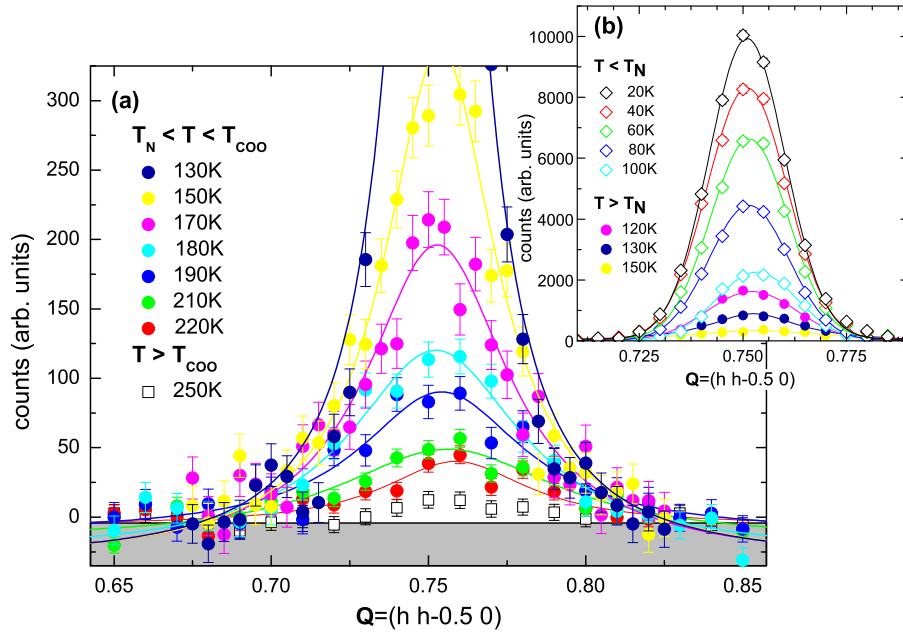


Figure 4.11: Thermal evolution of the magnetic correlations || chains Temperature dependence of the magnetic intensity along the scan depicted by line 2 in Fig. 4.9c, showing raw-data scans at selected temperatures above, (a), and below the Néel transition at $T_N = 110$ K, (b). Note that for the scans at 150 K and 130 K the scale on the ordinate is the same in (a) and (b). In all data a common background is subtracted. Lines correspond to fits with either Lorentzians or Gaussians as discussed in the text.

signal, below T_N the observed signal changes into a Gaussian profile with the width determined by the experimental resolution. The intensity of the reflection continuous to increase monotonically in the entire temperature range down to the lowest temperature investigated, $T = 3$ K.

For a quantitative analysis of the development of the diffuse magnetic scattering we modeled the observed spectra using always Lorentzian line shapes for the various diffuse contributions. The observed intensity then directly probes the square of the magnetic order parameter, whereas the width of the reflection, corrected for resolution effects, determines the inverse of the correlation length ξ in the direction of the scan [154]. The results of this analysis are summarized in Fig. 4.12.

Quite obviously, the frame for the discussion of the diffuse magnetic scattering is set by the charge and orbital order. Hence, Fig. 4.12a displays the thermal evolution of the two structural superlattice reflections $\mathbf{Q}_{OO} = (2.25\ 0.25\ 0)$ and $\mathbf{Q}_{CO} = (1.5\ 1.5\ 0)$, probing the orbital and the charge ordering, respectively. The obtained ordering temperature is consistent with $T_{CO} = 229$ K as determined from the analysis of the specific heat of the same sample [64], and is furthermore in good agreement with the recent literature [7, 120].

Before we resume with the analysis of the magnetic correlations, we interrupt

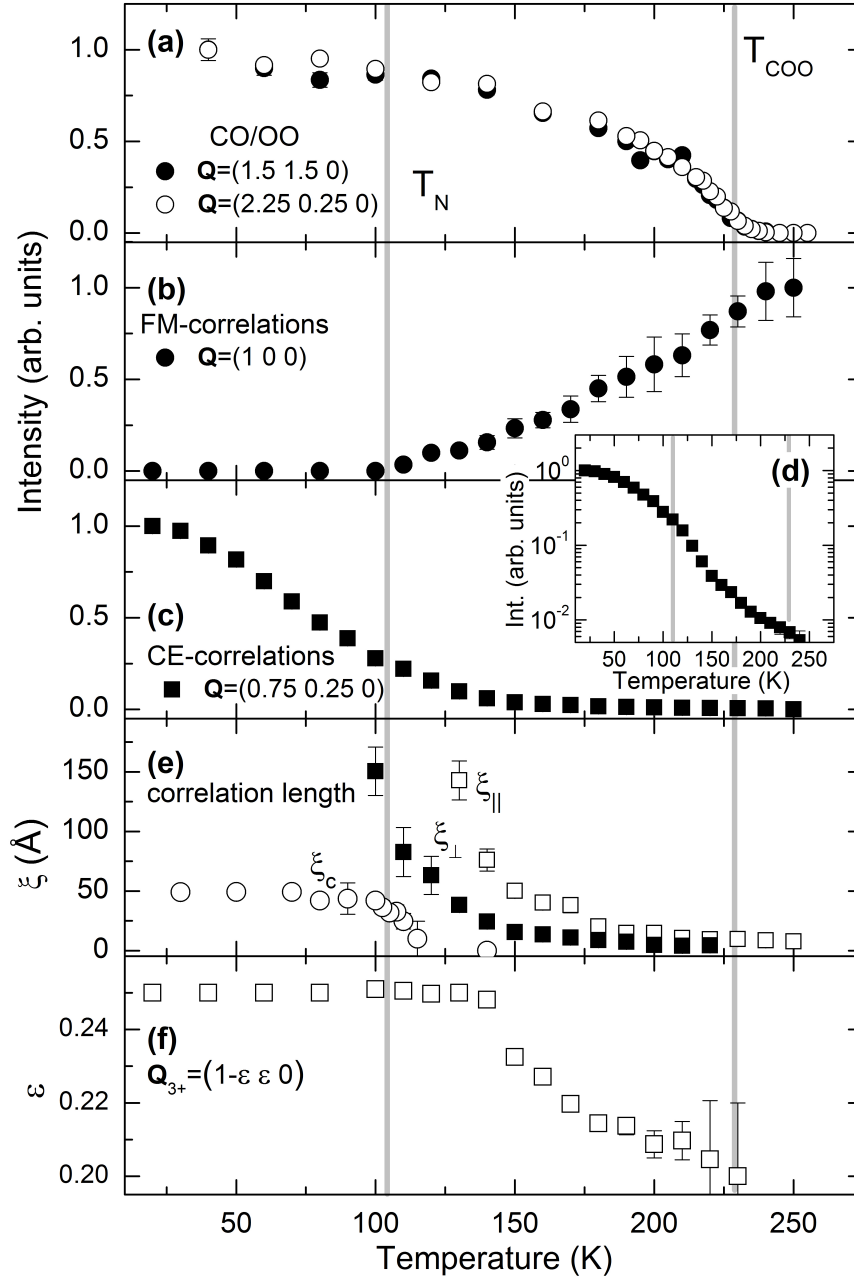


Figure 4.12: Development of the magnetic correlations in $\text{La}_{1/2}\text{Sr}_{3/2}\text{MnO}_4$ Summary of the results of the analysis of the diffuse magnetic scattering showing the temperature dependence of the intensity of the structural superstructure reflections $\mathbf{Q}_{\text{OO}} = (2.25\ 0.25\ 0)$ and $\mathbf{Q}_{\text{CO}} = (1.5\ 1.5\ 0)$, probing the orbital and the charge ordering, respectively, (a), of the intensity observed at the FM position $\mathbf{Q}_{\text{FM}} = (1\ 0\ 0)$, (b), and at the AFM position $\mathbf{Q}_{\text{mag}} = (0.75\ 0.25\ 0)$ on a linear, (c), and logarithmic scale, (d), of the determined correlation length ξ in a direction parallel to the chains, ξ_{\parallel} , perpendicular to the chains within the ab -plane, ξ_{\perp} , and along the tetragonal axis, ξ_c , (e), and of the position of the AFM signal along the line $\mathbf{Q} = (1 \pm \epsilon \mp \epsilon\ 0)$, (f).

the discussion at this point and comment briefly on the thermal evolution of the structural superstructure. As aforementioned, the direct observation of orbital ordering in this system using resonant x-ray scattering techniques was one of the first major achievements obtained with this advanced technique [116, 119–123]. In one of the pioneering works in this fields, Wilkins et al. report on an unusual correlation between the orbital and the magnetic order parameter. At T_N the intensity of the orbital superlattice reflection is drastically increased with the transition into the AFM-ordered phase, which was interpreted as an enhancement of the associated Jahn-Teller distortion at T_N [119, 123]. Later, it has been demonstrated that at the Mn $L_{2,3}$ -edge also magnetic correlations contribute to the x-ray scattering intensities, and the enhancement of the observed intensity below T_N has been ascribed to a magnetic origin [122]. In light of this discussion we mention, that our neutron studies do not find any evidence for an unusual enhancement of the intensity of the orbital-ordering related superstructure reflections around T_N . The temperature dependence of the orbital reflection $\mathbf{Q}_{OO} = (2.25\ 0.25\ 0)$ is similar to that of the charge ordering reflection $\mathbf{Q}_{CO} = (1.5\ 1.5\ 0)$, showing a rapid increase below T_{CO} and then nearly saturating below ≈ 150 K. More details about the neutron scattering results on the charge and orbital superstructure in $\text{La}_{1/2}\text{Sr}_{3/2}\text{MnO}_4$ can be found in [127].

Now we return to the discussion of the magnetic correlations. The temperature dependence of the intensity of the FM reflection $\mathbf{Q}_{FM} = (1\ 0\ 0)$ and of the CE-type reflection $\mathbf{Q}_{mag} = (0.75\ 0.25\ 0)$ as determined from the scans presented in Fig. 4.10 and Fig. 4.11 is shown in Fig. 4.12b–d. With the transition into the COO phase the FM correlations start to decrease linearly and vanish completely at T_N , below T_N no FM correlations can be detected in our neutron scattering data anymore. In contrast, the AFM correlations of the CE type observed at the quarter-indexed position $\mathbf{Q}_{mag} = (0.75\ 0.25\ 0)$ emerge with the transition into the COO-ordered phase. The peak intensity does not exhibit a clear anomaly around T_N , although the major increase is found below the Néel transition at T_N , and the progression of the AFM correlations appears continuous from T_{CO} down to lowest temperatures. The interpretation as a magnetic transition at $T_N \approx 110$ K is, nevertheless, justified by the divergence of the correlation length within the **ab**-plane, see Fig. 4.12e. Both in-plane correlation lengths, ξ_{\parallel} parallel and ξ_{\perp} perpendicular to the zig-zag chains, rapidly increase as the temperature decreases towards T_N . However, at all temperatures above T_N ξ_{\parallel} is always larger than ξ_{\perp} , demonstrating that the intrachain correlations are better defined than the interchain correlations. Close to T_N , the difference between ξ_{\parallel} and ξ_{\perp} is most pronounced, and ξ_{\parallel} diverges at slightly higher temperatures as ξ_{\perp} . Also included in Fig. 4.12e is the temperature dependence of the correlation length ξ_c along the tetragonal **c**-axis. In contrast to both in-plane correlations, the out-of plane correlations remain always finite below T_N exceeding $\xi_c \approx 50$ Å at $T = 10$ K, and disappear rapidly above T_N , see the discussion below.

Finally, Fig. 4.12f displays the evolution of the AFM peak position along the line $\mathbf{Q} = (1 \pm \varepsilon \mp \varepsilon 0)$, i. e. in a direction perpendicular to the chains. In this direction the value of the incommensurability ε directly reflects the modulation length between adjacent zig-zag chains. With the onset of the magnetic correlations at T_{CO} ε increases monotonically and locks into the commensurable value $\varepsilon = 0.25$ close to T_N . Hence, the modulation wavelength perpendicular to the chains *decreases* upon cooling until at T_N adjacent chains couple antiferromagnetically. Note, that in the perpendicular direction, i. e. parallel to the zig-zag chains, the signal is always centered at the commensurable position \mathbf{Q}_{mag} , see Fig. 4.11, meaning that the periodicity along the chains is constant and that single zig-zag fragments are stable elements.

As already depicted in Fig. 4.12e, we have also investigated the evolution of the magnetic correlations along the tetragonal \mathbf{c} -axis perpendicular to the MnO_2 -sheets. Fig. 4.13 presents raw-data scans along the path $\mathbf{Q} = (0.25 0.25 q_l)$ for various temperatures below T_{CO} . The position for $q_l = 0$, $\mathbf{Q} = (0.25 0.25 0)$, is equivalent to the quarter-indexed reflection $\mathbf{Q}_{mag} = (0.75 0.25 0)$, and the magnetic correlations around this position within the \mathbf{ab} -plane have already been discussed in detail. In contrast to the in-plane scans the scans along the $[001]$ -direction are structureless above T_N , and the magnetic scattering appears as a diffuse rod of intensity along q_l .⁹ Hence, for $T > T_N$ the magnetic correlations are restricted to single MnO_2 -layers and are entirely two dimensional. With the phase transition at T_N a well-defined structure develops along the rod, and two types of magnetic reflections centered around half- and integer-indexed q_l -values become visible. Both types of reflections can be associated with a different stacking of successive MnO_2 -planes along the \mathbf{c} -axis, and the observed distribution of intensity with the half-indexed q_l -reflections dominating agrees well with a former neutron study by Sternlieb et al. [54].¹⁰ The shape of both types of reflections can always be described assuming a Lorentzian line-shape, pointing to a finite correlation length along \mathbf{c} at all temperatures. Indeed, the correlation length ξ_c derived from the width of the reflection $\mathbf{Q} = (0.25 0.25 2.5)$ increases rapidly in a small temperature interval around T_N up to $\xi_c \approx 50 \text{ \AA}$, see Fig. 4.12e. Below T_N , however, the correlation length ξ_c does not show significant changes and stays constant down to lowest temperatures, in agreement with former studies [7].

Briefly summarizing the above results, finite FM zig-zag fragments begin to

⁹Note, that at all temperatures the intensity along the rod is indeed magnetic and significantly above the experimental background, as is evidenced by the scans crossing the rod within the plane, see e. g. Fig. 4.11.

¹⁰Note at this point, that the magnetic correlations along \mathbf{c} seem to depend sensitively on the exact stoichiometry. Similar data reported in Refs. [7, 43, 54] expose a significant contribution of two-dimensional scattering along $(0.25 0.25 q_l)$. In reverse, the well-defined signal along $[001]$ with no diffuse background observable emphasizes the high quality of our sample.

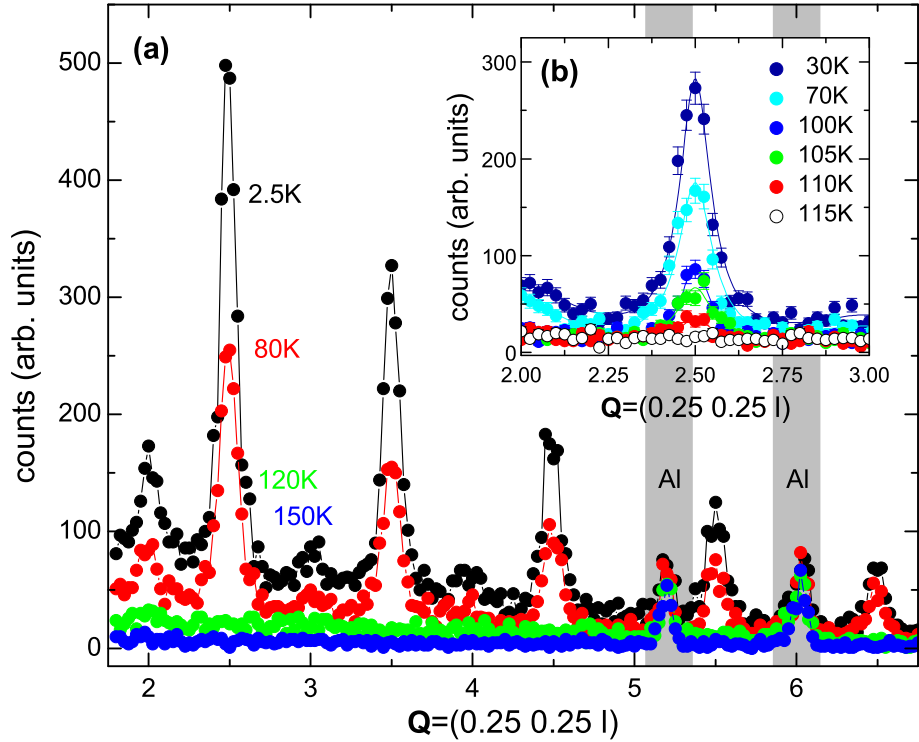


Figure 4.13: Magnetic correlations along the c -axis Raw-data scans along the line $(0.25\ 0.25\ q_l)$ determining the magnetic correlations along the tetragonal c -axis at various temperatures below T_{CO} , measured at the spectrometer G4.3. The gray-shaded areas mark spurious contributions by the scattering from Aluminium (a). Raw-data scans along $[001]$ centered around $q_l = 2.5$ for various temperatures close to T_N . Lines denote fits with Lorentzians as described in the text (b).

form as soon as the orbital ordering sets in at T_{CO} . Upon further cooling these elements rise continuously and the interchain correlations develop. Within this picture, the phase transition at T_N appears as a coherent long-range ordering of already preformed fragments, as is evidenced by the non-critical temperature dependence of the intensity of the magnetic CE-type superstructure reflections and the simultaneous divergence of the in-plane correlations lengths. This interpretation is fully supported by the measurements of the macroscopic magnetization and the specific heat.

Fig. 4.14 shows the temperature dependence of the in-plane electric resistivity ρ_{ab} [155], of the specific heat c_p [64], and of the macroscopic magnetization for a field applied parallel and perpendicular to the c -axis [64]. All three quantities exhibit a distinct anomaly at T_{CO} , but none around T_N . The electric resistivity ρ_{ab} displays a semiconducting behavior in the entire temperature region, only at $T_{CO} = 229\text{ K}$ ρ_{ab} shows a jump-like behavior with a considerable increase of the resistivity across the phase transition, see Fig. 4.14a. Clearly, this behavior re-

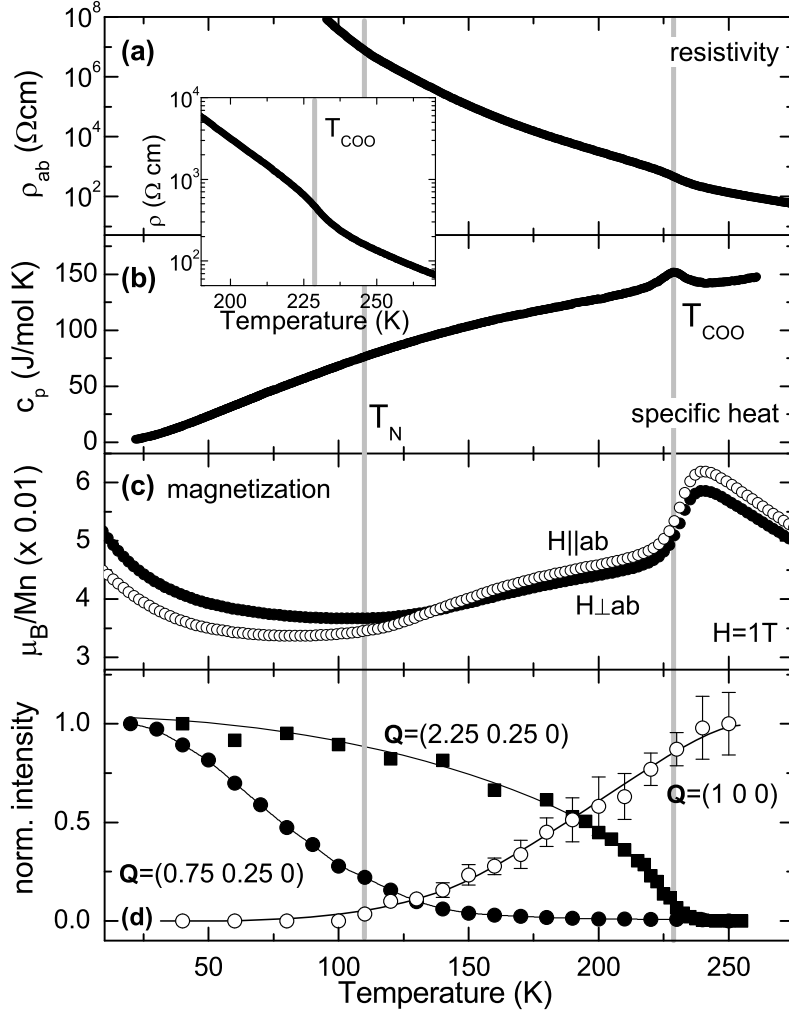


Figure 4.14: Temperature dependence of some macroscopic quantities Temperature dependence of the in-plane electric resistivity ρ_{ab} (a), the specific heat c_p (b), and the macroscopic magnetization for a field $H = 1$ T applied parallel and perpendicular to the ab -planes (c). Also included is the temperature dependence of the observed intensities of the FM reflection $Q_{\text{FM}} = (1 \ 0 \ 0)$, the OO reflection $Q_{\text{OO}} = (2.25 \ 0.75 \ 0)$ and the magnetic CE reflection $Q_{\text{mag}} = (0.75 \ 0.25 \ 0)$ (d). Data in (d) are the same as presented in Fig. 4.12, lines are included as guides to the eye, data in (a)-(c) are taken from Refs. [43, 64, 155].

flects the real-space ordering of the charge carriers at T_{CO} [42]. Also the specific heat, Fig. 4.14b, exhibits a pronounced, lambda-like anomaly at T_{CO} , suggesting a second-order character for the charge/orbital ordering transition, which is consistent with the continuous increase of the intensity of the characteristic superstructure reflections in Fig. 4.12. Below T_{CO} the specific heat seems to be determined by phononic contributions, and around T_N c_p gives no clear indica-

tion for an additional release of magnetic entropy, consistent with the formation of short-range magnetic correlations well above T_N . For further details on the specific heat of $\text{La}_{1/2}\text{Sr}_{3/2}\text{MnO}_4$ we refer to Ref. [64].

Contrary to the resistivity and to the specific heat, the magnetization M appears astonishingly structured and of special interest [9, 41, 42]. At highest temperatures $T_{\text{CO}} < T$, $M(T)$ increases linearly and the magnetization M_{\perp} with the field \mathbf{H} applied vertical to the MnO_2 -planes is always lower than M_{\parallel} with $\mathbf{H} \parallel \mathbf{ab}$, as the easy axis lies within the planes, see Fig. 4.14c. The magnetization reaches a maximum slightly above T_{CO} at $T \approx 240$ K and is strongly suppressed with the transition into the charge- and orbital-ordered phase, as might be expected for a *magnetic* phase transition at T_{CO} . Upon further cooling, the suppression of the magnetization continues linearly down to ≈ 90 K and scales roughly with the decrease of the observed intensity of the FM reflection Q_{FM} and with the onset of short-range antiferromagnetic correlations, see Fig. 4.14d. Quite remarkably, no anomalous behavior can be observed at the Néel transition, and the macroscopic magnetization continuously crosses T_N both for $\mathbf{H} \perp \mathbf{ab}$ and $\mathbf{H} \parallel \mathbf{ab}$, in strong contrast to the expected behavior for a classical antiferromagnet. Only the sequence of M_{\perp} and M_{\parallel} seems to resemble the conventional behavior, as below $T \approx 135$ K M_{\perp} is always larger than M_{\parallel} . Also notable is the low temperature behavior of the magnetization, as below $T \approx 50$ K both M_{\perp} and M_{\parallel} exhibit a significant Curie-like upturn. Usually, a low temperature upturn in the magnetization is associated with magnetic impurities, but in the case of $\text{La}_{1/2}\text{Sr}_{3/2}\text{MnO}_4$ it seems to appear as a generic feature and is observed in various studies using different sample crystals [42, 43]. However, for the moment we will neglect the low- T upturn, leave its detailed discussion to one of the following sections and focus on the high-temperature behavior of $M(T)$.

The most pronounced feature of the magnetization is the sudden drop of $M(T)$ at the charge/orbital ordering transition, which is not only observed in single-layered $\text{La}_{1/2}\text{Sr}_{3/2}\text{MnO}_4$, but also in charge-ordered perovskite manganites, as e. g. $\text{Nd}_{1/2}\text{Ca}_{1/2}\text{MnO}_3$ and $\text{Pr}_{0.5}(\text{Ca}, \text{Sr})_{0.5}\text{MnO}_3$ [100, 156, 157]. As is pointed out by Moritomo et al., the singular behavior at T_{CO} is attributed to the quenching of the double exchange interaction with the localization of the e_g -electrons in the charge-ordered state [42], which is further supported by ESR-measurements, associating the drop in $M(T)$ with the spin-susceptibility χ_s [158].

The unusual behavior of the macroscopic magnetization is fully consistent with the neutron results and the diffuse magnetic scattering discussed above. Fig. 4.15 pictures real-space sketches of the thermal evolution of the static magnetic correlations at various temperatures above T_N , as derived from the diffuse scattering presented above.¹¹ In the paramagnetic and disordered regime above T_{CO}

¹¹With the chosen experimental set-up “static” refers to magnetic correlations on a time-scale longer than 10^{-11} sec.

small FM clusters are formed, mediated by the double exchange mechanism, see Fig. 4.15a. As derived from the diffraction signal, the clusters are isotropic and their size is of the order of 2-3 lattice spacings ($\approx 8 \text{ \AA}$) for $T = 250 \text{ K}$. Consistent with the neutron data, well above T_{CO} the macroscopic magnetization exhibits a Curie-like behavior, and already an early work by Bouloux et al. finds a Curie-constant $\theta_C = 320 \text{ K}$ for the temperature regime between T_{CO} and 1100 K [159], which is roughly comparable with the results obtained on our and other crystals [43].

The transition into the charge- and orbital-ordered phase at T_{CO} suppresses the ferromagnetic correlations. The diffraction signal clearly demonstrates the on-set of short-range AFM correlations with the emergence of the COO phase, and the pronounced drop of the macroscopic magnetization $M(T)$ close to T_{CO} has to be associated with the competition between FM and AFM correlations. Just below T_{CO} , first zig-zag elements including 2–3 Mn^{3+} -sites begin to form, see Fig. 4.15b. The correlation length ξ_{\parallel} parallel to the chains is, however, significantly larger than ξ_{\perp} along the perpendicular direction, and single fragments are only loosely coupled to adjacent elements reflecting the different strength of the ferromagnetic and antiferromagnetic exchange J_{FM} and J_{AFM} , respectively: The diffraction signal perpendicular to the chains – associated with the interchain coupling – is not very well defined, but smeared out into a streak of magnetic intensity. The rod along the line $\mathbf{Q} = (1 \pm \varepsilon \mp \varepsilon 0)$ extends, however, only up to $\varepsilon \leq 0.25$, which nicely proves the stability of the single zig-zag fragments as any smaller modulation, i. e. $\varepsilon > 0.25$, is incompatible with the stacking of such elements: The shortest possible real-space modulation for adjacent zig-zag elements is $2\sqrt{2}a$, any shorter modulation, implying $\varepsilon > 0.25$, would break the zig-zag ordering, but is not observed.

Upon further cooling, the zig-zag fragments grow with a characteristic length ξ_{\parallel} parallel and ξ_{\perp} perpendicular to the chains, and more and more FM clusters are subsequently adapted into the CE-type pattern, see Fig. 4.15c. The competition of isotropic FM clusters and zig-zag fragments is directly reflected in the transfer of scattered intensity from the FM position $\mathbf{Q}_{FM} = (1 0 0)$ to the CE-type position $\mathbf{Q}_{mag} = (0.75 0.25 0)$ and the simultaneous linear decrease of the macroscopic magnetization between 200 K and T_N . As more fragments are formed, also the AFM correlations between the chains get subsequently established, and the AFM signal evolves along the line $\mathbf{Q} = (1 \pm \varepsilon \mp \varepsilon 0)$ until it locks into a well-defined signal centered at the commensurate CE-type position $\mathbf{Q}_{mag} = (0.75 0.25 0)$ with $\varepsilon = 0.25$. Finally, below T_N all preformed elements condense into the long-range CE ordering with a finite correlation length vertical to the MnO_2 -layers, thereby fully suppressing the FM correlations, see Fig. 4.15d. However, as already above T_N a major fraction of the spins has formed finite CE-like clusters – or is at least ordered into isolated zig-zag chains – the magnetic transition at the Néel temperature does not yield a sizable contribution to the specific heat, obviously

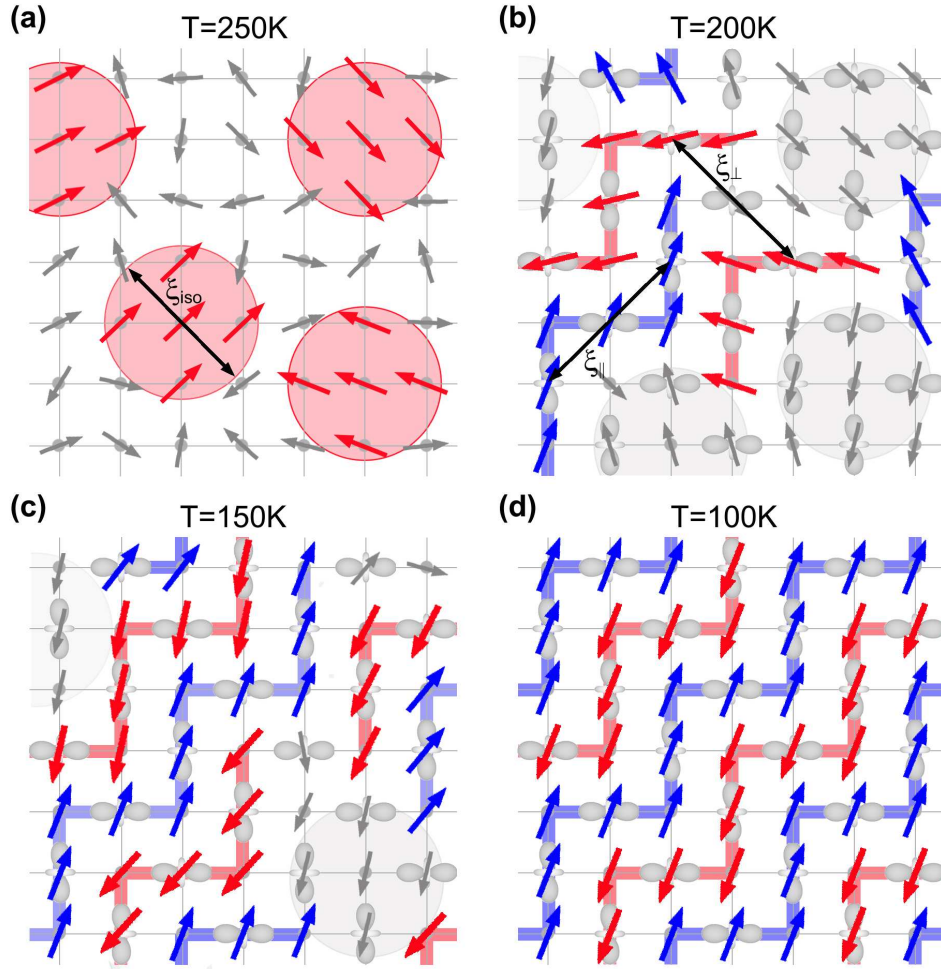


Figure 4.15: Real-space evolution of the magnetic correlations Sketches of the magnetic correlations in the MnO_2 -layers at various temperatures above T_{CO} (a), in the paramagnetic, but orbitally ordered state $T_{\text{CO}} > T > T_{\text{N}}$, (b) and (c), and in the long-range ordered phase below T_{N} , as derived from the results of the diffuse magnetic scattering presented above. Qualitatively, the four sketches are correlated to the intensity mappings presented in Fig. 4.9, as is indicated by the temperatures associated with each sketch.

there is no significant change of entropy at T_{N} , or, even more astonishing, to the magnetic susceptibility. The magnetic transition at T_{N} has to be regarded as the coherent three-dimensional ordering of (rather large) two-dimensional CE-like clusters, which are stabilized by the predominant FM exchange J_{FM} along the chains.

The observed sequence of magnetic phases – isotropic short-range correlations in the disordered regime above T_{CO} , coexistence of FM and anisotropic AFM correlations in the charge/orbital ordered regime for $T_{\text{N}} < T < T_{\text{CO}}$ and CE-type

correlations below T_N – agrees qualitatively very well with recent theoretical investigation on the charge-ordered structure of half-doped manganites. Solovyev has shown that the COO structure at half doping can be stabilized entirely by anisotropic magnetic interactions with a dominant FM coupling along the chains. In this concept the Néel transition corresponds to an order-disorder transition, which takes place between ferromagnetic zig-zag chains: “*Namely, only the long-range AFM order in the x direction disappears at T_N , whereas the FM coupling in the chains survives this transition. Thus, in the interval $T_N < T < T_{CO}$ we deal with a highly anisotropic one-dimensional spin disorder in the direction perpendicular to the chains (x)*” [160], which is in almost perfect agreement with the results of the diffuse magnetic scattering and the dominating ferromagnetic interaction. However, as the observed ferromagnetic correlations above T_N are rather weak, we think that a purely magnetic approach might be insufficient to explain the very stable charge- and orbital-ordered state in $\text{La}_{1/2}\text{Sr}_{3/2}\text{MnO}_4$. Indeed, the pure magnetic Hamiltonian proposed by Solovyev has recently been extended to include electron-phonon coupling as well as electronic Coulomb interactions, yielding similar results for a reasonable choice of parameters [57, 161].

4.2.3 Thermal evolution of the magnetic fluctuations

In the previous section we have discussed the thermal evolution of the CE-type ordering based on the results of *elastic* neutron experiments, or, to be more precise, studied the temperature dependence of the magnetic correlations on a time scale longer than 10^{-11} sec. In this paragraph we extend our analysis to include the faster magnetic fluctuations, which were studied by means of inelastic neutron scattering. The discussion of the “static” correlations has revealed, that above T_N isolated zig-zag chains are formed as a precursor of the CE-type ground state, which compete with isotropic FM correlations. The anisotropy of the magnetic correlations and the co-existence of AFM and isotropic FM correlations at higher temperatures should, however, also be visible in the (low energy) magnetic fluctuations.

The experiments on the temperature dependence of the magnetic excitations were all performed at the thermal spectrometers 1T and 2T at the LLB in Saclay. We used the same experimental setup as for the analysis of the spin-wave dispersion at low temperatures discussed above; incoming neutrons were, however, always selected with the PG monochromator. In addition to the low-temperature spectrum we studied the magnetic excitations at both sides of the magnetic phase transition at 100 K and 130 K, i. e. below and above T_N , in the COO phase at 200 K and in the disordered phase at 250 K.

The thermal evolution of the magnetic fluctuations at $E = 2.75$ meV around the CE-type reflection $\mathbf{Q} = (0.75 - 0.75 0)$ for a direction parallel and perpendicular to the propagation of the FM zig-zag chains is shown in Fig. 4.16. To compare the spectra at the different temperatures, the raw data are always corrected for the

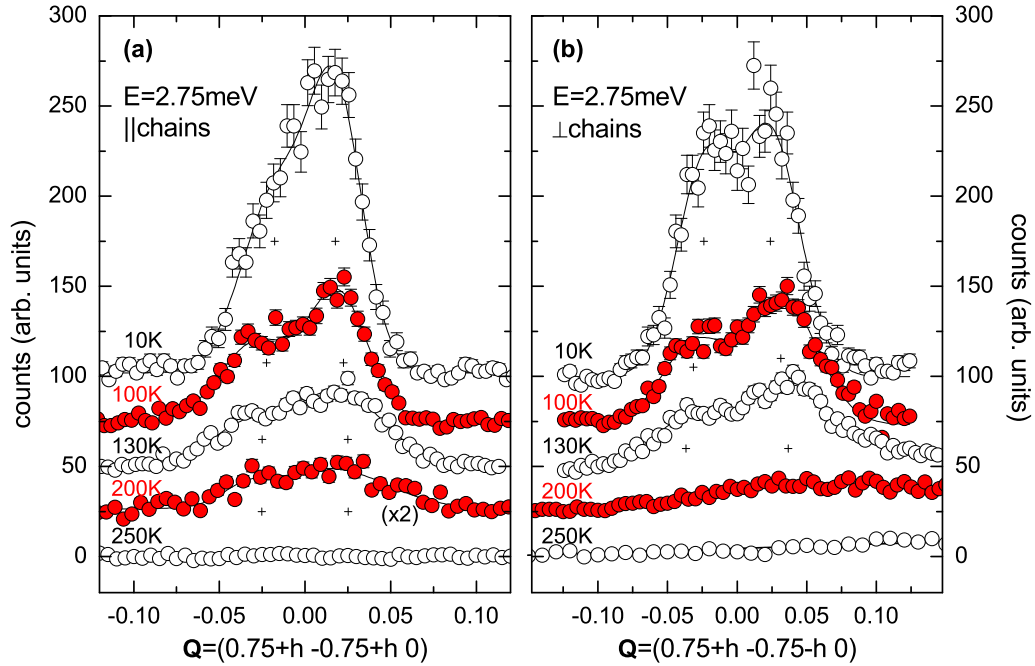


Figure 4.16: Thermal evolution of the magnetic fluctuations around a CE-type position Constant energy scans at $E = 2.75$ meV across the CE-type position $\mathbf{Q} = (0.75 - 0.75 0)$ for various temperatures in a direction parallel, (a), and perpendicular to the FM zig-zag chains, (b). All spectra are corrected for the Bose factor after the subtraction of a linear background. For clarity, subsequent spectra are shifted by a constant amount on the ordinate. Lines denote fits to the spectra as discussed in the text, small black crosses mark the centers of the fitted Gaussians.

different Bose factors after the subtraction of a linear background. With increasing temperature the magnon signal is suppressed, and the decrease in inelastic intensity is roughly comparable with the temperature dependence of the magnetic order parameter, see Fig. 4.12c. However, in spite of the isotropic evolution of the observed intensity, significant differences can be found in the shape of the magnon signal along the two distinct directions.

Let us start with the discussion of the temperature dependence of the inelastic signal in the direction parallel to the propagation of the zig-zag chains, Fig. 4.16a. At the lowest temperature investigated, $T = 10$ K, the spectrum can be decomposed into two magnon contributions centered at \mathbf{q} and $-\mathbf{q}$. However, as in this direction the dispersion is steep, the scan at $E = 2.75$ meV can not fully resolve the different contributions. With increasing temperature, the magnon signal slightly moves outward in \mathbf{Q} -space, and both contributions appear well resolvable in the spectrum recorded at 100 K. Hence, with increasing temperature the magnon frequency is slightly renormalized, which is confirmed by further scans at 4 meV (not shown) exhibiting a similar behavior. Upon further heating across the magnetic

transition at $T_N \approx 110$ K the inelastic response broadens, but does not shift in \mathbf{Q} -space anymore. We do not observe a significant change of the magnon frequencies between 100 K and 200 K, and the spectrum at 200 K exhibits a structure, which is well describable by two, though broadened, contributions centered at the same positions as at 100 K. Parallel to the zig-zag chains there is no further renormalization in the frequencies of the magnetic fluctuations, indicative of the strong ferromagnetic interaction J_{FM} in this direction.

The magnetic fluctuations along the perpendicular direction exhibit a different behavior, Fig. 4.16b. Again, at lowest temperatures two magnon contributions are clearly visible in the constant energy scan. However, as the dispersion in this direction is significantly reduced, both signals are now better separated. With increasing temperature the signal propagates outward, too, but this trend is enhanced compared to the direction parallel to the chains, and continues across the magnetic transition up to ≈ 130 K. In addition to the more pronounced softening of the magnon frequencies, the magnetic intensity is significantly smeared out at higher temperatures: At 130 K the signal develops a distinct asymmetry with an additional contribution along the streak $\mathbf{Q} = (0.75 - 0.75 0) + (h - h 0)$ and $h > 0$. At 200 K the difference between the spectra parallel and perpendicular to the chains is most obvious. While there is still a well-defined signal along $[110]$, i. e. parallel to the chains, the inelastic intensity has completely lost its structure in the $[1\bar{1}0]$ -direction and appears as a broad streak, comparable with the elastic scattering, directly pointing to the smaller energyscale of the interchain correlations.

Comparing the dynamic with the static correlations at $\omega = 0$, both resemble the anisotropic character of the CE-type correlations with the predominant character of the intrachain coupling J_{FM} . Following the discussion of the static diffuse scattering, we may now ask if there is any evidence for additional, purely ferromagnetic fluctuations at higher temperatures. In Fig. 4.17a we show constant energy scans around the FM position $\mathbf{Q}_{\text{FM}} = (100)$, taken at the same energy, $E = 2.75$ meV, and at the same temperatures as before. Notice, that $\mathbf{Q}_{\text{FM}} = (100)$ is also a valid Bragg position for the AFM CE-type ordering, however with a significantly reduced structure factor, see Fig. 4.8a. At $T = 10$ K the spectrum around \mathbf{Q}_{FM} appears similar to those recorded around the quarter-indexed reflection and the observed signal has to be ascribed to the already well-known spin-wave dispersion of the CE pattern. The thermal evolution of the fluctuations around \mathbf{Q}_{FM} is, however, in strong contrast to those discussed previously.

Already the spectrum at $T = 100$ K is qualitatively different from those around the quarter-indexed position; the two magnon signal associated with the AFM dispersion still dominates the spectrum, but in addition two weak features appear at the shoulders. With further increase of temperature the different signals merge into a broad feature at $\pm\mathbf{q}$, and the overall structure remains comparable up to highest temperatures. At $T = 250$ K the difference between the two

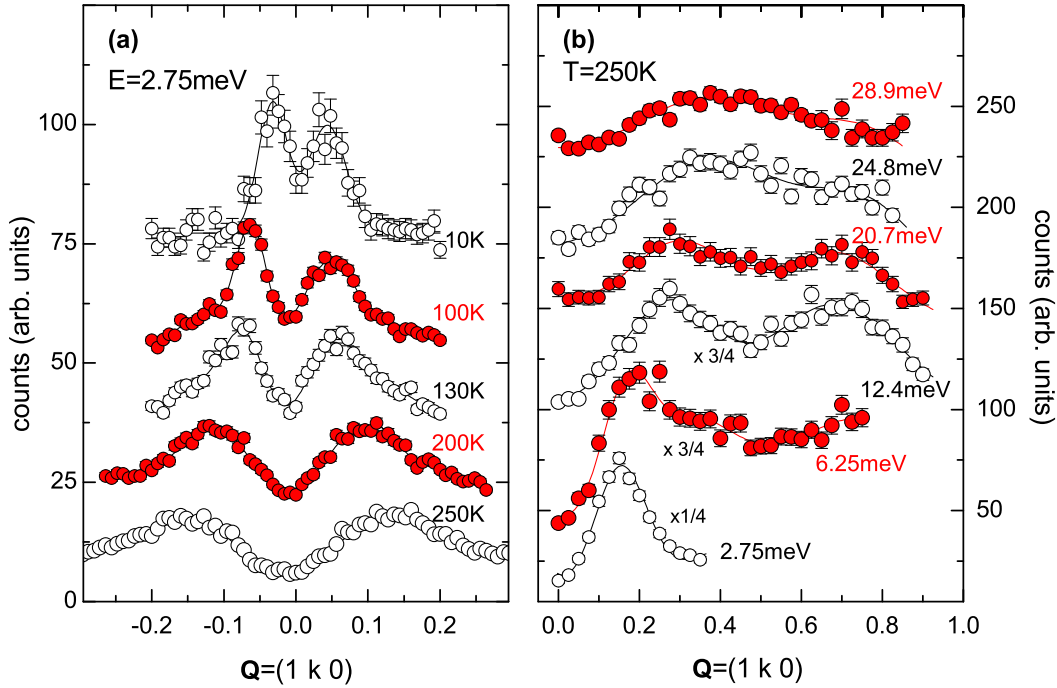
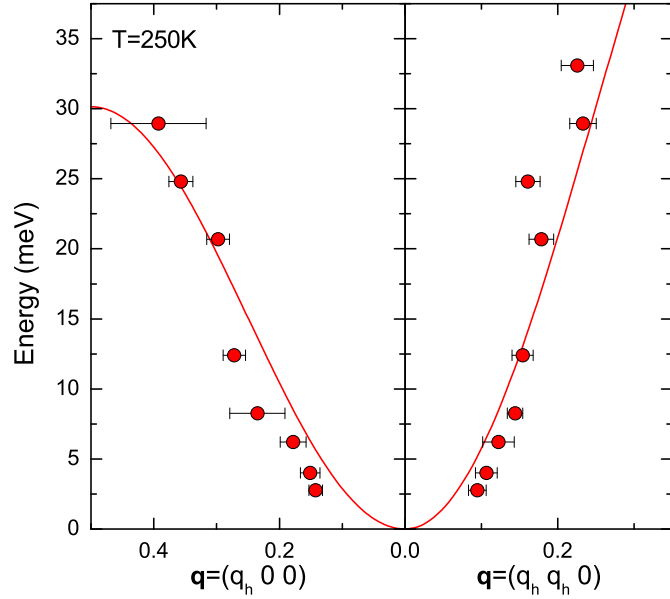


Figure 4.17: Evolution of the FM fluctuations Constant energy scans at $E = 2.75 \text{ meV}$ across the FM position $\mathbf{Q}_{\text{FM}} = (100)$ for various temperatures. The spectra are corrected for the Bose factor after the subtraction of a linear background (a). Raw-data scans aiming at the energy dependence of the ferromagnetic fluctuations for $T > T_{\text{CO}}$ (b). Data presented (a) were measured at the 1T-spectrometer, those in (b) at the 2T. For clarity, subsequent spectra are shifted by a constant amount on the ordinate in both panels. Lines denote fits to the spectra as discussed in the text.

Q -positions is most evident: Around the CE-type position $\mathbf{Q} = (0.75 - 0.75 0)$ no inelastic signal can be detected anymore, whereas the dynamic correlations around the FM position \mathbf{Q}_{FM} are easily separable from the experimental background. These fluctuations are entirely ferromagnetic in character – there is no evidence for short-range CE-type correlations at these temperatures – and the progression of the spin dynamics around \mathbf{Q}_{FM} directly mirrors the competition of the CE ordering with ferromagnetic phases, consistent with the development and the discussion of the static correlations: In conventional low-dimensional magnets the magnetic fluctuations persist well above T_{N} , representing the finite time scale of the magnetic correlations above T_{N} [162–166]. In the comparable two-dimensional $S = 1$ system La_2NiO_4 the antiferromagnetic fluctuations can be observed up to 600 K, corresponding to $2T_{\text{N}}$, in neutron scattering experiments [167], and the rapid suppression of the CE-type fluctuations in $\text{La}_{1/2}\text{Sr}_{3/2}\text{MnO}_4$ indicates the close competition of different magnetic phases.

To further quantify the properties of the FM fluctuations we show in Fig. 4.17b

Figure 4.18: q -dependence of the FM fluctuations at $T=250$ K Dispersion of the FM fluctuations within the MnO_2 -sheets for $T = 250$ K above T_{CO} . Solid lines denote the fit of the data using an isotropic spin-wave dispersion as explained in detail in the text.



representative raw-data scans aiming at the q -dependence of the spin dynamics for $T = 250$ K, i. e. in the disordered regime above T_{CO} characterized by isotropic FM short-range correlations. The \mathbf{Q} -scans illustrate, how the inelastic signal propagates along $[100]$; the response is always rather broad in \mathbf{Q} , and for $E \geq 12.4$ meV two features are observable in the data, which are, however, centered at equivalent q -values in neighboring (ferro-)magnetic Brillouin zones. With increasing energy both signals disperse towards the FM zone boundary at $q_k = 0.5$, which they finally reach close to 30 meV. In addition we have analyzed the q -dependence along the diagonal direction $[110]$, and the results are summarized in Fig. 4.18, presenting the dispersion of the FM fluctuations at $T = 250$ K up to a maximum energy of 35 meV.

The spin-wave relation for an isotropic Heisenberg ferromagnet on a square lattice with an isotropic nearest-neighbor exchange J_{iso} is rapidly calculated [69]:

$$\hbar\omega(\mathbf{q}) = 4J_{\text{iso}}S(2 - \cos(2\pi q_h) - \cos(2\pi q_k)). \quad (4.2)$$

Fitting this dispersion relation to the observation, the data are reasonably well described – the slight overestimation of the frequencies at the low q -limit might be attributed to the influence of the finite size of the FM clusters, $\xi_{\text{iso}} \approx 8 \text{ \AA}$. We do not find any evidence for a magnetic anisotropy at $\mathbf{q} = 0$, and obtain $2SJ_{\text{iso}} = 7.5(5)$ meV for the exchange interaction, which calls for the following final remarks: Describing the q -dependence of the spin fluctuations with only a single exchange parameter J_{iso} is a strong argument for *isotropic* magnetic correlations above T_{CO} – there is no evidence for any spatial anisotropy in the FM correlations, in strong contrast to the short range correlations below T_{CO} and the characteristics

of the CE-type ordering at lowest temperatures. The strength of the ferromagnetic exchange J_{iso} is considerably reduced compared to the FM intrachain coupling in the CE arrangement, $2SJ_{\text{iso}} = 7.5 \text{ meV}$ and $2SJ_{\text{FM}} \approx 18 \text{ meV}$, for $T = 250 \text{ K}$ and 10 K respectively, but still points to a sizable hopping of the e_g -electrons mediated through the double exchange mechanism, even though the system is insulating [168].¹² Furthermore, it is astonishing that J_{iso} is of the same size as the FM nearest-neighbor exchange in the metallic phases of the perovskite manganites, e. g. Ye et al. report $2SJ \approx 7.5 \text{ meV}$ for different $\text{Re}_{1-x}\text{A}_x\text{MnO}_3$ compounds with $x = 0.3$ [148].

4.3 Doping dependence of the COO order in $\text{La}_{1-x}\text{Sr}_{1+x}\text{MnO}_4$

Charge and orbital ordering in the 113-perovskite manganites exhibits a significant difference upon doping with additional electrons or holes, and the phase diagram of many different compounds exhibits a striking asymmetry with respect to half doping, which still is one of the important open issues in the physics of the CMR-effect [169, 170]: Upon hole doping, i. e. $x > 0.5$, charge and orbital ordering is rather stable, but gets incommensurate with stripe phases appearing for small e_g -electron densities [90, 91]. On the other side, the COO ordering reacts very sensitive on additional electrons, and for $x < 0.5$ the ordering is rapidly suppressed and transformed into FM metallic phases.¹³

The influence of electronic doping on the COO state in the single-layered system $\text{La}_{1-x}\text{Sr}_{1+x}\text{MnO}_4$ is, in contrast, only little studied so far, partly because single crystals of high quality are hard to grow for large Sr-contents [44]. The basic properties of the phase diagram in the intermediate to high doping regime have recently been elaborated using x-ray and neutron diffraction, as well as electron microscopy techniques [7, 44, 126]. The COO state persists in the overdoped regime up to high doping levels, $x \approx 0.85$, but gets incommensurate with the modulation wavelength depending linearly on the e_g -electron density n_e . The checkerboard charge ordering of the CE model transforms thereby into a stripe-like ordering, best observable around $x = 2/3$ and $3/4$ [44]. Electron doping, in contrast, again rapidly suppresses the ordered state and the COO-superlattice reflections disappear for $x < 0.4$ in diffraction experiments. A significant broadening of the COO reflections in the region $0.4 < x < 0.5$ was taken as first evidence for a

¹²One might even argue that the ferromagnetic coupling J_{iso} in the isotropic regime is well comparable with the coupling in the CE-ordered phase, as the effective moment in the high-temperature phase is considerably reduced compared to the ordered phase.

¹³Another notable feature in this context is the prediction of a ferroelectric phase for $0.4 < x < 0.5$, which would offer a new route to charge-controlled multiferroics [109], which, however, has not yet been observed experimentally.

phase separation between optimal doped COO patches and disordered regions in this regime of the phase diagram [7].

Hence, around half doping the phase diagram of two-dimensional $\text{La}_{1-x}\text{Sr}_{1+x}\text{MnO}_4$ resembles the basic properties of the three-dimensional perovskite manganites – despite the absence of FM metallic phases for large n_e , most likely due to an enhanced reduction of the one-electron bandwidth W . Furthermore, the results on the La/Sr-series are nicely supported by recent observations in closely related two-dimensional compounds, as e.g. $\text{Nd}_{1-x}\text{Sr}_{1+x}\text{MnO}_4$ [171–174], $\text{Nd}_{1-x}\text{Ca}_{1+x}\text{MnO}_4$ [175, 176], and $\text{Pr}_{1-x}\text{Ca}_{1+x}\text{MnO}_4$ [177–180], proving that the asymmetric response of the COO state with respect to doping of electrons or holes is an intrinsic feature of the ordered state.

Most of the above studies focus, however, on the structural part of the COO state. The documentation of the evolution of the magnetic properties as a function of n_e appears only fragmentary, and a systematic investigation of the doping dependence of the magnetic correlations is still lacking. Only Larochelle et al. report on neutron scattering results sensitive to the magnetic correlations [7]. For $x = 0.45$ the magnetic ordering is long range and similar to the optimal doped compound with $x = 0.5$, whereas for $x \leq 0.4$ a spin-glass regime is realized with short-range CE-like correlations existing close to $x = 0.4$. In the overdoped regime, $x > 0.5$, the magnetic correlations are again only of finite size, $\xi \approx 30 \text{ \AA}$ within the MnO_2 -planes. Even more astonishing, Larochelle et al. claim that the magnetic ordering remains commensurate for $x > 0.5$, although the structural superstructure is incommensurate in this regime. To extend these studies and to characterize the magnetic correlations close to half doping in more detail, we (re-)examine in the following the magnetic properties of the electron-doped compound $\text{La}_{0.6}\text{Sr}_{1.4}\text{MnO}_4$ ($x=0.4$) with a nominal Mn-valence $\text{Mn}^{3.4+}$, and of hole-rich $\text{La}_{0.4}\text{Sr}_{1.6}\text{MnO}_4$ ($x=0.6$) with an average valence $\text{Mn}^{3.6+}$ on the basis of elastic and inelastic neutron scattering experiments. The comparison of the magnetic ordering in all three compounds under investigation, $x = 0.4, 0.5$ and 0.6 , will finally allow us to construct a comprehensive magneto-orbital phase diagram of the $\text{La}_{1-x}\text{Sr}_{1+x}\text{MnO}_4$ -series around half doping.

The measurements presented below aiming at the static and dynamic spin correlations in $\text{La}_{0.6}\text{Sr}_{1.4}\text{MnO}_4$ and $\text{La}_{0.4}\text{Sr}_{1.6}\text{MnO}_4$ were performed with two large single crystals, grown for this purpose by P. Reutler and O. J. Schumann using the floating zone technique [43, 127]. Neutron scattering experiments using these crystals were performed at a number of different cold and thermal TAS-instruments situated at the four major reactor sources in Europe, including the spectrometers 1T, 4F and G4.3 at the LLB in Saclay, the instruments PANDA and PUMA installed at the FRM II in Munich, IN12 at the ILL in Grenoble, and the FLEX spectrometer at the HMI in Berlin. Since we were mainly interested in the in-plane correlations the scattering plane typically included the $[100]$ - and $[010]$ -directions of the tetragonal structure. As usual, in all experiments we fixed

the energy of the scattered neutrons to a certain energy, typically 14.7 meV on the thermal machines and 4.66 meV at the cold instruments, and changed the energy of the incoming neutrons to vary the energy transfer. To avoid contaminations by higher-harmonic neutrons, adequate filters, PG or cooled Beryllium, were always installed in the neutron's pathway behind the sample, and a sufficient reduction of $\frac{\lambda}{2}$ -neutrons turned out to be very crucial in all of these measurements, see the discussion below. The field dependence of the magnetic correlations in $\text{La}_{0.6}\text{Sr}_{1.4}\text{MnO}_4$ was determined using the 15 T-cryomagnet VM2 of the HMI.

4.3.1 CE-type correlations in electron-doped $\text{La}_{0.6}\text{Sr}_{1.4}\text{MnO}_4$

We begin with the electron-rich compound $\text{La}_{0.6}\text{Sr}_{1.4}\text{MnO}_4$, $x=0.4$. As already pointed out in the discussion of the optimal-doped sample $\text{La}_{1/2}\text{Sr}_{3/2}\text{MnO}_4$, the frame for the analysis of the magnetic correlations is set by the charge and orbital order. Hence, we show first in Fig. 4.19 raw-data scans characterizing the COO state in $\text{La}_{0.6}\text{Sr}_{1.4}\text{MnO}_4$. As is clearly seen in Fig. 4.19a, a sizable signal develops at the orbital-order position $\mathbf{Q}_{\text{OO}} = (2.25\ 0.25\ 0)$ below $T_{\text{CO}} \approx 210$ K, which rapidly increases in intensity upon further reduction of temperature.¹⁴ The shape of the signal sharpens with decreasing T , but is always broader than the experimental resolution, and the orbital correlations remain finite down to lowest temperatures. From the width of the observed signal at 3 K we obtain a correlation length $\xi_{\text{OO}} \approx 20(1)$ Å, which is isotropic within the MnO_2 -layers – we do not find a significant difference in the correlations parallel and perpendicular to the direction of the zig-zag chains, in good agreement with the results reported in Ref. [7].

Concomitant with the appearance of the orbital ordering at T_{CO} , we observe the onset of structural scattering centered at the CO-position $\mathbf{Q}_{\text{CO}} = (1.5\ 1.5\ 0)$ (raw data not shown), which clearly has to be ascribed to the checkerboard charge ordering. Upon cooling, the signal at \mathbf{Q}_{CO} exhibits a similar behavior as the orbital reflection \mathbf{Q}_{OO} , but the observed intensity at \mathbf{Q}_{CO} is significantly lower. Similar to the orbital ordering, the correlation length associated with the charge ordering is finite down to lowest temperatures, and for $T = 3$ K we obtain $\xi_{\text{CO}} \approx 13(1)$ Å within the planes, roughly comparable with ξ_{OO} .

To compare these observations with the COO ordering in the half-doped compound, we normalize the intensity of the various superstructure reflections on the fundamental Bragg reflection $\mathbf{Q} = (1\ 1\ 0)$.¹⁵ The results for lowest temperatures

¹⁴We recall that \mathbf{Q}_{OO} is also a valid magnetic Bragg position in the CE scheme. For a large modulus $|Q|$, however, the magnetic form factor determining the magnetic intensity is negligible, and at $\mathbf{Q}_{\text{OO}} = (2.25\ 0.25\ 0)$ practically all scattering is nuclear.

¹⁵The normalization based on a single reflection using triple-axis data is always somewhat questionable, as especially strong Bragg reflections may suffer from large extinction effects, resulting in a misleading interpretation of the observed intensity. However, as more advanced procedures are hard to realize this method is often the only practicable solution.

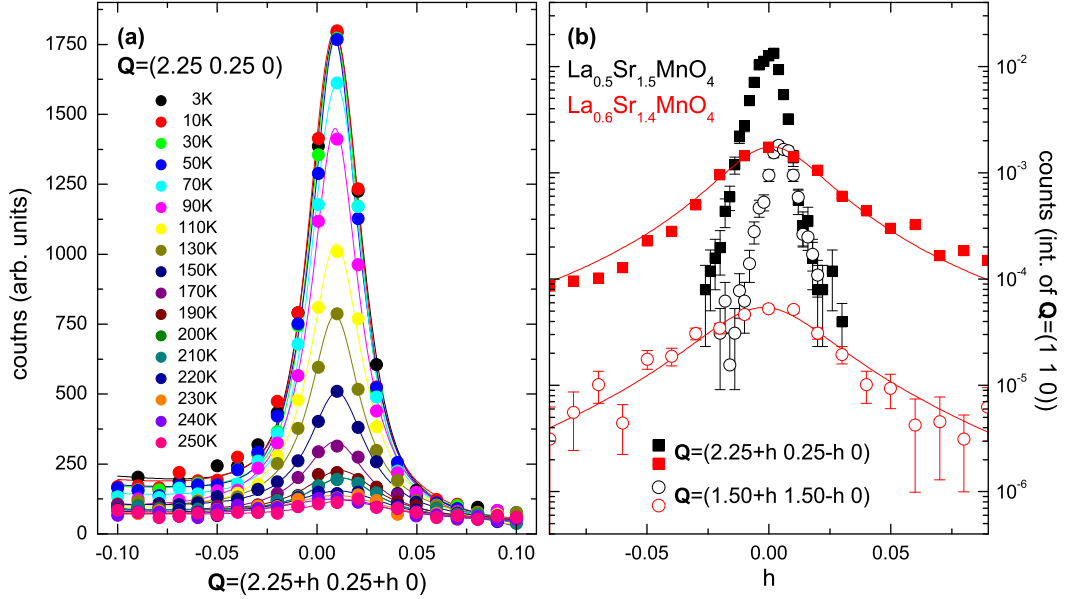


Figure 4.19: COO correlations in $\text{La}_{0.6}\text{Sr}_{1.4}\text{MnO}_4$ Raw-data scans tracking the temperature dependence of the OO-reflection $\mathbf{Q}_{\text{OO}} = (2.25\ 0.25\ 0)$ in the electron-doped compound $\text{La}_{0.6}\text{Sr}_{1.4}\text{MnO}_4$ (a). Comparison of the typical CO- and OO-reflections $\mathbf{Q}_{\text{OO}} = (1.5\ 1.5\ 0)$ and $\mathbf{Q}_{\text{CO}} = (2.25\ 0.25\ 0)$ for the two compounds $\text{La}_{1/2}\text{Sr}_{3/2}\text{MnO}_4$ (black symbols) and $\text{La}_{0.6}\text{Sr}_{1.4}\text{MnO}_4$ (red symbols) at low temperatures (b). The data in (b) are normalized on the intensity of the $\mathbf{Q} = (1\ 1\ 0)$ Bragg reflection. In both panels lines denote fits to the data as described in the text. All data were recorded at the cold instrument IN12, but with the neutron energy fixed to $E_f = 11.9$ meV in order to reach larger parts of reciprocal space.

are shown in Fig. 4.19b. The position of the COO reflections is similar in both samples, but for $\text{La}_{0.6}\text{Sr}_{1.4}\text{MnO}_4$ the width is substantially broadened, signaling the finite correlation length. In addition, the peak intensity for both \mathbf{Q}_{CO} and \mathbf{Q}_{OO} is reduced by at least one order of magnitude, e. g. we find $I_{\mathbf{Q}_{\text{OO}}}/I_{(110)} \approx 0.0015$ for $\text{La}_{0.6}\text{Sr}_{1.4}\text{MnO}_4$, compared to $I_{\mathbf{Q}_{\text{OO}}}/I_{(110)} \approx 0.013$ in $\text{La}_{1/2}\text{Sr}_{3/2}\text{MnO}_4$,¹⁶ and our neutron results are in good agreement with previous observation using x-ray scattering techniques [7, 126]. Following these works, we may thus conclude, that the COO structure in $\text{La}_{0.6}\text{Sr}_{1.4}\text{MnO}_4$ consists of finite-size clusters with dimensions of the order of 20 Å, referred to as *nanopatches* in Ref. [7].

¹⁶The integrated intensity is similar for both compounds, indicating that the ordering in $\text{La}_{0.6}\text{Sr}_{1.4}\text{MnO}_4$ incorporates a macroscopic fraction of the crystal, as is furthermore confirmed by a detailed crystallographic investigation of the charge and orbital order in $\text{La}_{0.6}\text{Sr}_{1.4}\text{MnO}_4$ [127].

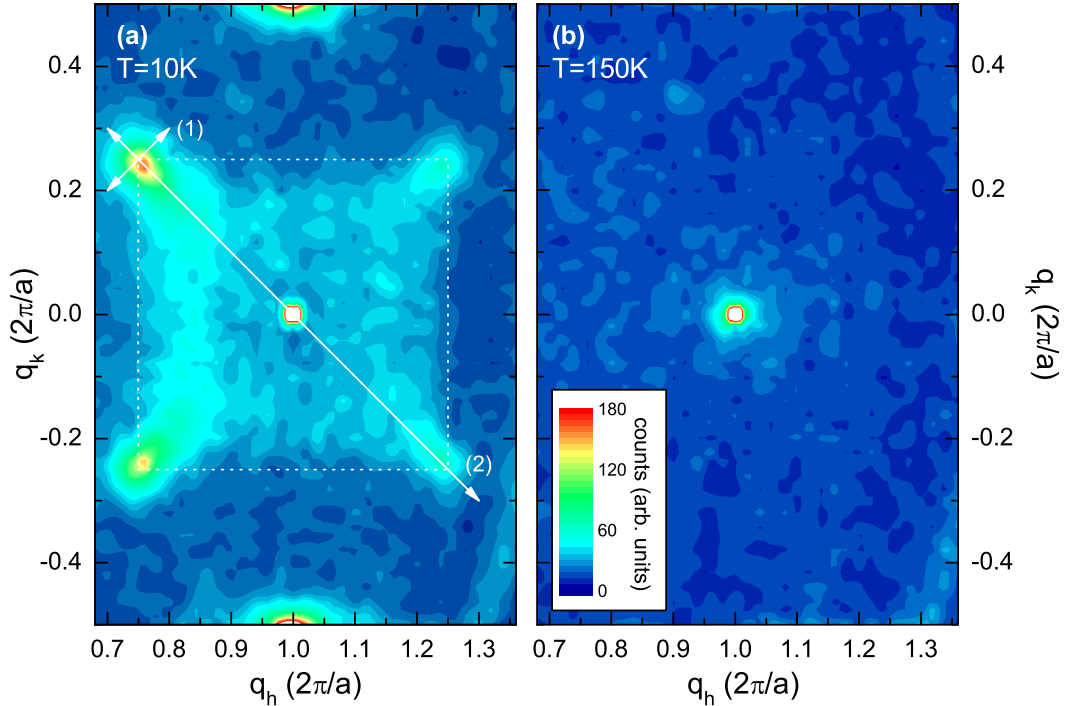


Figure 4.20: Elastic magnetic scattering in $\text{La}_{0.6}\text{Sr}_{1.4}\text{MnO}_4$ Mapping of reciprocal space around $\mathbf{Q}_{\text{FM}} = (100)$ including typical quarter-indexed CE positions for $T=10\text{ K}$ (a), and $T=150\text{ K}$ (b). The two white lines in (a) depict the direction of the two scans investigated below in more detail, the dotted white square marks the borders of the diffuse magnetic intensity, see text for details. Both contour plots were derived from a grid of data with $0.68 \leq q_h \leq 1.36$, $-0.5 \leq q_k \leq 0.5$ and $\Delta q_h = \Delta q_k = 0.02$ recorded at the spectrometer IN12 with $E_f = 4.66\text{ meV}$.

Magnetic order in $\text{La}_{0.6}\text{Sr}_{1.4}\text{MnO}_4$

How does the magnetic ordering react on the diluted orbital order with only a finite correlation length? In Fig. 4.20 we show a mapping of reciprocal space including the typical quarter-indexed positions characteristic of the CE ordering, as e.g. $\mathbf{Q}_{\text{mag}} = (0.75\ 0.25\ 0)$, as well as the FM position $\mathbf{Q}_{\text{FM}} = (100)$ for two different temperatures, $T = 10\text{ K}$ and $T = 150\text{ K}$. Clearly, magnetic scattering is visible around several \mathbf{Q} -positions.¹⁷

At 10 K strong scattering is observed around the characteristic quarter- and half-indexed positions, representing the ordering on the Mn^{3+} - and Mn^{4+} -sites, Fig. 4.20a. However, in contrast to $\text{La}_{1/2}\text{Sr}_{3/2}\text{MnO}_4$ the quarter-indexed reflec-

¹⁷Larochelle et al. were not able to observe magnetic scattering in their neutron scattering experiment on $\text{La}_{0.6}\text{Sr}_{1.4}\text{MnO}_4$ [7], which for us is somehow difficult to understand as the magnetic intensity is not too weak. Most likely, both samples differ slightly in the stoichiometry suppressing the magnetic correlations in the sample used by Larochelle.

tions, take $\mathbf{Q}_{\text{mag}} = (0.75\ 0.25\ 0)$ as an example, are not resolution limited and exhibit furthermore an anisotropic profile: Parallel to the propagation of the chains, i. e. along $[1\ 1\ 0]$ around $\mathbf{Q}_{\text{mag}} = (0.75\ 0.25\ 0)$, the signal appears well defined, but in the perpendicular direction the signal exhibits a distinct asymmetry with a broad tail towards $\mathbf{Q}_{\text{FM}} = (1\ 0\ 0)$. Diffuse magnetic intensity is furthermore observable within the entire square defined by the four quarter-indexed positions $(1 \pm \frac{1}{4} \pm \frac{1}{4}\ 0)$ centered around \mathbf{Q}_{FM} . No such scattering is visible outside this square.

In addition, a sharp and intense signal is visible at the integer-indexed position $\mathbf{Q}_{\text{FM}} = (1\ 0\ 0)$, usually representing two-dimensional FM correlations breaking the body centering of the nuclear unit cell. In a TAS-experiment, however, intensity appearing at \mathbf{Q}_{FM} always has to be treated with care, since nuclear scattering can also contribute at \mathbf{Q}_{FM} via higher-harmonic neutrons or stacking faults in the tetragonal lattice. Hence, we checked very carefully the efficiency of the Beryllium filter excluding a contribution of $\frac{\lambda}{2}$ -neutrons¹⁸ – no higher-order signal could be detected at $(0.5\ 0.5\ 0)$ and the fraction of $2\mathbf{k}_f$ -neutrons is less than 0.05%. A structural contribution due to stacking faults, which also would break the body centering, is excluded by the temperature dependence of the signal, see below, and we finally ascribe the signal at \mathbf{Q}_{FM} to (ferro-)magnetic correlations. What appears astonishing is the width of the FM signal, as it is resolution limited and much sharper than the quarter-indexed AFM signal. At this point it is interesting to note that the main characteristics of the scattering for $T = 10\ \text{K}$ in $\text{La}_{0.6}\text{Sr}_{1.4}\text{MnO}_4$ resemble the basic properties of the similar mapping in $\text{La}_{1/2}\text{Sr}_{3/2}\text{MnO}_4$ not at 10 K, but at temperatures close to the magnetic phase transition at T_N where CE correlations compete with FM clusters, compare e. g. Fig. 4.20a with Fig. 4.9c,d.

At $T = 150\ \text{K}$, Fig. 4.20b, the diffuse scattering and the intensity around the CE-type positions has disappeared, and only a single signal around \mathbf{Q}_{FM} is detectable. Again, the topography of the mapping resembles the main features of the scattering in $\text{La}_{1/2}\text{Sr}_{3/2}\text{MnO}_4$ not at 150 K, but at higher temperatures well above the COO transition, see Fig. 4.9a. In order to characterize the changes in the magnetic correlations more accurately, we decided to further study the temperature dependence along the same two scans as in the discussion of the thermal evolution of the static correlations in $\text{La}_{1/2}\text{Sr}_{3/2}\text{MnO}_4$, depicted in Fig. 4.20a by two white lines. Scan 1 runs along $[1\ 1\ 0]$ crossing the CE-type position \mathbf{Q}_{mag} and is especially sensitive to the correlations within the zig-zag chains. The second scan is oriented perpendicular and connects the two positions $(0.75\ 0.25\ 0)$ and $(1\ 0\ 0)$, thereby testing the diffuse scattering as well as the FM response at \mathbf{Q}_{FM} .

The temperature dependence along scan 1 is shown in Fig. 4.21. Clearly, at $\mathbf{Q}_{\text{mag}} = (0.75\ 0.25\ 0)$ a magnetic signal is detectable above the experimental background below $T_N = 110\ \text{K}$, which we tentatively define as the Néel temperature

¹⁸Higher harmonics with $n \geq 3$ are already cut-off by the long neutron-guide, at which IN12 is situated.

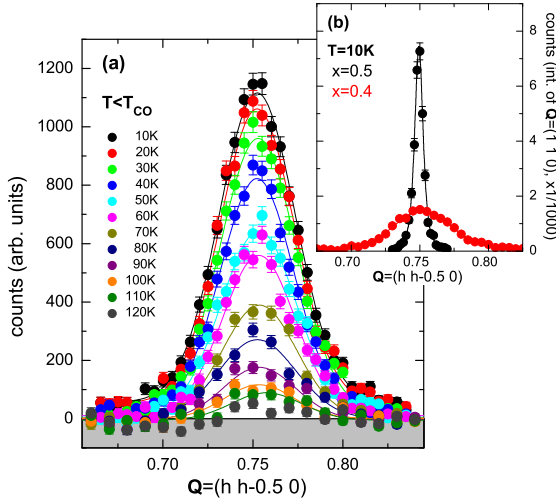


Figure 4.21: Temperature dependence of the CE-type correlations ||chains Thermal evolution of the magnetic intensity along line 1 depicted in Fig. 4.20a measured at IN12 (a). Comparison of the magnetic reflection $\mathbf{Q}_{\text{mag}} = (0.75 \ 0.25 \ 0)$ for the two compounds $\text{La}_{1/2}\text{Sr}_{3/2}\text{MnO}_4$ and $\text{La}_{0.6}\text{Sr}_{1.4}\text{MnO}_4$ (b). In (b) data are normalized on the intensity of the (110) reflection. Lines denote fits to the data as discussed in the text, a common background has been subtracted in all data.

T_N . Upon further cooling, the signal rapidly increases in intensity, but remains always significantly broadened pointing to finite-size correlations. From the width of the signal at 10 K we estimate a correlation length, which is of the same order as for the orbital ordering, $\xi \approx 20 \text{ \AA}$. The difference in the magnetic correlations between the two systems $\text{La}_{0.6}\text{Sr}_{1.4}\text{MnO}_4$ and $\text{La}_{1/2}\text{Sr}_{3/2}\text{MnO}_4$ is already evident by comparing the raw data. In Fig. 4.19b we plot the CE response at \mathbf{Q}_{mag} for both compounds normalized on the intensity of the tetragonal (110) Bragg reflection: Comparing the two reflections, the broadening of the peak shape in the underdoped compound is apparent. The absolute magnetic intensity is reduced, too, but the suppression is less pronounced than for the charge- and orbital-ordering reflections.

The temperature dependence along scan 2 is shown in Fig. 4.22, and the interpretation of the magnetic scattering in the perpendicular direction is more challenging.¹⁹ At highest temperatures, $T \geq 240 \text{ K}$, the signal consists of a single Lorentzian-shaped response centered around \mathbf{Q}_{FM} . Upon cooling, the Lorentzian-like signal is suppressed, and below T_N magnetic intensity is partly transferred across the streak $(1 \ 0 \ 0) \rightarrow (0.75 \ 0.25 \ 0)$ to the CE-type position, similar to the observations in $\text{La}_{1/2}\text{Sr}_{3/2}\text{MnO}_4$. However, additional magnetic contributions can also be identified, not detectable in the half-doped sample. Below T_N diffuse magnetic scattering develops along the streak with a broad maximum around $\mathbf{Q} = (1 - q_h \ q_h \ 0)$ and $q_h \approx 0.15$, which monotonically increases in intensity down to $T=10 \text{ K}$. The diffuse scattering is restricted to $q_h \leq 0.25$ with the CE position as a strict border, forming the “diffuse-square” visible in the contour plot Fig. 4.20a. In addition, at the FM position \mathbf{Q}_{FM} a sharp, Gaussian-shaped signal

¹⁹Please note that the presentation in Fig. 4.22 is similar to Fig. 4.10, analyzing the interchain correlations in $\text{La}_{1/2}\text{Sr}_{3/2}\text{MnO}_4$, which allows an easy comparison between both compounds.

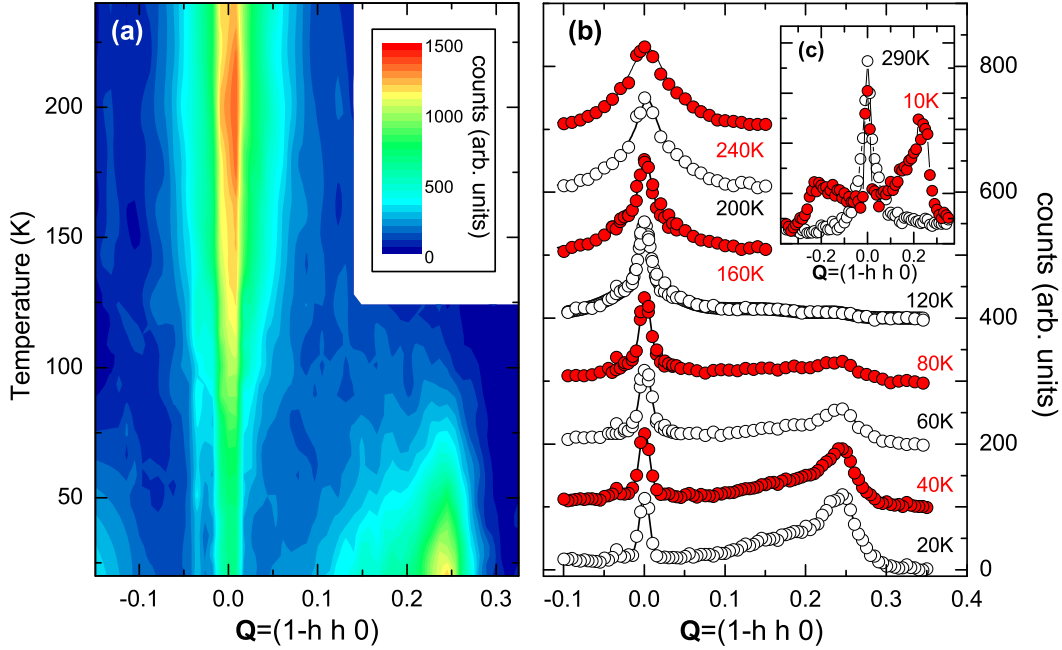


Figure 4.22: Thermal evolution of the diffuse scattering \perp chains Temperature dependence of the magnetic intensity along line 2 depicted in Fig. 4.20a. Data were collected between 20 K and 240 K with temperature steps of 10 K at the spectrometer IN12 (a). Raw-data scans underlying the contour plot in (a). For clarity, subsequent scans are shifted vertically by 100 counts (b). Direct comparison of the 10 K and 290 K data (c). Data in (a) and (b) were recorded with $E_f = 8.04$ meV, those presented in (c) with $E_f = 4.66$ meV. In (a) and (b) a minor contamination by second-harmonic neutrons has been subtracted.

can be distinguished on top of the broad Lorentzian below ≈ 200 K, which persists down to lowest temperatures.

The drastic changes in the magnetic scattering for $T = 290$ K and 10 K can most impressively be summarized by directly comparing the 290 K and 10 K data, see Fig. 4.22c. The Lorentzian-shaped signal at high temperatures is completely suppressed and transformed into a sharp signal at Q_{FM} and at the neighboring quarter-indexed CE-type positions, with sizable diffuse intensity appearing between these two reflections. Moreover, the comparison of the raw data excludes a sizable sharp contribution at Q_{FM} for $T = 290$ K, which excludes a structural contribution due to stacking faults in the tetragonal lattice, proving the magnetic origin of the signal.²⁰

To acquire a more quantitative description of the thermal evolution, we modeled all data assuming different magnetic contributions. The scans along $[110]$

²⁰As aforementioned, a contamination of second-harmonic neutrons is below the detection limit with $E_F = 4.66$ meV.

presented in Fig. 4.21 can well be described by a single Gaussian, whereas the complex structure in the perpendicular direction requires several features. To contain consistency in the description, we model all spectra along $[1\bar{1}0]$ including a Lorentzian representing the broad FM signal centered around \mathbf{Q}_{FM} , a Gaussian to account for the sharp component at the same position, and two further components to incorporate the diffuse AFM and well-defined CE-type scattering. In the refinement all of these components were allowed to vary independently, resulting in a satisfying fit of the data, see Fig. 4.22b. The results of this analysis are summarized in Fig. 4.23.

To start with, we show in Fig. 4.23a the temperature dependence of the CO and the OO superstructure reflections as derived from the analysis of the data in Fig. 4.19. Both, charge and orbital ordering exhibit a similar temperature dependence with only a slow increase below $T_{\text{CO}} \approx 200$ K.²¹ In contrast to the steep rise of the order parameter below T_{CO} in $\text{La}_{1/2}\text{Sr}_{3/2}\text{MnO}_4$, the major increase in intensity in $\text{La}_{0.6}\text{Sr}_{1.4}\text{MnO}_4$ is found below ≈ 150 K and the intensity curve possesses an inflection point around 100 K.

Fig. 4.23b,c present the thermal evolution of the different magnetic components identified in the raw-data scans. At \mathbf{Q}_{FM} , two distinct contributions have to be considered, a Lorentzian component observed at high temperatures, depicted as “broad” in Fig. 4.23b, and a Gaussian component, marked as “sharp”, which grows on top of the broad signal upon cooling. With decreasing temperature the broad signal at \mathbf{Q}_{FM} is continuously weakened and completely diminished below ≈ 70 K, showing a similar behavior as the FM response in the optimal-doped sample. On the contrary, the sharp contribution at \mathbf{Q}_{FM} monotonically increases from ≈ 225 K down to low temperatures, with the major increase between 200 K and 100 K.

The discussion of the AFM correlations in $\text{La}_{0.6}\text{Sr}_{1.4}\text{MnO}_4$ also has to be divided into two parts – there is a well-defined signal centered at the quarter-indexed position, and a diffuse component in-between the CE position and \mathbf{Q}_{FM} , which are signed as “sharp” and “diffuse” in Fig. 4.23c, respectively. However, both signals become simultaneously visible below $T_{\text{N}} \approx 110$ K and display a similar T-dependence upon cooling, which is furthermore comparable with that in $\text{La}_{1/2}\text{Sr}_{3/2}\text{MnO}_4$. More interestingly, the analysis of the position of the CE-type contribution around $(0.75\ 0.25\ 0)$ reveals, that the CE ordering is shifted to slightly incommensurable values, as for low temperatures the CE reflection is centered at $\mathbf{Q} = (1 \pm \varepsilon \mp \varepsilon\ 0)$ and $\varepsilon = 0.2427(3)$, see Fig. 4.23d.

The temperature dependence of the in-plane correlations in the half doped compound $\text{La}_{1/2}\text{Sr}_{3/2}\text{MnO}_4$ in the previous section has finally been completed by a short remark on the magnetic correlations perpendicular to the MnO_2 -sheets. Although

²¹The agreement between the thermal evolution of the two reflections, $\mathbf{Q}_{\text{CO}} = (1.5\ 1.5\ 0)$ and $\mathbf{Q}_{\text{OO}} = (2.25\ 0.25\ 0)$, provides another clear indication for the purely nuclear origin of the observed intensity at \mathbf{Q}_{OO} .

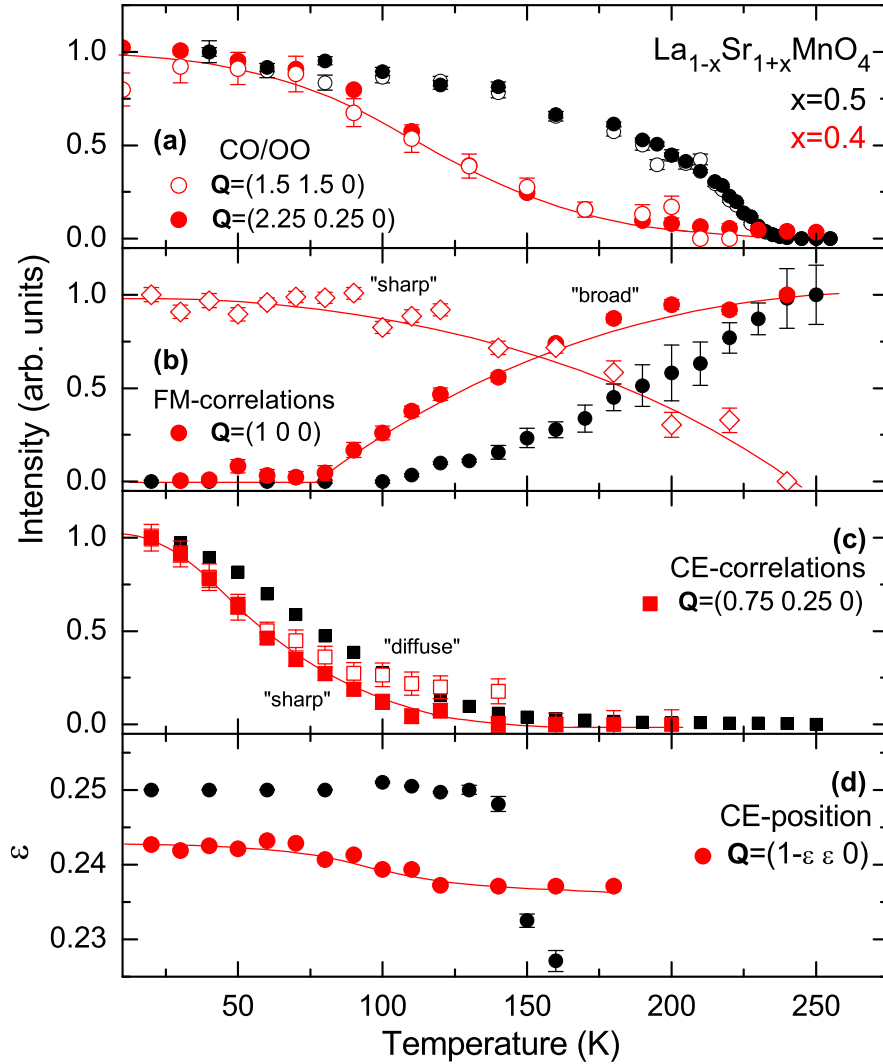


Figure 4.23: Development of the magnetic correlations in $\text{La}_{0.6}\text{Sr}_{1.4}\text{MnO}_4$
 Summary of the analysis of the thermal evolution of the magnetic scattering showing the temperature dependence of the intensity of the structural superstructure reflections $Q_{\text{OO}} = (2.25\ 0.25\ 0)$ and $Q_{\text{CO}} = (1.5\ 1.5\ 0)$, probing the orbital and the charge ordering, respectively, (a), of the intensity of the sharp Gaussian-shaped and the broad Lorentzian signal at the FM position $Q_{\text{FM}} = (1\ 0\ 0)$ (b), and of the diffuse AFM and the sharp CE signal at $Q_{\text{mag}} = (0.75\ 0.25\ 0)$ (c). Temperature dependence of the observed position of the CE-type signal along the line $Q = (1 \pm \varepsilon\ \mp \varepsilon\ 0)$ (d). Red symbols denote the underdoped compound $\text{La}_{0.6}\text{Sr}_{1.4}\text{MnO}_4$, while black symbols mark for comparison the half-doped system $\text{La}_{1/2}\text{Sr}_{3/2}\text{MnO}_4$. Lines are included as guides to the eye, data for $\text{La}_{1/2}\text{Sr}_{3/2}\text{MnO}_4$ are the same as presented in Fig. 4.12.

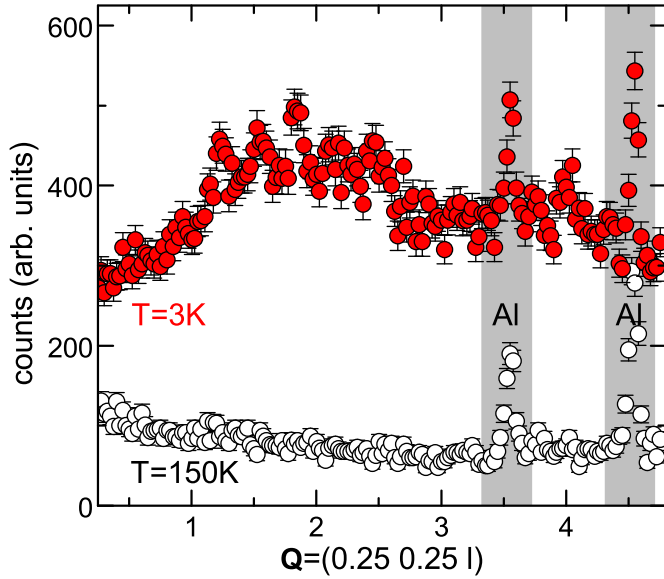


Figure 4.24: Magnetic correlations along the c -axis
 Raw-data scans along the line $\mathbf{Q} = (0.25\ 0.25\ q_l)$ aiming at the magnetic correlations along the tetragonal c -axis for $T = 3\text{ K}$ and 150 K . Gray-shaded areas mark spurious contaminations by scattering from Aluminium.

the ordering along \mathbf{c} is not perfectly three dimensional, the analysis has revealed well defined reflections along $\mathbf{Q} = (0.25\ 0.25\ q_l)$ in the ordered state, pointing to a finite magnetic correlation length $\xi_c \approx 50\text{ \AA}$ parallel to \mathbf{c} in $\text{La}_{1/2}\text{Sr}_{3/2}\text{MnO}_4$. In Fig. 4.24 we show the similar analysis for the doped sample $\text{La}_{0.6}\text{Sr}_{1.4}\text{MnO}_4$: The comparison between the 150 K and 3 K data proves the magnetic character of the scattering at low temperatures – besides the spurious intensity from the Al-scattering – but well-defined magnetic reflections are not observed along $[001]$. Instead, the magnetic intensity is uniformly distributed along the rod $\mathbf{Q} = (0.25\ 0.25\ q_l)$ and the short-range CE-type correlations are entirely two dimensional and restricted to single MnO_2 -layers in the case of $\text{La}_{0.6}\text{Sr}_{1.4}\text{MnO}_4$.²²

Macroscopic magnetization Following the discussion of the half-doped compound, we now turn to the analysis of the macroscopic magnetization $M(T, B)$, which is plotted in Fig. 4.25 for $\text{La}_{1/2}\text{Sr}_{3/2}\text{MnO}_4$ and $\text{La}_{0.6}\text{Sr}_{1.4}\text{MnO}_4$. Also included is the intermediated compound $\text{La}_{0.55}\text{Sr}_{1.45}\text{MnO}_4$ [43, 64]. The magnetization of all three compounds exhibits some common features, which are best analyzed by dividing $M(T)$ into three different temperature regimes, indicated by the gray lines in Fig. 4.25a.

At high temperatures above T_{CO} , $M(T)$ follows a Curie-Weiss like behavior and is comparable for all three compounds. The increase of magnetization with T in this region is clearly associated with the short-range FM correlations identified in

²²The slight modulation of the observed scattering has to be attributed to the change of the scattering geometry as the angle between \mathbf{Q} and the \mathbf{ab} considerably increases along the line $\mathbf{Q} = (0.25\ 0.25\ q_l)$ for $q_l = 0 \dots 5$.

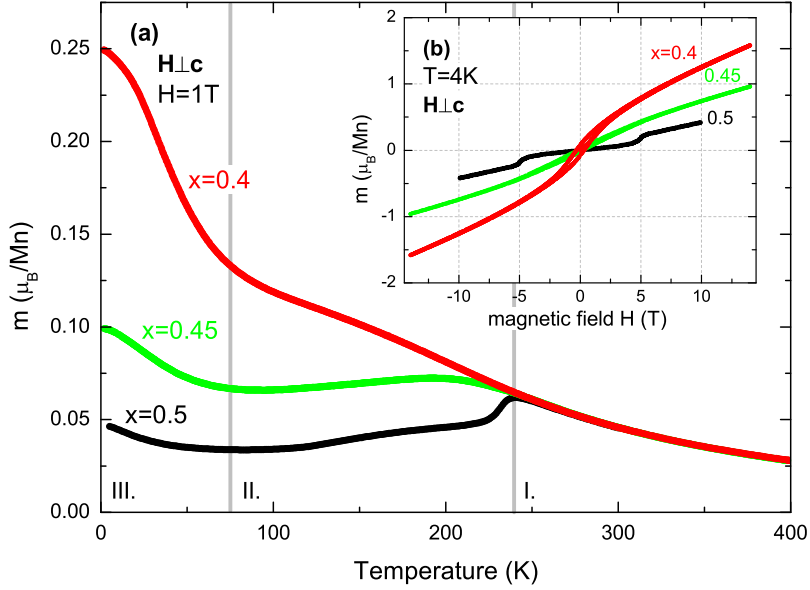


Figure 4.25: Macroscopic magnetization in $\text{La}_{0.6}\text{Sr}_{1.4}\text{MnO}_4$ Temperature dependence of the macroscopic magnetization $M(T)$ for $\text{La}_{1-x}\text{Sr}_{1+x}\text{MnO}_4$ and $x = 0.4, 0.45, 0.5$ for $\mathbf{H} \perp \mathbf{c}$ and $H = 1 \text{ T}$. Vertical gray lines mark the borders of the three different temperature regimes discussed in the text (a). Magnetization M as a function of magnetic field $\mathbf{H} \perp \mathbf{c}$ at low temperatures $T = 4 \text{ K}$ (b). Data are taken from Refs. [43, 64].

the neutron scattering experiments both in $\text{La}_{1/2}\text{Sr}_{3/2}\text{MnO}_4$ and $\text{La}_{0.6}\text{Sr}_{1.4}\text{MnO}_4$, and which in the orbitally disordered regime are driven by the classical Zener mechanism [77]. The onset of the charge and orbital ordering suppresses the magnetization in all three compounds, but the effect is significantly weakened with doping: In $\text{La}_{1/2}\text{Sr}_{3/2}\text{MnO}_4$, $M(T)$ exhibits a sharp kink at T_{CO} and continuously decreases with temperature forming a local minimum near $\approx 75 \text{ K}$, whereas for the electron-doped compounds the drop in $M(T)$ at T_{CO} is severely reduced. In $\text{La}_{0.55}\text{Sr}_{1.45}\text{MnO}_4$ the magnetization displays a broad local maximum around $T_{\text{CO}} \approx 200 \text{ K}$, while for $\text{La}_{0.6}\text{Sr}_{1.4}\text{MnO}_4$ the charge and orbital ordering has no comparable effect on the magnetization – only a slight deviation from the Curie-like behavior at high temperatures can be observed below 200 K , consistent with the strong reduction of the orbital ordering found in the neutron scattering experiments.²³ Note, that in contrast to $\text{La}_{1/2}\text{Sr}_{3/2}\text{MnO}_4$ there is no distinct anomaly in the electric resistivity $\rho(T)$ and in the specific heat $c(T)$ at T_{CO} in $\text{La}_{0.6}\text{Sr}_{1.4}\text{MnO}_4$, again pointing to the finite correlation length of the COO ordering in this com-

²³These results are consistent with a first preliminary experiment on $\text{La}_{0.55}\text{Sr}_{1.45}\text{MnO}_4$, as compared to $\text{La}_{1/2}\text{Sr}_{3/2}\text{MnO}_4$ the COO-superstructure reflections are weakened, but well stronger than for $x = 0.4$.

pound [42, 64, 155].

In the low temperature regime below ≈ 70 K all three compounds show a distinct upturn in $M(T)$, which scales with the e_g -electron density n_e and is most pronounced in $\text{La}_{0.6}\text{Sr}_{1.4}\text{MnO}_4$, reaching at 4 K a maximum value of $0.25 \mu_{\text{B}}/\text{Mn}$ for $H = 1$ T, well comparable with published data [42]. Obviously, this unusual behavior can not be associated with the antiferromagnetic ordering of the CE type, but rather points to FM correlations. Furthermore it is noteworthy, that close to half doping the absolute value of the low-temperature magnetization seems to depend sensitively on the exact stoichiometry of the sample, as the reported values in the literature are not consistent [42, 43].²⁴

To further investigate the properties of the ferromagnetic correlations at low temperatures we show in Fig. 4.25b the field dependence $M(H)$ of the macroscopic magnetization at 4 K and $\mathbf{H} \perp \mathbf{c}$ for all three compounds [43, 64]. In the half-doped sample $\text{La}_{1/2}\text{Sr}_{3/2}\text{MnO}_4$ a distinct anomaly is observable around 5 T with a jump-like increase of the magnetization, which is ascribed to a spin-flop transition within the CE-ordered phase [43]. In the two underdoped compounds a similar effect is absent, and both $M(H)$ -curves are right-curved with $\frac{\partial^2 M}{\partial H^2} < 0$ in the entire field-range up to 14 T, indicative of ferromagnetic correlated moments. For the highest fields available – 10 T in the case of $\text{La}_{1/2}\text{Sr}_{3/2}\text{MnO}_4$ and 14 T for the doped samples – the magnetization is still not saturating, but the size of the induced moment increases monotonically upon doping and reaches in $\text{La}_{0.6}\text{Sr}_{1.4}\text{MnO}_4$ already a sizable value of $\approx 1.5 \mu_{\text{B}}/\text{Mn}$. Even more interestingly, with increasing electron doping the $M(H)$ -curves develop a distinct hysteresis upon ramping the field, clearly documenting the existence of FM ordered parts as already deduced from the sharp contribution at $\mathbf{Q}_{\text{FM}} = (100)$, and we find a small remanent magnetization of $0.08 \mu_{\text{B}}/\text{Mn}$ $\text{La}_{0.6}\text{Sr}_{1.4}\text{MnO}_4$ at $T = 4$ K.

Field dependence of the magnetic correlations To study the impact of the magnetic field on the magnetic correlations we have investigated the field dependence of several magnetic superstructure reflections at the spectrometer FLEX using the 15 T-cryomagnet VM2 of the HMI in Berlin. In this experiment the sample was mounted with the two reflections (110) and (001) defining the scattering plane and the field applied along the vertical direction. As the FM correlations are expected to be long-ranged due to the applied field, the magnetic superstructure reflections will be situated on top of the fundamental structural Bragg reflections. Hence, to track even small changes in the FM correlations we decided to focus on the Bragg position $\mathbf{Q} = (002)$, which has only a weak structural contribution.

²⁴Although inhabited in the macroscopic data of our sample, a FM response could not be detected in the neutron experiments in $\text{La}_{1/2}\text{Sr}_{3/2}\text{MnO}_4$ – most likely due to the weakness of the FM correlated moments. From the magnetization data the size of these moments is estimated to be of the order of $0.04 \mu_{\text{B}}/\text{Mn}$ [43], suppressing the FM signal by a factor of ≈ 40 in diffraction experiments.

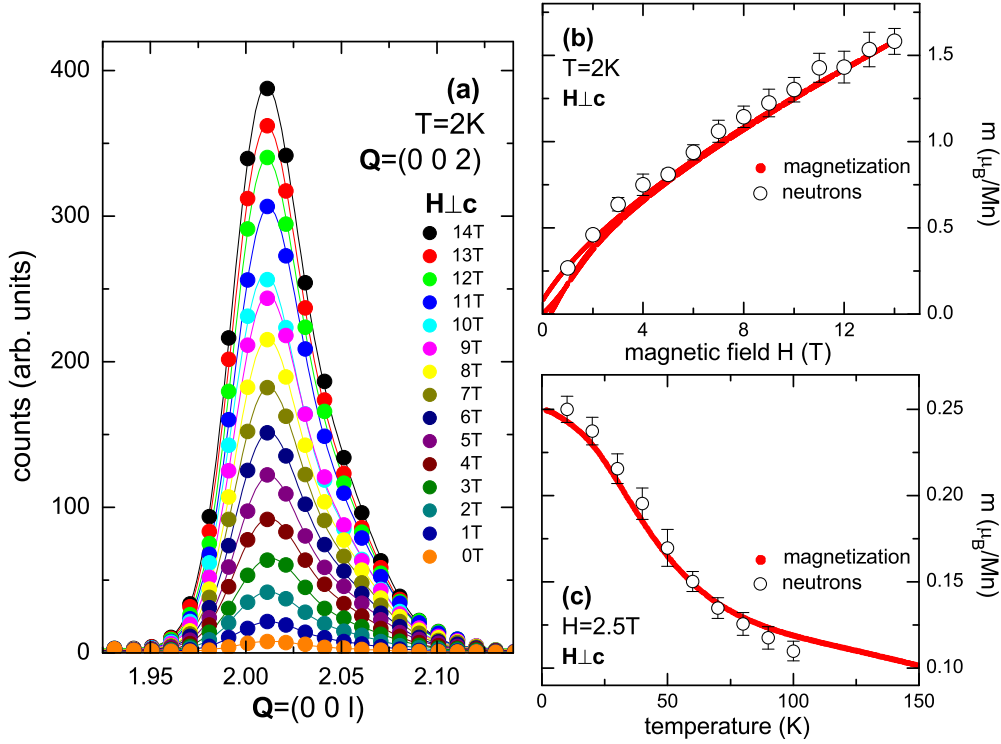


Figure 4.26: Field dependence of the FM scattering Field dependence of the nuclear and FM Bragg reflection $Q = (002)$ in the low-temperature phase at $T = 2\text{K}$ recorded at the FLEX spectrometer using the 15 T-cryomagnet VM2 and the field applied along $[110]$. Lines correspond to fits to the data as described in the text, the asymmetric profile has to be attributed to a slight misalignment in the experimental setup (a). Comparison of the change in the magnetization derived from the neutron data with the results from the macroscopic magnetization as a function of applied field at $T = 2\text{K}$ (b), and as a function of temperature at a constant field, 2.5 T in the neutron case and 1 T for the macroscopic data (c).

The field dependence of the (002) reflection is shown in Fig. 4.26. With increasing field the observed intensity rapidly increases, and for the maximum field available, $H = 14\text{T}$, the signal has gained a factor of 50 compared to zero field, see Fig. 4.26a.²⁵ This enormous increase of intensity has to be attributed to the induced three dimensional ferromagnetic correlations already revealed in the field-dependence of the macroscopic magnetization. To compare the magnetization with the neutron results of Fig. 4.26a, we extract the magnetic component from the observed signal by subtracting the zero-field and zero-field cooled response, which fixes the structural scattering at $Q = (002)$. The magnetic intensity is

²⁵Please note that the asymmetric profile of the reflection has to be assigned to a slight misalignment in the experimental setup.

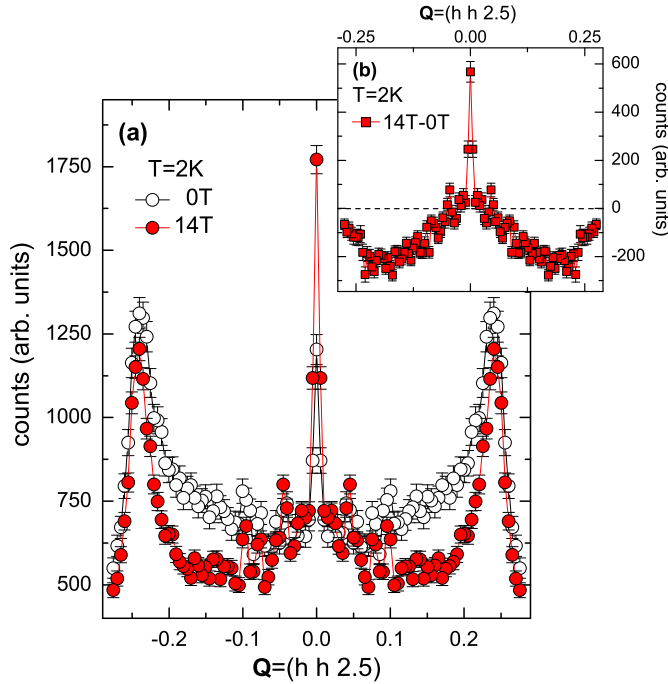


Figure 4.27: Field dependence of the AFM CE-type scattering Field dependence of the magnetic scattering along the line $(0.25\ 0.25\ 2.5) \rightarrow (0\ 0\ 2.5)$ at low temperature $T = 2\text{ K}$ (a). Difference spectra (b), calculated from the data presented in (a). In order to increase the statistics the data are symmetrized with respect to the position $\mathbf{Q} = (0\ 0\ 2.5)$.

then directly proportional to the square of the induced moment, cf. Chap. 2. The neutron data scale almost perfectly with the macroscopic data, thereby calibrating the neutron intensity in absolute units, see Fig. 4.26b.

We have also investigated the temperature dependence of the magnetic signal up to 100 K for a constant field of 2.5 T. Again, the increase of the neutron intensity upon cooling nicely agrees with the observed increase of the macroscopic magnetization in this temperature regime, see Fig. 4.26c, and we find a one-to-one correspondence between the induced moment in the magnetization and the FM correlations in the neutron data.

What appears more astonishing is the response of the AFM CE-type correlations to the applied magnetic field: In Fig. 4.27 we show raw-data scans at $T=2\text{ K}$ in zero and high field, $H = 14\text{ T}$, connecting the two AFM CE positions $(\pm 0.25 \pm 0.25\ 2.5)$. As the magnetic correlations in zero field are two dimensional, this scan is equivalent to the path $(0.75\ 0.25\ 0) \rightarrow (1\ 0\ 0)$ already discussed in more detail, see Fig. 4.22. Indeed, for $H = 0\text{ T}$ the scan along $(q_h\ q_k\ 2.5)$ exhibits an asymmetric response with a sharp border for $q_h > 0.25$ and significant diffuse intensity in-between the two quarter indexed positions, very similar to the characteristic features discussed before. The sharp signal at $\mathbf{Q} = (0\ 0\ 2.5)$ reflects the almost uncorrelated stacking of two-dimensional ferromagnetic clusters along the \mathbf{c} -direction and has to be compared with the FM scattering observed at $\mathbf{Q}_{\text{FM}} = (1\ 0\ 0)$. Interestingly, all three components reveal a different response to the strong magnetic field: For $H = 14\text{ T}$ the diffuse magnetic scattering is com-

pletely suppressed, whereas the quarter-indexed reflections are not affected. Both the width and the intensity of the reflections at $\mathbf{Q} = (\pm 0.25 \pm 0.25 2.5)$ remain unchanged, and the well-defined CE-type scattering persists in the strong magnetic field. Moreover, the CE reflections acquire a nearly symmetric shape, which most likely is hidden in the diffuse background for $H = 0$ T. The (pseudo)-FM position (00 2.5) is also influenced by the strong magnetic field. For $H = 14$ T the intensity at (00 2.5) is considerably enhanced, pointing to some misaligned FM clusters along c even for the strong field, but the increase of intensity can not be compared with the behavior of the (00 2) reflection as discussed before.

Evidence for microscopic phase separation The different response of the diffuse and the well defined CE-type scattering around the quarter-indexed positions to an applied magnetic field yields strong evidence for a magnetically heterogeneous state in $\text{La}_{0.6}\text{Sr}_{1.4}\text{MnO}_4$ [2, 5, 86]. However, before developing a qualitative picture of the magnetic ordering in $\text{La}_{0.6}\text{Sr}_{1.4}\text{MnO}_4$ we summarize the main experimental observations such a model has to reproduce:

- At low temperatures the system is charge and orbital ordered. However, the ordering is only finite with a correlation length $\xi \approx 20$ Å within the planes.
- Well-defined magnetic scattering is observed around the typical half- and quarter-indexed positions. The ordering of the Mn^{3+} -sites is slightly incommensurate and restricted to single MnO_2 -sheets. The magnetic correlation length within the planes is finite and comparable to that of the COO order.
- Diffuse AFM scattering persists down to lowest temperatures. The diffuse intensity is restricted to a square centered around an integer-indexed reflection with sharp borders defined by the four surrounding quarter-indexed positions. A strong magnetic field suppresses the diffuse scattering, in contrast to the CE-like scattering at the quarter positions, which remains unchanged up to 14 T.
- In addition to the AFM scattering a considerable response is observed at $\mathbf{Q}_{\text{FM}} = (100)$, representing two-dimensional FM correlations. In an external field the FM correlations are strongly enhanced, and the macroscopic magnetization reveals a sizable induced moment of $1.5 \mu_{\text{B}}/\text{Mn}$ for $\mathbf{H}_{[110]} = 14$ T.

According to the discussion of the properties of the half-doped compound the most stable elements of the CE structure are the FM zig-zag chains. It appears reasonable that these fragments also constitute the building blocks of the magnetic ground state in $\text{La}_{0.6}\text{Sr}_{1.4}\text{MnO}_4$. In order to acquire some physical intuition into the properties of these elements, we consider in the following a simple toy-model treating different arrangements of FM zig-zag fragments in real and reciprocal space, see Fig. 4.28.

To construct the real-space structures shown in the left panel of Fig. 4.28 we consider stable spin- $\frac{1}{2}$ zig-zag elements along $[110]$ on a grid of 128×128 points. Within each chain, neighboring sites are coupled ferromagnetically with a probability p_{\parallel} , yielding a correlation length ξ_{\parallel} (in units of the grid) along the chains given by $p_{\parallel} = \exp(-\frac{1}{\xi_{\parallel}})$. To build-up the real-space pattern shown, the spin arrangement of each zig-zag path is calculated independently from the neighboring chains, and the coupling between adjacent chains is subsequently included with a probability p_{\perp} of an AFM alignment along a *single row* of the grid. As long as the correlation length ξ_{\parallel} is infinite, this procedure yields a well defined correlation perpendicular to the chains and reproduces the CE pattern in the limit $p_{\parallel} = p_{\perp} = 1$, see Fig.4.28a. However, as soon as the correlations along the chains become finite, the algorithm does not take into account the domain structure within the chains and the perpendicular correlations are not taken into account properly. In this case the correlation length ξ_{\perp} is not well defined and the chains are treated as isolated objects. Nevertheless, since the magnetic coupling between the chains is only weak, adjacent chains can be considered as isolated and this simple approach seems well justified.²⁶

The right panel of Fig. 4.28 shows the Fourier transformations of the corresponding real-space structures, calculated using the two-dimensional FFT algorithm implemented in the Matlab package. In order to compare the calculation with the experiment, the data shown are broadened by a Gaussian mimicking the finite experimental resolution. In addition, the simulated picture of reciprocal space is finally superimposed by its 90° -twin to take into account the twinning induced by the OO transition in a sample crystal.

Let us now discuss the different configurations. In Fig. 4.28a both the intra- and interchain correlations are long-ranged, $\xi_{\parallel} = \xi_{\perp} = \infty$, and the real-space pattern resembles the perfect CE ordering. The associated response in reciprocal space consists of sharp reflections at the quarter- and half-indexed position, corresponding to the correlations on the corner and bridge sites, respectively. In a first step, Fig. 4.28b, we keep the long-range ordering within, but weaken the correlations perpendicular to the chains, $\xi_{\parallel} = \infty$ and $\xi_{\perp} = 5$. In consequence, some chains flip and form FM clusters with the neighboring sites. In Fourier space an additional sharp signal appears at $\mathbf{Q}_{\text{FM}} = (100)$, which is connected with the quarter-positions via a diffuse x -shaped streak representing the different modulation wavelengths perpendicular to the chains. Interestingly, the diffuse intensity around the half-indexed reflections is less pronounced signalling a significantly reduced structure factor. If we now additionally reduce the correlation length within the chains the clustering in the real-space structures is enhanced, Fig. 4.28c and

²⁶Improving this model to take explicitly into account the domain structure and the finite correlations between adjacent chains would require a Quantum Monte Carlo simulation at finite temperatures [181].

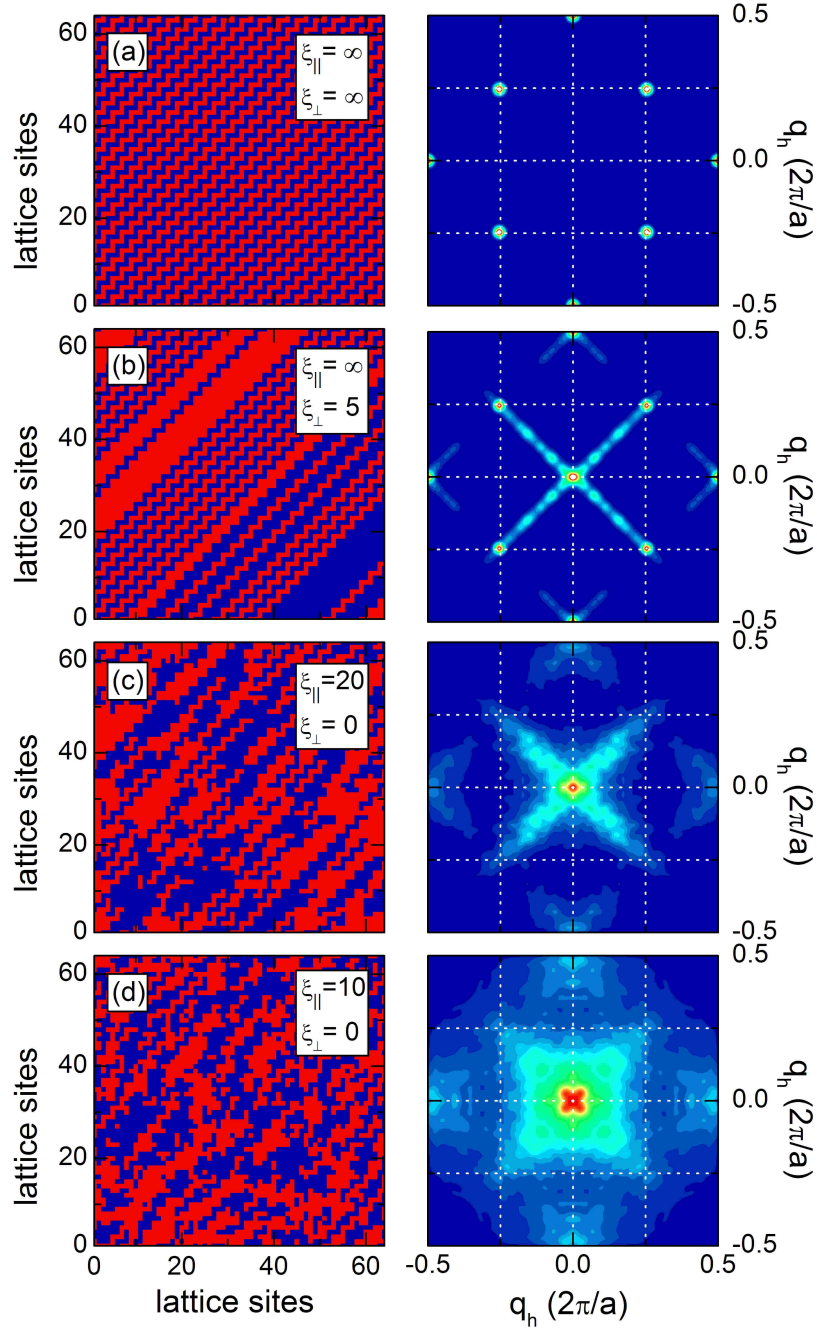


Figure 4.28: Simulation of the evolution of the CE order upon electron doping Calculated real-space images of the magnetic ordering for different values $\xi_{||}$ and ξ_{\perp} of the intra- and interchain correlation length. The two spin states $\pm\frac{1}{2}$ are represented by red and blue color, respectively (**left**). Symmetrized Fourier transformation calculated from the real-space structures depicted in the left panel (**right**). All calculations were performed on a grid of 128×128 points, for clarity in the left panel only the first 64×64 points are shown. For more details see the text.

d, and the sharp CE-type reflections disappear in the simulated diffraction pattern. Simultaneously, with decreasing ξ_{\parallel} the diffuse x -like signal gains intensity and smears out, but remains always confined to the square centered around \mathbf{Q}_{FM} : Due to the stability of the zig-zag elements the shortest real-space modulation perpendicular to the chains possible is $\lambda_{\text{min}} = 2\sqrt{2}$, corresponding to the $(\frac{1}{4} \frac{1}{4} 0)$ -reflections in reciprocal space. Finally, for very short correlations, $\xi_{\parallel} \approx 10$, the diffuse scattering is nearly equally distributed in the entire square and combines with the weaker diffuse scattering around the half-indexed positions.

The simulated diffraction patterns of Fig. 4.28 contain all characteristic elements of the observed magnetic scattering in $\text{La}_{0.6}\text{Sr}_{1.4}\text{MnO}_4$, at least if we combine two of them, and we are finally in a position to combine all the pieces of the puzzle and to construct a phenomenological picture of the magnetic ordering: At low temperatures $\text{La}_{0.6}\text{Sr}_{1.4}\text{MnO}_4$ is a heterogenous system with two magnetic phases coexisting on a microscopic scale. One of the two phases is perfectly CE ordered. In the diffraction data this phase is associated with the sharp reflections at the quarter positions and the ordering pattern can roughly be associated with the arrangement depicted in Fig. 4.28a. From the width of the reflections the average size of these CE clusters is found to be of the order of 20 Å. The CE clusters are stable in a strong magnetic field, very similar to the long-range CE ordering in the half-doped compound.

The second phase is connected with the diffuse magnetic intensity and the FM response at \mathbf{Q}_{FM} . Comparing the experimental data at low temperatures with the simulations shown in Fig. 4.28c and d, this phase is characterized by loosely bound zig-zag fragments with finite length. From the diffraction data the width of this “disordered” clusters is hard to estimate, but the comparison with the simulation suggests a size of $\approx 30 - 40$ Å, comparable with the spatial dimensions of the CE clusters. The magnetic correlations in this phase should be much weaker than in the strictly CE-ordered phase, and the strong impact of an applied field observed in the magnetization as well as in the field-dependent diffraction experiments originates in the response of this “disordered” regions to a magnetic field: An applied field can easily align the loosely coupled spins and induce large magnetic moments. Consequently, the diffuse magnetic scattering is suppressed and transformed into well defined FM scattering.

In conclusion, the results of the elastic neutron diffraction experiments presented above give strong support for a magnetically inhomogeneous state in electron-doped $\text{La}_{0.6}\text{Sr}_{1.4}\text{MnO}_4$ at low temperature. However, so far we have not commented on the microscopic origin of the phase separation, and in our opinion it seems very unlikely that the different phases base on purely magnetic interactions. Note, that we have not yet discussed the influence of the extra electrons, as compared to the optimal-doped compound each fifth Mn^{4+} is substituted by a Mn^{3+} -ion with localized e_g -electron in $\text{La}_{0.6}\text{Sr}_{1.4}\text{MnO}_4$. The additional electrons severely disturb the charge and orbital lattice of the CE pattern, and will influence the sen-

sible balance of electronic, magnetic and lattice degrees of freedom – most likely the additional e_g -electrons will localize on the cornering sites of the zig-zag structure occupying the out-of plane states with $d_{3z^2-r^2}$ -symmetry. Therefore, it seems plausible that the magnetic phase separation is coupled to a charge segregation into hole- and electron-rich regions. In this picture the magnetically CE-ordered phase is hole rich with a 1:1-ratio of Mn^{3+} and Mn^{4+} similar to $\text{La}_{1/2}\text{Sr}_{3/2}\text{MnO}_4$, whereas the magnetic “disordered” phase is coupled to the electron-rich regimes containing *all* excess electrons. A first indication for this scenario is given by the observed slight incommensurability of the CE reflections, which can be interpreted as a local strain in the lattice originating from the magnetic ordering via the underlying orbital ordering. However, this hypothesis surely has to be tested by further experiments sensitive to phase separation in both the spin and the lattice channel, as e. g. small angle neutron scattering.

4.3.2 Magnetic correlations in hole-doped $\text{La}_{0.4}\text{Sr}_{1.6}\text{MnO}_4$

In contrast to electron doping, the COO state is very stable upon removing electrons, and COO phenomena are reported in $\text{La}_{1-x}\text{Sr}_{1+x}\text{MnO}_4$ up to large Sr-concentrations $x \leq 0.85$ [44]. It is well established, that for $x > 0.5$ the COO state is incommensurate with the incommensurability ε_{OO} depending linearly on the density n_e of e_g -electrons, $\varepsilon_{\text{OO}} = \frac{1-2n_e}{4}$ [126]. As aforementioned, the evolution of the magnetic state is only little explored, Laroche et al. report on *commensurate* short-range magnetic correlations with an in-plane correlation length $\xi = 29 \text{ \AA}$ in $\text{La}_{0.4}\text{Sr}_{1.6}\text{MnO}_4$ ($x = 0.6$), in contrast to the incommensurate character of the orbital correlations [7]. As in these complex ordered systems the magnetic and orbital degrees of freedom are typically closely correlated this contrasting behavior is very astonishing. Hence, we have decided to (re-)examine the magnetic correlations in $\text{La}_{0.4}\text{Sr}_{1.6}\text{MnO}_4$ using elastic and inelastic neutron scattering. As we will demonstrate in the following, the result of Laroche et al. is not correct, and the magnetic ordering for $x = 0.6$ is – in agreement with the orbital correlations – incommensurate.

Before proceeding with the description of the magnetic ordering, we make a short remark on the orbital correlations in $\text{La}_{0.4}\text{Sr}_{1.6}\text{MnO}_4$. At $T_{\text{CO}} = 255 \text{ K}$, we observe the onset of structural scattering characteristic for the COO transition. The orbital ordering is incommensurate and the typical orbital superstructure reflections are shifted longitudinally peaking at $\mathbf{Q}_{\text{OO}} = (2.25 - \varepsilon_{\text{OO}} \ 0.25 - \varepsilon_{\text{OO}} \ 0)$ with $\varepsilon_{\text{OO}} = 0.043(1)^{27}$ [46]. Both, the COO-transition temperature T_{CO} and the incommensurability ε_{OO} are in good agreement with the published data for $x = 0.6$ [44, 126].

²⁷Determining the average valence with the help of the scaling relation $\varepsilon(x)$ the observed incommensurability yields a slight non-stoichiometry $x = 0.588$.

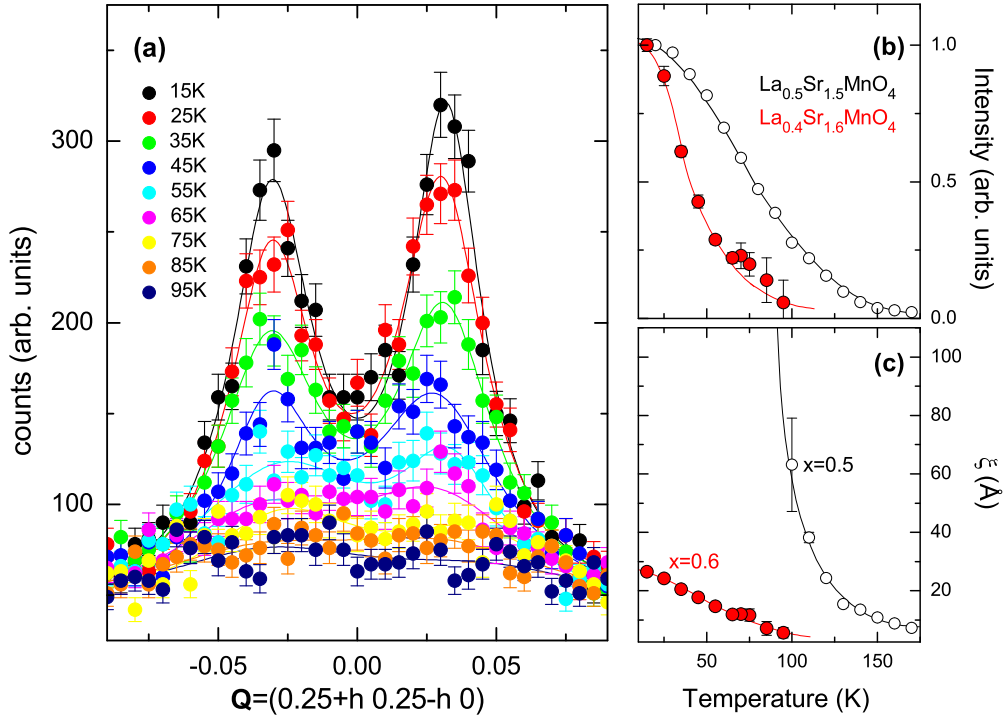


Figure 4.29: Temperature dependence of the magnetic correlations for $x=0.6$ Temperature dependence of the magnetic intensity along the line $\mathbf{Q} = (0.25+q_h, 0.25-q_h, 0)$, i.e. parallel to the propagation of the zig-zag chains, in $\text{La}_{0.4}\text{Sr}_{1.6}\text{MnO}_4$, recorded at the spectrometer G4.3 with $E_f = 14.7$ meV (a). Comparison of the thermal evolution of the magnetic intensity of the magnetic CE-type reflections (b), and of the in-plane magnetic correlation length (c) for the two compounds $\text{La}_{1/2}\text{Sr}_{3/2}\text{MnO}_4$ and $\text{La}_{0.4}\text{Sr}_{1.6}\text{MnO}_4$. Lines depicted in (a) are fits to the data, in (b) and (c) included as guides to the eye.

In Fig. 4.29 we show the development of the magnetic order in $\text{La}_{0.4}\text{Sr}_{1.6}\text{MnO}_4$. Fig. 4.29a pictures the temperature dependence of the magnetic scattering in a transversal direction along the line $\mathbf{Q} = (0.25+q_h, 0.25-q_h, 0)$. Clearly, magnetic intensity develops below $T_N \approx 95$ K with two well-defined reflections centered at $\mathbf{Q} = (0.25 \pm \varepsilon_{\text{SO}}, 0.25 \mp \varepsilon_{\text{SO}}, 0)$ and $\varepsilon_{\text{SO}} = 0.030(1)$. Scanning along the perpendicular direction we do not find a splitting of the magnetic intensity. To confirm these observations, which are contradicting the results published by Laroche et al.,²⁸ we checked very carefully the magnetic scattering in different magnetic Brillouin zones at low temperatures, but all yield similar results. Hence, the magnetic or-

²⁸In the neutron scattering experiments reported by Laroche et al. in Ref. [7] the scattering plane was defined by $[110]/[001]$, allowing only to test the magnetic correlations perpendicular to the orientation of the zig-zag chains. Obviously, these authors did not check the third direction before publishing and hence misinterpreted the magnetic intensity appearing at the commensurate position $\mathbf{Q} = (0.25, 0.25, 0)$.

dering in $\text{La}_{0.4}\text{Sr}_{1.6}\text{MnO}_4$ is incommensurate, as is the orbital order. Furthermore, both the magnetic and the orbital correlations are incommensurably modulated *parallel* to the zig-zag chains.²⁹

Not explicitly shown here is the magnetic ordering on the Mn^{4+} -sites. At the half-indexed positions magnetic scattering becomes visible below T_N as well, but, contrary to the quarter-reflections, this scattering is centered at the commensurate positions $(\frac{n}{2} 0 0)$ and the ordering of the Mn^{4+} -spins is not affected by the hole-doping [46].

To further characterize the magnetic transition in $\text{La}_{0.4}\text{Sr}_{1.6}\text{MnO}_4$ we show in Fig. 4.29 the thermal evolution of the intensity of the magnetic superstructure reflections, Fig. 4.29b, and of the magnetic correlation length ξ_{\parallel} parallel to the zig-zag chains, Fig. 4.29c. As aforementioned, magnetic scattering is detectable below $T_N \approx 95$ K, but the magnetic ordered parameter rises only little close to T_N , the major increase is found below ≈ 50 K. The magnetic correlation length ξ_{\parallel} along the chains exhibits a gradual increase at T_N and remains finite down to low temperatures, in contrast to the well defined transition in the optimal doped compound $\text{La}_{1/2}\text{Sr}_{3/2}\text{MnO}_4$. At lowest temperatures we find $\xi_{\parallel} = 27(1) \text{ \AA}$, which is comparable with the magnetic correlation length ξ_{\perp} in the perpendicular direction, but is in strong contrast to the almost long-range orbital ordering [46].

Evidence for stripe ordering in $\text{La}_{0.4}\text{Sr}_{1.6}\text{MnO}_4$ The propensity of various systems to form stripe phases has attracted a huge interest over the last years [182–185], e. g. it has been suggested that dynamically fluctuating stripe phases may be of central importance for an understanding of the physics of the high-temperature superconductors [186–188]. Today, stripe phases are well established in single-layered nickelates [189, 190] and cuprates [184, 191], and there is a first evidence for stripe phenomena in isostructural layered cobaltates as well [192]. Typical for all these systems is a linear scaling of the incommensurability ε with n_e and a close correlation between the magnetic and the structural modulations, suggesting a stripe scenario also for the overdoped regime of the COO state in charge-ordered manganites.

Indeed, different stripe pictures have been proposed to explain the COO phenomena in various manganite compounds at high doping levels, which today still are discussed controversially [193]. In a “Wigner-Crystal” approach, isolated electron-rich Mn^{3+} -stripes are separated as far as possible to reduce the Coulomb repulsion of the charged objects [91, 194]. On the contrary, the proposal of a bi-stripe

²⁹At first sight, this result appears confusing as the orbital superstructure reflection is shifted longitudinally, whereas the magnetic reflections are found in a transverse scan. However, we recall that the magnetic and orbital correlations associated with the *same* twin do not contribute at the same quarter-indexed positions; at $\mathbf{Q} = (0.25 0.25 0)$ we test the orbital correlations of twin 1 with the chains along $[1\bar{1}0]$ and, at the same time, the magnetic correlations of twin 2 with the chains along $[1\bar{1}0]$.

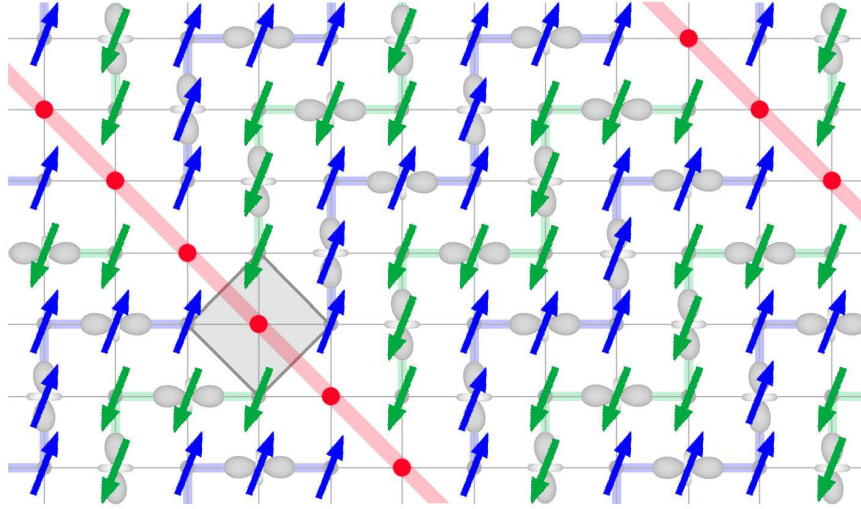


Figure 4.30: Stripe ordering of the excess Mn^{4+} in $\text{La}_{0.4}\text{Sr}_{1.6}\text{MnO}_4$ Sketch of the possible charge and orbital arrangement in hole-doped $\text{La}_{0.4}\text{Sr}_{1.6}\text{MnO}_4$. The additional holes form stripes aligned perpendicular to the propagation of the zig-zag chains. Across the stripes the orbital ordering of the remaining e_g -electrons acquires a phase shift π , whereas the magnetic ordering of the Mn^{4+} across the stripes is frustrated and the phase is not well defined. The gray-shaded area marks a plaquette which is magnetically frustrated, see text for details.

ordering suggests the existence of coupled Mn^{3+} -stripes embedded in an electron-depleted background, yielding the same orbital arrangement as for half doping within the stripes. The exact mixing of the electron- and hole-rich regions is determined by the lever rule following the exact stoichiometry of the compound, and the ordering appears incommensurate in diffraction experiments [90]. It is noteworthy that for $x = 0.5$ both models are indistinguishable and reproduce the CE-type COO ordering.

Regarding the results of the previous sections it appears very tempting to extend the “bi-stripe” picture to describe the incommensurate ordering in $\text{La}_{0.4}\text{Sr}_{1.6}\text{MnO}_4$, as in contrast to the “Wigner Crystal” this approach naturally contains the existence of stable zig-zag elements. In Fig. 4.30 we sketch a possible real-space ordering scheme for $\text{La}_{0.4}\text{Sr}_{1.6}\text{MnO}_4$, which reproduces all characteristic results of our elastic neutron scattering experiments: Compared to $\text{La}_{1/2}\text{Sr}_{3/2}\text{MnO}_4$, each fifth Mn^{3+} -ion is transformed into a Mn^{4+} -site in $\text{La}_{0.4}\text{Sr}_{1.6}\text{MnO}_4$, and a regular spacing of the additional holes along the zig-zag chains results in a stripe ordering of the excess holes oriented perpendicular to the propagation of the chains. The Mn^{4+} -stripes cut the zig-zag chains and provoke a modulation *parallel to the chains* of both the orbital and the spin ordering on the three-valent sites. Moreover, the magnetic ordering on the regular Mn^{4+} -sites is not affected, and the arrangement reproduces qualitatively the experimentally observed superstructure

reflections.³⁰ The model predicts furthermore the existence of a new type of nuclear superstructure reflection associated with the regular spacing of the stripes, which is not observed so far. However, the related structural distortions are supposed to be very small and the intensity of the corresponding Bragg reflections might be too weak to be detected in a neutron scattering experiment.

Let us inspect the ordering scheme of Fig. 4.30 in more detail. The orbital superstructure reflections are modulated longitudinally in the experiment. Therefore, the stripes must be aligned perpendicular to the propagation vector \mathbf{k}_{OO} of the orbital modulation and, hence, perpendicular to the zig-zag chains. Regarding only the orbital ordering on the Mn^{3+} -sites, two alternatives are possible, as the orbital occupation across the stripe might be either in-phase with the undistorted pattern of the CE structure, or acquires an additional phase-shift π , which is the situation shown in Fig. 4.30. However, only the second alternative results in an incommensurate modulation, as is observed in diffraction experiments – the first alternative would in contrast imply a reduction of the structure factor, but the modulation wavelength would remain commensurate. Clearly, the modulation wavelength is determined by the spatial distance between two stripes and the incommensurability ε_{OO} depends linearly on the electron concentration n_e . For $x = 0.6$ this stripe model results in an incommensurability $\varepsilon_{\text{OO}} = 0.05$, which is quite close to the experimentally observed value.

Next we consider the charge ordering. Although we have no experimental information of the evolution of the charge-order reflection \mathbf{Q}_{CO} , the magnetic reflections associated with the ordering of the Mn^{4+} -ions are not affected by the additional holes and are observed at the commensurate position $\mathbf{Q} = (\frac{1}{2} 0 0)$ [46]. This leads to the conclusion, that the commensurate modulation of the charge density persists in overdoped $\text{La}_{0.4}\text{Sr}_{1.6}\text{MnO}_4$. The commensurate ordering on the Mn^{4+} -sites also sets strict conditions for the insertion of the stripes into the CE background. In Fig. 4.30 the stripes are neighbored by two Mn^{4+} -sites. However, one might imagine more sophisticated models in which the stripe intersects a Mn^{3+} - Mn^{4+} pair – deplete one of the two Mn^{4+} -rows adjacent to each stripe in Fig. 4.30 – or the strips might include two (or even more) Mn-sites, forming a kind of double stripe. However, both scenarios violate the observed commensurate ordering on the Mn^{4+} -sites.³¹

Focusing now on the magnetic ordering of the zig-zag elements, the situation appears more tricky. The magnetic coupling between two zig-zag chains on both

³⁰It is not clear to us how an alternative approach starting from the “Wigner Crystal” model can preserve the commensurate ordering of the regular Mn^{4+} -spins, and simultaneously presume an incommensurate ordering on the Mn^{3+} -sites. However, we want to remark, that recent results of transition electron microscopy on $\text{Nd}_{1-x}\text{Ca}_{1+x}\text{MnO}_4$ and $x > 0.5$ seem to be inconsistent with the bi-stripe model [175].

³¹Nevertheless, we can not exclude a more complicated structure including the formation of “triple-stripes”, which seems, however, very unlikely.

sides of the stripes is mediated by an exchange interaction between two Mn^{4+} -species, which is weakly antiferromagnetic [32]. As in the CE pattern adjacent zig-zag chains are aligned AFM, the nearest-neighbor exchange in each plaquette at the border of the stripe is magnetically frustrated, see Fig. 4.30, and the magnetic coupling is determined by a higher-order process. Similar to the orbital sector, the magnetic ordering may remain unchanged across the stripe or acquire an additional phase shift, which is the situation depicted in Fig. 4.30. Due to the frustration the actual arrangement may consist of a fine mixing of both alternatives [90]. Therefore, the magnetic incommensurability ε_{SO} is not strictly correlated with the wavelength of the charge and orbital modulation by a rational fraction, as is found in the nickelates and cuprates [184, 185]. The influence of the magnetic frustration furthermore provides an explanation for the reduced magnetic correlation length ξ_{SO} , which is found to be much shorter than that for the orbital ordering, and for the sluggish increase of the magnetic order parameter below T_{N} .

Spin dynamics in $\text{La}_{0.4}\text{Sr}_{1.6}\text{MnO}_4$

Motivated by the discussion of the optimal-doped compound $\text{La}_{1/2}\text{Sr}_{3/2}\text{MnO}_4$ we have also investigated the magnetic excitation spectrum of $\text{La}_{0.4}\text{Sr}_{1.6}\text{MnO}_4$: How does the stripe ordering of the additional holes affect the spin-wave dispersion of the CE type?

To characterize the properties of the magnon spectrum in the stripe-ordered phase of $\text{La}_{0.4}\text{Sr}_{1.6}\text{MnO}_4$ we performed two inelastic neutron scattering experiments at the cold instrument 4F and at the thermal spectrometer 1T.1, both installed at the Orphée reactor in Saclay. To follow the magnon dispersion starting from the incommensurable Bragg positions the scattering plane included the directions [100] and [010] of the tetragonal structure in both experiments. At the cold instrument we fixed the energy of the scattered neutrons to 4.66 meV to improve the experimental resolution, whereas at the thermal spectrometer we chose $E_f = 14.7$ meV in order to gain in the neutron intensity. Typical raw-data scans are presented in Fig. 4.31 and 4.32.

Compared to the spectrum of the half-doped compound, in $\text{La}_{0.4}\text{Sr}_{1.6}\text{MnO}_4$ pronounced differences can be found in the spin-wave excitations along the direction of the zig-zag chains, Fig. 4.31. At low energies, $E < 1.0$ meV, the inelastic response is centered at the incommensurable Bragg-positions $\mathbf{Q} = (0.25 \pm \varepsilon_{\text{SO}} \ 0.25 \mp \varepsilon_{\text{SO}} \ 0)$. For slightly higher energies a strong signal develops at the commensurate position $\mathbf{Q} = (0.25 \ 0.25 \ 0)$, which upon further increase of energy is, however, rapidly suppressed. For $E \geq 5$ meV the signal close to the quarter-indexed position has finally lost its structure and the spectra are dominated by the spin-wave response propagating from the neighboring half-indexed positions towards the commensurable zone center at $\mathbf{Q} = (0.375 \ 0.125 \ 0)$.

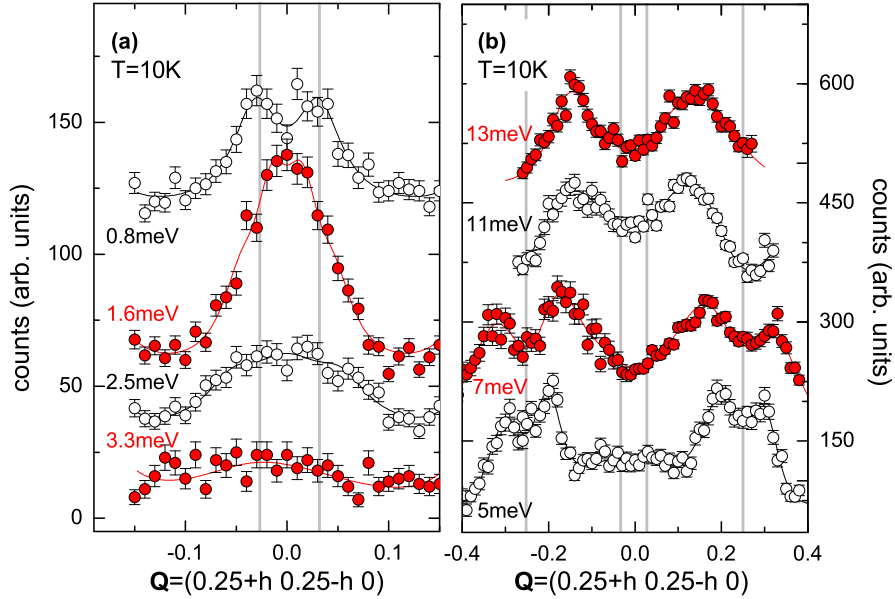


Figure 4.31: Raw-data scans at finite energies for $\text{La}_{0.4}\text{Sr}_{1.6}\text{MnO}_4$ (I.) Raw-data scans at $T = 10\text{K}$ aiming at the spin-wave dispersion in $\text{La}_{0.4}\text{Sr}_{1.6}\text{MnO}_4$ in the direction of the zig-zag chains, i. e. parallel to the magnetic incommensurability, below 4 meV (a), and at higher energies (b). Data shown in (a) are recorded at the cold instrument 4F with $E_f = 4.66\text{ meV}$, those in (b) at the thermal spectrometer 1T.1 and $E_f = 14.7\text{ meV}$. Lines represent fits to the data as described in the text, vertical gray bars mark the positions of the magnetic Bragg reflections.

The observed behavior appears well understandable by assuming different spin-wave branches with similar spin stiffness, dispersing outward from the two incommensurable Bragg positions. For $E < 5\text{ meV}$, all spectra can be accurately modeled assuming four different magnon contributions centered at $\mathbf{Q}_0 \pm \mathbf{q}(\omega)$ and $\mathbf{Q}_0 = (0.25 \pm \varepsilon_{\text{SO}} \ 0.25 \mp \varepsilon_{\text{SO}} \ 0)$. Within this picture, the strong enhancement of the inelastic structure factor at the commensurate position for $E = 1.6\text{ meV}$ corresponds to the crossing of the modes traveling in opposite directions, similar to the observations in stripe-ordered cuprates and nickelates, where a resonance appears at the inflection point of the famous hourglass dispersion [165, 195–197]. For higher energies these excitations seem to lose their structure factor and the different contributions merge into the strong magnon signal propagating from the half-indexed positions.

As the static ordering on the Mn^{4+} -sites remains commensurate we do not expect similar anomalies in the magnon frequencies associated with the half-indexed reflections. Indeed, the inelastic response around these positions exhibits a conventional behavior and the estimated magnon frequencies are comparable with the dispersion in the half-doped compound $\text{La}_{1/2}\text{Sr}_{3/2}\text{MnO}_4$ investigated in the

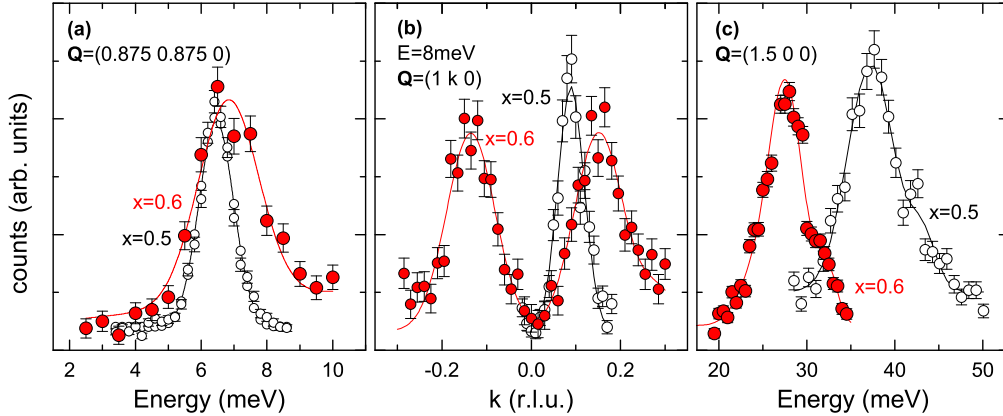


Figure 4.32: Raw-data scans at finite energies for $\text{La}_{0.4}\text{Sr}_{1.6}\text{MnO}_4$ (II.) Raw-data scans aiming at the spin-wave dispersion in $\text{La}_{0.4}\text{Sr}_{1.6}\text{MnO}_4$ perpendicular to the zig-zag chains **(b)**, and along $[100]$ **(b)** and **(c)**. Full, colored symbols mark the data for $\text{La}_{0.4}\text{Sr}_{1.6}\text{MnO}_4$, open symbols represent the optimal doped compound $\text{La}_{1/2}\text{Sr}_{3/2}\text{MnO}_4$ discussed in the previous sections. All data were recorded at the thermal instrument 1T.1 using the PG monochromator and $E_f = 14.7$ meV. Lines denote fits to the data as described in the text.

very beginning of this chapter, see below.

To further characterize the \mathbf{q} -dependence of the magnetic excitations we have studied the dispersion perpendicular to the propagation of the zig-zag chains and along the $[100]$ -direction, i.e. rotated by 45° with respect to the chains. In Fig. 4.32 we show representative examples of these data together with the corresponding scans in $\text{La}_{1/2}\text{Sr}_{3/2}\text{MnO}_4$. All scans on $\text{La}_{0.4}\text{Sr}_{1.6}\text{MnO}_4$ were geared to the structure factor calculations for the half-doped sample, see Fig. 4.8, and our observations along these two directions yield some remarkable similarities between both compounds. A typical counting time for the data shown is, depending on the energy, 1-4 min/point.

Perpendicular to the chains, path $\Gamma - \mathbf{B}$ in the notation of Fig. 4.7, the magnetic excitations are not affected by the formation of the stripes and we could easily follow the dispersion throughout the entire Brillouin zone – the energy scan at the zone-boundary $\mathbf{B} = (0.875\ 0.875\ 0)$ yields almost the same magnon frequency for $\text{La}_{0.4}\text{Sr}_{1.6}\text{MnO}_4$ as for $\text{La}_{1/2}\text{Sr}_{3/2}\text{MnO}_4$, see Fig. 4.32a. Note however, that for $x = 0.6$ the signal is slightly broadened, reflecting the finite length scale of the static correlations. For intermediate energies the structure factor calculations exhibit also a finite contribution around the integer-indexed positions, and along the line $\mathbf{Q} = (1\ q_k\ 0)$, path $\Gamma - \mathbf{A}$, we could follow the acoustic and the first optic branch throughout the entire zone. At the Γ -point we estimate an upper cut-off energy for the first magnon band of $27.5(4)$ meV.³² In this direction the magnon

³²Remember that the calculations for the half-doped compound predict an additional magnon-

frequencies are slightly renormalized compared to $\text{La}_{1/2}\text{Sr}_{3/2}\text{MnO}_4$, but the overall agreement between both compounds is still remarkable, see the comparison of the raw data in Fig. 4.32b,c.

Combining the results of different magnetic Brillouin zones we finally obtain the spin-wave dispersion of the overdoped compound $\text{La}_{0.4}\text{Sr}_{1.6}\text{MnO}_4$, which is shown in Fig. 4.33. To compare the dispersion with the half-doped compound we neglect the slight incommensurability and the complex behavior of the low-energy excitations, since these are irrelevant for the discussion of the overall properties of the \mathbf{q} -dependence of the magnetic excitations. As is already evidenced in the raw-data scans presented above, the dispersion perpendicular to the chains, i.e. path $\Gamma - \mathbf{B}$, is very similar for both compounds, and the magnon frequencies at the zone-boundary \mathbf{B} amount to 6.5(1) meV and 6.8(2) meV for $\text{La}_{1/2}\text{Sr}_{3/2}\text{MnO}_4$ and $\text{La}_{0.4}\text{Sr}_{1.6}\text{MnO}_4$, respectively. In the two other directions the magnon frequencies are softened in the overdoped compound – the upper cut-off energy at the Γ -point in the doped systems amounts to 27.5(4) meV, which has to be compared to 36.2(6) meV in the case of $\text{La}_{1/2}\text{Sr}_{3/2}\text{MnO}_4$ – but the overall shape of the dispersion is well comparable: The dispersion along the chains, path $\Gamma - \mathbf{C}$, is more pronounced and extends to higher energies than in the perpendicular direction, reflecting the dominant character of the ferromagnetic exchange J_{FM} within the zig-zag chains. The first optical band, folded back into the first Brillouin zone, connects with the acoustic branch at the zone-boundary \mathbf{C} and exhibits an upward dispersion towards the zone-center Γ , very similar to the dispersion in $\text{La}_{1/2}\text{Sr}_{3/2}\text{MnO}_4$. In the intermediate direction along $[100]$, path $\Gamma - \mathbf{A}$, the frequencies of both the acoustic and the optic branch are slightly renormalized, too, and are similar to those along the path $\Gamma - \mathbf{C}$.

In summary, besides the striking differences at very low energies the magnon dispersion of the stripe-ordered compound $\text{La}_{0.4}\text{Sr}_{1.6}\text{MnO}_4$ exhibits the same characteristic properties, a significant anisotropy in the dispersion parallel and perpendicular to the chains and a dispersive optical band, as the half-doped system $\text{La}_{1/2}\text{Sr}_{3/2}\text{MnO}_4$ with perfect CE order – there is only a slight softening of the magnon frequencies. The main result derived from the analysis of the magnetic correlations in $\text{La}_{1/2}\text{Sr}_{3/2}\text{MnO}_4$ has been the dominant character of the FM zig-zag elements, the CE ordering has to be considered as a loose coupling of stable zig-zag fragments, and together with the stripe ordering of the excess holes this approach provides also a qualitative explanation for the observed behavior in $\text{La}_{0.4}\text{Sr}_{1.6}\text{MnO}_4$.

In the stripe approach presented above the additional Mn^{4+} -sites order into regular rows aligned perpendicular to the orientation of the zig-zag chains. The stripes intersect the FM chains, but the region between two stripes remains perfectly CE ordered. The AFM correlations of adjacent zig-zag elements perpendic-

band at higher energies, which could not be observed so far.

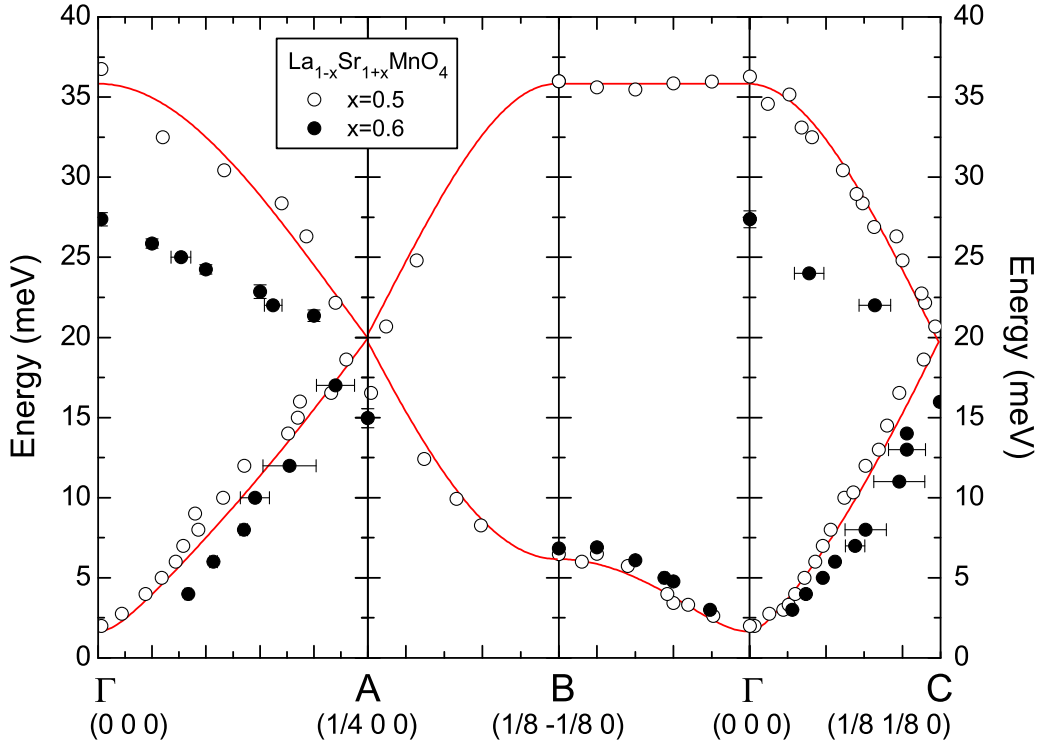


Figure 4.33: Magnon dispersion in $\text{La}_{0.4}\text{Sr}_{1.6}\text{MnO}_4$ Comparison of the dispersion of the magnetic excitations in $\text{La}_{1/2}\text{Sr}_{3/2}\text{MnO}_4$ and $\text{La}_{0.4}\text{Sr}_{1.6}\text{MnO}_4$ along the main symmetry directions $[100]$, path $\Gamma - \text{A}$, perpendicular and parallel to the propagation of the zig-zag chains, paths $\Gamma - \text{B}$ and $\Gamma - \text{C}$, respectively. Full circles denote the data for $\text{La}_{0.4}\text{Sr}_{1.6}\text{MnO}_4$, open symbols those of $\text{La}_{1/2}\text{Sr}_{3/2}\text{MnO}_4$ already presented in Fig. 4.7. Small red lines give the fit of the dispersion in the half-doped compound as discussed in the beginning of this chapter.

ular to the chains are not altered, and hence it appears plausible that along this direction the magnon dispersion in $\text{La}_{0.4}\text{Sr}_{1.6}\text{MnO}_4$ is directly comparable to that in $\text{La}_{1/2}\text{Sr}_{3/2}\text{MnO}_4$, as is observed.

In contrast, the alignment of the stripes affects the magnetic correlations within the zig-zag chains. Consequently, the spin dynamics is altered and the low-energy part of the dispersion is considerably changed: For low energies we find different magnon signals propagating outward from the incommensurable magnetic Bragg positions and a significant enhancement of the magnetic structure factor at the intersection point of the different branches. However, for higher energies well above this “resonance” the magnon dispersion resembles again the properties of the pure CE ordering – with increasing \mathbf{q} the magnetic fluctuations are more sensitive to the short-range correlations, and hence probe especially the magnetic coupling within the zig-zag fragments.

In conclusion, our results of the elastic and inelastic neutron scattering exper-

iments reveal that both the orbital and the magnetic ordering in the overdoped compound $\text{La}_{0.4}\text{Sr}_{1.6}\text{MnO}_4$ is incommensurate. The static correlations might be understood by a regular arrangement of the additional holes into stripes aligned perpendicular to the propagation of the FM zig-zag chains in the CE arrangement. The ordering between two stripes is similar to the half-doped compound and the magnon dispersion of both systems is remarkably similar, highlighting once more the dominant character of the FM intrachain coupling and the stability of the zig-zag fragments.

4.3.3 Magneto-orbital phase diagram

To close this chapter we summarize the above results and construct the magneto-orbital phase diagram of the single-layered manganites $\text{La}_{1-x}\text{Sr}_{1+x}\text{MnO}_4$ around half doping, which is shown in Fig. 4.34. The basic structural, electronic and magnetic properties of the phase diagram of the $\text{La}_{1-x}\text{Sr}_{1+x}\text{MnO}_4$ -series have already been elaborated in former publications [7, 43, 46] and [senff05a], but our systematic neutron scattering investigation presented in this chapter extends, and partly corrects the published results. For completeness, we have also included the low-doping regime in the phase-diagram Fig. 4.34, which is characterized by a preferred occupation of the out-of-plane $3d_{3z^2-z^2}$ orbitals and an antiferromagnetic ordering as discussed in detail in Chap. 3.

At half doping, $x = 0.5$, the ground state is characterized by the commensurate ordering of charge, spin and orbital degrees of freedom according to the classical CE-type picture. However, the neutron scattering results have revealed, that this state competes with short-range isotropic correlations: The charge and orbital disordered phase above $T_{\text{CO}}^{0.5} = 229$ K is characterized by isotropic FM correlations within the MnO_2 layers. Below the COO transition at T_{CO} , these correlations are suppressed by and transformed into anisotropic AFM correlations of the CE type, and they finally disappear close to the transition into the long-range ordered CE state at $T_{\text{N}}^{0.5} = 110$ K.

Electron doping destabilizes the charge and orbital ordered state, and for $x = 0.4$ both the COO and the magnetic correlations are finite. Above the COO transition at $T_{\text{CO}}^{0.4} = 210$ K short-range isotropic FM correlations exist as well, but in contrast to the optimal doped systems these are no longer suppressed by the onset of the CE-type correlations and persist down to lowest temperatures. The ground state in the underdoped regime is no longer homogenous, but phase separated on a microscopic scale into regions with nearly perfect CE order and regions with loose FM correlations.

In contrast, the charge and orbital ordered state is quite robust against the doping of additional holes, and the overall behavior for $x = 0.6$ is very similar to the case of half doping. The excess holes localize in a regular arrangement and form electron-poor stripes aligned perpendicular to the characteristic zig-zag

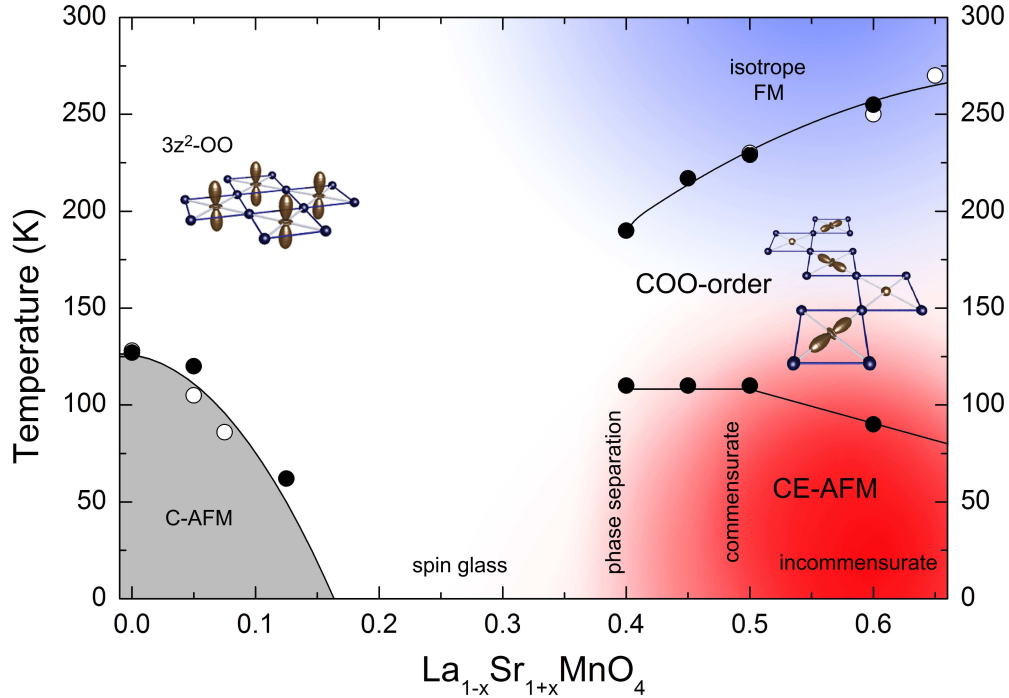


Figure 4.34: Revised phase diagram of single-layered $\text{La}_{1-x}\text{Sr}_{1+x}\text{MnO}_4$ Magneto-orbital phase diagram of the single-layered manganites $\text{La}_{1-x}\text{Sr}_{1+x}\text{MnO}_4$ including the results of this chapter (full circles) and from the literature [7] (open circles).

chains of the CE structure. The ordering pattern for $x > 0.6$ is incommensurate with the tetragonal crystallographic lattice, and around half doping the phase diagram of single layered $\text{La}_{1-x}\text{Sr}_{1+x}\text{MnO}_4$ resembles the main features of the three-dimensional perovskites.

4.4 Conclusions

We analyzed the static and dynamic magnetic properties of the charge, orbital and magnetic ordered state observed in $\text{La}_{1-x}\text{Sr}_{1+x}\text{MnO}_4$ around half doping. The ordered state is generic for very different types of manganites, but although predicted more than 50 years ago, the exact nature of the ground state is still discussed controversially today.

The determined spin-wave dispersion of the optimal-doped compound $\text{La}_{1/2}\text{Sr}_{3/2}\text{MnO}_4$ is in excellent agreement with model calculations based on the classical CE-type arrangement proposed by Goodenough [8], and rejects a recent alternative picture for the charge- and orbital-ordered state consisting of magnetically coupled dimers [9]. The \mathbf{q} -dependence of the magnetic excitations exhibits

an anisotropic character with a steep dispersion parallel to the FM zig-zag chains, and the dispersion is only weak in the perpendicular direction, reflecting the different energy scales of the FM and AFM exchange interactions within and between the zig-zag elements. In conclusion, the CE-ordered state has to be considered as a weak antiferromagnetic ordering of strongly coupled ferromagnetic chains.

The difference of the intra- and interchain coupling also governs the thermal evolution of the magnetic ordering, which is discussed subsequently to the spin-dynamics. The long-range magnetic ordering of the CE type melts at the Néel transition, but static short-range correlations persist well above T_N . These correlations are connected with the existence of FM zig-zag elements above T_N , and for $T_N < T < T_{CO}$ the system has to be considered as an electronically smectic-like crystal of one-dimensional zig-zag fragments. The Néel transition at T_N must be regarded as the long-range AFM ordering of already existing FM-ordered zig-zag elements. Furthermore we show, that for $T_N < T < T_{CO}$ the CE-type ordering closely competes with FM correlations. The disordered state above T_{CO} is characterized by isotropic short-range FM correlations, which coexist and compete with the AFM correlations of the CE type below T_{CO} , and are finally suppressed at T_N . The simultaneous existence of AFM CE type and FM correlations is very remarkable, as the competition of these two states is considered as the key for a quantitative understanding of the CMR-effect in perovskite manganites.

The competition of the AFM CE type and the isotropic FM correlations can be considerably manipulated by electron doping. In the doped compound $\text{La}_{0.6}\text{Sr}_{1.4}\text{MnO}_4$ the CE-type correlations are significantly weakened and the ordering is only of finite dimensions. Concomitantly, the isotropic FM correlations existing above T_{CO} are no longer suppressed completely by the onset of the CE-type correlations, but persist down to lowest temperatures, and the magnetic ground state of $\text{La}_{0.6}\text{Sr}_{1.4}\text{MnO}_4$ consists of a heterogenous mixture of CE and FM regions coexisting on a microscopic scale at low temperatures.

On the contrary, the CE state is stable against the doping with additional holes. Both, the orbital and the magnetic ordering is incommensurate in $\text{La}_{0.4}\text{Sr}_{1.6}\text{MnO}_4$, which due to similarities with observations in cuprates and nickelates is understood by a stripe-like ordering of the excess holes perpendicular to the orientation of the zig-zag chains. We studied the full magnon dispersion in the overdoped compound, but besides a complex behavior at low energies the excitation spectrum is well comparable with the optimal doped compound $\text{La}_{1/2}\text{Sr}_{3/2}\text{MnO}_4$, and the phase diagram of the single-layered manganites $\text{La}_{1-x}\text{Sr}_{1+x}\text{MnO}_4$ exhibits the same asymmetric behavior with respect to half doping as has been observed in the three-dimensional perovskite systems, rendering the different response to electron or hole doping a fundamental property of the charge and orbital ordered state.

5 Magnetic excitations in multiferroic TbMnO₃

TbMnO₃ is the prototype of a recently discovered novel class of magnetic and simultaneously ferroelectric materials, in which the ferroelectric (FE) properties are intimately coupled to the magnetic degrees of freedom resulting in gigantic magnetoelectric effects. In conventional ferroelectrics, a detailed knowledge of the dynamics of the system is usually of great importance, as one of the transverse optical phonons softens towards the phase transition and condenses according to the Lyddane-Sachs-Teller relation [198]. As in the magnetic ferroelectrics the ferroelectric phase is closely correlated with the magnetic degrees of freedom, these modes are no longer of pure phononic origin, but are proposed to possess a magnetic component as well, forming a new type of quasiparticle: strongly hybridized magnon-phonon excitations, referred to today as electromagnons [199, 200]. Hence, a comprehensive experimental and theoretical understanding of the dynamic magnetic correlations of TbMnO₃ seems very desirable in favor of a fundamental understanding of the coupling between magnetism and ferroelectricity and of the possibility of tuning these systems towards new technological applications.

The magnetoelectric effect (ME), the induction of magnetization by an electric field or of polarization by a magnetic field, has been predicted by P. Curie at the end of the 19th century and has been experimentally confirmed in Cr₂O₃ in the 1960s [201, 202]. Technical applications were, however, hampered by the restricted number of systems and of the weakness of the effect: Expanding the free energy in powers of the electric polarization \mathbf{P} and of the magnetization \mathbf{M} , the magnetoelectric effect is in leading order given by the tensor α_{ij} , which linearly couples \mathbf{P} to an applied magnetic field \mathbf{H} and \mathbf{M} to an electric field \mathbf{E} .¹ With conventional materials typical values for α_{ij} of the order of 10 ps m⁻¹ can be achieved, which corresponds to the magnetization obtained by the reversal of one out of 10⁵ spins in an electric field of 10⁶ V cm⁻¹ [201]. Furthermore, it can be shown that the ME response is limited by the product of the magnetic and

¹To be more precise, the expansion of the free energy also contains higher-rank tensors coupling electric and magnetic field. However, the contribution of these terms is very small and it is common practice to refer to the linear coupling as *the* magnetoelectric effect.

electric susceptibilities [203]:

$$\alpha_{ij}^2 < \chi_{ii}^{\text{elec}} \chi_{jj}^{\text{mag}}. \quad (5.1)$$

The strongest ME response is, therefore, to be expected for systems with large electric *and* magnetic susceptibility, hence systems with simultaneous ferroelectric and (anti-)ferromagnetic order, which in the following we refer to as multiferroic.² However, symmetry arguments require strict conditions for the coexistence of ferroelectric and magnetic order as both time and spatial inversion invariance have to be broken, and multiferroicity has been considered as a very rare phenomenon in the past [201, 205, 206]. Indeed, until five years ago only a couple of multiferroic systems were known, like e. g. BiFeO₃ or some hexagonal manganites RMnO₃ with small rare earth ions R=Sc, In,...,Lu [207–209]. In all of these compounds, however, the transition temperatures of the ferroelectric and the magnetic ordering, $T_{FE} \simeq 1000$ K and $T_{SO} \simeq 100$ K respectively, typically differ by an order of magnitude, and a macroscopic ME response is, if existent at all, very small [11].

It has been recognized only recently [12, 13, 210], that certain types of *incommensurable* magnetic structures may induce ferroelectricity leading to sizable magnetoelectric effects and the possibility to switch the electric polarization by an applied magnetic field and vice versa, which seems very advantageous in the light of possible technical applications. In the last few years multiferroicity has indeed been found in a variety of different incommensurable magnets such as perovskite manganites RMnO₃ with R=Gd, Tb and Dy [6, 211, 212], RMn₂O₅ with R=Tb, Ho and Dy [213, 214], spinel chromates CoCr₂O₄ [215], vanadates Ni₂V₂O₃ [216], spin-chain cuprates LiCu₂O₂ [217, 218], delafossite CuFeO₂ [219], and huebnerite MnWO₄ [220, 221].

In this emerging field of incommensurable multiferroics TbMnO₃ serves as a model system, partly due to fundamental, partly due to more practical reasons. The polarization in TbMnO₃ is one of the largest for this class of materials, ME effects are very pronounced and the transition temperatures are relatively high [6, 212]. Furthermore, large single crystals of high quality can easily be grown and TbMnO₃ does not suffer from strong neutron absorption, so that reliable data sets on the magnetic structure are available [222, 223].

In this chapter we report on the magnetic excitations of multiferroic TbMnO₃. The chapter is organized as follows: First, we summarize the main physical properties of TbMnO₃ and introduce the basic theoretical concepts behind the magnetoelectric coupling in this system. The discussion of the experimental results starts with a comprehensive analysis of the zone-center modes in the FE phase,

²According to the original definition by Schmid [204], a crystal is called multiferroic when two or more of the primary ferroic properties are united in the same phase. However, it is practical to treat this definition in a less strict sense and to include antiferromagnetic phases as well.

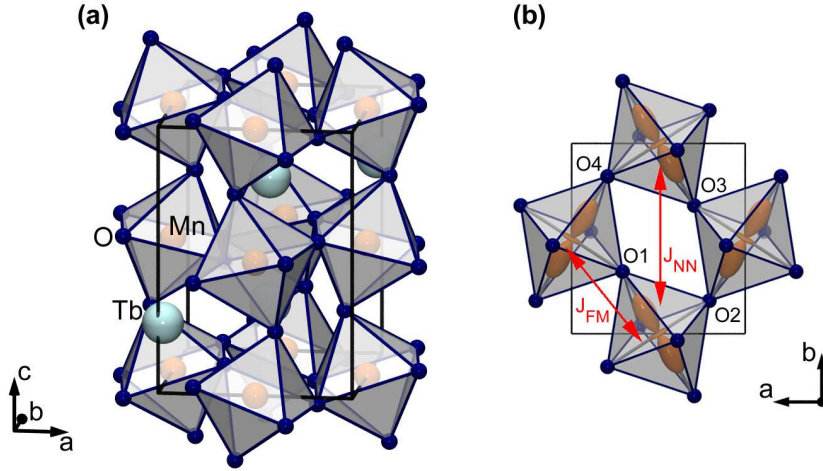


Figure 5.1: Crystal structure of TbMnO_3 Orthorhombic perovskite structure of TbMnO_3 of space-group symmetry $Pbnm$ (a). Sketch of the ab -plane of the $Pbnm$ -structure showing the staggered ordering of the single-occupied Mn e_g -orbitals in rare-earth manganites RMnO_3 and the relevant magnetic exchange paths, the FM nearest-neighbor coupling J_{FM} along the bonds and the AFM next-nearest neighbor exchange J_{NN} via the bridging oxygen sites $O1$ and $O3$ along b (b). A similar exchange along a is excluded due to the underlying orbital lattice and the large distance between $O2$ and $O4$.

which turn out to be most relevant for the observed ferroelectricity and the magnetoelectric coupling. Subsequently, we study the temperature dependence of the spectrum across the ferroelectric transition and present the zone-center excitations in the paraelectric phase. The discussion of the zone-center modes is finally closed by the analysis of the magnetic-field dependence of the magnon spectrum. Subsequently, we focus on the \mathbf{q} -dependence of the magnetic excitations and study the spin-wave dispersion along the main symmetry directions in the ferro- and in the paraelectric phase, and discuss the strength of the relevant magnetic exchange interactions.

The main results on the excitation spectrum of TbMnO_3 presented in this chapter are published in [senff07a] and [senff07d].

5.1 Basic properties and multiferroicity in TbMnO_3

TbMnO_3 crystallizes in the orthorhombic symmetry of space group $Pbnm$ with room temperature lattice constants $a = 5.302 \text{ \AA}$, $b = 5.857 \text{ \AA}$ and $c = 7.402 \text{ \AA}$ [224, 225], see Fig. 5.1. Comparing with the isostructural parent compound of the

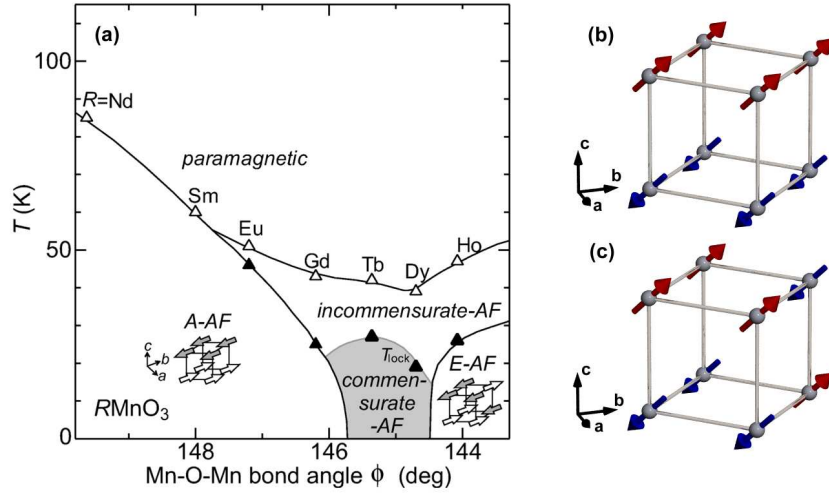


Figure 5.2: Phase diagram of the rare-earth manganites $RMnO_3$ Magnetic phase diagram of the rare-earth manganites after Kimura et al. [228]. For large rare-earth ions the A -type and for small the E -type ordering is stabilized. In the gray-shaded region in-between for $R=Tb$ and Dy an incommensurable (although falsely depicted here as commensurable) region develops as the ground state (a). Sketch of the ordering of the Mn-moments in the A -type (b) and the E -type ordering (c) as being realized in the end members $LaMnO_3$ and $HoMnO_3$, respectively.

CMR-manganites $LaMnO_3$ the reduction of the ionic radius on the rare-earth site, 1.040 Å for eightfold coordinated Tb^{3+} and 1.160 Å for La^{3+} [226], results in an enhancement of the typical $GdFeO_3$ distortions, which, together with the stable staggered ordering of the $d_{3x^2-r^2}/d_{3y^2-r^2}$ -orbitals [227], determine the magnetic ground state in the series of isovalent rare-earth manganites $RMnO_3$ [228, 229].

With an increasing rotation of the MnO_6 -octahedra for smaller rare-earth ions the $Mn-O-Mn$ bond angle and, consequently, the FM exchange J_{FM} between nearest neighbors within the ab -planes reduces, while an additional AFM exchange path between next-nearest Mn-sites arises along b : The enhancement of the cooperative rotation of the MnO_6 -octahedra around the c -axis decreases the distance between the two oxygen sites $O1$ and $O3$ (referring to the notation in Fig. 5.1b) and allows for a significant exchange interaction J_{NN} between next-nearest Mn-sites along $[010]$. Simultaneously, the distance between $O2$ and $O4$ increases and suppresses a similar interaction along $[100]$ [228].³ The competition of J_{FM} with J_{NN} subsequently destabilizes the ferromagnetic coupling within the ab -planes, and the famous A -type ordering of $LaMnO_3$ finally transforms for $|J_{NN}| > |J_{FM}|$ into the E -type ordering with an AFM correlation of the Mn-moments along $[010]$ and an “up-up-down-down” configuration along the bonds

³For $TbMnO_3$ a structural refinement yields $d_{O1-O3}=3.0994$ Å and $d_{O2-O4}=4.9792$ Å at room temperature [224].

for orthorhombic $HoMnO_3$, the end member of the isostructural perovskite manganites, see Fig. 5.2 [230].⁴

In the regime $|J_{NN}| \lesssim |J_{FM}|$ the magnetic system is heavily frustrated, and in-between the two commensurable ground states, the A -type with magnetic propagation vector $\mathbf{k}_A = (0\ 0\ 0)$ and the E -type with $\mathbf{k}_E = (0\ \frac{1}{2}\ 0)$ ⁵, an incommensurable magnetic ordering with modulation $\mathbf{k}_{Mn} = (0\ \varepsilon_b\ 0)$ and $0 < \varepsilon_b < \frac{1}{2}$ is observed for $TbMnO_3$ and $DyMnO_3$ [228]. As we will discuss in the following paragraphs, this incommensurable magnetic ordering generates the observed ferroelectric polarization and drives the gigantic ME effects.

5.1.1 Magnetoelectric effect in $TbMnO_3$

The incommensurable magnetic structure of $TbMnO_3$ has first been investigated in an early work by Quezel et al. [231]. The network of Mn-spins undergoes at the Néel temperature $T_N = 42\text{ K}$ a transition into an incommensurable ordered phase with modulation vector $\mathbf{k}_{Mn} = (0\ \varepsilon_b\ 0)$ and, depending on temperature, $\varepsilon_b \approx 0.28$. This phase is regarded as a sinusoidal modulation with the Mn-moments aligned collinear along the \mathbf{b} -axis. Further anomalies in the magnetic susceptibility at $T_{Tb} = 7\text{ K}$ and $T_{FE} = 28\text{ K}$ are attributed to the ordering of the Tb-spins and to a second magnetic transition in the Mn-sublattice, respectively [231].

In a more recent work, this second Mn-transition at T_{FE} has been interpreted as a “lock-in” transition of the modulation vector into the constant, but still incommensurable value $\varepsilon_b = 0.275$. Furthermore, together with the magnetic superstructure weak lattice modulations appear in diffraction experiments below T_{FE} with a propagation vector \mathbf{k}_L twice that of the magnetic ordering, $\mathbf{k}_L = 2\mathbf{k}_{Mn}$, which are understood as second harmonics to the magnetic ordering pointing to a close coupling of the lattice to the magnetic subsystem via exchange striction [6, 211, 232]. Associated with the appearance of the structural modulations the onset of a spontaneous electric polarization \mathbf{P}_c parallel to the orthorhombic \mathbf{c} -axis is observed at T_{FE} . The value of the polarization of $P_c = 0.08\ \mu\text{C}/\text{cm}^2$ at 10 K [6] is small compared to conventional ferroelectrics as $BaTiO_3$ with $P = 26\ \mu\text{C}/\text{cm}^2$ [233], but typical for so called improper ferroelectrics, in which the ferroelectric order appears as a secondary effect [234].

As in $TbMnO_3$ the lattice modulation itself seems to be closely related to a modulation of the magnetic subsystem, a strong correlation between the electric polarization and the magnetization might be expected. Indeed, Kimura et al. report on a drastic impact of an applied magnetic field on the ferroelectric properties and gigantic ME effects [6]: A magnetic field applied parallel to the

⁴For smaller rare earth ions as e. g. Er the orthorhombic structure is unstable and crystals grown under ambient conditions have hexagonal symmetry.

⁵Throughout this chapter we refer to the standard orthorhombic setting of the $Pbnm$ -structure to index vectors of reciprocal space.

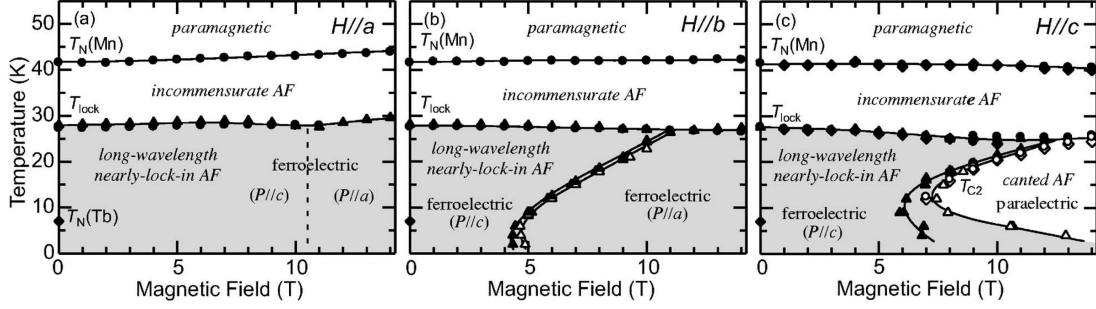


Figure 5.3: Magneto-electric phase diagram of TbMnO_3 for magnetic fields along the \mathbf{a} - (a), \mathbf{b} - (b) and \mathbf{c} -axis (c). Gray regions indicate ferroelectric phases. Taken from [212].

\mathbf{a} - or the \mathbf{b} -axis flops the electric polarization by 90° from \mathbf{c} to \mathbf{a} as \mathbf{P}_c is completely suppressed and \mathbf{P}_a emerges spontaneously above the critical field exceeding a value of $P_a \approx 0.04 \mu\text{C}/\text{cm}^2$ at 10 K and $H_b = 9$ T. It is this ability to switch the electric polarization in TbMnO_3 by an applied magnetic field which has triggered the huge amount of work in this field in the last years, and which renders the new multiferroic systems so interesting for possible technical applications. In contrast, a magnetic field applied along \mathbf{c} again suppresses \mathbf{P}_c , but the high-field state is paraelectric as no finite polarization is observed above the critical field H_c [212]. A summary of the complete magneto-electric phase diagram of TbMnO_3 is given in Fig. 5.3.

We note, that similar phase diagrams have been reported for the closely related rare-earth manganites DyMnO_3 and GdMnO_3 [212, 235]. In the later compound the magnetic ground state is supposed to be commensurate and of the A -type, but an electric polarization can easily be induced by applying small magnetic fields.

5.1.2 Spiral ordering in TbMnO_3

An important step towards the understanding of the ME phenomena observed in TbMnO_3 has been the theoretical prediction of the induction of an electric polarization by certain types of magnetic spiral ordering [12, 13, 210] and the simultaneous experimental observation of such a spiral in TbMnO_3 [222, 223].

Based on the broken invariance of both time and spatial inversion symmetry in a multiferroic system, it can be shown [13], that the polarization \mathbf{P} induced by a magnetization \mathbf{M} for an orthorhombic lattice has to be of the form

$$\mathbf{P} \propto [(\mathbf{M} \cdot \nabla)\mathbf{M} - \mathbf{M}(\nabla \cdot \mathbf{M})]. \quad (5.2)$$

Considering a spatially varying magnetization \mathbf{M} with the moments rotating in a plane spanned by \mathbf{b} and \mathbf{c} around a third axis \mathbf{a} ,

$$\mathbf{M} = M_b \hat{\mathbf{b}} \cos(\mathbf{k} \cdot \mathbf{x}) + M_c \hat{\mathbf{c}} \sin(\mathbf{k} \cdot \mathbf{x}) + M_a \hat{\mathbf{a}}, \quad (5.3)$$

the resulting electric polarization is calculated to obey the fundamental equation

$$\langle \mathbf{P} \rangle \propto M_b M_c \cdot \mathbf{k} \times \hat{\mathbf{a}}. \quad (5.4)$$

Hence, the electric polarization induced by a spin modulation of the form given by eq. 5.3 is determined by the vector product between the propagation vector \mathbf{k} and the unit vector $\hat{\mathbf{a}}$ characterizing the rotation of the ordered moments in the incommensurable structure [13]. Eq. 5.4 obviously implicates, that a collinear sinusoidal structure can not account for the finite electric polarization observed in TbMnO₃, as might have been guessed since such a structure does not break spatial inversion symmetry. For non-collinear ordering schemes the induction of a finite polarization depends on the relative orientation of \mathbf{k} and $\hat{\mathbf{a}}$: with $\mathbf{k} \parallel \mathbf{b}$ and the rotation of the moments around \mathbf{a} , the central equation 5.4 predicts a finite polarization along \mathbf{c} , as is observed in TbMnO₃.

Within this phenomenological argumentation the observed polarization can be predicted qualitatively correct, but the underlying microscopic mechanism responsible for the coupling of the lattice to the magnetic modulation can not be explained. At present, different theoretical alternatives can be found in the literature, which, however, both are based on the Dzyaloshinsky-Moriya interaction (DMI) [236, 237]: On the one side the DMI is proposed to induce a polarization of the electronic orbits without the involvement of the lattices degrees of freedom [12, 238, 239], whereas in a second approach the DMI induces a FE lattice displacement and helps to stabilize the helical magnetic structure [210].

The above interpretation is strongly supported by the results of neutron diffraction experiments published nearly simultaneously with the theoretical considerations on the spiral structures. Refining more than 900 first-order magnetic Bragg reflections above and below the FE transition, Kenzelmann et al. show that the transition from the para- into the ferroelectric phase in TbMnO₃ coincides with a rearrangement of the magnetic structure as predicted by eq. 5.4 [222]. At $T = 35$ K, i. e. in the AFM but paraelectric phase, the magnetization \mathbf{M} of the Mn-sublattice can be refined as a longitudinal sinusoidal modulation of the form

$$M_b^{\text{SDW}} = M_{b,0} \cdot \cos(\mathbf{k}_{\text{Mn}} \mathbf{x}), \quad (5.5)$$

with $M_a^{\text{SDW}} = M_c^{\text{SDW}} \equiv 0$, $M_{b,0}^{\text{SDW}} = 2.90 \mu_B$ and $\mathbf{k}_{\text{Mn}} \parallel \mathbf{b}$, see Fig. 5.4a. Within the ferroelectric phase at $T = 15$ K the Mn-spins order instead in a spiral structure with the moments confined to the \mathbf{bc} -plane and rotating around \mathbf{a} , see Fig. 5.4b, describable by

$$\begin{aligned} M_b^{\text{FE}} &= M_{b,0}^{\text{FE}} \cdot \cos(\mathbf{k}_{\text{Mn}} \mathbf{x} + \delta_b) \text{ and} \\ M_c^{\text{FE}} &= M_{c,0}^{\text{FE}} \cdot \sin(\mathbf{k}_{\text{Mn}} \mathbf{x} + \delta_c), \end{aligned} \quad (5.6)$$

where $M_a^{\text{FE}} \equiv 0$, $M_{b,0}^{\text{FE}} = 3.9 \mu_B$ and $M_{c,0}^{\text{FE}} = 2.8 \mu_B$, i. e. an elliptical spiral with the long axis of the ellipse close to \mathbf{b} . The phases δ_i could not be resolved in

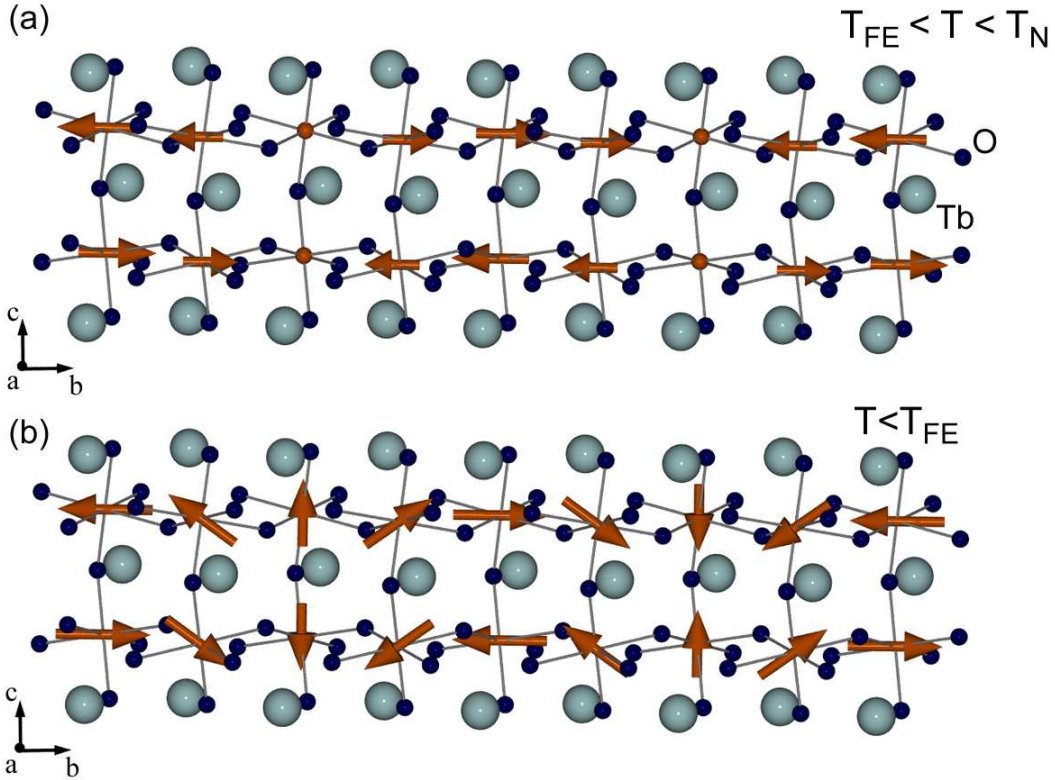


Figure 5.4: Magnetic structure of TbMnO_3 Collinear magnetic ordering in the bc -plane of TbMnO_3 for $T_{\text{FE}} < T < T_{\text{N}}$ with the modulation vector set to $\mathbf{k}_{\text{Mn}} = (00.250)$ for simplicity (a). Elliptic spiral ordering of the Mn-subsystem in the FE regime according to eq. 5.6 with the moments confined to the bc -plane and the spin-rotation axis parallel to \mathbf{a} . The phases δ_b and δ_c are arbitrarily set to 0 and $\frac{\pi}{2}$, respectively (b). As in the A-type ordering the magnetic correlations are ferromagnetic along \mathbf{a} (not shown) and always antiferromagnetic along \mathbf{c} .

the experiment. At $T = 15$ K, also the Tb-subsystem adapts already a sizeable magnetization, probably as a consequence of the exchange field from the Mn ordering [222]. The Tb-system itself orders at $T_{\text{Tb}} = 7$ K with a propagation vector $\mathbf{k}_{\text{Tb}} = (00.420)$ and the Tb-moments probably aligned parallel to \mathbf{a} [222, 232].

At this point we have to mention a problem of nomenclature, as the magnetic structure in the ferroelectric phase described by eq. 5.6 is not a classical spiral, but a cycloid. The main difference between both geometrical objects concerns the chirality. In a strict sense, only the spiral possesses a well defined chirality – a screw might be either left- or right-handed – whereas the helicity for a cycloid is not well defined – obviously, it is impossible to construct a right-handed cycloid. However, it is common practice in the actual literature to refer to the magnetic structure of TbMnO_3 as a spiral, or sometimes conical spiral, and a “chirality” is often adopted

to describe the direction of the rotation axis in the cycloid structure. We will follow this convention for the rest of the discussion, but comment on the actual situation whenever the misuse of the terminology might cause a misunderstanding.

Returning to the magnetic order, the above argumentation is further supported by a work on substituted $\text{Tb}_{1-x}\text{Dy}_x\text{MnO}_3$ [223], as for a well chosen Dy-substitution $x = 0.59$ with $T_N = 41$ K and $T_{\text{FE}} = 22$ K the modulation $\varepsilon_b \simeq \frac{1}{3}$ is commensurate and temperature independent, therefore definitively excluding a simple “lock-in” scenario for TbMnO_3 . Furthermore, the authors again find a reorientation of the spin structure at T_{FE} from a collinear to a spiral structure similar to pure TbMnO_3 . The observed sequence of magnetic transitions from the paramagnetic into the paraelectric sinusoidal SDW phase at T_N and subsequently into the ferroelectric spiral phase at $T_{\text{FE}} < T_N$ is a consequence of the magnetic anisotropy. While for an isotropic system the ground state is a (circular) spiral, an anisotropic system is expected to undergo a transition to the sinusoidal state with \mathbf{M} along the easy axis first, before at lower temperatures an (elliptical) spiral is stabilized [13, 240]. Finally, the close interplay between the spiral ordering and the electric polarization in TbMnO_3 has been revealed by Yamasaki et al. in a polarized neutron diffraction experiment [241]: “The helicity of the magnetic structure can be controlled by an applied electric field and the cycloid is inverted from a counterclockwise to a clockwise rotation by the inversion of the field”.⁶

Polarization flop in magnetic fields To handle the observed strong ME effects in TbMnO_3 , obviously the impact of a magnetic field on the spiral structure has to be considered.

In weak magnetic fields the spins rotate in the easy plane (\mathbf{bc}) and, consequently, with $\mathbf{k}_{\text{Mn}} \parallel \mathbf{b}$ the polarization is induced along \mathbf{c} . A strong field will flop the spiral, so that the rotation axis of the spins is aligned parallel to the field and the spiral is conical [240]. However, the simple adaption of this argument to the case of TbMnO_3 does not reproduce the observed phase diagram: With the field applied parallel to \mathbf{b} , the spiral should be forced into the \mathbf{ac} -plane and according to eq. 5.4 this flop of the spiral should suppress the electric polarization. Instead, for this configuration the polarization in TbMnO_3 is observed to be finite and flopped by 90° from \mathbf{c} to \mathbf{a} , see Fig. 5.3, suggesting the spins to rotate around \mathbf{c} as \mathbf{k}_{Mn} stays along \mathbf{b} in the high-field phase [242, 243].

However, the observed magnetoelectric phase diagram can qualitatively be reproduced phenomenologically taking into account the complex behavior of the rare-earth spins [13], which exhibit a complex response to an applied field show-

⁶As aforementioned, a helicity is not well defined in TbMnO_3 . We think, the experiment by Yamasaki et al. has to be interpreted as selecting a structure with modulation vector \mathbf{k}_{Mn} against the $-\mathbf{k}_{\text{Mn}}$ modulation by applying an electrical field, which is nevertheless a very interesting result and consistent with the mechanism proposed by Katsura et al. [12].

ing several metamagnetic transitions [231]. The important influence of the Tb-subsystem on the multiferroic properties in TbMnO₃ has furthermore been demonstrated by experiments on substituted rare-earth manganites: The partial substitution of Tb by Gd can flop the electric polarization from \mathbf{c} to \mathbf{a} even without applying an external field [244]. Completely replacing the magnetic Tb-ions by a mixture of Eu and Y with quenched $4f$ -magnetic moments but similar ionic radii, the ground state is shown to be ferroelectric with $\mathbf{P} \parallel \mathbf{a}$ and flops under an applied field to $\mathbf{P} \parallel \mathbf{c}$, just opposite to the observations in TbMnO₃ [245, 246]. Moreover, in the related compound DyMnO₃ the onset of the Dy-spin ordering is shown to enhance the electric polarization by more than a factor of 2, providing the most impressive example of the strong influence of the magnetism on the rare-earth side on the FE phenomena [247, 248].

To resume today's understanding of the multiferroic properties of TbMnO₃, the zero-field regime of the magnetoelectric phase diagram of TbMnO₃ is qualitatively well understood and the emergence of the ferroelectric phase is correlated with a reorientation in the magnetic subsystem from a collinear into a spiral structure.⁷ The gigantic ME effects in strong magnetic fields may originate in a flop of the rotation axis of this spiral under an applied magnetic field, which seems evident but remains to be confirmed by experiments in the case of TbMnO₃.⁸

5.2 Spin-wave spectrum at the magnetic zone center

The experiments on the magnetic excitation spectrum in TbMnO₃ presented in this chapter have been performed on the thermal spectrometers PUMA and 1T.1 installed at the FRM II in Munich and at the Laboratoire Léon Brillouin (LLB) in Saclay, respectively, and at the cold spectrometers PANDA at the FRM II, 4F.2 at the LLB and IN14 at the ILL in Grenoble.

The large single crystal of volume 1 cm³ used for our studies has been grown in the group of D. Argyriou at the HMI in Berlin using the floating zone technique. The high quality of our specimen has been verified using neutron and x-ray diffraction, as well as susceptibility measurements yielding transition temperatures of $T_N = 42.3$ K and $T_{\text{spiral}} = 27.9$ K, in good agreement with the literature.

In all experiments on the cold spectrometers the sample was mounted with the scattering plane defined by the directions [0 1 0] and [0 0 1] of the orthorhombic crystal structure. Only to study the magnetic dispersion in the [1 0 0] direction at the PUMA spectrometer a peculiar mounting was used with the direction [0 4 2]

⁷To stress the magnetic character of the FE transition we will refer to the FE transition temperature as T_{spiral} instead of T_{FE} in the following.

⁸For Eu_{0.75}Y_{0.25}MnO₃ the flop of the magnetic spiral has recently been confirmed [10].

vertical to the scattering plane, so that reflections of the type ($h0.281$) were easily accessible without tilting the scattering plane too much.

Typically, at the cold spectrometers the energy of the analyzed neutrons was fixed to 4.66 meV, corresponding to $k_f = 1.50 \text{ \AA}^{-1}$, but to increase the experimental resolution some scans were repeated with the final energy fixed to 2.98 meV ($k_f = 1.20 \text{ \AA}^{-1}$). In order to suppress higher-order contaminations a nitrogen-cooled Be-filter was installed in the neutron's pathway behind the sample. At the experiments at the thermal spectrometers we usually worked in the constant k_f -mode and the energy on the analyzer side set to 8.04 meV ($\hat{=} 1.97 \text{ \AA}^{-1}$) or 14.7 meV ($\hat{=} 2.662 \text{ \AA}^{-1}$). Due to technical problems with the PUMA spectrometer some scans, however, had to be performed with the initial energy of the neutrons held fixed to $E_i = 14.7 \text{ meV}$ and the variation of E_f was used to determine the energy transfer. At the thermal spectrometers we always used a PG filter to avoid spurious contributions by second harmonic neutrons. In all experiments the collimation of the neutron divergence was relaxed as much as possible to take full advantage of focusing effects and to increase the neutron flux on the sample.

Experiments using polarized neutrons were done at the IN14 with the Cryopad device ensuring full control of the neutron's polarization [68], the magnetic field dependence of the magnon spectrum was studied using the superconducting 15T vertical magnet of the PANDA spectrometer.

5.2.1 Tb crystal-field excitations and data treatment

In all recorded spectra on the magnetic excitations spectrum of TbMnO_3 a pronounced peak is always present at an energy transfer $E_{\text{CEF}} \approx 4.5 \text{ meV}$, which seems not to depend explicitly on \mathbf{Q} , see Fig. 5.5. In accordance with the literature [249], we attribute this feature to a low-lying crystal field excitation (CEF) of the Tb-subsystem. Following Hund's rules, Tb^{3+} with 8f electrons has the ground state configuration 7F_6 , which in a spherical symmetry is 13-fold degenerate. In a crystalline environment this degeneracy can (partly) be removed, the orthorhombic C_2 -symmetry in TbMnO_3 completely splits the J_z -levels giving rise to 13 non-degenerate singlet states [250].

In Fig. 5.5 energy scans for various values of \mathbf{Q} are shown. Common to all scans is a feature at $\approx 4.5 \text{ meV}$. The scans with low $|\mathbf{Q}|$ are, however, dominated by the inelastic magnetic signal from the Mn-subsystem, see the discussion below. Fitting the data with Gaussians allows to estimate the relative intensity of this feature and correcting for resolution effects the $|\mathbf{Q}|$ -dependence of the intensity can be fitted to the square of the magnetic form factor for a Mn^{3+} and Tb^{3+} ion [21]: We find a nice agreement with the $|\mathbf{Q}|$ -dependence of a Tb^{3+} -form factor, while the matching with a Mn^{3+} -form factor is only poor, see Fig. 5.5b. Hence, we attribute this excitation to the Tb-sublattice and as no dispersion can be resolved

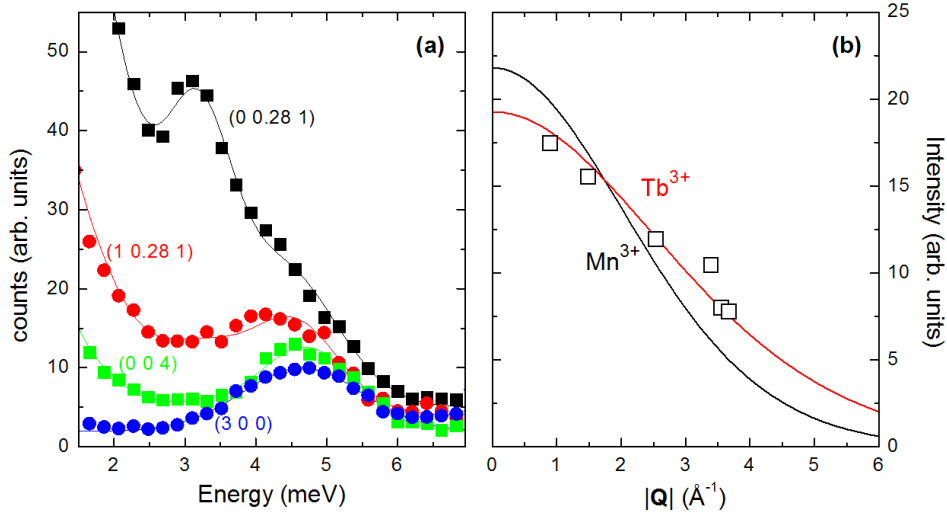


Figure 5.5: Tb crystal-field excitation Energy scans at different scattering vectors \mathbf{Q} at low temperature $T = 4.5$ K taken at the PUMA spectrometer. In all scans a Tb CEF excitation is visible at $E \approx 4.5$ meV, for low $|\mathbf{Q}|$ the spectra are, however, dominated by Mn-magnetic scattering at lower energies. Lines correspond to fits with Gaussians (a). Fit of the intensity of the 4.5 meV-feature to the square of the magnetic form factor of Mn^{3+} and Tb^{3+} (b).

we identify it with a low-lying crystal-field excitation (CEF) between two different J_z -states.

The CEF excitation superimposes the spin-wave spectrum and severely hampers the analysis of the data. To achieve an unique description of the relevant magnetic excitations the width and the position of the CEF excitation were always fixed within a 10%-interval in the fitting process of all inelastic data presented below. The relative intensity of the CEF excitation was allowed to vary within the borders of 10% according to the $|\mathbf{Q}|$ -dependence set by the Tb^{3+} -form factor.

In addition to the correction of the Tb-CEF excitation, the data taken at the PUMA spectrometer with k_i fixed have to be corrected for resolution effects before comparing with the data acquired in the usual constant k_f mode. Due to the variation of the analyzer scattering angle $2\vartheta_{\text{Ana}}$ the resolution volume at the secondary part of the spectrometer changes significantly for various energy transfers and scales with $k_f^3 \cot(\vartheta_{\text{Ana}})$ [19]. In the presentation below, this resolution factor has always been corrected in the constant- k_i data sets.

5.2.2 Spin-wave spectrum in the spiral phase

Fig. 5.6 presents the magnetic excitation spectrum at $T = 17$ K in the spiral phase at the magnetic zone center $\mathbf{Q} = (00.2750)$ measured at the PANDA spectrometer with the final energy fixed to 4.66 meV. The typical counting time for the data

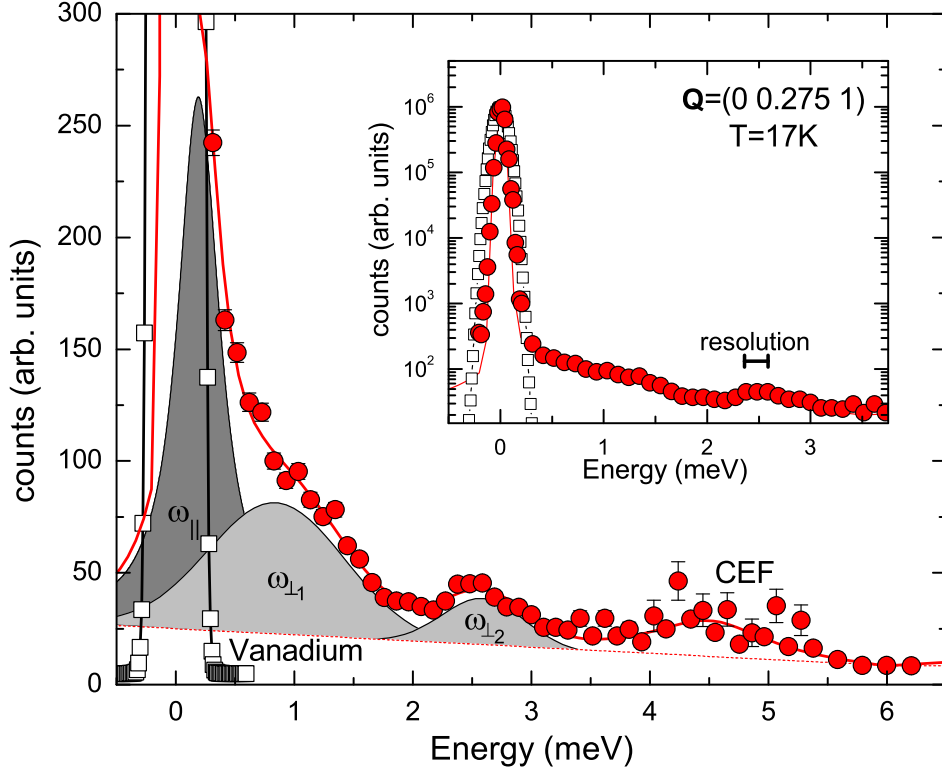


Figure 5.6: Magnetic excitation spectrum in the spiral phase at $Q = (00.2751)$ Energy scan at the magnetic zone center $Q = (00.2751)$ at $T = 17\text{K}$ in the spiral phase on a linear and a logarithmic scale taken at the PANDA spectrometer with the final energy fixed to $E_f = 4.66\text{meV}$. Data are shown as red circles, while lines correspond to the fit as described in the text. For comparison, a vanadium scan probing the experimental energy resolution at the elastic line is included by open squares. The calculated resolution at an energy transfer of $E = 2.5\text{meV}$ is marked by a black bar.

shown is 8 min/point. Clearly, the scattered intensity is dominated by the elastic contribution centered at $E = 0\text{meV}$, but in addition several inelastic signals can be resolved: A separated excitation is visible at $\hbar\omega_{\perp 2} \approx 2.5\text{meV}$, and a second feature is distinguishable around $\hbar\omega_{\perp 1} \approx 1.0\text{meV}$ at the tail of the elastic line. Comparing the elastic contribution with the energy resolution of the spectrometer, which is calculated to be $(\Delta E)_{0\text{meV}} = 0.136\text{meV}$, the observed signal differs around $\approx 0.5\text{meV}$ significantly from the incoherent signal of a Vanadium standard sample. This deviation cannot be attributed to the influence of $\omega_{\perp 1}$ alone and points to a third, low-lying excitation with $\hbar\omega_{\parallel} \lesssim 0.2\text{meV}$. As aforementioned, at $\approx 4.5\text{meV}$ a fourth excitation is observed which, however, has to be ascribed to a low-lying crystal-field excitation of the Tb-subsystem.

To model the observed spectrum we assume a linear background, which is well justified by the comparison of several scans at various points in reciprocal space.

The magnetic excitations ω_{\perp_1} and ω_{\perp_2} can be well described by a Gaussian line shape, while we tentatively describe the soft mode at low energies by a Lorentzian. Within this description we achieve a good agreement with the observed intensity, yielding the eigenfrequencies $\hbar\omega_{\parallel} = 0.19(8)$ meV, $\hbar\omega_{\perp_1} = 1.05(1)$ meV and $\hbar\omega_{\perp_2} = 2.61(2)$ meV. The width of the two higher-energy, Gaussian-shaped excitations $\omega_{\perp_{1/2}}$ is slightly broader than the experimental resolution, while the soft mode seems to be strongly overdamped with an energy width comparable to its frequency ω_{\parallel} .

To further separate the soft mode from the elastic contribution we have repeated the same scan as above with the final energy fixed to $E_f = 2.98$ meV, see Fig. 5.7. The change from $k_f = 1.50 \text{ \AA}^{-1}$ to $k_f = 1.20 \text{ \AA}^{-1}$ increases the experimental resolution by a factor of ≈ 2.5 , $(\Delta E)_{0\text{meV}} = 0.056$ meV instead of 0.136 meV, which, however, has to be paid by a drastic loss of count rate – for a similar statistic the counting time is increased by a factor 5. Typical counting times for the data presented in Fig. 5.7 are 30 min/point, which restricts this configuration only to a few selected scans in our time-limited experiments.

As can be seen by the comparison with the relaxed resolution, the high-resolution data yield qualitatively the same spectrum with the soft mode at low energies and the magnon feature around 1.05 meV. However, the increase of resolution significantly sharpens the elastic line, see the comparison in Fig. 5.7a, and the additional contribution due to the soft mode becomes apparent as an asymmetric broadening. The asymmetry of the low-energy part of the spectrum with respect to $\omega \rightarrow -\omega$ reflects the principle of detailed balance (cf. Chap. 2) and points to its inelastic origin – elastic scattering is always expected to give a symmetric contribution.

The asymmetric line shape of an overdamped soft mode is usually described by a damped harmonic oscillator:

$$f(\omega, \omega_0) \propto \frac{1}{1 - \exp(-\frac{\hbar\omega}{k_B T})} \times \frac{4\omega\omega_0\Gamma_0}{[\omega^2 - (\omega_0^2 + \Gamma_0^2)]^2 + 4\omega^2\Gamma_0^2}, \quad (5.7)$$

with a damping constant Γ_0 for the mode at ω_0 [251]. However, describing our data with a model consisting of three different contributions, two Gaussians representing the elastic line and the mode at 1.05 meV and a damped oscillator for the soft mode, the fitting process is not stable and does not converge towards a reasonable solution. Instead, replacing the oscillator by two Lorentzians with equal width Γ centered at ω_{\parallel} and $-\omega_{\parallel}$ yields an accurate description, see Fig. 5.7. Within the best fit we obtain an eigenfrequency $\omega_{\parallel} = 0.07(4)$ meV for the low-lying mode, but we cannot unambiguously rule out a slightly different, or even vanishing frequency within his phenomenological model.

To gain more insight into the physical origin of the different spin-wave components in the spiral phase of TbMnO₃, we next extend our analysis to the use of

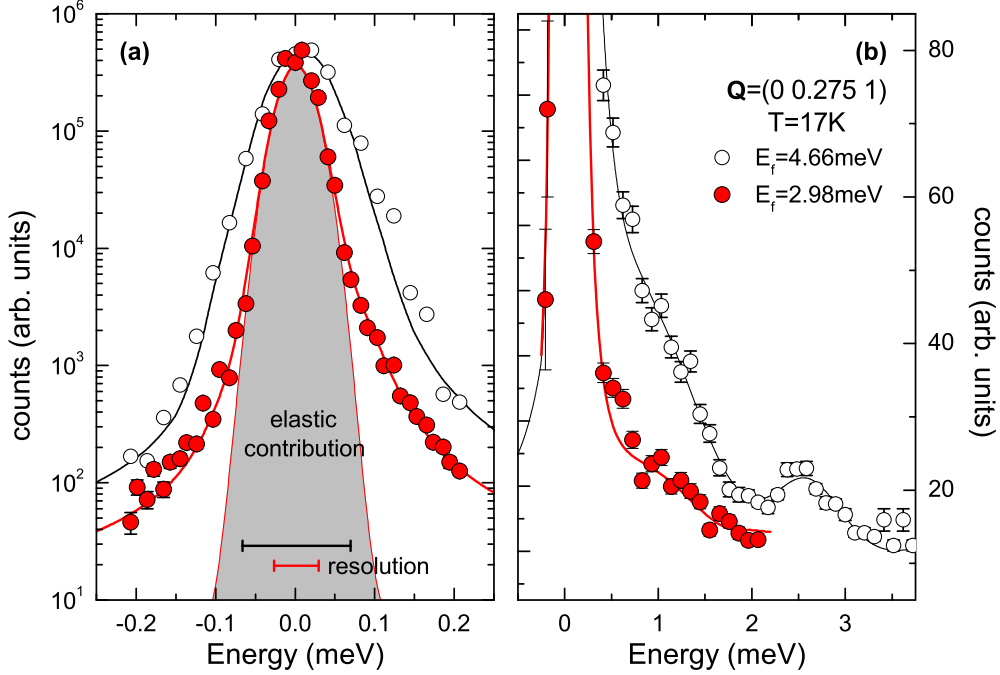


Figure 5.7: High-resolution spectrum at $Q = (00.2751)$ The same scan as in Fig. 5.6, but with $E_f = 2.98$ meV instead of 4.66 meV, on a logarithmic (a) and a linear scale (b). Data with increased resolution are shown in red, while open symbols are the same data as presented in Fig. 5.6. Lines correspond to the fit as described in the text and the gray-shaded area marks the elastic contribution. The calculated resolution at $E = 0$ meV is given by a red and a black bar for $E_f = 2.98$ meV and 4.66 meV, respectively.

polarized neutrons. The polarization analysis of the excitation spectrum has been performed on the IN14 spectrometer. Again, the energy of the analyzed neutrons was fixed to $E_f = 4.66$ meV, since a better resolution with $E_f = 2.98$ meV, although desirable, seemed not to be practicable due to the increased counting time. Note, that in an experiment with polarized neutrons the neutron flux is already suppressed by a factor of 5-10 compared to an unpolarized experiment because of the restriction to a certain polarization and the more complex devices. Typical counting times for the polarized data presented below are ≈ 18 min/point for each polarization channel.

In our experiment, the polarization analysis was achieved using the Cryopad-device. However, here we will not use the full power of Cryopad enabling full three-dimensional polarization analysis and restrict ourselves to the classical longitudinal polarization analysis, discussed in the introductory chapter 2. Nevertheless, Cryopad ensures the precise control of the polarization essential for a substantial data analysis: Our experimental setup yielded flipping ratios on fun-

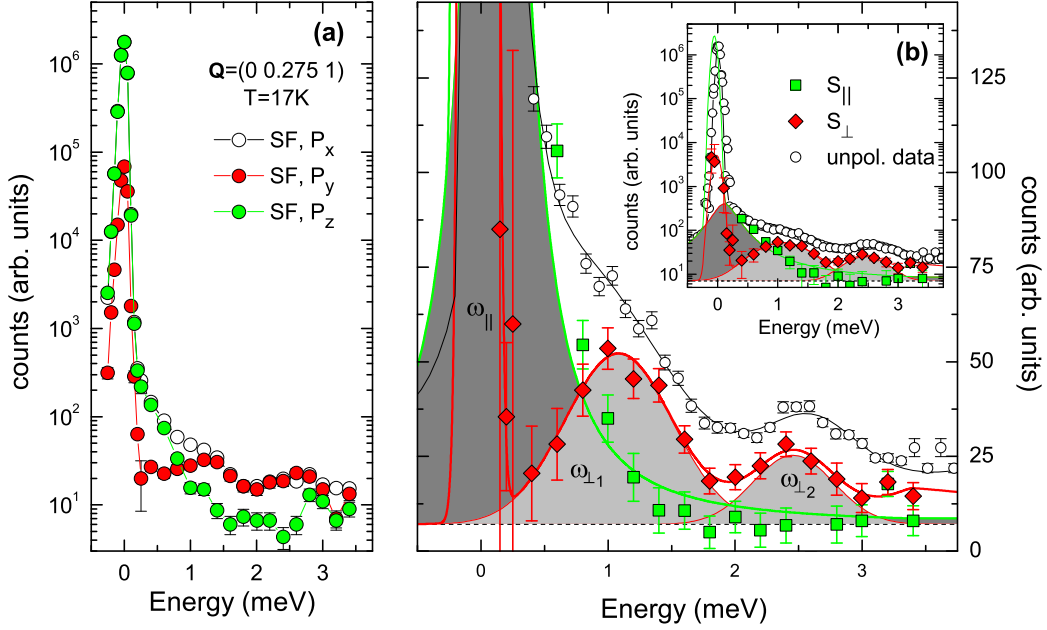


Figure 5.8: Polarization analysis of the magnon spectrum in the spiral phase Energy scans at the magnetic zone center $\mathbf{Q} = (0.0.275\ 1)$ at $T = 17\text{K}$ using polarized neutrons with spin-quantization axis along x , y and z for the spin-flip channel taken at the IN14 spectrometer (a). Longitudinal polarization analysis based on the data presented in (a) with the magnetization S_{\parallel} within and S_{\perp} perpendicular to the spiral plane shown in green and red symbols, respectively. Data are shifted by $+5$ to avoid negative count rates on the log-scale. Open circles are the same data as presented in Fig. 5.6 acquired using unpolarized neutrons. Lines correspond to fits as described in the text (b).

damental Bragg peaks as good as $I^{\text{NSF}} : I^{\text{SF}} = 35$ and an accuracy of 2% in the transverse polarization terms. As usual, we have chosen a coordinate system for the spin space with $\mathbf{x} \parallel \mathbf{Q}$, $\mathbf{y} \perp \mathbf{Q}$ within and $\mathbf{z} \perp \mathbf{Q}$ and perpendicular to the scattering plane. With \mathbf{a} vertical to the scattering plane, this setup allows to determine the components of the magnetization within and perpendicular to the \mathbf{bc} -plane, i.e. the plane of the magnetic spiral: Under the reasonable assumption of a polarization independent experimental background, subtracting the different spin-flip intensities for $\mathbf{P} \parallel \mathbf{x}, \mathbf{y}, \mathbf{z}$ directly yields the components S_{\parallel} parallel and S_{\perp} perpendicular to the spiral plane of the total magnetization, cf. Tab. 2.1.2 in Chap. 2. The results of the longitudinal polarization analysis of the magnetic excitation spectrum in the spiral phase at $T = 17\text{K}$ and $\mathbf{Q} = (0.0.275\ 1)$ are shown in Fig. 5.8.

In the S_{\perp} -channel two inelastic features are well distinguishable. Comparing with the above unpolarized data the analysis of the spectrum is now more instructive, as there is no overlap with the elastic signal and the excitations ap-

		Energy (meV)	Polarization
sliding mode	ω_{\parallel}	0.11 ± 0.05	$\parallel \mathbf{bc}$
orthogonal modes	$\omega_{\perp 1}$	1.07 ± 0.05	$\parallel \mathbf{a}$
	$\omega_{\perp 2}$	2.50 ± 0.08	$\parallel \mathbf{a}$

Table 5.1: Overview of the observed energies and polarization schemes of the magnetic zone-center excitations in the spiral phase at $T = 17$ K determined using polarized neutrons.

pear well separated. Fitting the excitations with Gaussian line shapes, we obtain $\hbar\omega_{\perp 1} = 1.07(5)$ meV and $\hbar\omega_{\perp 2} = 2.50(8)$ meV, which is in excellent agreement with the above results using unpolarized neutrons. Again, the width of the excitations is slightly broader than the experimental resolution.

In addition to the inelastic features, a sharp response is obvious at the elastic position in the S_{\perp} -channel, which turns out to be an artefact due to an experimental loss of polarization. As can be seen in the raw data scans in Fig. 5.8a, the ratio of the elastic count rate in the S_z and the S_y spin-flip (SF) channel matches within 10% the observed flipping ratio $I^{\text{NSF}} : I^{\text{SF}} \simeq 35$. The S_y NSF signal measures the same magnetic contributions as the S_z SF channel and the observed elastic spin-flip intensity in S_y must be attributed to an experimental loss of spin polarization. The static magnetization has, hence, no component along \mathbf{a} , which is in perfect congruence with a magnetic spiral in the \mathbf{bc} -plane [222]. The artificially observed elastic S_y SF signal serves, however, as a rough estimate of the experimental resolution, and will be helpful for the interpretation of the results in the S_{\parallel} -channel.

In the S_{\parallel} -channel the spectrum consists of a single peak centered around the elastic position $E = 0$ meV. The tail of the peak is significantly broader than the experimental resolution, as is nicely proven by the comparison between S_{\parallel} and S_{\perp} and which, in consistence with the unpolarized data, has to be attributed to a third, low-lying magnetic mode. We model the data by a Gaussian describing the elastic part and, as before, a Lorentzian for the inelastic contribution. The best fit gives a satisfying description and yields $\hbar\omega_{\parallel} = 0.11(5)$ meV for the energy of the soft mode.

Comparing the polarized with the unpolarized measurements, both methods render similar results concerning the number of magnon branches and their eigenfrequencies at the incommensurable zone center, thus proving the magnetic origin of the different excitations. However, the longitudinal polarization analysis goes beyond and allows to decompose the excitation spectrum, thereby corroborating the analysis of the unpolarized data: At the A -type zone center $\mathbf{Q} = (00.281)$ the excitation spectrum within the spiral phase consists of three different magnon

branches. Two of them, the modes ω_{\perp_1} and ω_{\perp_2} with higher energy, are polarized along \mathbf{a} , perpendicular to both the local ordered moment and the plane of the spiral, while the third mode ω_{\parallel} is very soft and polarized parallel to the spiral plane \mathbf{bc} . In the following we will call the \mathbf{a} -polarized modes orthogonal and refer to the \mathbf{bc} -polarized mode as the sliding mode, as has already been indicated by the tentative labeling of the different modes.

Magnetic excitations in a spiral magnet The theoretical treatment of magnetic excitations in spiral magnets has been under discussion since 50 years. However, early publications focus on “proper” spirals, in which the rotation axis of the spiral is parallel to the propagation vector and therefore does not induce ferroelectricity [240, 252]. A theoretical investigation of the magnon spectrum in multiferroic spiral magnets and its relevance for the magneto-electric coupling has been reported only very recently [253]. Indeed, in their work Katsura et al. predict three different magnon branches, two polarized along \mathbf{a} and the third within the spiral plane, just as we observe in TbMnO₃.

For simplicity, we consider for the moment a perfect, circular spiral with vector chirality $\mathbf{S}_i \times \mathbf{S}_j$ along \mathbf{a} and propagation vector $\mathbf{k}_{\text{spiral}} \parallel \mathbf{b}$. Then, we may describe the local moment at the site \mathbf{r}_i as

$$\mathbf{S}_i = S_0 \cdot \cos(\mathbf{k}_{\text{spiral}} \cdot \mathbf{r}_i) \mathbf{e}_b + S_0 \cdot \sin(\mathbf{k}_{\text{spiral}} \cdot \mathbf{r}_i) \mathbf{e}_c. \quad (5.8)$$

One possible magnetic excitation within this structure polarized within the rotational \mathbf{bc} -plane is the phason of the spiral, i. e. a transversal fluctuation of the local moment around the rotation axis \mathbf{a} : The mode only alters the phase of the spiral with respect to the underlying crystal lattice, but leaves the orientation within the spin system constant – hence we refer to it as phason or sliding mode. The polarization pattern of this mode is sketched in Fig. 5.9a. To analyze the coupling of this mode to the induced electric polarization we need to generalize the central equation 5.4 controlling the polarization and obtain:

$$\mathbf{P} \propto \sum_i \mathbf{r}_{i,i+1} \times (\mathbf{S}_i \times \mathbf{S}_{i+1}), \quad (5.9)$$

with the distance vector $\mathbf{r}_{i,i+1}$ connecting adjacent spins \mathbf{S}_i and \mathbf{S}_{i+1} [12]. Note, that for a spiral the cross product $\mathbf{S}_i \times \mathbf{S}_{i+1}$ is constant and we reproduce eq. 5.4. The sliding mode does obviously not affect the cross product between neighboring spins and therefore does not couple to the electric polarization.

As the high moment ordered structure observed in TbMnO₃ excludes a longitudinal spin fluctuation, we identified the observed \mathbf{bc} -polarized, low-lying excitation ω_{\parallel} with the sliding mode. The observed small finite energy can be explained by pinning effects and the asymmetry of the spiral ordering, which is elliptic instead of circular in the case of TbMnO₃.

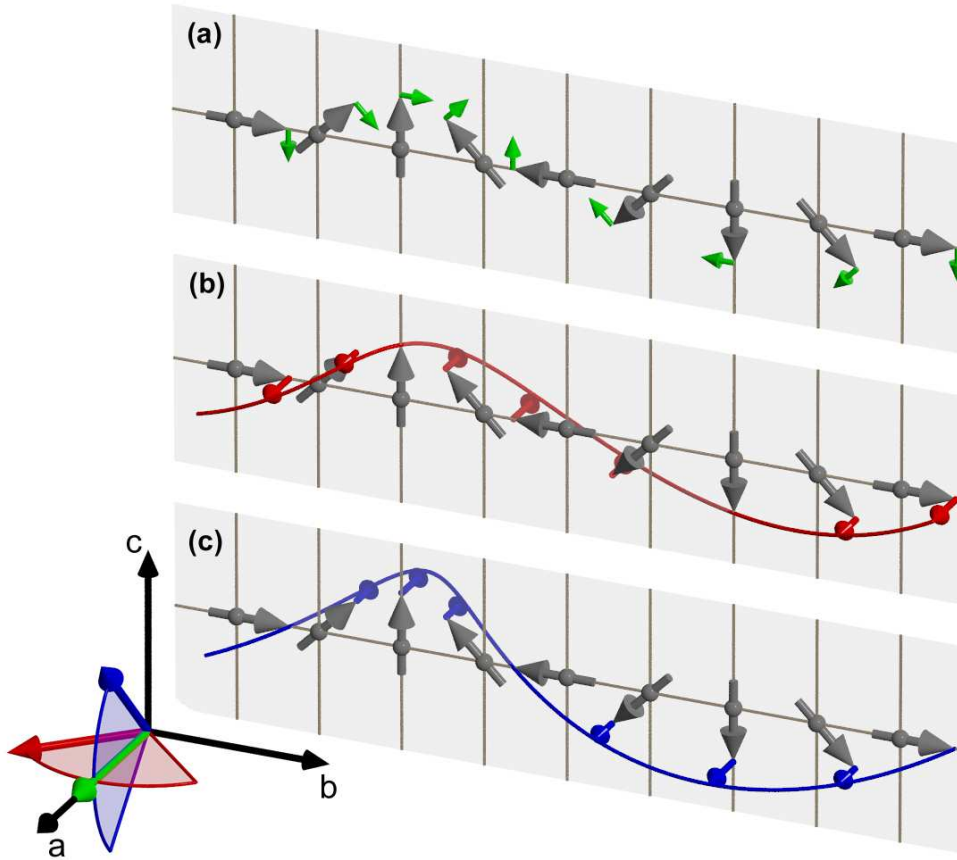


Figure 5.9: Magnetic excitations in a spiral magnet Sketch of the polarization schemes of the different magnon excitations at $\mathbf{Q} = \mathbf{k}_{\text{spiral}}$ in a spiral ordering as described in the text. The static spin structure is marked by thick gray and the local fluctuations by smaller, colored arrows. In addition, in the left corner the vector product $\mathbf{S}_i \times \mathbf{S}_{i+1}$ is shown for the sketched instantaneous spin arrangement with the different modes marked by the color scheme. The \mathbf{bc} -polarized sliding mode can be regarded as a rotation of the spin plane around \mathbf{a} (a). For the \mathbf{a} -polarized modes the fluctuations can either be in-phase with the static \mathbf{b} -component (b), or with the static \mathbf{c} -component (c), resulting in a rotation of the spiral plane around \mathbf{c} and \mathbf{b} , respectively.

Next, we answer the question why there are two \mathbf{a} -polarized branches: At the magnetic zone center the fluctuations along \mathbf{a} can be considered as standing waves, which cant the spins out of the \mathbf{bc} -plane, thereby inducing a time dependent magnetization $S_i^a(\mathbf{q}, \omega)$ along \mathbf{a} at the site \mathbf{r}_i :

$$S_i^a(\mathbf{q} = 0, \omega) = S_0^a \cos(\mathbf{k}_{\text{spiral}} \mathbf{r}_i + \delta) \cdot \cos(\omega t). \quad (5.10)$$

The fluctuation necessarily possesses the same wavelength as the static spin structure, but the oscillation can be either in-phase with the static \mathbf{b} -component of the

spiral given by eq. 5.8, cosinusoidal modulated, or with the static \mathbf{c} -component yielding a sinusoidal fluctuation. The arising polarization patterns are distinct and are shown in Fig. 5.9b and c.

For small amplitudes S_0^a we can evaluate eq. 5.9 for the excited state at $\mathbf{q} = 0$ and obtain with the phase difference φ_0 between adjacent sites for the cosinusoidal modulation

$$(\mathbf{S}_i \times \mathbf{S}_{i+1})^{\cos} = (\sin(\varphi_0), S_0^a \sin(\varphi_0) \cdot \cos(\omega t), 0), \quad (5.11a)$$

and for the sinusoidal modulation

$$(\mathbf{S}_i \times \mathbf{S}_{i+1})^{\sin} = (\sin(\varphi_0), 0, S_0^a \sin(\varphi_0) \cdot \cos(\omega t)). \quad (5.11b)$$

Hence, both modes affect the plane of the spiral, and inspecting eqs. 5.11 more closely we find, that in the cosinusoidal case the spiral plane oscillates around \mathbf{c} , while the sinusoidal mode rotates it around \mathbf{b} , see Fig. 5.9. However, Katsura et al. have shown that only the sinusoidal mode couples to an uniform lattice displacement along \mathbf{a} and to the ferroelectric polarization. Neglecting the finite energy due to single-ion anisotropy, this mode would be the Goldstone boson of the multiferroic transition [254]. The second \mathbf{a} -polarized mode is entirely decoupled from the polarization and gapped by the effective spin anisotropy introduced by the spin-lattice interaction [253].

In consequence, we attribute the two observed orthogonal magnons $\omega_{\perp 1/2}$ to the two different \mathbf{a} -polarized modes just discussed. Both branches possess a finite energy due to magnetic anisotropy effects, and we are now left with the identification of the \mathbf{b} - and \mathbf{c} -rotation modes. In a perfect circular spiral only the later one is expected to couple to the FE lattice distortion, but due to magnetic anisotropy the spiral is elliptic in TbMnO₃ and both modes might slightly mix rendering the actual situation more complex. Nevertheless, at least one of the two modes is closely connected with a fluctuation of the static electric polarization, and this mode should be detectable in IR spectroscopy as well. Hence, we interrupt the discussion of our neutron data at this point and continue with a brief summary of recent results of optical spectroscopy on TbMnO₃ published by Pimenov et al. [255]. As we will demonstrate next, comparing the IR data with our neutron results yields a comprehensive and unambiguous picture of the magnetic excitations in the ferroelectric phase of TbMnO₃.

IR spectroscopy and identification of the electromagnon response In Fig. 5.10 we show the frequency dependence of the dielectric properties both with and without the external magnetic field for TbMnO₃ as published by Pimenov et al. [255]. The data in the ferroelectric state at $T = 12$ K without magnetic field and with the electric a.c. component $\mathbf{e} \parallel \mathbf{a}$ show two broad relaxation-like excitations with frequencies $\nu_1 = 10 \text{ cm}^{-1}$ and $\nu_2 = 20 \text{ cm}^{-1}$, corresponding to

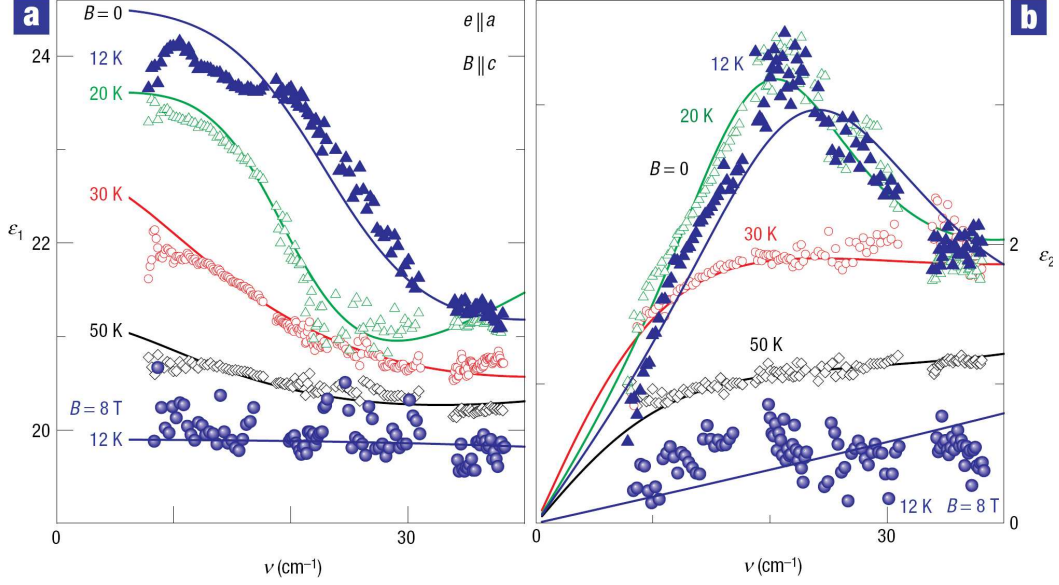


Figure 5.10: Dielectric function of TbMnO_3 in the THz regime Frequency dependence of the real (a), and imaginary (b) part of the terahertz-dielectric function in TbMnO_3 with $\mathbf{e} \parallel \mathbf{a}$ and $\mathbf{B} \parallel \mathbf{c}$, as published by Pimenov et al. [255]. Open spheres represent the data without external field, filled spheres those in the CA-AFM state obtained by applying $B = 8 \text{ T}$ along \mathbf{c} . Filled triangles are the corresponding data for $B = 0 \text{ T}$.

$\hbar\omega_1 = 1.24 \text{ meV}$ and $\hbar\omega_2 = 2.48 \text{ meV}$, respectively. Note, that in Ref. [255] only the mode at higher energies is discussed, but a second mode at lower energies is well visible for $T = 12 \text{ T}$. Both modes seem to be connected with the modulated magnetic structure, as they are suppressed with the transition into the canted AFM phase induced by the magnetic field $H_c = 8 \text{ T}$ applied along \mathbf{c} . However, the very unusual point concerning these modes is the close correlation to the polarization of the electric a. c. component: Both modes are well visible for $\mathbf{e} \parallel \mathbf{a}$, but not if the electric component is aligned along \mathbf{b} . In contrast, both modes are not sensitive to the orientation of the magnetic component of the a. c. field, and the authors conclude that the modes are new hybrid spin-lattice excitations which can be excited by an electric field and which they therefore refer to as *electromagnons*. Subsequently to the publication by Pimenov et al., recent publications have proven the existence of similar excitations in other multiferroic compounds as e. g. TbMn_2O_5 , YMn_2O_5 [256], and $(\text{Eu}, \text{Y})\text{MnO}_3$ [257].

Comparing the IR data with our neutron results, and regarding the discussion of the magnetic excitations in a spiral magnet presented above, the origin of the unusual properties of the electromagnons in the IR data is quite obvious – these excitations are indeed hybridized phonon-magnon excitation, predicted to exist in magnetic ferroelectrics by Russian groups already in the 1970's [199, 200, 258], and

the IR signal has to be combined with the two orthogonal modes $\omega_{\perp 1/2}$ identified in our neutron data. The agreement both of the polarization dependence and of the energies of the modes between IR and neutron data is excellent. The frequencies $\hbar\omega_1 = 1.24$ meV and $\hbar\omega_2 = 2.48$ meV of the IR experiment have to be compared with those of the two orthogonal modes $\hbar\omega_{\perp 1} = 1.07$ meV and $\hbar\omega_{\perp 2} = 2.50$ meV determined from the neutron data, proving that both techniques probe the same fundamental excitation: In the IR spectroscopy the lattice part is tested, while we sense the magnetic channel of the hybridized phonon-magnon excitation in the neutron experiment. As aforementioned, the fact that both orthogonal modes $\omega_{\perp 1/2}$ couple to the electric polarization has to be attributed to the mixing of the **b**- and **c**-rotation mode of a perfect spiral due to the complex magnetic anisotropy; a further identification seems, hence, meaningless.

To resume the discussion of the excitation spectrum in the spiral phase at $T=17$ K, the observed three branches of the spectrum can well be interpreted based on the theory developed by Katsura et al. [253]. The lowest, **bc**-polarized mode is the sliding mode of the magnetic spiral ordering, this mode does not couple to the electric polarization. The two **a**-polarized branches correspond to the rotation of the spiral plane around the **c** and the **b** axis. The excellent agreement with recent results of IR spectroscopy proves that both modes are correlated to the dynamic electric polarization, and are finally interpreted as a new type of fundamental excitation in a multiferroic systems: electromagnons – strongly hybridized magnon-phonon excitations.

5.2.3 Spin-wave spectrum in the spin-density wave phase

Next, we focus on the magnetic excitation spectrum in the paraelectric SDW phase above T_{spiral} . We have analyzed the magnon spectrum at $T = 32$ K in detail using unpolarized neutrons on the PANDA spectrometer as well as polarized neutrons on IN14.

In Fig. 5.11a we compare the energy scan at the *A*-type zone center $\mathbf{Q} = (0\ \varepsilon_b\ 1)$ at $T = 32$ K with the spectrum at $T = 17$ K discussed so far. In the SDW phase the spectrum is less structured than in the spiral phase, and with the standard configuration of the PANDA spectrometer and the energy of the analyzed neutrons set to $E_f = 4.66$ meV only a broad signal centered around $E \approx 1.5$ meV can be resolved. An additional inelastic contribution seems to be hidden at low energies, as the tail of the elastic line deviates significantly from the expected experimental resolution and exhibits a comparable line shape as in the spiral phase.

A satisfying description of the observed data appears challenging, as a “minimal model” consisting of two inelastic contributions, a Lorentzian for the low-energy excitation and a Gaussian for the broad feature, does not result in a fully satisfying fit. However, adding further contributions to this model, the fitting process does not result in a unique description and various alternatives model the spectrum

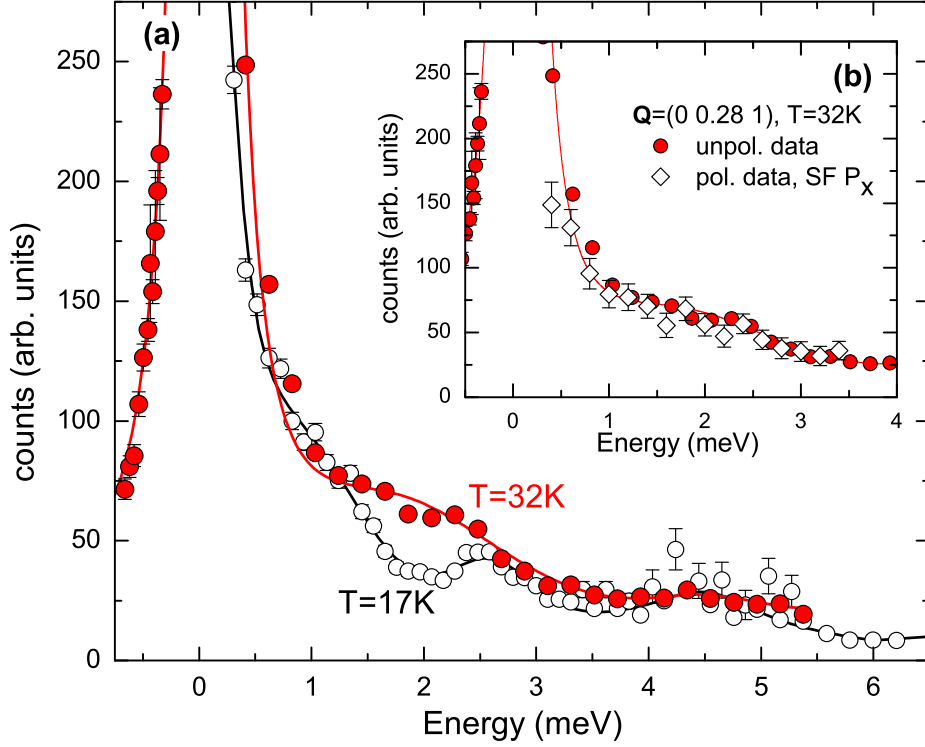


Figure 5.11: Spin-wave spectrum at $T = 32\text{K}$ and comparison with spiral phase Energy scan at the incommensurable zone center $\mathbf{Q} = (0\ 0.28\ 1)$ in the SDW phase at $T = 32\text{K}$ taken at the PANDA spectrometer with the energy of the final neutrons fixed to $E_f = 4.66\text{meV}$. Open symbols are the same data as presented in Fig. 5.6 for $T = 17\text{K}$. Lines correspond to the fit with a “minimal model” as described in the text (a). Comparison of the unpolarized data for $T = 32\text{K}$ measured at the PANDA spectrometer with the scattered intensity in the spin-flip P_x -channel in the polarized experiment at IN14 (b).

equally well. The unpolarized data do not allow to resolve all the details of the excitation spectrum in the SDW phase. In the following we will show that the use of polarized neutrons enables to decompose the spectrum into at least *four* different magnon branches.

In the inset of Fig. 5.11 some of the results of the polarized experiment on IN14 are superimposed on top of the unpolarized data. With the polarization \mathbf{P} parallel to the scattering vector \mathbf{Q} , the scattering in the spin-flip channel is the sum of all magnetic contributions: The polarized spectrum scales nicely with the unpolarized data, thereby proving the magnetic character of the signal. Once more, we now make use of the full power of the longitudinal polarization analysis by taking the differences between the measured intensities in the spin-flip channel for different choices of the quantization axis, and we obtain the dynamic spin correlations S_{\perp} perpendicular and S_{\parallel} parallel to the scattering plane, which in

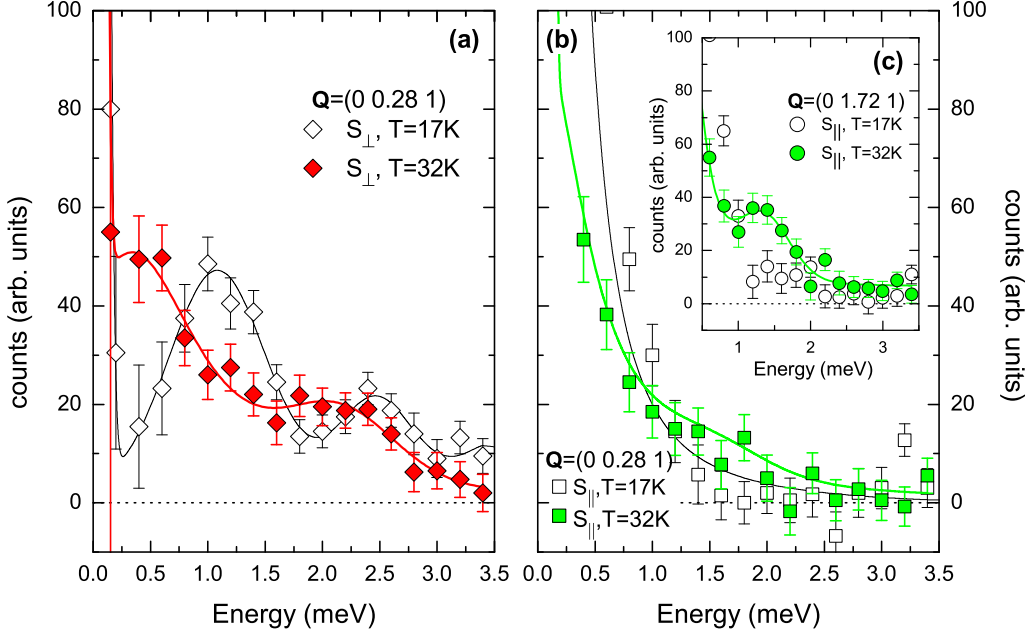


Figure 5.12: Polarization analysis of the magnon spectrum in the SDW phase Longitudinal polarization analysis of the magnetic excitation spectrum in the SDW phase with the magnetization S_{\perp} perpendicular, (a), and S_{\parallel} parallel, (b) and (c), to the bc -plane. (b) and (c) compares the magnetic scattering at the two equivalent A -type zone centers $\mathbf{Q}_1 = (0\ 0.28\ 1)$ and $\mathbf{Q}_2 = (0\ 1.72\ 1)$ for the S_{\parallel} -channel. Colored symbols always represent $T = 32\text{K}$ -data and open data taken at $T = 17\text{K}$; for $\mathbf{Q} = (0\ 0.28\ 1)$ the 17 K-data are the same as presented in Fig. 5.8. Lines correspond to fits as described in the text.

our case was chosen to be the bc -plane. The results of this analysis for $T = 32\text{K}$ are shown in Fig. 5.12.

We start with the discussion of S_{\perp} , i.e. in our configuration the dynamic magnetization parallel to the a -axis. Like in the spiral phase, two contributions can be resolved in S_{\perp} for $T = 32\text{K}$. However, compared to the spectrum in the FE-spiral phase the intensities appear to be smeared out and the two signals are significantly broadened and shifted to lower energies. The observed spectrum can best be described assuming a Lorentzian line shape for the low-energy mode, which again appears to be overdamped, and a Gaussian for the higher-energy mode. This model yields the eigenfrequencies $\hbar\omega_1^a = 0.31(9)\text{ meV}$ and $\hbar\omega_2^a = 2.16(10)\text{ meV}$ for the two a -polarized modes.

To understand the different contributions in the S_{\parallel} -channel we have to compare the spectra recorded at two equivalent magnetic Bragg positions $\mathbf{Q}_1 = (0\ 0.28\ 1)$ and $\mathbf{Q}_2 = (0\ 1.72\ 1)$. At \mathbf{Q}_1 , a low-lying excitation is clearly visible as a broad contribution close to the elastic line. However, the comparison with the 17 K-data suggests an additional contribution centered around $\approx 1.5\text{ meV}$, as the intensity

		Energy (meV)	Polarization
soft modes	ω_1^c	0.10 ± 0.10	$\parallel \mathbf{bc}$
	ω_1^a	0.31 ± 0.09	$\parallel \mathbf{a}$
hard modes	ω_2^c	1.32 ± 0.08	$\parallel \mathbf{c}$
	ω_2^a	2.16 ± 0.10	$\parallel \mathbf{a}$

Table 5.2: Summary of the results of the longitudinal polarization analysis in the SDW phase at $T = 32$ K with the eigenfrequencies and polarization patterns of the four observed zone-center modes.

is increased around this energy transfer in the SDW phase. Further support for a second contribution to S_{\parallel} is given by the spectrum determined at \mathbf{Q}_2 , where this signal appears enhanced compared to \mathbf{Q}_1 and which is clearly absent in the spiral phase at $T = 17$ K. Describing both spectra assuming, as usual, a Lorentzian line shape for the low-energy mode and a Gaussian for the second excitation, we obtain as the best fit $\hbar\omega_1^c = 0.10(10)$ meV and $\hbar\omega_2^c = 1.32(8)$ meV for the energies of the two S_{\parallel} -contributions. However, the fitting process occurs to be unstable against the refinement of the low-energy mode, and the reported value of $\hbar\omega_1^c$ has to be considered as a crude approximation. A detailed analysis of the low-energy behavior would require a significant increase of the experimental resolution to separate the inelastic contribution from the elastic scattering. Nevertheless, our data clearly prove the existence of a low-lying mode below $\hbar\omega \lesssim 0.15$ meV in the S_{\parallel} channel at $T = 32$ K.

Considering now only the fourth mode ω_2^c , the observed strong \mathbf{Q} -dependence allows us even to go beyond the longitudinal polarization analysis for this particular mode: The polarization analysis can only differentiate between fluctuations parallel and perpendicular to the \mathbf{bc} -scattering plane. However, in neutron scattering only the component of the magnetization perpendicular to the scattering vector \mathbf{Q} contributes to the cross section. With the different choice of the two zone centers \mathbf{Q}_1 and \mathbf{Q}_2 we significantly affect this selection rule, as \mathbf{Q}_1 spans an angle of 19.49° with the \mathbf{c}^* -axis, while \mathbf{Q}_2 includes an angle of 65.29° with \mathbf{c}^* . Taking the orthogonal complement from the projections onto \mathbf{c}^* we expect, after the correction of the different form factors, an intensity ratio for a purely \mathbf{c} -polarized mode of $I_{\mathbf{Q}_1} : I_{\mathbf{Q}_2} = 1 : 4.99$, which is in fair agreement with the observed intensity ratio for ω_2^c , $I_{\mathbf{Q}_1}^{\text{obs}} : I_{\mathbf{Q}_2}^{\text{obs}} = 1 : 4.29(82)$. Hence, we conclude that the mode ω_2^c has a transversal character with a polarization pattern predominantly parallel \mathbf{c} , i. e. perpendicular to the ordered moment. Due to the strong overlap with the elastic line and the resulting uncertainties in the determination of the spectral weights a similar analysis for the low-energy mode ω_1^c is, unfortunately, not possible.

In conclusion, using the longitudinal polarization analysis we resolve four different magnon contributions in the magnetic excitation spectrum of the paraelectric SDW phase at $T = 32$ K, two modes at very low energies, which we will refer to as “soft modes” in the following, and two branches with finite energies, which we will tentatively label “hard modes”, see Table 5.2 for a summary. In each of these two groups, one mode is polarized along \mathbf{a} , whereas the other mode is polarized within the \mathbf{bc} -plane. Moreover, comparing different \mathbf{Q} -position we can show that the hard mode ω_2^c possess an entirely transversal character and corresponds to a magnetic fluctuation along the \mathbf{c} -direction.

Magnetic excitations in a collinear spin-density structure Magnetic excitations in spin-density wave structures have been studied both experimentally and theoretically for more than a decade, as they seem to be crucial for the understanding of the complex phase diagram of elemental Chromium and related systems [259, 260]. In metallic Chromium, however, the incommensurable ordering stems from nesting effects at the Fermi surface and it is not obvious how to adopt these well developed theories to the case of a localized system like TbMnO₃.

Instead, we will follow the discussion of the magnetic excitations in the spiral phase and extend the above arguments to the case of a collinear order. In a spin-density wave structure with modulation vector \mathbf{k}_{SDW} and the ordered moments aligned along \mathbf{b} the spin \mathbf{S}_i at the site \mathbf{r}_i may be described as

$$\mathbf{S}_i = S_0 \cdot \cos(\mathbf{k}_{\text{SDW}}\mathbf{r}_i + \delta)\mathbf{e}_b. \quad (5.12)$$

Applying similar arguments as for the analysis of the spiral phase to the SDW structure, we expect up to six different magnon branches at $\mathbf{q} = 0$: Two modes with similar polarization along each of the three orthorhombic axes. We will now discuss whether or not these modes are degenerate and if they all contribute in our neutron scattering experiments.

We start with the two branches polarized along \mathbf{b} , i. e. along the direction of the ordered moment. In a conventional magnet, take a simple ferromagnet as an example, longitudinal modes do not exist within linear spin-wave theory [69]. However, the incommensurate character of the SDW ordering activates them in our case. At the magnetic zone center, $\mathbf{q} = 0$, a sinusoidal fluctuation along \mathbf{b} possess the same wavelength as the static modulation, but it can be either in-phase or out-of-phase with the ordered structure. The later case corresponds to the phason mode of the SDW structure, as it oscillates the phase δ of the SDW with respect to the underlying crystal lattice. Similar to the phason mode of the spiral phase, the energy of this sliding mode is expected to be very low. The second \mathbf{b} -polarized mode, the in-phase oscillation, corresponds to the “magnitudon”, as it yields a fluctuation of the amplitude of the local moment around its mean value. In principle, such a mode can also exist in a conventional magnet, but usually it

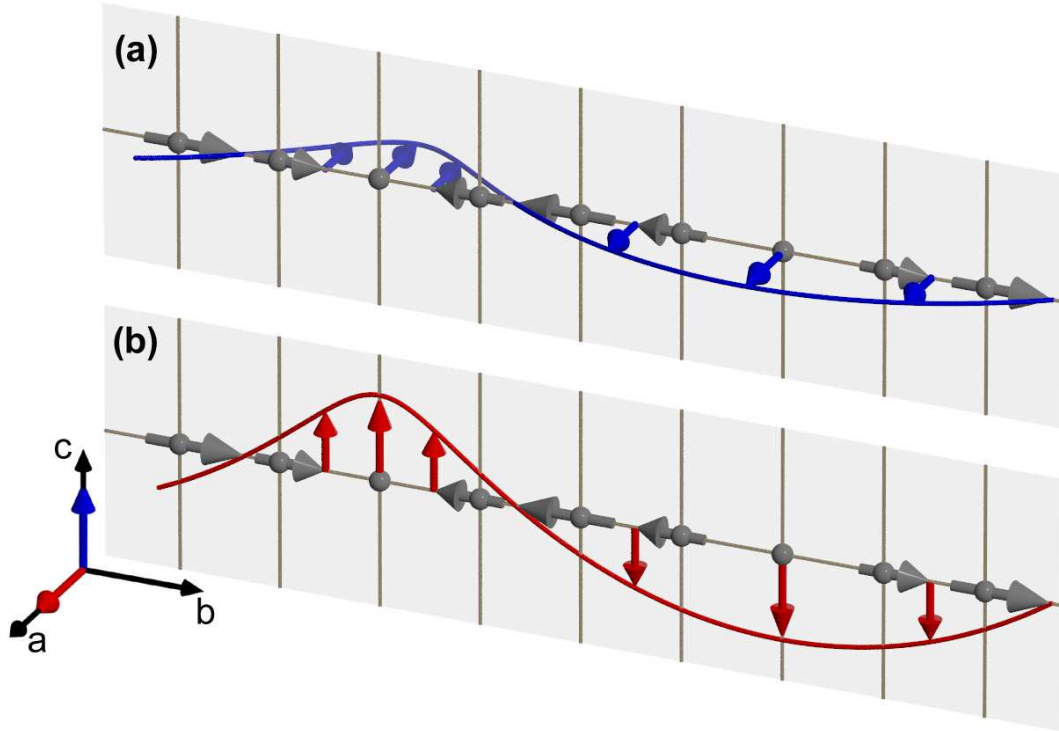


Figure 5.13: Magnetic excitations in a SDW structure Polarization schemes of the two $\frac{\pi}{2}$ -modes in a SDW arrangement. The \mathbf{a} polarized mode transforms the SDW structure into a magnetic spiral constraint to the \mathbf{ab} -plane (a), while the \mathbf{c} -polarized mode results in a \mathbf{bc} -spiral. This mode is the magnetic soft mode of the FE transition at T_{spiral} (b). In the left corner the vector product $\mathbf{S}_i \times \mathbf{S}_{i+1}$ is shown for the excited states with the different modes marked by the color code.

is very hard, and we do not expect it to contribute in the low-energy regime we are interested in.

The transverse magnetic fluctuations along \mathbf{a} and \mathbf{c} can again be divided into two different groups, according to the relative phase of the oscillation with respect to the ordered moment. At the magnetic zone center, the two in-phase modes retain the collinear spin configuration, and these modes correspond to the tilting of the magnetic structure along \mathbf{a} and \mathbf{c} , respectively. Hence, at $\mathbf{q} = 0$ both modes test the effective magnetic anisotropy Λ_i along \mathbf{a} and \mathbf{c} and are, therefore, expected to possess a finite energy in the case of TbMnO_3 . However, both in-phase modes, one polarized along \mathbf{a} and one along \mathbf{c} , are irrelevant for the ferroelectric transition and the magnetoelectric coupling, as the cross product between adjacent sites obviously vanishes in the collinear arrangement.

In contrast, the two out-of-phase, or $\frac{\pi}{2}$ -modes, are most relevant for the ferroelectric transition and couple to an electric polarization even in the paraelectric phase. The polarization schemes of both modes are shown in Fig. 5.13. Both

		polar.	phase	frequency	hybridized
Phason	ω_1^b	$\parallel \mathbf{b}$	0	soft	no
Magnitudon	ω_2^b	$\parallel \mathbf{b}$	$\frac{\pi}{2}$	hard	no
<i>ac</i> -spiral	ω_1^a	$\parallel \mathbf{a}$	$\frac{\pi}{2}$	soft	yes
<i>a</i> -tilt	ω_2^a	$\parallel \mathbf{a}$	0	Λ_a	no
<i>bc</i> -spiral	ω_1^c	$\parallel \mathbf{c}$	$\frac{\pi}{2}$	soft	yes
<i>c</i> -tilt	ω_2^c	$\parallel \mathbf{c}$	0	Λ_c	no

Table 5.3: Overview of the possible magnetic excitations in the collinear SDW arrangement summarizing the polarization pattern, the phase with respect to the static ordering, the expected frequency, and the possible coupling to a varying electric field of the various modes. For more details see the text.

transform the SDW ordering into a spiral structure – for the \mathbf{a} -polarized mode the spiral is constraint to the \mathbf{ab} -plane, while the \mathbf{c} -mode results in a \mathbf{bc} -spiral. Evaluating the central equation 5.9 for the excited states we obtain with φ_0 denoting the phase difference between neighboring sites

$$\begin{aligned} (\mathbf{S}_i \times \mathbf{S}_{i+1})^{\mathbf{a}\text{-pol}} &= (0, 0, \sin(\varphi_0)) \cdot \cos(\omega t) \quad \text{and} \\ (\mathbf{S}_i \times \mathbf{S}_{i+1})^{\mathbf{c}\text{-pol}} &= (\sin(\varphi_0), 0, 0) \cdot \cos(\omega t) \end{aligned} \quad (5.13)$$

for the \mathbf{a} and the \mathbf{c} polarized mode, respectively. Hence, with the modulation vector $\mathbf{k}_{\text{SDW}} \parallel \mathbf{b}$ the \mathbf{a} -mode should couple to an electric polarization \mathbf{P}_a along \mathbf{a} , and the \mathbf{c} -mode to an electric polarization \mathbf{P}_c along \mathbf{c} . Close to T_{FE} the energy of both modes is expected to be very low, since these modes condensate at the phase transition into the ferroelectric spiral phase. At zero field, it is the \mathbf{bc} -spiral which is realized in TbMnO₃, and, consequently, the $\frac{\pi}{2}$ -mode polarized along \mathbf{c} is the associated magnetic soft mode of the ferroelectric transition. The $\frac{\pi}{2}$ -mode along \mathbf{a} should be slightly harder – we recall, however, that a modest magnetic field flops the electric polarization and the energy of both $\frac{\pi}{2}$ -modes associated with the different orientations of the spiral is, therefore, expected to be comparable.

An overview of the possible spin-wave branches of the SDW structure is given in Tab. 5.3, summarizing the polarization pattern, the phase with respect to the static ordering, the expected frequency, and the possible coupling to an external a. c. electric field of the different modes. What still remains is the identification of the experimentally observed modes with the different modes just discussed, i. e. we have to combine the frequencies of Tab. 5.2 with the results given in Tab. 5.3. However, following the different character of the various branches associating the observed spin-wave excitations with one of the above modes appears apparent, and is already indicated by the labeling of the magnon branches in Tab. 5.3.

The polarized neutron experiment has revealed two \mathbf{a} -polarized excitations at $\hbar\omega_1^a = 0.31$ meV and $\hbar\omega_2^a = 2.16$ meV, respectively. Consequently, we attribute

these two modes with the ferroelectric **ab**-spiral mode, ω_1^a , and with the **a**-tilt mode, ω_2^a . The other four modes should all be detectable in the $S_{||}$ -channel, but we observe only two further components. As aforementioned, the longitudinal in-phase mode, the magnitudon, is expected to possess an energy beyond the energy range of our experiment, so that we are left with three modes. Two of these excitations, the sliding mode ω_1^b and the **bc**-spiral mode ω_1^c are very soft and we attribute the observed low-energy response in the $S_{||}$ -channel at $\hbar\omega_1^c \approx 0.1$ meV to the superposition of these two modes – with the energy resolution available we can not resolve a splitting of these two modes and they appear degenerate in the experiment.⁹ The third mode possesses a finite energy, $\hbar\omega_2^c = 1.32$ meV, and we have demonstrated that this mode is predominantly polarized along **c**. Hence, we attribute it with the in-phase **c**-mode.

The classification scheme just described is consistent with the phase diagram of TbMnO₃ and with the results of Pimenov et al., revealing an electromagnon response in the paraelectric SDW phase above T_{FE} [255]. In zero field the magnetic **bc**-spiral is stabilized, in agreement with our classification scheme as the **bc**-spiral mode is lower in energy than the corresponding mode polarized along **a**. A similar argument also confirms the identification of the two tilt excitations: Macroscopic measurements unambiguously show, that the orthorhombic **a**-axis is the magnetically hard axis [212]. As for $\mathbf{q} = 0$ the two tilt modes basically sense the magnetic anisotropy, the mode polarized along **a** should be highest in energy, as is found experimentally, and the observed level scheme of the different excitations is consistent with the macroscopic properties of TbMnO₃. Furthermore, in the IR data a electromagnon response is observed in the paraelectric phase for $T_{\text{FE}} < T$, too [255]. Compared to the FE phase the polarization of the electromagnons is the same, but the signal is shifted to lower energies and appears to be smeared out, see Fig. 5.10. This response has to be ascribed to the $\frac{\pi}{2}$ -modes ω_1^a polarized along **a**, which couples to an a. c. electric field and possesses a phonic counterpart.

5.2.4 Thermal evolution of the spin-wave spectrum

Having analyzed the magnetic excitation spectrum for the spiral phase at $T = 17$ K and for the SDW phase at $T = 32$ K in great detail, we now turn to the discussion of the thermal evolution and the apparent changes of the spin-wave spectrum across the ferroelectric spiral transition. For this purpose we have investigated the magnon spectrum at $\mathbf{Q} = (0 \ \varepsilon_b \ 1)$ for various temperatures below and above T_{spiral} using the high neutron flux of the PUMA spectrometer with the energy of the initial neutrons fixed to $E_i = 14.7$ meV. At a thermal instrument, the experimen-

⁹We stress, however, the very different character of both modes, since only the **bc**-spiral mode is connected with the ferroelectric transition. The phason and the spiral mode are both very soft, however due to very different reasons, and in this sense the observed degeneracy is accidental.

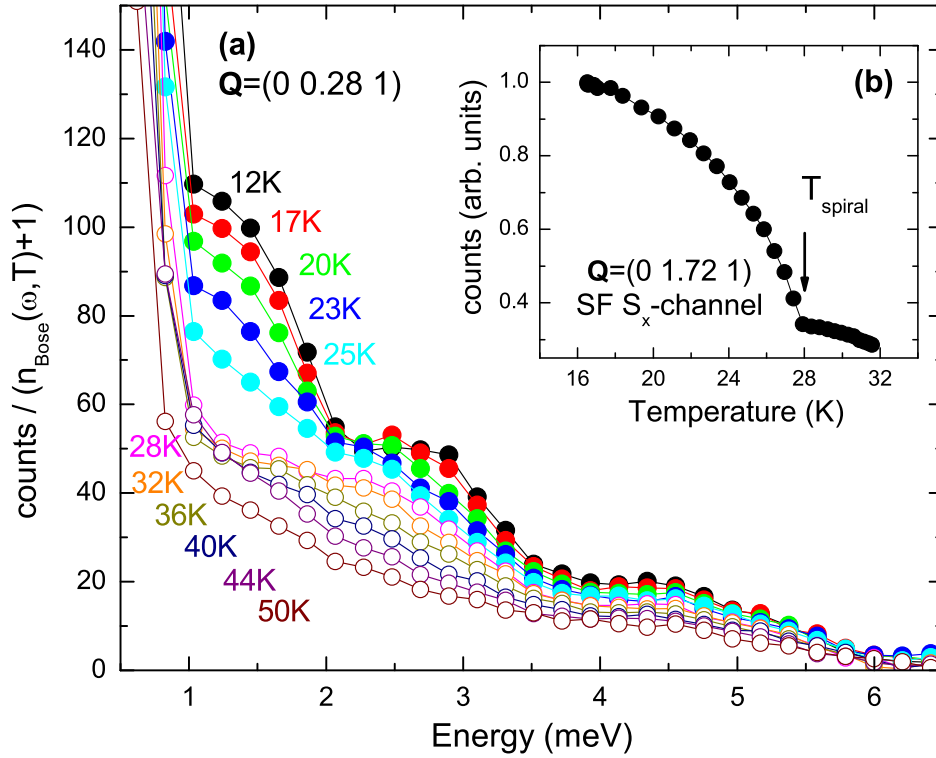


Figure 5.14: Temperature dependence of the zone-center spectrum Energy spectrum at the incommensurate zone center $Q = (00.281)$ measured at the thermal spectrometer PUMA. Full circles represent temperatures $T < T_{\text{spiral}}$, open symbols stand for $T > T_{\text{spiral}}$. The data are corrected for the population factor $(n(\omega, T) + 1)$ after the subtraction of a linear background (a). Polarization analysis of the development of the elastic spin-flip intensity for the quantization axis parallel to $Q = (01.721)$, recorded at the spectrometer IN14 (b). Lines are always included as guides to the eye.

tal resolution is significantly lower than on a cold source, but the high neutron flux provokes low counting times, essential for an extensive analysis of the temperature dependence; a typical counting time for the data presented in Fig. 5.14 is 1 min/point, which has to be compared to counting times of 8 min/point for sufficient, but still lower statistics on a cold spectrometer. To compare the scans at different temperatures, the data have to be corrected for the different Bose contributions. However, the Bose factor changes slightly within the resolution volume of a thermal instrument, and the correction would require the four-dimensional convolution of the resolution function with the dispersion surface. As it is not obvious how to perform such an analysis with the available data, we tentatively correct each data point by the Bose factor for the “nominal” energy, neglecting the small influence of the finite resolution in the correction. The results are presented in Fig. 5.14.

To characterize precisely the transition from the SDW into the ferroelectric spiral phase we show in the inset of Fig. 5.14 elastic data of the polarized experiment at the IN14. The temperature dependence of the spin-flip signal with the quantization axis parallel $\mathbf{Q} = (0\ 1.72\ 1)$, which is entirely magnetic intensity, exhibits a sharp, but continuous upturn at the transition temperature $T_{\text{spiral}} = 28\text{ K}$. As aforementioned, the chosen A -type Bragg-reflection $\mathbf{Q} = (0\ 1.72\ 1)$ includes an angle of 65.29° with the \mathbf{c}^* -axis of reciprocal space. Since only the component of the magnetization perpendicular to the scattering vector contributes to the cross section, the observed increase of the intensity at T_{spiral} essentially reflects the increase of the static \mathbf{c} -component of the magnetization as the spin-density wave transforms into the spiral ordering. Clearly, the transition is continuous and the phase transition is of second order, consistent with the reported thermodynamics of the FE transition [261, 262].

Considering the excitation spectrum in Fig. 5.14, magnetic fluctuations are resolvable even in the paramagnetic phase at $T = 50\text{ K}$ as a broad and structureless contribution. With decreasing temperature the inelastic signal increases in intensity and in the SDW phase below T_N magnetic scattering is visible in the entire energy range below $E = 3.5\text{ meV}$. As we have shown before, the excitation spectrum consists of at least four different contributions in the SDW regime. Due to the relaxed experimental resolution of the thermal instrument we integrate over sizable parts of the dispersion surface of the different modes, and in consequence the different modes can not be resolved anymore but appear as a single, rather broad feature in the energy scans. With the ferroelectric transition the spectrum changes significantly and two excitations seem to emerge continuously from the unmodulated structure. Upon further cooling down to $T = 12\text{ K}$ the spectral weight of these features rapidly increases and both signals appear well separated.

The data reveal nicely the drastic changes of the magnetic excitation spectrum at the SDW-to-spiral transition at T_{spiral} . Concomitant with the ferroelectric transition the excitation spectrum gets dominated by two well defined features, and comparing the thermal data with the detailed analysis of the spin-wave spectrum at $T = 17\text{ K}$ these modes obviously have to be associated with the two electromagnon features $\omega_{\perp 1/2}$. However, a reliable analysis of the thermal evolution close to the phase transition on the basis of the thermal data appears, unfortunately, impossible, as the relaxed resolution does not allow to reconstruct the behavior of the magnetic soft mode of the ferroelectric phase transition close to T_{spiral} . It seems, however, very intriguing to follow the thermal evolution of the ferroelectric soft mode and to characterize the temperature dependence of the electromagnon modes across the ferroelectric transition in more detail. Such an analysis, however, surely requires a careful and very time-consuming study on a cold triple-axis instruments using polarized neutrons in combination with an excellent energy resolution.

5.2.5 Field dependence of the spin-wave spectrum

The field dependence of the magnetic superstructure is obviously the key to the understanding of the gigantic magnetoelectric effects observed in $TbMnO_3$. However, unlike the thermal evolution of the magnetic structure in zero field, the impact of an applied magnetic field on the spiral structure has not yet been studied in detail, and the assumption of a field induced flop of the chirality of the spiral, which would imply the observed flop of the electric polarization from \mathbf{c} to \mathbf{a} , has not yet been confirmed by neutron-diffraction experiments for $TbMnO_3$. As such an experiment is extremely difficult to perform – a reliable data set on the magnetic structure requires the integration of a huge set of magnetic reflections within a large solid angle, whereas the cryomagnet supplying strong enough magnetic fields significantly restricts the experimentally accessible parts of reciprocal space – recent publications on $TbMnO_3$ focus on the evolution of only a few magnetic reflections with the field applied along various directions [242, 243, 263]. Nevertheless, in the closely related compound $Eu_{0.75}Y_{0.25}MnO_3$ the high field magnetic structure has been determined very recently and, indeed, concomitantly with the electric polarization the chirality of the magnetic spiral flops by 90° [10].

In the case of $TbMnO_3$, using x-ray and neutron diffraction techniques it has been shown that the polarization flop for $\mathbf{H} \parallel \mathbf{a}$ and $\mathbf{H} \parallel \mathbf{b}$ coincides with a transition into a commensurate magnetic phase with propagation vector $(0\ 0.25\ 1)$ [242, 243]. With the field applied along \mathbf{c} , the ferroelectric order melts and, simultaneously, the incommensurate modulation disappears, while a simple magnetic structure with propagation vector $(0\ 1\ 0)$ is stabilized [263]. These diffraction results are supplemented by experiments on the thermal expansion and magnetostriction, which unravel the first-order nature of the field induced incommensurate-to-commensurate transition [262].

We have studied the impact of a magnetic field on the excitation spectrum in the spiral phase. The experiment has been performed on the PANDA spectrometer using a 15 T cryomagnet.¹⁰ The geometry of the magnet together with the magnetic modulation along the \mathbf{b} axis restricts the possible choices for the scattering plane to the \mathbf{bc} -plane with the field applied along the vertical \mathbf{a} axis. However, in this configuration a maximum field of 12 T is well suited to switch between the two magnetic phases. The PANDA spectrometer was operated using the standard configuration with the energy of the scattered neutrons fixed typically to $E_f = 4.66$ meV. All measurements presented in this section were performed at $T = 17$ K.

Field dependence of the elastic signal Before we consider the spin-wave spectrum we begin with the discussion of the field dependence of the elastic magnetic

¹⁰Due to technical reasons the maximum field reachable was limited to 12 T at the time of the experiment.

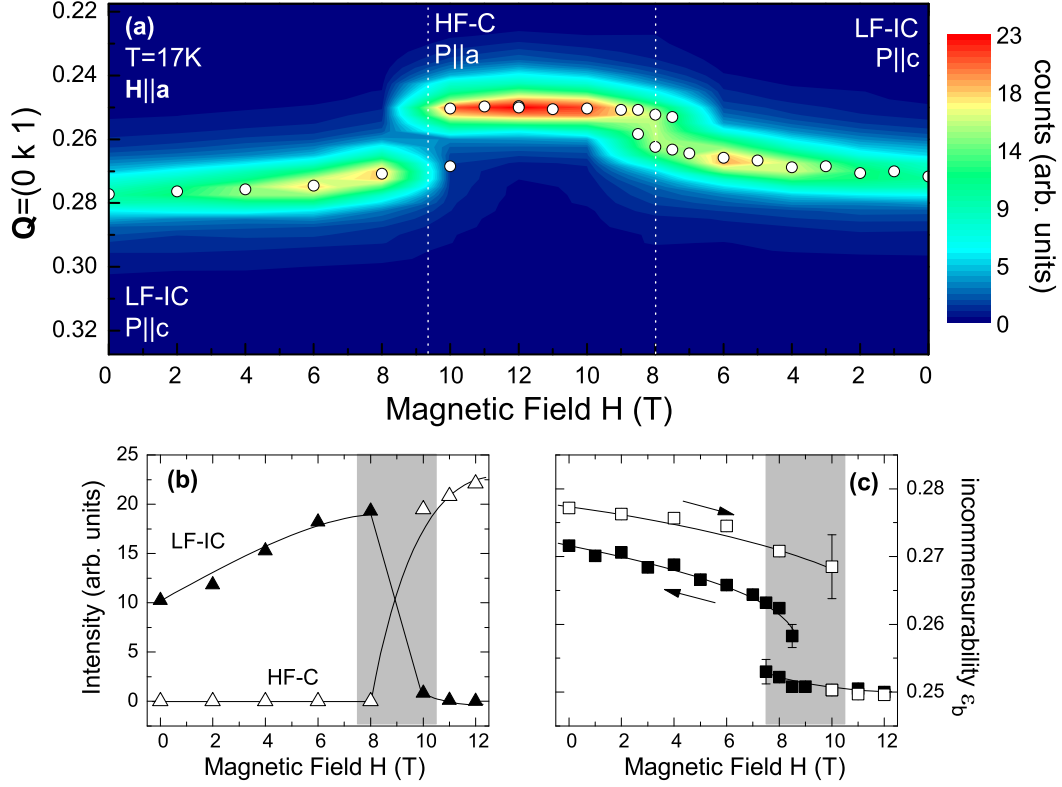


Figure 5.15: Field dependence of the magnetic modulation Intensity mapping of a cut through reciprocal space along the line $(0 k 1)$ for a complete field cycle $H_a = 0 \text{ T} \rightarrow 12 \text{ T} \rightarrow 0 \text{ T}$ with the field applied along \mathbf{a} . Open points mark the positions of the magnetic Bragg reflections and dotted lines denote the phase transitions between the low-field incommensurable (LF-IC) and the high-field commensurable structure (HF-C) as found by thermodynamic measurements [261, 262] (a). Intensity of the magnetic superstructure reflection $\mathbf{Q} = (0 \varepsilon_b 1)$ with the applied field increasing from 0 T to 12 T (b) and field dependence of the incommensurability ε_b for the complete field cycle (c). The gray-shaded regions mark regimes with coexistence of both magnetic phases.

signal. Figure 5.15 summarizes the evolution of the magnetic superstructure reflection $\mathbf{Q} = (0 \varepsilon_b 1)$ with a magnetic field applied along \mathbf{a} .

Upon increasing field we find a continuous increase of the magnetic intensity. The magnetic modulation remains nearly unchanged up to 8 T, and we observe only a slight decrease of the zero-field incommensurability $\varepsilon_b^0 = 0.2772(1)$. With further increasing field $\varepsilon_b(H)$ exhibits a sharp discontinuity around a critical field $H_{\uparrow}^a \approx 9 \text{ T}$, and for $H > H_{\uparrow}^a$ the magnetic intensity appears centered around the commensurable position $\mathbf{Q} = (0 0.25 1)$. In the vicinity of the first order transition a region of coexistence of both incommensurable (IC) and commensurable (C) phases can be observed, and the 10 T-data can best be described assuming two different magnetic contributions. Ramping the field down again the commen-

surable phase is stable until the critical field $H_{\uparrow}^a \approx 8$ T, below H_{\uparrow}^a the system switches back into the incommensurable magnetic modulation. Again, around the phase transition a region of phase coexistence can be found, which appears broader than with increasing field. The pronounced hysteresis and the size of the critical fields H_{\uparrow}^a and H_{\downarrow}^a is in good congruence with the reported phase diagram based on high-precision thermal expansion measurements [262].

Besides the magnetic hysteresis a complete field cycle $H_a = 0$ T \rightarrow 12 T \rightarrow 0 T reveals an unusual behavior of the magnetic incommensurability. Upon decreasing field the incommensurability does not fully recover its initial value ε_b^0 at zero field, see Fig. 5.15c: Switching back from the HF-C into the LF-IC phase the magnetic incommensurability $\varepsilon_b(8$ T $_{\downarrow}) \approx 0.2624(3)$ is significantly reduced compared to the initial upward run. With further decreasing field ε_b slightly increases, but stays always well below the value obtained when ramping up the magnetic field. After the complete magnetic cycle we determine a magnetic incommensurability $\varepsilon_b^* = 0.2716(1)$ at zero field, which is reduced by $\approx 2\%$ compared to the incommensurability ε_b^0 before switching on the field. The full magnetic incommensurability $\varepsilon_b^0 = 0.277$ can only be recovered by heating up the sample above the spiral transition temperature to $T = 35$ K and subsequently cooling down to 17 K. Hence, in the spiral phase the magnetic system memorizes its magnetic history even at zero field, and the size of the magnetic incommensurability at zero field depends on the magnetic diary of the sample.

To take into account this magnetic memory effect and to ensure always identical conditions in the investigation of the field dependence of the magnon spectrum, all data presented below have been obtained in an upward run of the field after a careful check of the magnetic incommensurability at zero field.

Magnetic excitations In Fig. 5.16, the magnetic excitation spectra recorded at the magnetic zone center $\mathbf{Q}_1 = (0 \varepsilon_b 1)$ is shown for various magnetic fields up to 12 T. However, before we analyze the changes in the spin-wave spectrum of the Mn-sublattice we first have to briefly consider the impact of the magnetic field on the Tb crystal-field excitations.

We observe the lowest excitation within the Tb³⁺ J -multiplet at $E_{\text{CEF}} = 4.5$ meV, which for $g = 2$ corresponds to a magnetic energy of ≈ 78 T. Since in the orthorhombic symmetry the 7F_6 -configuration splits into 13 singlet states [250] we thus can neglect the influence of the applied field on the CEF-level scheme. Indeed, up to a maximum field of 12 T we do not observe any changes in the neutron spectra for energies $E > 3.5$ meV, see Fig. 5.16c. Hence, in the following analysis we will always disregard the influence of the magnetic field on the Tb crystal-field excitations.

In contrast, in the energy region of the magnon excitations below 3.5 meV drastic changes can be observed: For low magnetic fields the structure of the spectrum

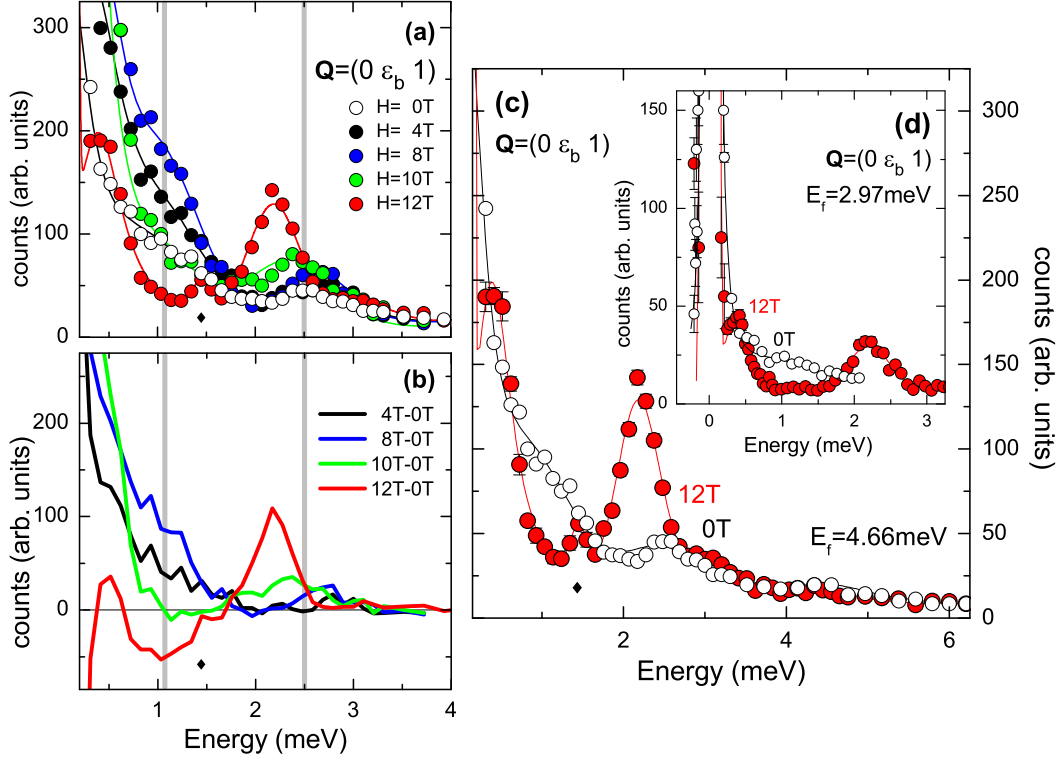


Figure 5.16: Field dependence of the magnetic excitation spectrum Energy scans for various magnetic fields applied parallel to \mathbf{a} at the magnetic zone center $Q_1 = (0 \ \varepsilon_b \ 1)$ at $T=17\text{K}$. Colored lines are fits to the data as described in the text and vertical gray lines mark the position of the two orthogonal modes $\omega_{\perp 1/2}$ in zero field (a). Difference spectra between the data in finite and zero field presented in (a) (b). Comparison of the spectra at $H = 0\text{T}$ and 12T recorded with $E_f = 4.66\text{meV}$ (c), and with enhanced resolution and $E_f = 2.98\text{meV}$ (d). In the 12T -data a spurious contribution is always visible around $\approx 1.5\text{meV}$, marked by small black diamonds, for $E_f = 4.66\text{meV}$. All scans were taken at the PANDA spectrometer. The zero-field data are the same as presented previously.

at $Q_1 = (00.281)$ does not change significantly and for 4T and 8T we find the same characteristic three magnon branches of the spiral ordering as in zero field. However, within the experimental configuration with $E_f = 4.66\text{meV}$, only the two orthogonal modes are well resolvable, the low-lying phason mode is superimposed with the elastic signal and appears as a broadening of the tail of the magnetic Bragg reflection. All spectra for the LF-IC phase can be described using comparable parameter sets as for the zero field data and the fitting process always yields energies for the two orthogonal modes $\omega_{\perp 1/2}$ similar to the frequencies previously obtained for $H = 0\text{T}$. The energy and the width of the phason mode were fixed to their zero-field values in the refinement. With increasing field, all modes

gain neutron intensity, which is consistent with the field response of the elastic magnetic signal.

At the transition into the HF-C phase, the magnon spectrum changes considerably and for $H = 12$ T the data exhibit remarkable differences compared with the low-field spectra, see e. g. the difference spectra in Fig. 5.16b: The 12 T-spectrum is dominated by two intense excitations centered around ≈ 0.5 meV and ≈ 2.0 meV. A third excitation, though weaker, is resolvable around ≈ 3.0 meV, but the inelastic intensity at 1 meV is completely suppressed with the transition into the high field phase. An additional, sharp feature is detectable in the data taken at 12 T around ≈ 1.5 meV, marked in Fig. 5.16 by small diamonds. However, we ascribe this feature to a spurious contribution, as it disappears by changing the wavelength, see Fig. 5.16d, is not visible at equivalent Bragg positions, and does not exhibit a significant dispersion, in contrast to all other observable signals. Therefore, we will ignore this feature in the following discussion.

To resolve the behavior of the phason mode across the IC-to-C transition in more detail, we have repeated the scan at $H = 12$ T with the analyzer energy fixed to 2.98 meV, see Fig. 5.16d. With the enhanced experimental resolution the low-lying excitation appears better separated and the Bragg tail develops a Gaussian line shape in the high-field phase.¹¹ Following the previous analysis of the low-field spectra the description of the high-field data is straightforward. Using a Lorentzian for the low-energy and Gaussian line shapes for the two higher-energy modes, the combination of both data sets yields the frequencies $\omega_{\perp 1}^C = 0.44(1)$ meV, $\omega_{\perp 2}^C = 3.06(2)$ meV and $\omega_{\parallel}^C = 2.20(2)$ meV for the three different magnon branches of the HF-C phase.

So far, we have not yet considered the spectrum at $H = 10$ T. At this critical field close to the first-order phase transition the analysis of the elastic data proves the coexistence of both LF-IC and HF-C phases, and the inelastic spectrum can well be explained assuming two different contributions, too. At $H = 10$ T the observed spectrum deviates considerably from the low-field data as the magnon branch at 1.05 meV is severely suppressed. However, the structure of the high-field phase observed for $H = 12$ T has not yet developed completely and the data are well described by scaling a weighted summation of the 8 T and 12 T models to the 10 T-spectrum, see Fig. 5.16a.

Resuming the field dependence of the spectra at $\mathbf{Q} = (0 \ \varepsilon_b \ 1)$ presented so far, our neutron data unravel three different magnon branches for the commensurate high-field phase with polarization $\mathbf{P} \parallel \mathbf{a}$, similar to the spin-wave spectrum of the spiral phase with polarization \mathbf{P}_c at zero field. However, unlike to the zero field phase the strong magnetic field does not allow us to use polarized neutrons to explore the polarization schemes of the different modes in the HF-C phase.

¹¹Notice the different shape of the elastic line in the zero-field data, which once more points to the inelastic contribution of the low-lying phason mode

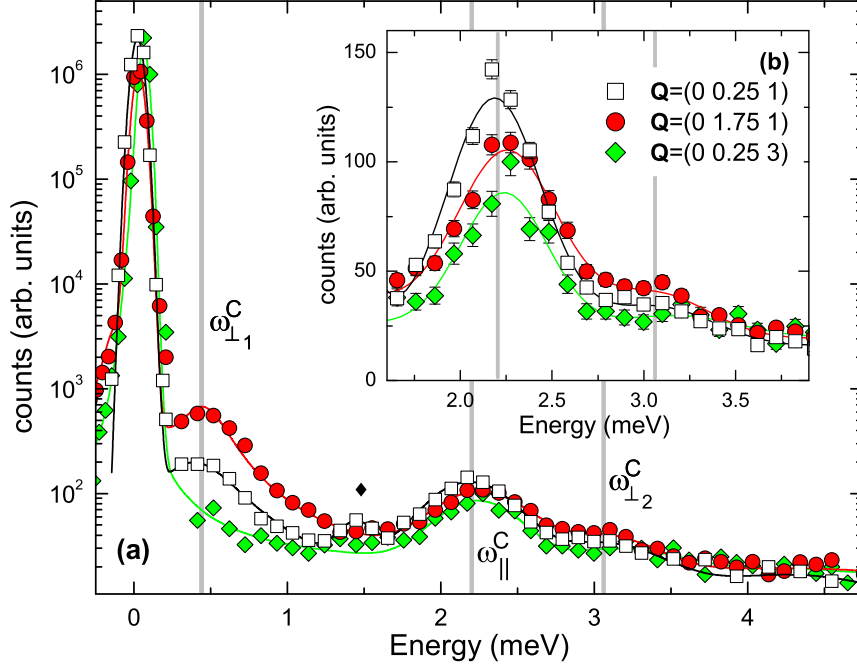


Figure 5.17: \mathbf{Q} -dependence of the spectrum at $H = 12\text{T}$ Energy spectrum of the spin-wave excitations in the HF-C phase at $H = 12\text{T}$ measured at the three equivalent A -type zone centers $\mathbf{Q}_1 = (00.25\ 1)$, $\mathbf{Q}_2 = (01.75\ 1)$ and $\mathbf{Q}_3 = (00.25\ 3)$ on a logarithmic (a) and linear scale (b). Solid lines correspond to the fits as described in the text and vertical gray bars mark the positions of the three magnon branches of the HF-C phase. Measurements were performed at the PANDA spectrometer with the energy of the scattered neutrons fixed to $E_f = 4.66\text{ meV}$. Small diamonds mark regions with spurious contributions, see text.

Nevertheless, as we will show next applying the fundamental selection rules of magnetic neutron scattering, the \mathbf{Q} -dependence of the scattered intensities may suggest at least a qualitative classification.

In Fig. 5.17 we compare the spectra for $H = 12\text{T}$ obtained at the three A -type zone centers $\mathbf{Q}_1 = (00.25\ 1)$, $\mathbf{Q}_2 = (01.75\ 1)$ and $\mathbf{Q}_3 = (00.25\ 3)$. Because of the limited beam time the energy of the scattered neutrons was fixed to $E_f = 4.66\text{ meV}$ for these scans, although an improved resolution might have been desirable. All spectra exhibit a similar structure, and the data recorded at \mathbf{Q}_2 and \mathbf{Q}_3 yield the same energies for three magnon branches as the one at \mathbf{Q}_1 discussed before. Of course, such a behavior has to be expected, as all three \mathbf{Q} -vectors are equivalent Bragg positions in reciprocal space. However, with the different choices of the scattering vector \mathbf{Q} we substantially affect the scattering geometry; while \mathbf{Q}_1 and \mathbf{Q}_3 include only a small angle α with the \mathbf{c}^* -axis, $\alpha_1 = 17.53^\circ$ and $\alpha_3 = 6.01^\circ$, respectively, \mathbf{Q}_2 and \mathbf{c}^* span an angle of 65.67° . As only the component of the magnetization perpendicular to the scattering vector \mathbf{Q} contributes to the

magnetic cross section, a magnetic fluctuation along $\mathbf{c} = \mathbf{c}^*$ will thus give an intense response at \mathbf{Q}_2 , while its intensity at \mathbf{Q}_1 and \mathbf{Q}_3 should be significantly reduced.

Considering first the \mathbf{Q} -dependence of the intensity for the branch $\omega_{\perp 1}^C$ in Fig. 5.17, the mode appears most intense at \mathbf{Q}_2 , whereas it is hardly detectable at \mathbf{Q}_3 . This behavior reminds of the properties of a fluctuation with a large \mathbf{c} -component. Indeed, correcting the intensities for the different magnetic form factors the observed ratio $I_{\omega_{\perp 1}, \mathbf{Q}_1}^{\text{obs}} : I_{\omega_{\perp 1}, \mathbf{Q}_2}^{\text{obs}} = 1 : 4.8(4)$ resembles the expected behavior for a purely \mathbf{c} -polarized mode with $I_{\mathbf{Q}_1} : I_{\mathbf{Q}_2} = 1 : 6.2$, providing a predominant contribution along \mathbf{c} for $\omega_{\perp 1}$. Regarding next the mode ω_{\parallel}^C , the \mathbf{Q} -dependence of the scattered intensity is reversed compared to that of $\omega_{\perp 1}^C$, and the distribution of spectral weight follows the magnetic form factor, as the observed intensity decreases continuously from \mathbf{Q}_1 to \mathbf{Q}_3 . The third branch $\omega_{\perp 2}^C$ again resembles the behavior of the first mode and the signal is most pronounced at \mathbf{Q}_2 .

Summarizing the \mathbf{Q} -dependencies of the different magnon branches, we conclude that the two modes $\omega_{\perp 1}^C$ and $\omega_{\perp 2}^C$ possess a different character than the third mode ω_{\parallel}^C . In analogy with the analysis of zero-field excitations we tentatively refer to the branches $\omega_{\perp 1/2}^C$ as orthogonal modes in the following, while the mode ω_{\parallel}^C may be labeled as the sliding mode. However, while in the zero field phase the longitudinal polarization analysis clearly confirms an \mathbf{a} -character for the two orthogonal modes, the \mathbf{Q} -dependence of the modes $\omega_{\perp 1/2}^C$ suggests a polarization along \mathbf{c} for these modes in the HF-C phase. The sliding mode seems to change its polarization pattern across the polarization-flop transition, too; in the LF-IC phase the phason is polarized within the \mathbf{bc} -plane, whereas we can exclude a significant component along \mathbf{c} of the sliding mode ω_{\parallel}^C in the HF-C phase.

Experimental evidence for the field-induced flop of the magnetic spiral As has been mentioned several times already, on the basis of the theory developed by Katsura et al. [12] and Mostovoy [13] the magnetic field-induced flop of the electric polarization from \mathbf{P}_c to \mathbf{P}_a may be understood by the change of the chirality of the magnetic spiral structure from a rotation around the \mathbf{a} -axis with the moments in the \mathbf{bc} -plane to a rotation around \mathbf{c} with the spins confined to the \mathbf{ab} -plane. What would such an interpretation imply for the magnon spectrum in the high-field phase?

Following the discussion of the magnetic excitations in the spiral phase at zero field [253], we expect three low-lying magnon branches for an \mathbf{ab} -spiral. However, as the spins rotate around \mathbf{c} instead of \mathbf{a} , the polarization pattern of the different modes are supposed to be interchanged: The phason mode of the spiral is no longer polarized within the \mathbf{bc} -plane, but should correspond to a fluctuation parallel to the \mathbf{ab} -plane, and the two orthogonal modes $\omega_{\perp 1/2}$ polarized initially

		$H = 0$ T		$H = 12$ T	
		Energy (meV)		Energy (meV)	
sliding mode	ω_{\parallel}	0.11 ± 0.05	$\parallel \mathbf{bc}$	2.20 ± 0.02	$\parallel \mathbf{ab}$
orthogonal modes	$\omega_{\perp 1}$	1.07 ± 0.05	$\parallel \mathbf{a}$	0.44 ± 0.01	$\parallel \mathbf{c}$
	$\omega_{\perp 2}$	2.50 ± 0.08	$\parallel \mathbf{a}$	3.06 ± 0.02	$\parallel \mathbf{c}$

Table 5.4: Comparison of the observed energies and estimated polarization schemes of the magnetic zone center excitations in the LF-IC and the HF-C phase at $T = 17$ K.

along \mathbf{a} are expected to transform into \mathbf{c} -polarized fluctuations in the high-field structure. These considerations agree nicely with our observations of the field dependence. Indeed, for $H = 12$ T we find three well-separated magnon branches, two of them are predominantly polarized parallel and the third perpendicular to \mathbf{c} , just opposite to the polarization patterns in zero field, see table 5.4.

Considering the energy scheme of the spin-wave spectrum, the sequence of the different magnon branches has also been affected by the spiral-flop transition. While in zero field the phason mode of the spiral is very low in energy, $\hbar\omega_{\parallel} \lesssim 0.11$ meV, it is significantly increased in the HF-C spiral as we find $\hbar\omega_{\parallel}^C = 2.20$ meV. This distinct behavior might be attributed to different pinning potentials; in the HF-C phase the magnetic field \mathbf{H}_a is applied parallel to the spin-rotation plane of the \mathbf{ab} -spiral and, consequently, the phase of the spiral might be fixed by the applied field resulting in a substantial hardening of the phason mode.¹² In contrast, the energy of the two orthogonal modes $\omega_{\perp 1/2}^C$ is comparable with their zero-field counterparts. Moreover, from the above analysis it is evident, that at least one of these two modes should be hybridized with a phonon and, as the spiral is rotated by 90° , couple to the dynamic electric polarization along \mathbf{c} . Hence, a comparison of our high-field neutron data with IR spectroscopy seems very desirable, but, unfortunately, optical data acquired in the proper experimental setup – i. e. electric a. c. component \mathbf{e} parallel to \mathbf{c} and a sufficient magnetic field applied along \mathbf{a} – are, best to our knowledge, not yet available.

In summary, with a magnetic field \mathbf{H} applied parallel \mathbf{a} the magnetic excitation spectrum exhibits significant changes at the critical field inducing the flop of the electric polarization. Similar to the zero-field spectrum we are able to resolve three different magnon branches in the high-field phase. The different polarization schemes of the various modes, two are polarized predominantly along and one perpendicular to \mathbf{c} , strongly supports the interpretation of a field-induced flop

¹²The field should even affect the static properties of the spiral as a parallel configuration of the ordered moment to the field is more favorable than an antiparallel. A plausible magnetic structure would thus consist of the rotation of the spins around a finite value $\mathbf{S} = (S_a 00)$ within the \mathbf{ab} -plane, i. e. a spiral around a finite moment S_a .

of the chirality of the magnetic spiral structure from a rotation around \mathbf{a} in the low-field to a rotation around \mathbf{c} in the high-field phase.

5.3 Spin-wave dispersion in TbMnO₃

So far we have only considered the magnetic excitation spectrum for $\mathbf{q} = 0$, i. e. at the center of the magnetic Brillouin zone. In this section we will extend the analysis and discuss the spin-wave dispersion along the \mathbf{a} -, \mathbf{b} -, and \mathbf{c} -direction of the orthorhombic crystal structure at two different temperatures, in the ferroelectric spiral phase at $T = 23$ K, and in the paraelectric SDW phase at $T = 32$ K. A comprehensive analysis of the full magnon dispersion will yield detailed insights into the strength of the relevant magnetic exchange couplings and allows to compare the magnetic interactions in TbMnO₃ underlying the complex magnetic structure with those of other, less distorted perovskite manganites with commensurable ordering schemes.

Experiments to determine the spin-wave dispersion in TbMnO₃ were performed at the same spectrometers as used for the analysis of the spectrum at $\mathbf{q} = 0$: at the thermal instruments 1T.1 and PUMA, and at the cold machines 4F.2 and PANDA, installed at the LLB in Saclay and at the FRM2 in Munich, respectively. Data using polarized neutrons were acquired at the IN14 spectrometer. As pointed out in the previous discussion, to fully resolve all details of the excitation spectrum an excellent resolution is desirable, but often not practicable due to the restricted amount of beamtime. In order to achieve a comprehensive overview of the complete \mathbf{q} -dependence of the excitation spectrum we usually used the high flux of the thermal instruments with relaxed experimental resolution. As before, selected scans were then repeated at the cold instruments with significantly increased resolution to extract the different contributions in the spectra. The determination of the dispersion is further complicated by the Tb-CEF, which at finite \mathbf{q} strongly interferes with the spin-wave signal.

To cope with all of these difficulties, we present the different branches of the dispersion in order of increasing complexity: First we will discuss the magnon dispersion along the \mathbf{c} - and the \mathbf{a} -direction of the orthorhombic crystal structure, starting with the spectrum in the spiral phase at $T = 23$ K, followed by the discussion of the SDW phase at 32 K. Along these directions the magnetic coupling is always anti-, respectively ferromagnetic [222], and the shape of the dispersion is basically determined by the nearest-neighbor exchange coupling J_{AFM} and J_{FM} . Finally, we deal with the dispersion along \mathbf{b} , i. e. parallel to the modulation \mathbf{k} of the magnetic structure. Here, the spin-wave spectrum is strongly affected by the competition of the two magnetic interactions responsible for the complex magnetic structure, the FM coupling J_{FM} between nearest neighbors and the AFM exchange J_{NN} of next-nearest neighbors along \mathbf{b} , and the shape of the dispersion strongly

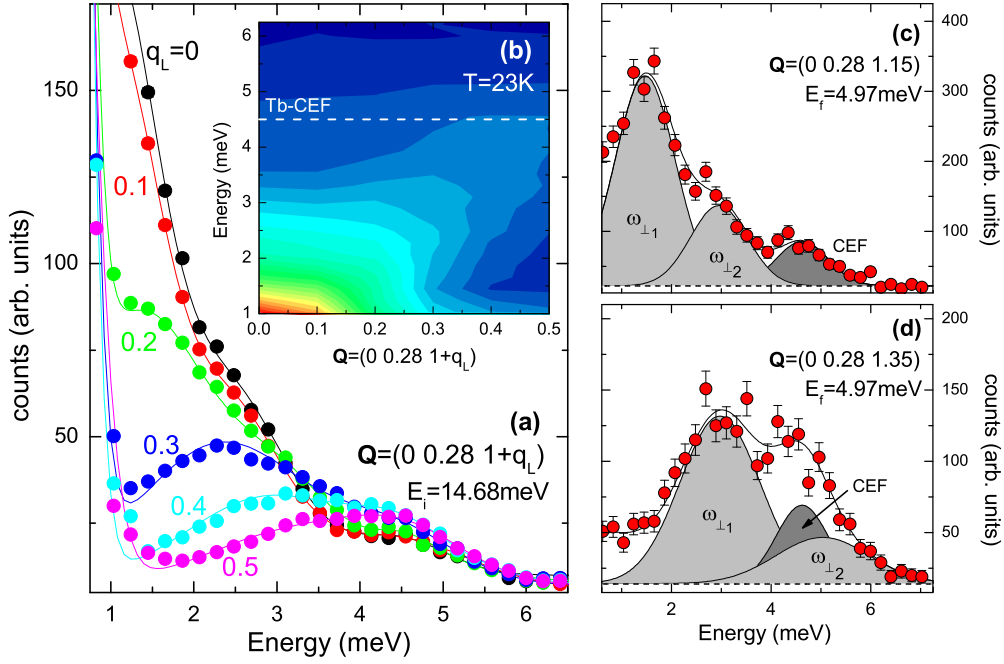


Figure 5.18: Analysis of the spin-wave dispersion (I.) Raw-data scans at $\mathbf{Q} = (00.281 + q_L)$ to determine the spin-wave dispersion in the FE spiral phase at $T = 23$ K along \mathbf{c} , recorded at the PUMA spectrometer with $E_i = 14.7$ meV (a). Contour plot of the dispersion calculated from the data shown in (a), blue corresponds to low, red to high neutron count rate (b). Energy scans along $(00.281 + q_L)$ taken at the spectrometer 4F.2 with $E_f = 4.97$ meV and enhanced experimental resolution for $q_L = 0.15$ (c), and 0.35 (d). Lines denote fits to the data with Gaussians, in (c) and (d) the various contributions to the spectra are marked by the gray-shaded profiles, see text for details. Note that the CEF excitation is described by the same parameter set in (c) and (d).

deviates from that of a simple antiferromagnet.

5.3.1 Dispersion along \mathbf{a} and \mathbf{c} : nearest-neighbor exchange

As aforementioned, we begin with the discussion of the dispersion along \mathbf{c} , as this turns out to be most instructive. In Fig. 5.18, we present representative energy scans along $\mathbf{Q} = (00.281 + q_L)$ to determine the magnon dispersion in the FE spiral phase at $T = 23$ K, measured at the PUMA spectrometer with relaxed resolution and E_i fixed to 14.7 meV, Fig. 5.18a, and with increased energy resolution and $E_f = 4.97$ meV recorded at the cold spectrometer 4F.2, Fig. 5.18c,d. Starting at the zone center, $\mathbf{q} = 0$, the data clearly reveal, how the inelastic signal propagates with increasing \mathbf{q} through the Brillouin zone. At the zone boundary, $q_L = 0.5$, the signal appears centered around 4 meV, and partly overlaps with the Tb-CEF excitation, which is visible in all scans around $E_{\text{CEF}} = 4.5$ meV.

From the extensive analysis of the zone-center spectrum it is clear, that in the FE phase the spectrum at $\mathbf{q} = 0$ consists of three contributions, the spiral mode ω_{\parallel} at very low, and the two orthogonal modes $\omega_{\perp_{1,2}}$ at finite energies. For small momentum transfers $|\mathbf{q}|$ close to the zone center, this decomposition of the spectrum should be valid as well, and in order to resolve the different contributions, Fig. 5.18c shows the spectrum for $q_l = 0.15$ recorded with enhanced energy resolution $\Delta E \approx 150 \mu\text{eV}$. Indeed, in addition to the CEF excitation two additional modes are resolvable around 1.5 meV and 3 meV, which we identify with the two \mathbf{a} -polarized modes $\omega_{\perp_{1,2}}$. A third excitation at lower energies can not be resolved due to the strong overlap with the incoherent elastic signal. Note however, that at $\mathbf{q} = 0$ the phason mode was also hard to detect using unpolarized neutrons, the final identification of the soft mode has only been achieved by the use of polarized neutrons. For larger magnon momenta \mathbf{q} , both modes remain resolvable in the spectra, but close to the zone boundary the energy of the second mode ω_{\perp_2} becomes comparable with those of the CEF excitation, significantly hampering the analysis of the data. Hence, for a quantitative analysis of the spectra, great care has to be taken on a consistent description of the Tb crystal field.

Keeping these annotations in mind, we are now prepared to interpret all observed spectra and to extract the magnon dispersion along \mathbf{c} for the spiral phase. For a quantitative modeling of the data we included two different magnon contributions in addition to the elastic line at $E = 0 \text{ meV}$ and the CEF excitation. In the fitting process, we always assumed Gaussian profiles for the different components. Of course, the starting point for the description were the results derived in the analysis of the zone-center spectrum. Moreover, to handle the influence of the crystal field, a common parameter set was used for the CEF excitation in all spectra, which was not allowed to vary during the refinement. At the end, the analysis of the thermal data was checked against the results obtained from the data collected on the cold instruments, so that finally a consistent picture was achieved. Using this procedure, the refinement yields a reasonable description for all observed spectra, see Fig. 5.18. However, before we proceed with the discussion of the results of this analysis, we first continue with the spin-wave dispersion in the paraelectric SDW phase, and with the \mathbf{q} -dependence of the magnetic excitation spectrum parallel to \mathbf{a} , which were both analyzed in a similar way.

In Fig. 5.19, we show typical scans to determine the spin-wave dispersion along \mathbf{c} in the paraelectric phase at $T = 32 \text{ K}$. Again, the data nicely prove how the inelastic signal propagates with increasing $|\mathbf{q}|$ towards the zone boundary. However, compared to the spectra in the FE spiral phase the signal appears now broader and less structured. Following the discussion of the zone-center spectrum, the different shape of the spectra appears reasonable, as the four different magnon branches of the SDW phase can only be resolved with the help of polarized neutrons. With unpolarized neutrons, however, we sum over the different branches and the spectrum can tentatively be modeled assuming two different contributions: a broad

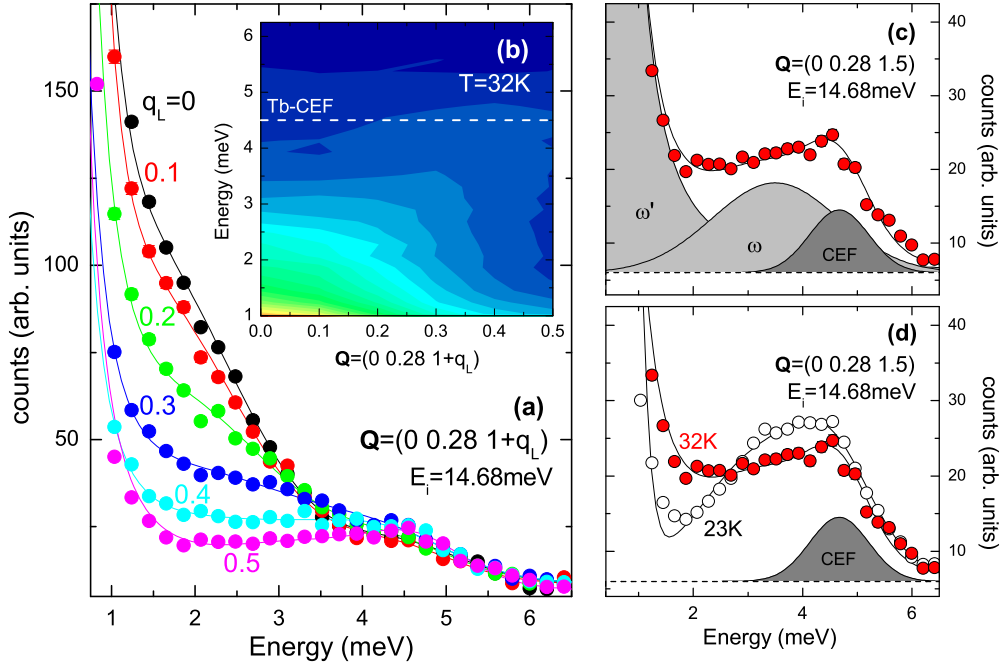


Figure 5.19: Analysis of the spin-wave dispersion (II.) Raw-data scans at the same positions as presented in Fig. 5.18, but taken in the paraelectric SDW phase at $T = 32\text{ K}$ (a). Contour plot of the dispersion calculated from the data shown in (a) (b). Note that the intensity scale in the contour plot is the same as in Fig. 5.18b. Exemplary analysis of the zone-boundary spectrum at $q_L = 0.5$ showing the decomposition into the different contributions (c). Comparison of the zone-boundary spectra in the spiral and in the SDW phase, the parameter set for the CEF excitation is the same for both spectra (d). In all panels lines denote fits to the data as described in the text.

Gaussian at finite energies, and a Lorentzian describing the low energy mode close to the tail of the elastic line. This decomposition holds for all spectra along the line $Q = (0\ 0.28\ 1 + q_L)$ up to the zone boundary with $q_L = 0.5$, see Fig. 5.19c. A dispersion can, however, only be resolved for the mode at finite energies, the low-energy contribution remains always within the energy resolution of the elastic line and cannot be analyzed properly with the existing data.

Along \mathbf{a} the magnetic coupling is always ferromagnetic for both magnetic phases [222], and the magnetic Brillouin zone extends up to integer-indexed values for q_h , i. e. along the line $Q = (q_h\ 0.28\ 1)$ the spin-wave disperses up to $q_h = \pm 1$. Typical scans aiming at the dispersion in this direction for $T = 23\text{ K}$ and 32 K are shown in Fig. 5.20. It is immediately clear, that along \mathbf{a} the spin-wave signal extends to higher energies than along \mathbf{c} , reaching up to 8 meV at the zone boundary.

In the spiral phase, Fig. 5.20a and b, the magnetic intensity is again split into two spin-wave branches, and the splitting appears to persist throughout the whole magnetic zone. Both modes propagate continuously and “tunnel” through the Tb

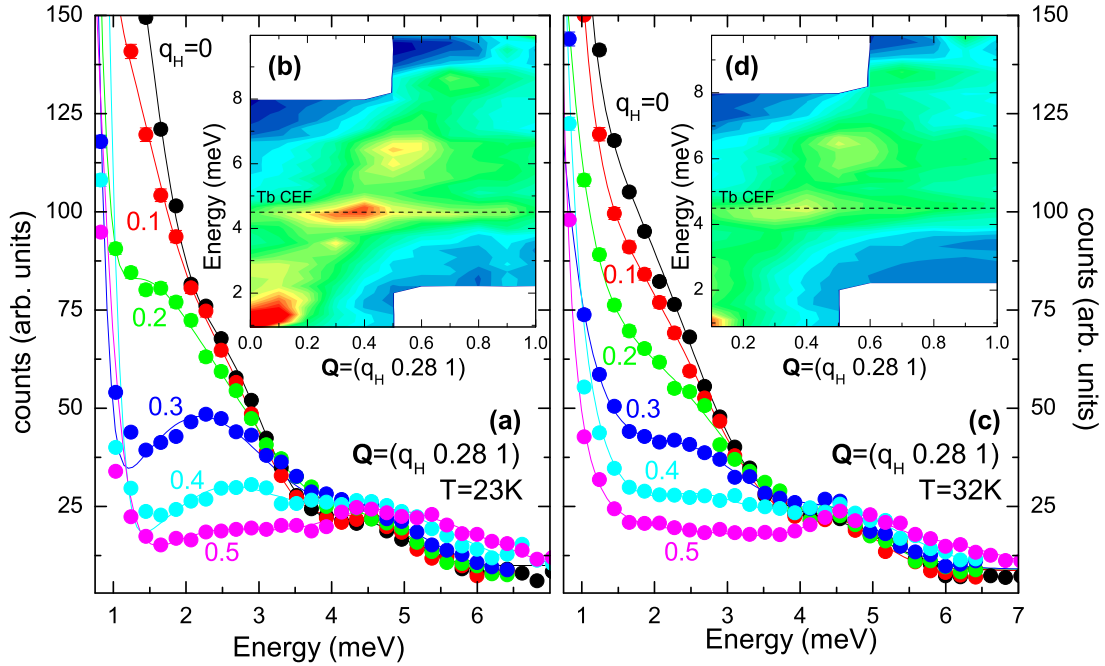


Figure 5.20: Analysis of the spin-wave dispersion (III.) Raw-data scans at $Q = (q_h, 0.28, 1)$ to determine the low-energy part of the spin-wave dispersion in the FE spiral-phase at $T = 23\text{K}$ along \mathbf{a} , recorded at the PUMA spectrometer with $E_i = 14.7\text{meV}$ (a). Contour plot of the inelastic structure factor $S(Q, \omega)$ for $Q = (q_h, 0.28, 1)$ calculated from a grid of data as shown in (a) for $0 \leq q_h \leq 1$ and $\Delta q_h = 0.1$. Blue denotes low, red high neutron intensity (b). The same scans as presented in (a), but for $T = 32\text{K}$, i.e. in the SDW phase (c). Contour plot of $S(Q, \omega)$ for 32K , similar to (b) (d). Note that the intensity scale is the same in (b) and (d).

CEF excitation touching the zone boundary $Q = (1, 0.28, 1)$ at 6meV and 8meV , respectively. Note, how the spin wave interferes with the CEF excitation in the intensity mapping around $q_h = 0.4$, Fig. 5.20b, and we stress once more that a consistent description of the Tb-CEF is essential for the quantitative analysis of the magnon dispersion: For all spectra we used the same parameter set to describe the parasitic contribution of the crystal field.

In the paraelectric phase at 32K the spectra with small $|\mathbf{q}|$ appear less structured with a single, broad magnon contribution at finite energies, similar to the spectra along the antiferromagnetic \mathbf{c} -direction, see Fig. 5.20c. However, for $q_h \geq 0.5$ the magnon signal splits again into two contributions centered around 6meV and 8meV , resembling the high-energy behavior in the spiral phase. The splitting appearing in the paraelectric phase may be associated with a different \mathbf{q} -dependence of the various magnon branches of the SDW structure, the polarization analysis has revealed four different contributions at $\mathbf{q} = 0$, but a detailed discussion of this aspect would require more reliable experimental data, as e.g. a study

with polarized neutrons and enhanced experimental resolution. Consequently, in our analysis we included a single, broad magnon contribution for the low $|\mathbf{q}|$ -range and two magnon signals for the high-energy region, resulting in a satisfying description of the data.

The results of the above analysis are summarized in Fig. 5.21, presenting the spin-wave dispersion along \mathbf{a} and \mathbf{c} for the ferroelectric spiral and the paraelectric SDW phase. As aforementioned, with the relaxed resolution of the thermal instrument we were not able to resolve all details and the presentation is somehow oversimplified, the actual situation might be more complex, especially in the SDW phase. Nevertheless, Fig. 5.21 provides a complete overview of the spin-wave dispersion including the most important properties. To further inspect the dispersion, the full spin Hamiltonian \mathcal{H} as given by Katsura et al. has to be diagonalized [253], which is an ambitious theoretical task for the incommensurable magnetic structure present in TbMnO₃ [264] and surely beyond the scope of this thesis. However, as the magnetic coupling in the \mathbf{ac} -plane of TbMnO₃ is the same as for the commensurable A -type ordering of LaMnO₃ – the magnetic correlations are strictly FM along \mathbf{a} and AFM along \mathbf{c} – we may directly compare the observed spin-wave dispersion with dispersion relations derived for LaMnO₃: The spiral ordering develops from the A -type structure by a modulation of the magnetic correlations along [010] due to the emergence of a frustrating AFM exchange J_{NN} between next-nearest neighbors along \mathbf{b} . The magnetic correlations in the perpendicular directions are not affected, and the overall shape of the spin-wave dispersion should remain the same along \mathbf{a} and \mathbf{c} .

The magnon excitations in LaMnO₃ were first studied by Moussa et al. and by Hirota et al. [144, 146]. Based on a simple spin-only Hamiltonian

$$\mathcal{H} = - \sum_{i,j} J_{i,j} \mathbf{S}_i \mathbf{S}_j - \Lambda \sum_i S_i^{z2} \quad (5.14)$$

with a FM exchange J_{FM} between nearest neighbors within the \mathbf{ab} -planes, an AFM exchange J_{AFM} along \mathbf{c} , and a single-ion anisotropy Λ , the following spin-wave relations are derived:

$$\hbar\omega(\mathbf{q}) = 2S\sqrt{A(\mathbf{q})^2 + B(\mathbf{q})^2}, \quad (5.15)$$

with $A(\mathbf{q})$ and $B(\mathbf{q})$ defined by

$$A(\mathbf{q}) = +2J_{\text{FM}} [2 - \cos(\pi(q_h + q_k)) - \cos(\pi(q_h - q_k))] - 2J_{\text{AFM}} + \Lambda,$$

and $B(\mathbf{q}) = -2J_{\text{AFM}} \cos(\pi q_l)$.

The simple model can, of course, not predict the splitting of the magnon branches observed in TbMnO₃, but neglecting for the moment this unusual behavior and treating all branches separably, the simplified spin-wave relations describe

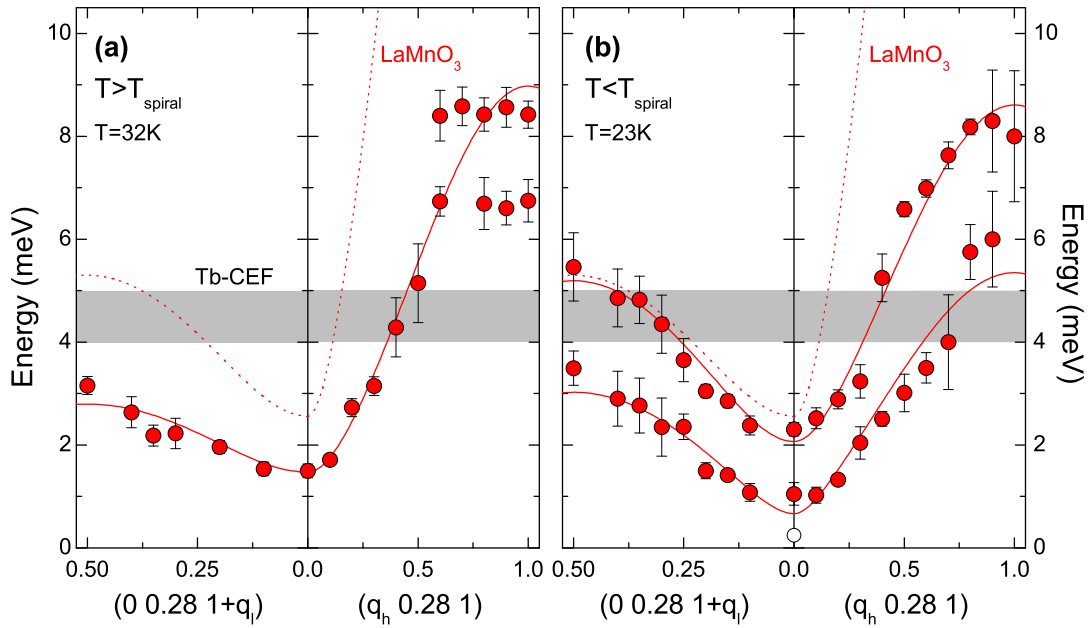


Figure 5.21: Spin-wave dispersion in the ac -plane Spin-wave dispersion of $TbMnO_3$ along a and c in the paraelectric SDW phase at $T = 32$ K (a), and in the ferroelectric spiral phase at $T = 23$ K (b). Solid lines denote fits to the experimentally observed dispersion as described in the text, dotted lines mark the magnon dispersion of $LaMnO_3$ as derived from the analysis given in [144, 146].

accurately the observed dispersion of the different modes in both magnetic phases, see Fig. 5.21. The obtained values for the magnetic exchange interactions and the strength of the single-ion anisotropy are summarized in Tab. 5.5, e.g. from the magnon dispersion in the paraelectric SDW-phase we extract the parameters $J_{FM} = 0.20(1)$ meV, $J_{AFM} = -0.30(2)$ meV, and $\Lambda = 0.11(1)$ meV. There are no significant changes of the exchange integrals upon the magnetic transition at T_{spiral} , as the bandwidth of the different modes remains approximately constant, and the magnetic transition from the SDW to the spiral ordering is solely driven by the complex magnetic anisotropy [13, 240].

Furthermore, our results agree qualitatively with those reported in an earlier spin-wave study on $TbMnO_3$ derived using the same semi-empirical analysis [249]. However, Kajimoto et al. only discuss the magnetic excitation spectrum of the ferroelectric phase at 10 K. In contrast to our argumentation they do not observe a splitting of the magnon frequencies, which most likely has to be attributed to the poor experimental resolution, as the results presented in Ref. [249] are based only on thermal neutron data.¹³ Furthermore, Kajimoto et al. do not analyze

¹³The authors, nevertheless, note a significant broadening of the magnon signal close to the magnetic zone center, which they can resolve into three different branches in a first test

		J_{FM}	J_{AFM}	Λ	T_N
TbMnO ₃	SDW	0.20(1) meV	-0.30(2) meV	0.11(1) meV	42 K
	Spiral, $\omega_{\perp 1}$	0.10(1) meV	-0.37(3) meV	0.02(1) meV	
	Spiral, $\omega_{\perp 2}$	0.15(1) meV	-0.60(3) meV	0.11(2) meV	
TbMnO ₃ ^[249]	Spiral ¹	0.15 meV	-0.50 meV	0.13 meV	42 K
PrMnO ₃ ^[249]	A-type	0.56 meV	-0.60 meV	0.08 meV	100 K
LaMnO ₃ ^[146]	A-type	0.84 meV	-0.61 meV	0.15 meV	140 K
LaMnO ₃ ^[144]	A-type	0.83 meV	-0.58 meV	0.17 meV	140 K

¹Data presented in Ref. [249] were all recorded in the spiral phase at $T = 10$ K, the splitting of the magnon modes is not discussed.

Table 5.5: Results of the analysis of the spin-wave dispersion using the simplified model described in the text, and comparison with the exchange constants obtained in different RMnO₃ compounds showing the *A*-type ordering. Note that the different authors use different definitions of J and Λ . The values given have been converted to the Hamiltonian eq. 5.14, which is the convention used in [144].

the magnon-dispersion starting at the incommensurable zone center, but from the commensurable *A*-type Bragg position.

The values of the nearest-neighbor magnetic exchanges integrals J_{FM} and J_{AFM} obtained for TbMnO₃ should be compared to those of LaMnO₃ with a less distorted orthorhombic structure and an *A*-type ordering. In Fig. 5.21 the magnon dispersion of LaMnO₃ as derived from the analysis given in Ref. [144] is included by the dotted line. It is immediately clear, that the dispersion along \mathbf{c} , and hence the strength of the antiferromagnetic coupling J_{AFM} , is similar in both compounds. Along \mathbf{a} , the spin-wave dispersion is significantly flattened in TbMnO₃; for LaMnO₃ the magnon band extends up to ≈ 33 meV, whereas the zone-boundary frequency in TbMnO₃ amounts to 8 meV, directly demonstrating the reduction of the FM interaction J_{FM} . Indeed, the AFM coupling in TbMnO₃ is comparable with $J_{AFM} = -0.58$ meV obtained for LaMnO₃ [144], whereas the FM exchange is strongly suppressed, $J_{FM} = 0.83$ meV for LaMnO₃ and ≈ 0.2 meV for TbMnO₃, respectively.

In a mean-field approach [265], the Néel temperature T_N is correlated with the magnetic interactions via

$$T_N = \frac{2}{3}S(S+1) \sum_i |J_i| = \frac{2}{3}S(S+1) (4J_{FM} + 2|J_{AFM}|). \quad (5.16)$$

measurement using cold neutrons. Obviously, these mode have to be identified with the phason and the two orthogonal modes.

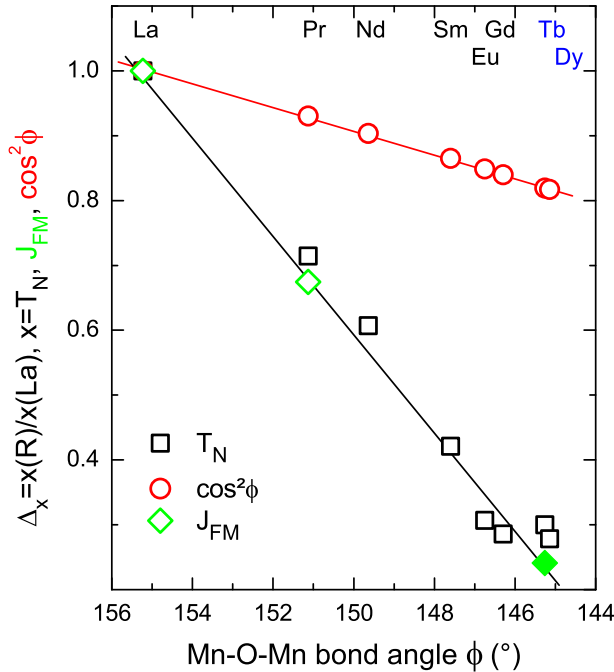


Figure 5.22: Scaling of T_N and J_{FM} in the $RMnO_3$ -series Development of the Néel temperature T_N , of the ferromagnetic coupling J_{FM} , and of $\cos^2 \phi$ as a function of the average Mn–O–Mn bond angle ϕ in the series $RMnO_3$. Structural and magnetic data for the various compounds taken from the literature are denoted by open symbols [144, 225, 228, 229, 249, 269].

In Fig. 5.22 we plot the suppression of the Néel temperature T_N in the $RMnO_3$ -series as a function of the average Mn–O–Mn bond angle ϕ . Also depicted are all reported values on J_{FM} available to us, including the results of this thesis. The linear decrease in T_N scales perfectly with the observed softening of J_{FM} .¹⁴ As discussed in the introduction, the ferromagnetic correlations and the A -type ordering are destabilized by the enhancement of the structural distortion resulting in a reduction of the bond angle ϕ ; it is well established that T_N is closely coupled to $\cos^2 \phi$, in perovskite manganites as well as in nickelates and ferrates [266–269]. One may, however, ask, if the (relatively) small change in ϕ , the difference between $R=La$ and Tb is only 10° , is able to fully explain the rapid suppression of J_{FM} , and hence of T_N .

With the staggered orbital ordering the ferromagnetic coupling J_{FM} between adjacent Mn-sites in the ab planes is determined by the $e_g^1-O-e_g^0$ superexchange-path and can be parameterized as $J_{FM} = 4b^2/U$ and $b \approx d^{-3.5} \cos \phi$ [31, 227]. As the Mn-Mn distance d is almost constant in the $RMnO_3$ -series [225], J_{FM} includes only a factor proportional to $\cos^2 \phi$. However, the decrease in $\cos^2 \phi$ does not size that of J_{FM} , see Fig. 5.22, and the reduction of ϕ can only cover a fraction of the observed suppression of J_{FM} . Note on the other hand, that the AFM exchange along c is mainly mediated through the isotropic $t_{2g}^3-O-t_{2g}^3$ exchange, which is

¹⁴Note that the AFM exchange J_{AFM} is almost constant in the series of rare-earth manganites, and T_N is determined only by the size of J_{FM} .

expected to be almost independent of ϕ [267], in congruence with the experimental data.

To overcome this insufficient description, different authors have recently extended the above argumentation, taking explicitly into account the orbital degree of freedom and the role of the cooperative Jahn-Teller effect [229, 270]. Based on optical spectroscopy, Kim et al. have shown [270], that not only the binding angle ϕ is affected by the substitution of the smaller rare-earth ions, but also the orbital mixing angle θ determining the orbital ordering in the compound [28, 29], resulting in an additional decrease of J_{FM} . Zhou and Goodenough even point out, that the increase in the Jahn-Teller splitting ε_{JT} is the dominant factor in controlling $J_{FM}(R)$, in this scenario the cooperative octahedral-site rotations even play only a minor role [229].

In conclusion, the analysis of the spin-wave dispersion in the \mathbf{ac} -plane based on a semi-empirical model derived from the A -type ordering has revealed a pronounced softening of the ferromagnetic exchange interaction J_{FM} in the series of rare-earth manganites $RMnO_3$, which is the driving force behind the suppression of the Néel transition from $LaMnO_3$ to $TbMnO_3$. The microscopic origin of the huge decrease of J_{FM} is discussed controversially in the literature, a structural origin due to the reduction of the bond-angle ϕ alone is, however, not sufficient to explain the experimental results.

5.3.2 Dispersion along \mathbf{b} : magnetic frustration

Along the third crystallographic axis the magnetic ordering is frustrated due to the competition of the FM nearest-neighbor exchange J_{FM} and the AFM next-nearest neighbor exchange J_{NN} , resulting in the incommensurable modulated magnetic structure propagating along \mathbf{b} below T_N . The magnetic frustration will also affect the magnetic excitation spectrum and the dispersion along this direction will significantly differ from the simple behavior expected for the A -type arrangement.

However, before we proceed with the presentation of the experimental results, we first want to acquire some physical intuition of the spin dynamics in a frustrated system. In a simple approach, we expand the Hamiltonian eq. 5.14 to include an AFM exchange J_{NN} between next nearest neighbors along $[010]$ and calculate the Fourier components $J_{\mathbf{q}}$, resulting for $\mathbf{q}||\mathbf{b}$ in the dispersion relation

$$\hbar\omega(0q_k0) = 2S \left(\left[2J_{FM}(2 - 2\cos(\pi q_k)) + \frac{J_{NN}}{J_{FM}} \cos(2\pi q_k) \right] - 2J_{AFM} - 2J_{NN} + \Lambda \right)^2 - 4J_{AFM}^2 \right)^{\frac{1}{2}}. \quad (5.17)$$

Fig. 5.23 plots the dispersion given by eq. 5.17 for $\Lambda = J_{FM}$, $J_{AFM} = 0$ and various values of $\eta = |J_{NN}/J_{FM}|$. For small $\eta < \frac{1}{2}$ the spin-wave frequencies increase monotonically from the A -type zone center with $q_k = 0$ to the zone boundary at

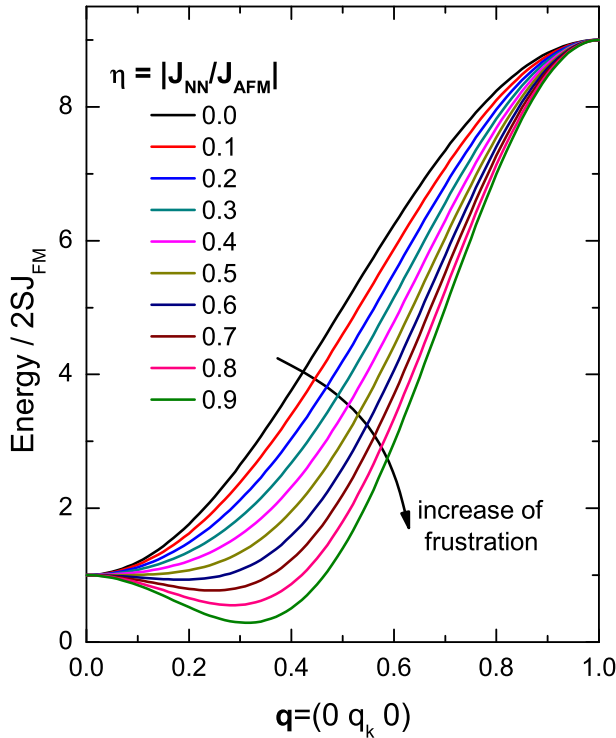


Figure 5.23: Magnon dispersion for various values of the magnetic frustration. Shape of the spin-wave dispersion along $[0\ 1\ 0]$ calculated from eq. 5.17 for various values of $\eta = |\frac{J_{\text{NN}}}{J_{\text{FM}}}|$.

$q_k = 1$, resembling the shape of the dispersion of LaMnO_3 with $\eta \approx 0$. For $\eta > \frac{1}{2}$, however, the shape of the dispersion changes and develops a local minimum at $q_{k0} = \frac{1}{\pi} \arccos(-\frac{1}{2\eta})$: The static A -type order is suppressed and transformed into an incommensurable arrangement with modulation q_{k0} . The observed value of the static incommensurability, $\varepsilon_b \approx 0.28$ in TbMnO_3 , thus points to a strong magnetic frustration $J_{\text{NN}} = -0.78J_{\text{FM}}$, nicely reproducing the value of η derived in a mean-field approximation [228]. The maximum magnon frequency, in contrast, does not depend on the frustration η , for all values of η the zone-boundary energy amounts to $2S[(8J_{\text{FM}} - 2J_{\text{AFM}} + \Lambda)^2 - 4J_{\text{AFM}}^2]^{1/2}$, independent of J_{NN} .¹⁵

The experimentally observed dispersion along the line $\mathbf{Q} = (0\ q_k\ 1)$ is shown in Fig. 5.24. The data were collected at the cold spectrometer PANDA with the energy on the analyzer side fixed to $E_f = 4.66\text{ meV}$, compared with the above discussion of the thermal data yielding a significantly enhancement of the experimental resolution. Already at first sight, the intensity mapping in Fig. 5.24a

¹⁵It is interesting to note, that at this point the discussion touches again the charge and orbital ordering in half-doped manganites, studied extensively in Chap. 4. Konstantinidis and Patterson have derived the spin-wave spectrum for the Zener polaron picture by mapping the Hamiltonian for the Zener polaron ordering onto a Heisenberg model on a square lattice with frustrated magnetic exchange equivalent to the situation in the multiferroic manganites [110], and the conclusions presented in Ref. [110] are very similar to those discussed here.

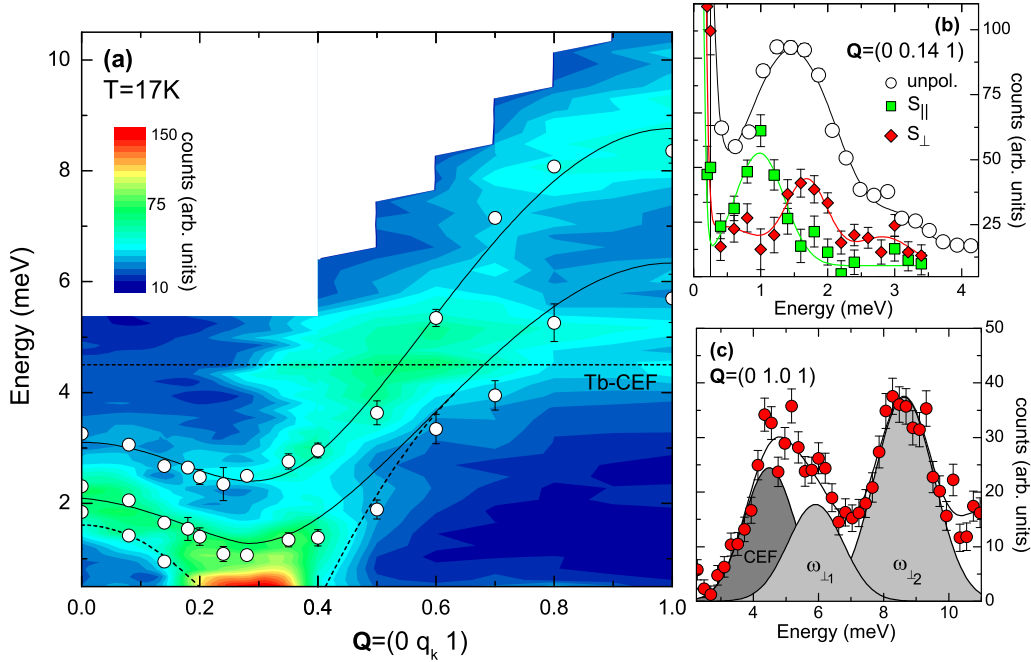


Figure 5.24: Analysis of the spin-wave dispersion along \mathbf{b} for $T=17\text{K}$ Intensity mapping along the line $\mathbf{Q} = (0 q_k 1)$ for $0 \leq q_k \leq 1$ calculated from a grid of energy scans with step size $\Delta q_k = 0.1$ measured in the spiral phase at $T = 17\text{K}$ at the cold spectrometer PANDA with enhanced experimental resolution and $E_f = 4.66\text{meV}$. White areas were not accessible in the scattering experiment. Open circles mark the estimated positions of the magnon signals, solid lines denote the fit with the dispersion relation eq. 5.17, for details see the text (a). Exemplary analysis of the magnon spectrum at $\mathbf{Q} = (00.141)$ using unpolarized and polarized neutrons (b), and at the boundary of the extended zone $\mathbf{Q} = (01.01)$ (c), showing the decomposition of the raw data into the different magnetic contributions. Lines denote fits to the data as described in the text. Data using polarized neutrons were collected at the IN14 spectrometer.

exhibits a more complex behavior than that expected for the simple A -type configuration. Starting at the initial A -type zone center $\mathbf{Q} = (001)$ the spin-wave frequencies soften and form a local minimum around $q_k = 0.28$. Upon further increase of q_k the dispersion exhibits a steep increase, and reaches the zone boundary of the extended zone scheme, $q_k = 1.0$, around $\approx 8.5\text{meV}$. Notice, that the dispersion in the perpendicular direction $[100]$, well describable by the simple dispersion relation eq. 5.15 derived for the A -type arrangement, extends to similar energies. There is also a splitting of the magnon frequencies observable along \mathbf{b} , and the second branch progresses up to $\approx 6\text{meV}$, again comparable with the dispersion along \mathbf{a} .

For the quantitative analysis of the data we proceed using the same systematic as above, i. e. treating the Tb crystal-field excitation hampering the identification of

the spin-wave signal with greatest care. In addition to the enhanced experimental resolution, we have also applied a longitudinal polarization analysis to resolve the different magnon contributions in the region $q_k \leq 0.28$. The polarized data were collected at the IN14 spectrometer using similar experimental conditions as in the PANDA measurement. Concerning the definition of the coordinate system for the spin space we use the usual convention: $\hat{x} \parallel \mathbf{Q}$, $\hat{y} \perp \mathbf{Q}$ and within, and $\hat{z} \perp \mathbf{Q}$ and perpendicular to the scattering plane, which was chosen to be parallel to the spiral-plane \mathbf{bc} .

An example of how the combination of unpolarized and polarized techniques enables us to deconvolute the observed spectrum into the different contributions is given in Fig. 5.24b. With the high flux of the PANDA instrument two magnon excitations are easily detectable around 1.5 meV and 3.0 meV. The polarization analysis, however, reveals that the first signal is composed of two distinct excitations with different character: One is polarized within the spiral plane at $\hbar\omega_{\parallel} = 0.98(4)$ meV, while the second is polarized perpendicular with energy $\hbar\omega_{\perp 1} = 1.69(9)$ meV. The third mode $\hbar\omega_{\perp 2} = 2.83(9)$ meV is also observed in the S_{\perp} -channel, and the three different branches obviously have to be associated with the sliding and the two orthogonal modes of the spiral structure introduced in the discussion of the zone center spectrum. All three modes can be followed starting from the magnetic zone center at $q_k = 0.28$ to the A -type position with $q_k = 0$, and the estimated dispersion of the different branches is superimposed onto the intensity mapping in Fig. 5.24b. All modes exhibit a comparable dispersion.

In the outward direction from $q_k = 0.28$ to $q_k = 1.0$, where the intensity mapping in Fig. 5.24 reveals a steep increase of the magnon frequencies, we have to rely only on the unpolarized data, as the polarization analysis at higher energies is not possible at the IN14 spectrometer. A representative example of the analysis for this region is shown in Fig. 5.24c, providing the decomposition of the spectrum at $\mathbf{Q} = (01.01)$, i.e. $q_k = 1$. The inelastic intensity appears split throughout the extended magnetic zone, and assuming two different magnon contributions in addition to the CEF excitations the observed spectrum is described reasonably well, yielding for $q_k = 1.0$ the spin-wave frequencies $\hbar\omega_1 = 5.7(4)$ meV and $\hbar\omega_2 = 8.3(2)$ meV.¹⁶ The dispersion of these two modes can be followed in the entire region $0.28 \leq q_k \leq 1.0$. A third magnetic mode, however, can not be resolved based on the unpolarized data, most likely due to the strong overlap of the sliding and the lowest orthogonal mode. The acquired dispersion is also superimposed onto the contour map in Fig. 5.24a, providing hence the full magnon dispersion along $[010]$ for the FE spiral phase at $T = 17$ K.

The shape of the observed dispersion resembles very much the properties of the empirical spin-wave calculation eq. 5.17. All magnon branches exhibit a local

¹⁶As usual, the parameters describing the Tb-CEF were not allowed to vary during the refinement of the data.

minimum in the spin-wave frequencies around $q_k = \varepsilon_b$ and a steep increase towards $q_k = 1$. Indeed, fitting the dispersion relation Eq. 5.17 to each of the observable branches results in a reasonable description of the data, see the solid lines in Fig. 5.24a.¹⁷ In the refinement J_{FM} and Λ are the only effective parameters – the size of the magnetic frustration η is fixed by the value of the static modulation to $\eta = 0.78$, and the shape of the dispersion is not sensible to the AFM exchange J_{AFM} – and the obtained values agree very well with those derived from the analysis of the dispersion along \mathbf{b} and \mathbf{c} , e. g. for the higher-energy mode $\hbar\omega_{\perp_2}$ we find here $J_{\text{FM}} = 0.11(4)$ meV and $\Lambda = 0.15(9)$ meV, which have to be compared with the values reported in Tab. 5.5. Note, that the consistency in the description can directly be extracted from the raw data, as the maximum magnon frequency, which is determined solely by J_{FM} , is similar both along \mathbf{a} and \mathbf{b} .

The last point remaining in the discussion of the \mathbf{q} -dependence of the magnetic excitations is the dispersion along $[010]$ in the paraelectric SDW phase. So, we finally present in Fig. 5.25 the analysis of the excitation spectrum along $\mathbf{Q} = (0q_k1)$ for $T = 32$ K. As the focus of the experiment at the IN14-spectrometer with polarized neutrons was laid on the spiral phase, the analysis of the spin-wave dispersion in the SDW phase has to be based entirely on unpolarized data. However, from the discussion of the zone-center spectrum we already know that without polarization analysis we can not resolve all the details of the spectrum, but sum over the different magnon branches – remember that we have identified four different modes at the zone center for the SDW phase using polarization analysis. Indeed, all spectra presented in 5.25a exhibit a very broad response, which in analogy to the previous discussion tentatively can be modeled assuming a Lorentzian-shaped mode at very low energies and a Gaussian-like excitation at higher energies, but which does not properly take into account the complex structure of the excitation spectrum, as revealed earlier.

Close to the magnetic zone center with $0 \leq q_k \leq 0.4$ all spectra are quite comparable. We do not find a significant change in the energy of the spin-wave frequencies, and all data for $q_k \leq 0.4$ nearly collapse onto a single curve, in strong contrast to the behavior in the spiral phase, see Fig. 5.25a,b. In the outward direction with $0.4 \leq q_k \leq 1.0$, however, the data reveal a steep dispersion, this time similar to the spiral phase. At $q_k = 0.5$ the magnetic signal is shifted towards higher energies and appears significantly broadened, see Fig. 5.25e. The rapid increase of the observed width towards $q_k = 0.5$ already signals the enhancement of the splitting of the magnon frequencies, and indeed, for larger values of $q_k \geq 0.8$ two different magnetic modes can be resolved. At the A -type zone boundary $q_k = 1.0$ the spectrum is similar to that of the spiral phase, although the data appear a bit scattered due to a lower statistic, Fig. 5.25c, and two distinct magnon

¹⁷A slight underestimation of the magnon energies at $q_k = 0$ may be attributed to a more complex magnetic anisotropy.

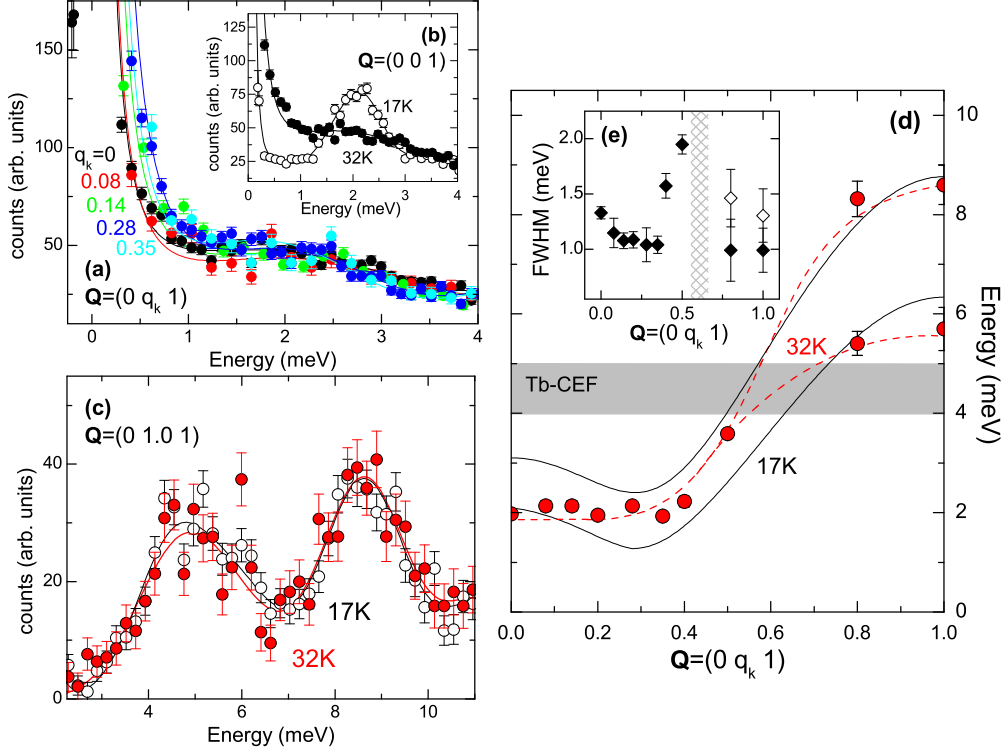


Figure 5.25: Analysis of the spin-wave dispersion along b for $T=32$ K Raw-data scans at $Q = (0 q_k 1)$ and $0 \leq q_k \leq 0.35$ measured in the paraelectric SDW phase at $T = 32$ K at the PANDA spectrometer with $E_f = 4.66$ meV (a). Comparison of the excitation spectra for $T = 17$ K and 32 K at $q_k = 0$ (b), and $q_k = 1.0$ (c). In (a)-(c) solid represent fits to the data as described in the text. Spin-wave dispersion along $[0 1 0]$ in the SDW phase at $T = 32$ K derived from the data presented in (a)-(c). For comparison, the dispersion in the FE phase at 17 K is shown by the solid black lines, dashed lines are included as guides to the eye (d). Estimated width (FWHM) of the magnon-signal (e). Towards the gray-shaded region the estimated width of the magnon signal significantly increases, being the precursor of the splitting of the different branches observable for $q_k \geq 0.8$.

branches can be identified centered at $\hbar\omega_1 = 5.4(5)$ meV and $\hbar\omega_2 = 8.6(1)$ meV.

The resulting spin-wave dispersion is presented in Fig. 5.25d, which also includes the dispersion for the ferroelectric spiral phase. The direct comparison between both phases reveals, that close to zone boundary of the extended zone at $q_k = 1.0$ the spin-wave frequencies are hardly affected by the reorientation in the static spin-structure – for short magnon wavelengths the spin-wave dispersion is comparable in both phases. On the other side, however, at the long-wavelength limit remarkable differences can be observed, as the resolved dispersion in the SDW phase is essentially flat, in contrast to the spiral phase, which exhibits a pronounced minimum in the spin-wave frequencies at $\mathbf{q} = \mathbf{k}_{\text{spiral}}$. At this point

the analysis of the magnon dispersion in the SDW has, however, to be treated very carefully: Especially for low energies the full complexity of the spin-wave spectrum as revealed earlier using polarized neutrons can not be resolved using unpolarized neutrons. Whether the different modes possess a significant \mathbf{q} -dependence in the low energy regime or not can not be answered with the existing data. A better understanding of the different behavior in the low \mathbf{q} -regime above and below T_{FE} would, however, require further experimental work and a detailed theoretical investigation. We may, however, conclude that on a length scale well shorter than the wavelength of the magnetic modulation the magnetic correlations are comparable for the SDW and the spiral ordering, and hence are the dynamics at large \mathbf{q} . The spiral ordering, however, significantly alters especially the magnetic correlations on a larger length scale, and the changes in the static spin-correlations are expected to be resumed in the spin dynamics for $|\mathbf{q}| \rightarrow 0$.

5.4 Conclusions

We presented a detailed analysis of the spin dynamics in the multiferroic compound TbMnO_3 , including the identification of the different spin-wave modes in the two incommensurable phases, the longitudinally modulated SDW and the ferroelectric phase with cycloidal order, as well as the temperature, momentum and field dependence of the different modes.

The dispersion of the magnetic excitations is discussed along all three orthorhombic axes for two selected temperatures above and below the ferroelectric transition at T_{FE} . In the \mathbf{ac} -plane, perpendicular to the magnetic modulation, the observed spin-wave dispersion is well comparable with those of the parent compound LaMnO_3 with a less distorted structure. Describing the observed data using a semi-empirical model we derive the strength of the nearest-neighbor exchange integrals. The AFM coupling J_{AFM} is similar for both LaMnO_3 and TbMnO_3 . The FM exchange J_{FM} in the planes is, in contrast, significantly reduced in the case of TbMnO_3 , and it is shown that the strength of J_{FM} controls the magnetic transition temperature in the series of rare-earth manganites RMnO_3 . The magnon dispersion parallel to the incommensurable propagation vector $\|\mathbf{b}$ is strongly affected by the AFM next-nearest neighbor exchange J_{NN} competing with J_{FM} ; for a strong magnetic frustration the commensurable A -type arrangement is destabilized and the magnon dispersion develops a local minimum. From the magnetic incommensurability and the observed position of the minimum in the spin-wave dispersion we finally deduce that the AFM next-nearest neighbor exchange is nearly comparable with the FM nearest-neighbor coupling and conclude that TbMnO_3 is magnetically heavily frustrated.

Using unpolarized, as well as polarized techniques we have shown, that in the FE spiral phase the excitation spectrum at the magnetic zone center consists of

three different branches. In consistence with the recent literature [253] we identify the different characters of the modes. The branch lowest in energy corresponds to the phason mode of the spiral, while the two other modes represent the twisting of the spiral plane. The comparison with IR data [255] furthermore allows to identify both modes as new collective excitations predicted to exist in magnetic ferroelectrics: hybridized magnon-phonon vibrations, or *electromagnons*.

Upon heating into the paraelectric SDW phase we find a drastic change of the excitation spectrum with the spiral-to-SDW transition. In the SDW phase four different magnon contributions can be identified experimentally, and following our previous discussion we attribute two of the different modes to the collinear rotation of the spin density wave around \mathbf{a} and \mathbf{c} . The other two modes are ascribed to the transformation of the SDW into a spiral ordering. Both modes are predicted to couple to an alternating electric field even in the paraelectric regime of the phase diagram, and one of these mode, the one which transforms the SDW ordering into the proper magnetic spiral confined to the \mathbf{bc} -plane, is identified as the magnetic soft mode of the ferroelectric transition, which condenses across the FE phase transition.

The strong coupling of ferroelectricity and magnetism in TbMnO₃ allows to flop the direction of the electric polarization by 90° by an external magnetic field [6]. Following the different theoretical approaches this effect originates in the flop of the rotation axis of the magnetic spiral [13], a prediction, which, however, remains to be tested by experiment. The response of the excitation spectrum to an applied field supports this interpretation, as we find a pronounced change in the spectrum with the first order transition at H_c . The high-field spectrum thereby consists again of three different modes, similar to the spectrum of the zero-field spiral phase, but the polarization pattern of the different modes is changed by 90°, providing the first experimental evidence for the predicted flop of the spiral plane.

6 Summary

In this thesis we studied the magnetic excitation spectrum of three different manganese oxides with complex magnetic ordering by means of inelastic neutron scattering. Two of the three compounds under investigation, LaSrMnO_4 and $\text{La}_{1/2}\text{Sr}_{3/2}\text{MnO}_4$, are structurally closely related, but correspond to different concentrations of charge carriers. Two-dimensional LaSrMnO_4 is electronically undoped and the physical properties are determined by a close correlation of orbital and magnetic degrees of freedom, whereas the doped system $\text{La}_{1/2}\text{Sr}_{3/2}\text{MnO}_4$ is well known to exhibit a cooperative ordering of charges, orbitals, and spins, typical of many different manganites with a rational fraction of charge carriers. The third compound under investigation, orthorhombic TbMnO_3 , is one of the prototypical examples for the emerging class of multiferroic oxides with pronounced magnetoelectric coupling, which recently have attracted a lot of interest.

The magnetic properties of undoped **LaSrMnO₄** reveal some unusual features at low temperatures, which are not consistent with the widely accepted simple antiferromagnetic G-type ordering proposed for this system, see e. g. Ref. [7]: The macroscopic susceptibility proves a non-vanishing magnetization in modest magnetic field for $T \rightarrow 0$ K [43], and a previous analysis of the spin-wave excitation spectrum of the ordered state finds three different excitation branches [46]. The revision of the excitation spectrum using polarized neutrons and the application of strong magnetic fields unambiguously proves the magnetic origin of all three modes. The observed behavior of one of the three branches agrees with the predictions of linear spin-wave theory; it possesses a transversal character, exhibits a pronounced dispersion, and splits in a magnetic field along the magnetic easy axis. This branch is the conventional magnon associated with the G-type antiferromagnetic ordering.

The two additional modes are shown to be polarized within the MnO_2 -planes of the layered structure, similar to the spin-wave mode, but they do not reveal a significant \mathbf{q} -dependence, and an unusual field dependence connects both modes with the existence of ferromagnetic domains uncovered by the analysis of the macroscopic susceptibility. Similarities with recent observations in perovskite manganites [71] lead to the conclusion that these two localized modes correspond to the magnetic excitations within small ferromagnetic polarons embedded in the antiferromagnetic matrix. The clusters are formed as a response to the influence of quenched disorder in the layered structure, and they are directly correlated with the unusual excitation spectrum and with the observed anomalies in the magnetic

susceptibility.

The hole-doped system $\text{La}_{1/2}\text{Sr}_{3/2}\text{MnO}_4$ with an equal ratio of three- and four-valent Mn-sites is well known for its stable ordering of charges, orbitals, and spins. However, although predicted 50 years ago, and despite its enormous relevance for the CMR-effect in perovskite manganites, the nature of the ordered state is still discussed controversially, and even the ground-state properties are not well established today. Our analysis of the spin-wave excitations in the ordered state at low temperatures is in excellent agreement with one of two contrasting models, namely the classical Goodenough model characterized by an AFM alignment of FM zig-zag chains [8], and rejects the second proposal containing tightly bound magnetic dimers [9]. The magnon dispersion is flat perpendicular to the zig-zag chains and very pronounced along the chains, directly mirroring the dominant magnetic exchange within the zig-zag chains: The complex magnetic arrangement has to be considered as a weak AFM coupling of stable FM elements.

This interpretation is strongly supported by the thermal evolution of the magnetic state. The analysis of the diffuse magnetic scattering in the paramagnetic state above the CE transition at T_N finds anisotropic magnetic scattering, which is associated with the existence of one-dimensional zig-zag fragments above T_N , and the magnetic phase transition at T_N corresponds to the melting of the AFM ordering of stable FM zig-zag fragments. Above T_N , and especially close the charge- and orbital-ordering transition at higher temperatures, the short-range CE-type correlations furthermore compete with isotropic ferromagnetic correlations, which dominate for $T_{CO} < T$. The disordered phase above T_{CO} is characterized by the existence of small isotropic ferromagnetic clusters, highlighting the close connecting of the charge ordered and FM states, which seems the key to the quantitative understanding of the CMR-effect.

The competition of ferromagnetic and antiferromagnetic CE-type correlations can decisively be influenced by doping, and the ordered states exhibit an anisotropic response to the influence of additional electrons or holes. Electron doping destabilizes the charge-ordered state, thereby enhancing the competition between ferromagnetic and CE-type antiferromagnetic correlations: FM clusters persist in the entire temperature region below 300 K, and the ground-state properties of electron-doped $\text{La}_{0.6}\text{Sr}_{1.4}\text{MnO}_4$ are interpreted on the basis of a heterogeneous mixture of CE and FM regions coexisting on a microscopic scale. In contrast, the ordered state is robust against the doping of additional holes. For $x > 0.5$ the orbital and the magnetic ordering is incommensurate, and the analysis of the magnetic correlations in hole-doped $\text{La}_{0.4}\text{Sr}_{1.6}\text{MnO}_4$ suggests a picture in which the additional holes replace some of the three-valent sites to form a regular arrangement of electron-poor stripes oriented perpendicular to the FM zig-zag chains.

The detailed investigation of the magnetic correlations for three different compounds of the $\text{La}_{1-x}\text{Sr}_{1+x}\text{MnO}_4$ -series with $x = 0.4, 0.5, 0.6$ finally results in the construction of the orbital and magnetic phase diagram for the series of single-

layered manganites around half doping. The topography of the phase diagram is well comparable with those of the related perovskite manganites in this doping region: The anisotropic response with respect to hole or electron doping has to be considered as an intrinsic feature of the charge- and orbital-ordered state.

TbMnO₃ is the prototypical compound for the new class of multiferroic oxides with close coupling between electric polarization and a non-collinear spiral-like magnetic order [6, 12, 13]. In the ferroelectric phase three different magnetic excitations can be identified by inelastic neutron scattering using polarized neutrons, and the comparison with theoretical considerations allows to ascribe the modes to the different excitations in a cycloidal structure. Furthermore, in systems with strong magnetoelectric coupling new collective excitations, considered as hybridized magnon-phonon oscillations, are predicted to exist for a long time [11]. The combination of the neutron with recent IR-spectroscopy results [255] permits the first unambiguous experimental verification of such *electromagnons* in a multiferroic compound, which are furthermore extensively characterized by studying the momentum, temperature, and field dependence.

Considering the \mathbf{q} -dependence of the magnetic excitations, the observed dispersion is well comparable with those of commensurate LaMnO₃ for $\mathbf{q}||\mathbf{ac}$, whereas the magnetic frustration along \mathbf{b} considerably affects the dispersion of the spin-wave excitation in this direction. Using linear spin-wave theory we derive the strength of all relevant magnetic interaction parameters for TbMnO₃. The antiferromagnetic exchange between nearest neighbors J_{AFM} is comparable with that of LaMnO₃, in contrast to the ferromagnetic exchange, which is considerably reduced. The antiferromagnetic next-nearest neighbor exchange J_{NN} competing with J_{FM} along \mathbf{b} , which is responsible for the incommensurate magnetic structure, is rather strong, $J_{\text{NN}} = 0.78J_{\text{FM}}$, and we conclude that TbMnO₃ is a heavily frustrated magnetic system.

In the paramagnetic phase $T_{\text{FE}} < T < T_{\text{N}}$ the magnetic structure consists of a longitudinal magnetic modulation. The spin-wave spectrum contains six distinct branches, but the use of polarized neutrons admits to unravel the two modes transforming the SDW structure into a magnetic spiral confined either in the \mathbf{bc} -plane with electric polarization \mathbf{P}_c , or in the \mathbf{ab} -plane and \mathbf{P}_a . These two modes are expected to hybridize with a phonon and couple to the electric susceptibility, even in the paraelectric phase, as is already confirmed by comparing with IR spectroscopy for the mode polarized along \mathbf{a} [255].

The strong magnetoelectric effects observed in TbMnO₃ are assumed to base upon the response of the spiral structure to an external field. A magnetic field is predicted to induce a spin flop from a \mathbf{bc} - to an \mathbf{ab} -spiral structure [13], corresponding to the reported flop of the electric polarization from \mathbf{P}_c to \mathbf{P}_a for $\mathbf{H}||\mathbf{a}, \mathbf{b}$ [6]. The observed field dependence of the magnetic excitations in the ferroelectric phase strongly supports this interpretation, as the excitation spectrum of the high-field phase is comparable with the zero-field spectrum, but with all polarization

6 Summary

patterns rotated by 90° , yielding the first experimental support for the predicted origin of the gigantic magnetoelectric effects observed in TbMnO_3 .

List of Figures

2.1	$ \mathbf{Q} $ -dependence of magnetic scattering	10
2.2	Spin waves in the FM Heisenberg model	11
2.3	General layout of a TAS-spectrometer	15
2.4	Cold triple-axis spectrometer 4F	16
2.5	Double-focusing PG monochromator at the PANDA spectrometer	17
2.6	The resolution function of a TAS instrument	20
3.1	Crystal structure of single-layered manganites	22
3.2	Electronic phase diagram of $\text{La}_{1-x}\text{Sr}_{1+x}\text{MnO}_4$	23
3.3	Magnetic G-type ordering in LaSrMnO_4	25
3.4	Macroscopic magnetization of LaSrMnO_4	26
3.5	Spin-wave dispersion in LaSrMnO_4	28
3.6	Polarization analysis of the magnetic excitation spectrum at $q=0$	31
3.7	Field dependence of the magnetic excitations in LaSrMnO_4 (I.)	34
3.8	Field dependence of the magnetic excitations in LaSrMnO_4 (II.)	35
3.9	Orbital polaron in LaSrMnO_4	37
4.1	Goodenough model of the COO state	44
4.2	Zener polaron ordering	45
4.3	Analysis of the superstructures in the COO state	49
4.4	Phonon dispersion in $\text{La}_{1/2}\text{Sr}_{3/2}\text{MnO}_4$	53
4.5	Anisotropy gap at the magnetic zone center	55
4.6	Raw-data scans to determine the magnon dispersion	57
4.7	Magnon dispersion in $\text{La}_{1/2}\text{Sr}_{3/2}\text{MnO}_4$	58
4.8	Simulated neutron intensity	60
4.9	Diffuse magnetic scattering in $\text{La}_{1/2}\text{Sr}_{3/2}\text{MnO}_4$	65
4.10	Thermal evolution of the magnetic correlations \perp chains	67
4.11	Thermal evolution of the magnetic correlations \parallel chains	68
4.12	Development of the magnetic correlations in $\text{La}_{1/2}\text{Sr}_{3/2}\text{MnO}_4$	69
4.13	Magnetic correlations along the c -axis	72
4.14	Temperature dependence of some macroscopic quantities	73
4.15	Real-space evolution of the magnetic correlations	76
4.16	Thermal evolution of the magnetic fluctuations around a CE-type position	78
4.17	Evolution of the FM fluctuations	80
4.18	q -dependence of the FM fluctuations at $T=250$ K	81

4.19	COO correlations in $\text{La}_{0.6}\text{Sr}_{1.4}\text{MnO}_4$	85
4.20	Elastic magnetic scattering in $\text{La}_{0.6}\text{Sr}_{1.4}\text{MnO}_4$	86
4.21	Temperature dependence of the CE-type correlations chains	88
4.22	Thermal evolution of the diffuse scattering \perp chains	89
4.23	Development of the magnetic correlations in $\text{La}_{0.6}\text{Sr}_{1.4}\text{MnO}_4$	91
4.24	Magnetic correlations along the c-axis	92
4.25	Macroscopic magnetization in $\text{La}_{0.6}\text{Sr}_{1.4}\text{MnO}_4$	93
4.26	Field dependence of the FM scattering	95
4.27	Field dependence of the AFM CE-type scattering	96
4.28	Simulation of the evolution of the CE order upon electron doping	99
4.29	Temperature dependence of the magnetic correlations for $x=0.6$	102
4.30	Stripe ordering of the excess Mn^{4+} in $\text{La}_{0.4}\text{Sr}_{1.6}\text{MnO}_4$	104
4.31	Raw-data scans at finite energies for $\text{La}_{0.4}\text{Sr}_{1.6}\text{MnO}_4$ (I.)	107
4.32	Raw-data scans at finite energies for $\text{La}_{0.4}\text{Sr}_{1.6}\text{MnO}_4$ (II.)	108
4.33	Magnon dispersion in $\text{La}_{0.4}\text{Sr}_{1.6}\text{MnO}_4$	110
4.34	Revised phase diagram of single-layered $\text{La}_{1-x}\text{Sr}_{1+x}\text{MnO}_4$	112
5.1	Crystal structure of TbMnO_3	117
5.2	Phase diagram of the rare-earth manganites RMnO_3	118
5.3	Magnetoelectric phase diagram of TbMnO_3	120
5.4	Magnetic structure of TbMnO_3	122
5.5	Tb crystal-field excitation	126
5.6	Magnetic excitation spectrum in the spiral phase at $\mathbf{Q} = (00.275\ 1)$	127
5.7	High-resolution spectrum at $\mathbf{Q} = (00.275\ 1)$	129
5.8	Polarization analysis of the magnon spectrum in the spiral phase	130
5.9	Magnetic excitations in a spiral magnet	133
5.10	Dielectric function of TbMnO_3 in the THz regime	135
5.11	Spin-wave spectrum at $T = 32\text{K}$ and comparison with spiral phase	137
5.12	Polarization analysis of the magnon spectrum in the SDW phase	138
5.13	Magnetic excitations in a SDW structure	141
5.14	Temperature dependence of the zone-center spectrum	144
5.15	Field dependence of the magnetic modulation	147
5.16	Field dependence the magnetic excitation spectrum	149
5.17	Q-dependence of the spectrum at $H = 12\text{T}$	151
5.18	Analysis of the spin-wave dispersion (I.)	155
5.19	Analysis of the spin-wave dispersion (II.)	157
5.20	Analysis of the spin-wave dispersion (III.)	158
5.21	Spin-wave dispersion in the ac-plane	160
5.22	Scaling of T_N and J_{FM} in the RMnO_3 -series	162
5.23	Magnon dispersion for various values of the magnetic frustration	164
5.24	Analysis of the spin-wave dispersion along \mathbf{b} for $T=17\text{K}$	165
5.25	Analysis of the spin-wave dispersion along \mathbf{b} for $T=32\text{K}$	168

Glossary of Symbols

Common symbols throughout all chapters

\mathbf{k}_i	wave vector of the neutron before the scattering process
\mathbf{k}_f	wave vector of the neutron after the scattering process
\mathbf{R}, \mathbf{r}	point in the direct lattice of a crystal
$\boldsymbol{\tau}$	point in the reciprocal lattice of a crystal
\mathbf{Q}	point in reciprocal space
\mathbf{q}	point in the first Brillouin zone of reciprocal space
$S(\mathbf{Q}, \omega)$	scattering function in neutron scattering experiments
T_N	Néel temperature
$I^{\text{SF/NSF}}$	intensity in the spin flip / non-spin flip channel in experiments using polarized neutrons
\mathbf{P}_i	polarization of the neutron before the scattering process
\mathbf{P}_f	polarization of the neutron after the scattering process

Chap. 3: Magnetic excitation spectrum of single-layered LaSrMnO_4

J_{AFM}	antiferromagnetic coupling between neighboring sites within the MnO_2 -layers
Λ	single-ion anisotropy in the antiferromagnetic ordered phase
ω_{sw}	spin-wave excitation related with the G-type ordering
ω_{cl}	magnetic excitation correlated with finite size clusters

Chap. 4: Spin-wave excitations in charge-ordered manganites

COO	Charge and orbital ordered state in half doped manganites
CE model	classical model for the charge ordering in half-doped manganites predicted by Goodenough

ZP model	alternative Zener polaron model for charge ordering in half-doped manganites
\mathbf{k}_{CO}	propagation vector of charge ordering
\mathbf{k}_{OO}	propagation vector of orbital ordering
$\mathbf{k}_{\text{Mn}^{3+}}$	propagation vector of the magnetic ordering of the Mn^{3+} spins
$\mathbf{k}_{\text{Mn}^{4+}}$	propagation vector of the magnetic ordering of the Mn^{4+} spins
J_{FM}	FM interaction between adjacent sites within the zig-zag chains
J_{AFM}	AFM interaction between adjacent sites on different zig-zag chains
$J_{\text{FM},2}$	FM interaction between cornering Mn^{4+} -sites of the zig-zag chains
J_{iso}	isotropic FM nearest neighbor exchange
\mathbf{Q}_{OO}	scattering vector related to orbital ordering
\mathbf{Q}_{CO}	scattering vector related to charge ordering
\mathbf{Q}_{mag}	scattering vector related to AFM correlations
\mathbf{Q}_{FM}	scattering vector related to ferromagnetic correlations
ξ_{\parallel}	in-plane correlation length parallel to the zig-zag chains
ξ_{\perp}	in-plane correlation length perpendicular to the zig-zag chains
ξ_c	magnetic correlation length along the c -axis
M_{\perp}	macroscopic magnetization perpendicular to the MnO_2 -planes
M_{\parallel}	macroscopic magnetization parallel to the MnO_2 -planes
n_e	e_g -electron density
ε_{OO}	incommensurability of the orbital ordering in the overdoped regime
ε_{SO}	incommensurability of the magnetic ordering

Chap. 5: Magnetic excitations in multiferroic TbMnO_3

\mathbf{P}	electric polarization
\mathbf{M}	magnetization
T_{FE}	ferroelectric transition temperature
T_{spiral}	transition temperature of the spiral ordering
\mathbf{k}_{Mn}	propagation vector of the magnetic ordering of the Mn-subsystem
\mathbf{k}_{Tb}	propagation vector of the magnetic ordering of the Tb-subsystem

ε_b	incommensurability of the magnetic modulation of the Mn-subsystem
ω_{\perp}	spin-wave excitation polarized perpendicular to the spiral plane
ω_{\parallel}	spin-wave excitation polarized parallel to the spiral plane
ω^C	spin-wave excitation in the high-field commensurable phase
J_{FM}	FM exchange interaction between nearest neighbors in the <i>ab</i> -plane
J_{NN}	AFM exchange interaction between next-nearest neighbors along <i>b</i> -direction

Bibliography

- [1] S. Soanes and A. Stevenson, *Oxford English Dictionary*, University Press, Oxford, 11. edition, 2004. [3](#)
- [2] E. Dagotto, *Complexity in strongly correlated electronic systems*, Science **309**, 257 (2005). [3](#), [41](#), [97](#)
- [3] J. G. Bednorz and K. A. Müller, *Possible high- T_c superconductivity in the Ba-La-Cu-O system*, Z. Phys. B **64**, 189 (1986). [3](#)
- [4] R. von Helmolt, J. Wecker, B. Holzapfel, L. Schultz, and K. Samwer, *Giant negative magnetoresistance in perovskite-like $La_{2/3}Ba_{1/3}MnO_3$ ferromagnetic films*, Phys. Rev. Lett. **71**, 2331 (1993). [3](#), [41](#)
- [5] G. C. Milward, M. J. Calderón, and P. B. Littlewood, *Electronically soft phases in manganites*, Nature **433**, 607 (2005). [3](#), [41](#), [97](#)
- [6] T. Kimura, S. Ishihara, H. Shintani, T. Arima, K. Takahashi, K. Ishizaka, and Y. Tokura, *Magnetic control of ferroelectric polarization*, Nature **426**, 55 (2003). [3](#), [116](#), [119](#), [170](#), [173](#)
- [7] S. Larochelle, A. Mehta, L. Lu, P. K. Mang, O. P. Vajk, N. Kaneko, J. W. Lynn, L. Zhou, and M. Greven, *Structural and magnetic properties of the single-layer manganese oxide $La_{1-x}Sr_{1+x}MnO_4$* , Phys. Rev. B **71**, 024435 (2005). [3](#), [22](#), [23](#), [24](#), [25](#), [26](#), [27](#), [28](#), [29](#), [39](#), [47](#), [64](#), [68](#), [71](#), [82](#), [83](#), [84](#), [85](#), [86](#), [101](#), [102](#), [111](#), [112](#), [171](#)
- [8] J. B. Goodenough, *Theory of the role of covalence in the perovskite-type manganites ($La,M(II)MnO_3$)*, Phys. Rev. **100**, 564 (1955). [4](#), [24](#), [41](#), [43](#), [44](#), [112](#), [172](#)
- [9] A. Daoud-Aladine, J. Rodríguez-Carvajal, L. Pinsard-Gaudart, M. T. Fernández-Díaz, and A. Revcolevschi, *Zener polaron ordering in half-doped manganites*, Phys. Rev. Lett. **89**, 097205 (2002). [4](#), [24](#), [41](#), [45](#), [74](#), [112](#), [172](#)
- [10] S.-W. Cheong and M. Mostovoy, *Multiferroics: A magnetic twist for ferroelectricity*, Nature Materials **6**, 13 (2007). [4](#), [124](#), [146](#)
- [11] G. A. Smolenskii and I. E. Chupis, *Ferroelectromagnons*, Sov. Phys. Usp. **25**, 475 (1983). [4](#), [116](#), [173](#)

- [12] H. Katsura, N. Nagaosa, and A. Balatsky, *Spin Current and Magnetoelectric Effect in Noncollinear Magnets*, Phys. Rev. Lett. **95**, 057205 (2005). [4](#), [116](#), [120](#), [121](#), [123](#), [132](#), [152](#), [173](#)
- [13] M. Mostovoy, *Ferroelectricity in spiral magnets*, Phys. Rev. Lett. **96**, 067601 (2006). [4](#), [116](#), [120](#), [121](#), [123](#), [152](#), [160](#), [170](#), [173](#)
- [14] F. Bloch, *On the magnetic scattering of neutrons*, Phys. Rev. **50**, 259 (1936). [5](#)
- [15] C. G. Shull, E. O. Wollan, and W. A. Strauser, *Magnetic structure of magnetite and its use in studying the neutron magnetic interaction*, Phys. Rev. **81**, 483 (1951). [5](#)
- [16] G. E. Bacon and K. Lonsdale, *Neutron Diffraction*, Rev. Prog. Phys. **16**, 1 (1953). [6](#)
- [17] W. Marshall and S. W. Lovesey, *Theory of Thermal Neutron Scattering*, Clarendon Press, Oxford, 1971. [6](#), [8](#), [9](#), [11](#), [12](#), [13](#)
- [18] G. L. Squires, *Introduction to the Theory of Thermal Neutron Scattering*, University Press, Cambridge, 1978. [6](#)
- [19] G. Shirane, M. Shapiro, and J. M. Tranquada, *Neutron Scattering with a Triple-Axis Spectrometer*, University Press, Cambridge, 2002. [6](#), [18](#), [126](#)
- [20] T. Chatterji, *Neutron Scattering from Magnetic Materials*, Elsevier, Amsterdam, 2006. [6](#), [12](#), [13](#), [31](#)
- [21] P. J. Brown, *Magnetic form factors*, in *International Tables for Crystallography*, edited by E. Prince, Vol. C, p. 454ff, Kluwer Academic, Dordrecht-Boston-London, 2004. [10](#), [56](#), [125](#)
- [22] R. M. Moon, T. Riste, and C. Koehler, *Polarization analysis of thermal-neutron scattering*, Phys. Rev. **181**, 920 (1969). [12](#), [13](#), [63](#)
- [23] P. Fulde and M. Loewenhaupt, *Magnetic excitations in crystal-field split 4f systems*, Adv. Phys. **34**, 589 (1986). [14](#)
- [24] M. J. Cooper and R. Nathans, *The resolution function in neutron diffractometry*, Acta. Cryst. **23**, 357 (1967). [18](#), [19](#)
- [25] B. Dorner, *The normalization of the resolution function for inelastic neutron scattering and its Applications*, Acta. Cryst. A **28**, 319 (1972). [18](#)
- [26] N. J. Chesser and J. D. Axe, *Derivation and experimental verification of the normalized resolution function for inelastic neutron scattering*, Acta. Cryst. A **29**, 160 (1973). [18](#)
- [27] A. Zheludev, *ResLib 3.3*, Oak Ridge National Laboratory (2006). [19](#), [55](#)

- [28] J. Kanamori, *Crystal distortions in magnetic compounds*, J. Appl. Phys. **31**, S14 (1960). [21](#), [163](#)
- [29] K. Kugel and D. Khomskii, *The Jahn-Teller effect and magnetism: Transition-metal compounds*, Sov. Phys. Usp. **25**, 231 (1982). [21](#), [24](#), [163](#)
- [30] Y. Tokura and N. Nagaosa, *Orbital physics in transition-metal oxides*, Science **288**, 462 (2000). [21](#), [41](#), [42](#)
- [31] P. W. Anderson, *Antiferromagnetism. Theory of superexchange interaction*, Phys. Rev. **79**, 350 (1950). [21](#), [43](#), [162](#)
- [32] J. Kanamori, *Superexchange interaction and symmetry properties of electron orbitals*, J. Phys. Chem. Solids **10**, 87 (1959). [21](#), [43](#), [106](#)
- [33] J. B. Goodenough, A. Wold, R. J. Arnett, and N. Menyuk, *Relationship between crystal symmetry and magnetic properties of ionic compounds containing Mn^{3+}* , Phys. Rev. **124**, 373 (1961). [21](#), [25](#), [43](#)
- [34] T. Mizokawa and A. Fujimori, *Electronic structure and orbital ordering in perovskite-type 3d transition-metal oxides studied by Hartree-Fock band-structure calculations*, Phys. Rev. B **54**, 5368 (1996). [21](#), [37](#)
- [35] J. Rodriguez-Carvajal, M. Hennion, F. Moussa, A. H. Moudden, L. Pinsard, and A. Revcolevschi, *Neutron-diffraction study of the Jahn-Teller transition in stoichiometric $LaMnO_3$* , Phys. Rev. B **57**, R3189 (1998). [21](#), [37](#)
- [36] E. Saitoh, S. Okamoto, K. T. Takahashi, K. Tobe, K. Yamamoto, T. Kimura, S. Ishihara, S. Maekawa, and Y. Tokura, *Observation of orbital waves as elementary excitations in a solid*, Nature **410**, 180 (2001). [21](#)
- [37] M. Grüninger, R. Rückamp, M. Windt, P. Reutler, C. Zobel, T. Lorenz, A. Freimuth, and A. Revcolevschi, *Quest for orbital waves*, Nature **418**, 39 (2002). [21](#)
- [38] L. Martín-Carrón and A. de Andrés, *Excitations of the orbital order in $RMnO_3$ manganites: Light scattering experiments*, Phys. Rev. Lett. **92**, 175501 (2004). [21](#)
- [39] W.-G. Yin, D. Volja, and W. Ku, *Orbital ordering in $LaMnO_3$: Electron-electron versus electron-lattice interactions*, Phys. Rev. Lett. **96**, 116405 (2006). [21](#)
- [40] A. Yamasaki, M. Feldbacher, Y.-F. Yang, O. K. Andersen, and K. Held, *Pressure-induced metal-insulator transition in $LaMnO_3$ is not of Mott-Hubbard type*, Phys. Rev. Lett. **96**, 166401 (2006). [21](#)
- [41] W. Bao, C. H. Chen, S. A. Carter, and S.-W. Cheong, *Electronic phase separation and charge ordering in $(Sr,La)_2MnO_4$: Indication of triplet bipolarons*, Sol. State Commun. **98**, 55 (1996). [22](#), [47](#), [74](#)

- [42] Y. Moritomo, Y. Tomioka, A. Asamitsu, Y. Tokura, and Y. Matsui, *Magnetic and electronic properties in hole-doped manganese oxides with layered structures: $La_{1-x}Sr_{1+x}MnO_4$* , Phys. Rev. B **51**, 3297 (1995). [22](#), [23](#), [24](#), [25](#), [29](#), [42](#), [47](#), [73](#), [74](#), [94](#)
- [43] P. Reutler, *Korrelierte Orbitale in $La_{1-x}Sr_{1+x}MnO_4$* , PhD thesis, RWTH Aachen, 2004. [22](#), [23](#), [24](#), [25](#), [26](#), [27](#), [28](#), [29](#), [33](#), [36](#), [39](#), [71](#), [73](#), [74](#), [75](#), [83](#), [92](#), [93](#), [94](#), [111](#), [171](#)
- [44] W. Norimatsu and Y. Koyama, *Evolution of orthorhombic domain structures during the tetragonal-to-orthorhombic phase transition in the layered perovskite $Sr_{2-x}La_xMnO_4$* , Phys. Rev. B **74**, 085113 (2006). [22](#), [23](#), [82](#), [101](#)
- [45] H. Weng, Y. Kawazoe, X. Wan, and J. Dong, *Electronic structure and optical properties of layered perovskites Sr_2MO_4 ($M = Ti, V, Cr, \text{ and } Mn$): An ab initio study*, Phys. Rev. B **74**, 205112 (2006). [22](#)
- [46] D. Senff, *Magnetische und orbitale Korrelationen in einfach geschichteten Manganaten*, Diploma Thesis, University of Köln, 2003. [22](#), [24](#), [25](#), [26](#), [27](#), [28](#), [33](#), [39](#), [101](#), [103](#), [105](#), [111](#), [171](#)
- [47] N. N. Kovaleva, A. V. Boris, C. Bernhard, A. Kulakov, A. Pimenov, A. M. Balbashov, G. Khaliullin, and B. Keimer, *Spin-controlled Mott-Hubbard bands in $LaMnO_3$ probed by optical ellipsometry*, Phys. Rev. Lett. **93**, 147204 (2004). [22](#)
- [48] A. Gößling, *Electronic structure of Titanates and layered Manganites probed by optical spectroscopy*, PhD thesis, University of Cologne, 2007. [22](#)
- [49] S. Kawano, N. Achiwa, N. Kamegashira, and M. Aoki, *Magnetic properties of K_2NiF_4 -type oxides Sr_2MnO_{4+x} ($0 \leq x \leq 0.2$)*, J. Phys. (Paris), Colloq. **49**, C8 (1988). [23](#), [25](#)
- [50] M. Bieringer and J. E. Greedan, *Structure and magnetism in $BaLaMnO_{4\pm\delta}$ ($\delta = 0, 0.1$) and $Ba_xSr_{1-x}LaMnO_4$. Disappearance of magnetic order for $x > 0.30$* , J. Mater. Chem. **12**, 279 (2002). [23](#), [25](#)
- [51] M. Merz, P. Reutler, B. Büchner, A. Arena, J. Dvorak, Y. U. Idzerda, S. Tokumitsu, and S. Schuppler, *$O1s$ and $Mn2p$ NEXAFS on single-layered $La_{1-x}Sr_{1+x}MnO_4$: Crystal field effect versus orbital coupling mechanism*, Eur. Phys. J. B **51**, 315 (2006). [23](#), [24](#), [37](#), [47](#)
- [52] M. Merz, G. Roth, P. Reutler, B. Büchner, D. Arena, J. Dvorak, Y. U. Idzerda, S. Tokumitsu, and S. Schuppler, *Orbital degree of freedom in single-layered $La_{1-x}Sr_{1+x}MnO_4$: Doping- and temperature-dependent rearrangement of orbital states*, Phys. Rev. B **74**, 184414 (2006). [23](#), [24](#), [25](#), [37](#)

-
- [53] C. Baumann, G. Allodi, B. Büchner, R. De Renzi, P. Reutler, and A. Revcolevschi, *Magnetism of $La_{1-x}Sr_{1+x}MnO_4$ as revealed by μSR* , Physica B **326**, 505 (2003). [24](#)
- [54] B. J. Sternlieb, J. P. Hill, U. C. Wildgruber, G. M. Luke, B. Nachumi, Y. Moritomo, and Y. Tokura, *Charge and magnetic order in $La_{0.5}Sr_{1.5}MnO_4$* , Phys. Rev. Lett. **76**, 2169 (1996). [24](#), [47](#), [54](#), [64](#), [71](#)
- [55] J. van den Brink, P. Horsch, F. Mack, and A. M. Oleś, *Orbital dynamics in ferromagnetic transition-metal oxides*, Phys. Rev. B **59**, 6795 (1999). [24](#)
- [56] K. T. Park, *Electronic structure calculations for layered $LaSrMnO_4$ and Ca_2RuO_4* , J. Phys. – Condens. Matter **13**, 9231 (2001). [24](#)
- [57] M. Daghofer, A. M. Oles, D. R. Neuber, and W. von der Linden, *Doping dependence of spin and orbital correlations in layered manganites*, Phys. Rev. B **73**, 104451 (2006). [24](#), [25](#), [37](#), [77](#)
- [58] W. B. Wu, D. J. Huang, G. Y. Guo, H.-J. Lin, T. Y. Hou, C. F. Chang, C. T. Chen, A. Fujimori, T. Kimura, H. B. Huang, A. Tanaka, and T. Jo, *Orbital polarization studied by soft x-ray linear dichroism*, J. Electron Spectroscopy and Related Phenomena **127-140**, 641 (2004). [24](#)
- [59] R. Kilian and G. Khaliullin, *Orbital polarons in the metal-insulator transition of manganites*, Phys. Rev. B **60**, 13458 (1999). [24](#), [37](#)
- [60] T. Mizokawa, D. I. Khomskii, and G. A. Sawatzky, *Orbital polarons and ferromagnetic insulators in manganites*, Phys. Rev. B **63**, 024403 (2000). [24](#), [25](#), [37](#)
- [61] P. Steffens, *Magnetism in layered Ruthenates*, PhD thesis, University of Cologne, 2007. [27](#)
- [62] L. J. de Jongh, *Magnetic Properties of Layered Transition-Metal Compounds*, Kluwer Academic Press, Dordrecht-Boston-London, 1990. [27](#), [34](#), [38](#), [54](#)
- [63] M. Benomar, *Einkristall-Präparation und Charakterisierung von dotiertem La_2MO_4 ($M=Co, Mn, Ni$)*, PhD thesis, University of Cologne, 2007. [29](#), [51](#)
- [64] M. Kriener, *Spinzustandsänderung, magnetische Ordnung und Metall-Isolator-Übergang in Kobaltaten*, PhD thesis, University of Cologne, 2005. [29](#), [68](#), [72](#), [73](#), [74](#), [92](#), [93](#), [94](#)
- [65] N. Hollmann, PhD thesis, University of Cologne, *in preparation*. [29](#)
- [66] R. Klingeler, private communication. [29](#)
- [67] P. Reutler, O. Friedt, B. Büchner, M. Braden, and A. Revcolevschi, *Growth of $La_{1-x}Sr_{1+x}MnO_4$ single crystals and characterization by scattering techniques*, J. Cryst. Growth **249**, 222 (2003). [29](#)

- [68] L. P. Regnault, F. Tasset, J. Lorenzo, T. Roberts, G. Dhalenne, and A. Revcolevschi, *Polarized neutron inelastic scattering on the spin-Peierls system CuGeO_3 : “Three-directional” versus “three-dimensional” polarization analysis*, Physica B **267-268**, 227 (1999). [30](#), [31](#), [125](#)
- [69] A. I. Akhiezer, V. G. Bar'yakhtar, and S. V. Peletminskii, *Spin Waves*, North-Holland Publishing Company, Amsterdam, 1968. [34](#), [81](#), [140](#)
- [70] P. V. Hendriksen, S. Linderoth, and P.-A. Lindgård, *Finite-size modifications of the magnetic properties of clusters*, Phys. Rev. B **48**, 7259 (1993). [36](#)
- [71] M. Hennion, F. Moussa, P. Lehouelleur, F. Wang, A. Ivanov, Y. M. Mukovskii, and D. Shulyatev, *Confined spin waves reveal an assembly of nanosize domains in ferromagnetic $\text{La}_{1-x}\text{Ca}_x\text{MnO}_3$ ($x = 0.17, 0.2$)*, Phys. Rev. Lett. **94**, 057006 (2005). [36](#), [37](#), [171](#)
- [72] M. Hennion, F. Moussa, P. Lehouelleur, P. Reutler, and A. Revcolevschi, *Metal-insulator transition of $\text{La}_{7/8}\text{Sr}_{1/8}\text{MnO}_3$ probed by spin waves: Stabilization of a two-dimensional stripe superstructure*, Phys. Rev. B **73**, 104453 (2006). [36](#), [37](#)
- [73] K. Rościszewski and A. M. Oleś, *Interplay between the orbital and magnetic order in monolayer $\text{La}_{1-x}\text{Sr}_{1+x}\text{MnO}_4$* , J. Phys. – Condens. Matter **19**, 186223 (2007). [37](#)
- [74] R. Mathieu, M. Uchida, Y. Kaneko, J. P. He, X. Z. Yu, R. Kumai, T. Arima, Y. Tomioka, A. Asamitsu, Y. Matsui, and Y. Tokura, *Bandwidth-disorder phase diagram of half-doped layered manganites*, Phys. Rev. B **74**, 020404 (2006). [37](#)
- [75] X. Z. Yu, T. Arima, Y. Kaneko, J. P. He, R. Mathieu, T. Asaka, T. Hara, K. Kimoto, Y. Matsui, and Y. Tokura, *Direct observation of the bandwidth-disorder induced variation of charge/orbital ordering structure in $\text{RE}_{0.5}(\text{Ca}_{1-y}\text{Sr}_y)_{1.5}\text{MnO}_4$* , J. Phys. – Condens. Matter **19**, 172203 (2007). [37](#)
- [76] Y. Tokura, A. Urushiba, Y. Moritomo, T. Arima, A. Asamitsu, G. Kido, and N. Furukawa, *Giant magnetotransport phenomena in filling-controlled Kondo lattice system: $\text{La}_{1-x}\text{Sr}_x\text{MnO}_3$* , J. Phys. Soc. Japan **63**, 3931 (1994). [41](#)
- [77] C. Zener, *Interaction between the d-Shells in the transition metals. II. Ferromagnetic compounds of manganese with perovskite structure*, Phys. Rev. **82**, 403 (1951). [41](#), [93](#)
- [78] P. W. Anderson and H. Hasegawa, *Considerations on double exchange*, Phys. Rev. **100**, 675 (1955). [41](#)
- [79] P. G. de Gennes, *Effects of double exchange in magnetic crystals*, Phys. Rev. **118**, 141 (1960). [41](#)

-
- [80] A. J. Millis, P. B. Littlewood, and B. I. Shraiman, *Double exchange alone does not explain the resistivity of $La_{1-x}Sr_xMnO_3$* , Phys. Rev. Lett. **74**, 5144 (1995). [41](#)
- [81] Y. Tokura, H. Kuwahara, Y. Moritomo, Y. Tomioka, and A. Asamitsu, *Competing instabilities and metastable states in $(Nd,Sm)_{1/2}Sr_{1/2}MnO_3$* , Phys. Rev. Lett. **76**, 3184 (1996). [41](#)
- [82] J. Geck, D. Bruns, C. Hess, R. Klingeler, P. Reutler, M. v. Zimmermann, S.-W. Cheong, and B. Büchner, *Anisotropic CE-type orbital correlations in the ferromagnetic metallic phase of $Nd_{1/2}Sr_{1/2}MnO_3$* , Phys. Rev. B **66**, 184407 (2002). [41](#)
- [83] J. C. Loudon, N. D. Mathur, and P. A. Midgley, *Charge-ordered ferromagnetic phase in $La_{0.5}Ca_{0.5}MnO_3$* , Nature **420**, 797 (2002). [41](#)
- [84] F. M. Woodward, J. W. Lynn, M. B. Stone, R. Mahendiran, P. Schiffer, J. F. Mitchell, D. N. Argyriou, and L. C. Chapon, *Field-induced avalanche to the ferromagnetic state in the phase-separated ground state of manganites*, Phys. Rev. B **70**, 174433 (2004). [41](#)
- [85] M. Uehara, S. Mori, C. H. Che, and S.-W. Cheong, *Percolative phase separation underlies colossal magnetoresistance in mixed-valent manganites*, Nature **399**, 560 (1999). [41](#)
- [86] A. Moreo, S. Yunoki, and E. Dagotto, *Phase separation scenario for manganese oxides and related materials*, Science **283**, 2034 (1999). [41](#), [97](#)
- [87] C. Sen, G. Alvarez, and E. Dagotto, *Competing ferromagnetic and charge-ordered states in models for manganites: The origin of the colossal magnetoresistance effect*, Phys. Rev. Lett. **98**, 127202 (2007). [41](#)
- [88] E. O. Wollan and W. C. Koehler, *Neutron diffraction study of the magnetic properties of the series of perovskite-type compounds $[(1-x)La, xCa]MnO_3$* , Phys. Rev. **100**, 545 (1955). [41](#), [43](#)
- [89] C. H. Chen and S.-W. Cheong, *Commensurate to incommensurate charge ordering and its real-space images in $La_{0.5}Ca_{0.5}MnO_3$* , Phys. Rev. Lett. **76**, 4042 (1996). [42](#)
- [90] S. Mori, C. H. Chen, and S.-W. Cheong, *Pairing of charge-ordered stripes in $(La,Ca)MnO_3$* , Nature **392**, 473 (1998). [42](#), [82](#), [104](#), [106](#)
- [91] P. G. Radaelli, D. E. Cox, L. Capogna, S.-W. Cheong, and M. Marezio, *Wigner-crystal and bi-stripe models for the magnetic and crystallographic superstructures of $La_{0.333}Ca_{0.667}MnO_3$* , Phys. Rev. B **59**, 14440 (1999). [42](#), [82](#), [103](#)
- [92] J. Geck, P. Wochner, S. Kiele, R. Klingeler, P. Reutler, A. Revcolevschi, and B. Büchner, *Orbital polaron lattice formation in lightly doped $La_{1-x}Sr_xMnO_3$* , Phys. Rev. Lett. **95**, 236401 (2005). [42](#)

- [93] P. G. Radaelli, D. E. Cox, M. Marezio, S. W. Cheong, P. E. Schiffer, and A. P. Ramirez, *Simultaneous structural, magnetic, and electronic transitions in $La_{1-x}Ca_xMnO_3$ with $x=0.25$ and 0.50* , Phys. Rev. Lett. **75**, 4488 (1995). [42](#), [44](#)
- [94] T. Kimura, R. Kumai, Y. Tokura, J. Q. Li, and Y. Matsui, *Successive structural transitions coupled with magnetotransport properties in $LaSr_2Mn_2O_7$* , Phys. Rev. B **58**, 11081 (1998). [42](#)
- [95] P. G. Radaelli, D. E. Cox, M. Marezio, and S.-W. Cheong, *Charge, orbital, and magnetic ordering in $La_{0.5}Ca_{0.5}MnO_3$* , Phys. Rev. B **55**, 3015 (1997). [44](#)
- [96] H. Kawano, R. Kajimoto, H. Yoshizawa, Y. Tomioka, H. Kuwahara, and Y. Tokura, *Magnetic ordering and relation to the metal-insulator transition in $Pr_{1-x}Sr_xMnO_3$ and $Nd_{1-x}Sr_xMnO_3$ with $x \sim 1/2$* , Phys. Rev. Lett. **78**, 4253 (1997). [44](#)
- [97] J. Blasco, J. García, J. M. de Teresa, M. R. Ibarra, J. Pérez, P. A. Algarabel, C. Marquina, and C. Ritter, *Charge ordering at room temperature in $(Tb,Ca)MnO_3$* , J. Phys. – Condens. Matter **9**, 10321 (1997). [44](#)
- [98] F. Damay, Z. Jírák, M. Hervieu, C. Martin, A. Maignan, B. Raveau, G. André, and F. Bourée, *Charge ordering and structural transitions in $Pr_{0.5}Sr_{0.41}Ca_{0.09}MnO_3$* , J. Magnetism Magnetic Materials **190**, 221 (1998). [44](#)
- [99] P. M. Woodward, D. E. Cox, T. Vogt, C. N. R. Rao, and A. K. Cheetham, *Effect of compositional fluctuations on the phase transitions in $(Nd,Sr)MnO_3$* , Chem. Mater. **11**, 3528 (1999). [44](#)
- [100] F. Millange, S. d. Brion, and G. Chouteau, *Charge, orbital, and magnetic order in $Nd_{0.5}Ca_{0.5}MnO_3$* , Phys. Rev. B **62**, 5619 (2000). [44](#), [74](#)
- [101] Z. Jírák, F. Damay, M. Hervieu, C. Martin, B. Raveau, G. André, and F. Bourée, *Magnetism and charge ordering in $Pr_{0.5}Ca_xSr_{0.5-x}MnO_3$ ($x=0.09$ and 0.5)*, Phys. Rev. B **61**, 1181 (2000). [44](#)
- [102] D. N. Argyriou, H. N. Bordallo, B. J. Campbell, A. K. Cheetham, D. E. Cox, J. S. Gardner, K. Hanif, A. dos Santos, and G. F. Strouse, *Charge ordering and phase competition in the layered perovskite $LaSr_2Mn_2O_7$* , Phys. Rev. B **61**, 15269 (2000). [44](#)
- [103] R. J. Goff and J. P. Attfield, *Charge ordering in half-doped manganites*, Phys. Rev. B **70**, 140404 (2004). [44](#), [48](#)
- [104] S. Yunoki, T. Hotta, and E. Dagotto, *Ferromagnetic, A-type, and charge-ordered CE-type states in doped manganites using Jahn-Teller phonons*, Phys. Rev. Lett. **84**, 3714 (2000). [45](#)

-
- [105] I. V. Solovyev and K. Terakura, *Magnetic spin origin of the charge-ordered phase in manganites*, Phys. Rev. Lett. **83**, 2825 (1999). [45](#), [62](#), [66](#)
- [106] J. van den Brink, G. Khaliullin, and D. Khomskii, *Charge and orbital order in half-doped manganites*, Phys. Rev. Lett. **83**, 5118 (1999). [45](#), [61](#), [66](#)
- [107] J. García, M. C. Sánchez, G. Subías, and J. Blasco, *High resolution x-ray absorption near edge structure at the Mn K edge of manganites*, J. Phys. – Condens. Matter **13**, 3229 (2001). [45](#)
- [108] K. J. Thomas, J. P. Hill, S. Grenier, Y.-J. Kim, P. Abbamonte, L. Venema, A. Rusydi, Y. Tomioka, Y. Tokura, D. F. McMorrow, G. Sawatzky, and M. van Veenendaal, *Soft x-ray resonant diffraction study of magnetic and orbital correlations in a manganite near half doping*, Phys. Rev. Lett. **92**, 237204 (2004). [45](#)
- [109] D. Efremov, J. van den Brink, and D. Khomskii, *Bond- versus site-centered ordering and possible ferroelectricity in manganites*, Nature Materials **3**, 853 (2004). [46](#), [50](#), [82](#)
- [110] N. P. Konstantinidis and C. H. Patterson, *Spin-polaron effective magnetic model for $La_{0.5}Ca_{0.5}MnO_3$* , Phys. Rev. B **70**, 064407 (2004). [46](#), [61](#), [164](#)
- [111] V. Ferrari, M. Towler, and P. B. Littlewood, *Oxygen stripes in $La_{0.5}Ca_{0.5}MnO_3$ from ab initio calculations*, Phys. Rev. Lett. **91**, 227202 (2003). [46](#), [50](#)
- [112] G. Zheng and C. H. Patterson, *Ferromagnetic polarons in $La_{0.5}Ca_{0.5}MnO_3$ and $La_{0.33}Ca_{0.67}MnO_3$* , Phys. Rev. B **67**, 220404 (2003). [46](#), [61](#)
- [113] C. I. Ventura and B. Alascio, *Magnons in the half-doped manganites*, Phys. Rev. B **68**, 020404 (2003). [46](#)
- [114] M. A. Mohan Ram, P. Ganguly, and C. N. R. Rao, *Magnetic properties of quasi-2-dimensional $La_{1-x}Sr_{1+x}MnO_4$ and the evolution of itinerant electron ferromagnetism in the $SrO \cdot (La_{1-x}Sr_xMnO_3)_n$ system*, J. of Solid State Chem. **70**, 82 (1987). [46](#)
- [115] M. Tokunaga, N. Miura, Y. Moritomo, and Y. Tokura, *High-field magnetization and magnetoresistance of $La_{0.5}Sr_{1.5}MnO_4$* , Phys. Rev. B **59**, 11151 (1999). [47](#)
- [116] Y. Murakami, H. Kawada, H. Kawata, M. Tanaka, T. Arima, Y. Moritomo, and Y. Tokura, *Direct observation of charge and orbital ordering in $La_{0.5}Sr_{1.5}MnO_4$* , Phys. Rev. Lett. **80**, 1932 (1998). [47](#), [70](#)
- [117] S. Ishihara and S. Maekawa, *Theory of anomalous x-ray scattering in orbital-ordered manganites*, Phys. Rev. Lett. **80**, 3799 (1998). [47](#)
- [118] I. S. Elfimov, V. I. Anisimov, and G. A. Sawatzky, *Orbital ordering, Jahn-Teller distortion, and anomalous x-ray scattering in manganites*, Phys. Rev. Lett. **82**, 4264 (1999). [47](#)

- [119] S. B. Wilkins, P. D. Spencer, P. D. Hatton, S. P. Collins, M. D. Roper, D. Prabhakaran, and A. T. Boothroyd, *Direct observation of orbital ordering in $La_{0.5}Sr_{1.5}MnO_4$ using soft x-ray diffraction*, Phys. Rev. Lett. **91**, 167205 (2003). [47](#), [70](#)
- [120] S. S. Dhesi, A. Mirone, C. D. Nadai, P. Ohresser, P. Bencok, N. B. Brookes, P. Reutler, A. Revcolevschi, A. Tagliaferri, O. Toulemonde, and G. van der Laan, *Unraveling orbital ordering in $La_{0.5}Sr_{1.5}MnO_4$* , Phys. Rev. Lett. **92**, 056403 (2004). [47](#), [68](#), [70](#)
- [121] D. J. Huang, W. B. Wu, G. Y. Guo, H.-J. Lin, T. Y. Hou, C. F. Chang, C. T. Chen, A. Fujimori, T. Kimura, H. B. Huang, A. Tanaka, and T. Jo, *Orbital ordering in $La_{0.5}Sr_{1.5}MnO_4$ studied by soft x-ray linear dichroism*, Phys. Rev. Lett. **92**, 087202 (2004). [47](#), [70](#)
- [122] U. Staub, V. Scagnoli, A. M. Mulders, K. Katsumata, Z. Honda, H. Grimmer, M. Horisberger, and J. M. Tonnerre, *Orbital and magnetic ordering in $La_{0.5}Sr_{1.5}MnO_4$ studied by soft x-ray resonant scattering*, Phys. Rev. B **71**, 214421 (2005). [47](#), [54](#), [70](#)
- [123] S. B. Wilkins, N. Stojic, T. A. W. Beale, N. Binggeli, C. W. M. Castleton, P. Bencok, D. Prabhakaran, A. T. Boothroyd, P. D. Hatton, and M. Altarelli, *Resonant soft x-ray scattering investigation of orbital and magnetic ordering in $La_{0.5}Sr_{1.5}MnO_4$* , Phys. Rev. B **71**, 245102 (2005). [47](#), [70](#)
- [124] J. Herrero-Martin, J. Garcia, G. Subias, J. Blasco, and M. C. Sanchez, *Polarized x-ray absorption spectra of $La_{1-x}Sr_{1+x}MnO_4$: Electronic state of Mn atoms*, Phys. Rev. B **72**, 085106 (2005). [47](#)
- [125] M. Haverkort, private communication. [47](#)
- [126] S. Larochelle, A. Mehta, N. Kaneko, P. K. Mang, A. F. Panchula, L. Zhou, J. Arthur, and M. Greven, *Nature of e_g -electron order in $La_{1-x}Sr_{1+x}MnO_4$* , Phys. Rev. Lett. **87**, 095502 (2001). [47](#), [82](#), [85](#), [101](#)
- [127] O. Schumann, PhD thesis, University of Cologne, in preparation. [47](#), [51](#), [70](#), [83](#), [85](#)
- [128] P. Mahadevan, K. Terakura, and D. D. Sarma, *Spin, charge, and orbital ordering in $La_{0.5}Sr_{1.5}MnO_4$* , Phys. Rev. Lett. **87**, 066404 (2001). [48](#)
- [129] H. Wu, private communication. [48](#)
- [130] E. E. Rodriguez, T. Proffen, A. Llobet, J. J. Rhyne, and J. F. Mitchell, *Neutron diffraction study of average and local structure in $La_{0.5}Ca_{0.5}MnO_3$* , Phys. Rev. B **71**, 104430 (2005). [48](#)

-
- [131] A. Trokiner, A. Yakubovskii, S. Verkhovskii, A. Gerashenko, and D. Khomskii, *¹⁷O NMR as a conclusive probe of charge-ordering models in half-doped manganites*, Phys. Rev. B **74**, 092403 (2006). [48](#)
- [132] J. M. Tranquada, K. Nakajima, M. Braden, L. Pintschovius, and R. J. McQueeney, *Bond-stretching-phonon anomalies in stripe-ordered $\text{La}_{1.69}\text{Sr}_{0.31}\text{NiO}_4$* , Phys. Rev. Lett. **88**, 075505 (2002). [51](#)
- [133] M. Braden, W. Reichardt, S. Shiryayev, and S. N. Barilo, *Giant phonon anomalies in the bond-stretching modes in doped BaBiO_3 : Comparison to cuprates manganites and nickelates*, Physica C **378**, 89 (2002). [51](#)
- [134] D. Reznik, L. Pintschovius, M. Ito, S. Iikubo, M. Sato, H. Goka, M. Fujita, K. Yamada, G. D. Gu, and J. M. Tranquada, *Electron-phonon coupling reflecting dynamic charge inhomogeneity in copper oxide superconductors*, Nature **440**, 1170 (2006). [51](#)
- [135] M. Braden, W. Reichardt, Y. Sidis, Z. Mao, and Y. Maeno, *Lattice dynamics and electron-phonon coupling in Sr_2RuO_4 : Inelastic neutron scattering and shell-model calculations*, Phys. Rev. B **76**, 014505 (2007). [52](#)
- [136] M. Braden, L. Pintschovius, T. Uefuji, and K. Yamada, *Dispersion of the high-energy phonon modes in $\text{Nd}_{1.85}\text{Ce}_{0.15}\text{CuO}_4$* , Phys. Rev. B **72**, 184517 (2005). [52](#)
- [137] M. Braden, unpublished results. [52](#)
- [138] K. Yamamoto, T. Kimura, T. Ishikawa, T. Katsufuji, and Y. Tokura, *Raman spectroscopy of the charge-orbital ordering in layered manganites*, Phys. Rev. B **61**, 14706 (2000). [54](#)
- [139] N. E. Bonesteel, *Theory of anisotropic superexchange in insulating cuprates*, Phys. Rev. B **47**, 11302 (1993). [54](#)
- [140] C. J. Peters, R. J. Birgeneau, M. A. Kastner, H. Yoshizawa, Y. Endoh, J. Tranquada, G. Shirane, Y. Hidaka, M. Oda, M. Suzuki, and T. Murakami, *Two-dimensional zone-center spin-wave excitations in La_2CuO_4* , Phys. Rev. B **37**, 9761 (1988). [54](#)
- [141] J. Rossat-Mignod, L. P. Regnault, C. Vettier, P. Burlet, J. Y. Henry, and G. Laperot, *Investigation of the spin dynamics in $\text{YBa}_2\text{Cu}_3\text{O}_{6+x}$ by inelastic neutron scattering*, Physica B **169**, 58 (1991). [54](#)
- [142] F. Krüger and S. Scheidl, *Spin dynamics of stripes*, Phys. Rev. B **67**, 134512 (2003). [59](#)
- [143] F. Krüger, *Fluctuations of spin and charge in stripe phases of layered antiferromagnets*, PhD thesis, University of Cologne, 2004. [59](#)

- [144] F. Moussa, M. Hennion, J. Rodriguez-Carvajal, H. Moudden, L. Pinsard, and A. Revcolevschi, *Spin waves in the antiferromagnet perovskite LaMnO_3 : A neutron-scattering study*, Phys. Rev. B **54**, 15149 (1996). [59](#), [61](#), [159](#), [160](#), [161](#), [162](#)
- [145] P. W. Anderson, *An approximate quantum theory of the antiferromagnetic ground state*, Phys. Rev. **86**, 694 (1952). [59](#)
- [146] K. Hirota, N. Kaneko, A. Nishizawa, and Y. Endoh, *Two-dimensional planar ferromagnetic coupling in LaMnO_3* , J. Phys. Soc. Japan **65**, 3736 (1996). [61](#), [159](#), [160](#), [161](#)
- [147] Y. Endoh, H. Hiraka, Y. Tomioka, Y. Tokura, N. Nagaosa, and T. Fujiwara, *Orbital nature of ferromagnetic magnons in manganites*, Phys. Rev. Lett. **94**, 017206 (2005). [61](#)
- [148] F. Ye, P. Dai, J. A. Fernandez-Baca, H. Sha, J. W. Lynn, H. Kawano-Furukawa, Y. Tomioka, Y. Tokura, and J. Zhang, *Evolution of spin-wave excitations in ferromagnetic metallic manganites*, Phys. Rev. Lett. **96**, 047204 (2006). [61](#), [82](#)
- [149] N. Furukawa, *Spin excitation spectrum of $(\text{La},\text{A})\text{MnO}_3$* , J. Phys. Soc. Japan **65**, 1174 (1996). [61](#)
- [150] T. Ishikawa, K. Ookura, and Y. Tokura, *Optical response to orbital and charge ordering in a layered manganite: $\text{La}_{1/2}\text{Sr}_{3/2}\text{MnO}_4$* , Phys. Rev. B **59**, 8367 (1999). [62](#)
- [151] J. H. Jung, J. S. Ahn, J. Yu, T. W. Noh, J. Lee, Y. Moritomo, I. Solovyev, and K. Terakura, *Optical investigations of the charge gap in orbital-ordered $\text{La}_{1/2}\text{Sr}_{3/2}\text{MnO}_4$* , Phys. Rev. B **61**, 6902 (2000). [62](#)
- [152] Y. S. Lee, S. Onoda, T. Arima, Y. Tokunaga, J. P. He, Y. Kaneko, N. Nagaosa, and Y. Tokura, *In-plane anisotropy of the electronic structure for the charge- and orbital-ordered state in half-doped manganite with layered structure*, Phys. Rev. Lett. **97**, 077203 (2006). [62](#)
- [153] F. Ye, J. A. Fernandez-Baca, P. Dai, J. W. Lynn, H. Kawano-Furukawa, H. Yoshizawa, Y. Tomioka, and Y. Tokura, *Electronically smecticlike liquid-crystal phase in a nearly half-doped manganite*, Phys. Rev. B **72**, 212404 (2005). [66](#)
- [154] H. Stanley, *Introduction to Phase Transitions and Critical Phenomena*, University Press, Oxford, 1971. [68](#)
- [155] I. Klassen, *Aufbau eines Magnetkryostaten für Transportmessungen im Hochtemperaturbereich*, Diploma Thesis, University of Cologne, 2006. [72](#), [73](#), [94](#)
- [156] N. Kumar and C. N. R. Rao, *The nature of charge ordering in rare-earth manganites and its strong dependence on the size of the A-site cations*, J. of Solid State Chem. **129**, 363 (1997). [74](#)

- [157] Y. Tomioka and Y. Tokura, *Bicritical features of the metal-insulator transition in bandwidth-controlled manganites: Single crystals of $Pr_{1-x}(Ca_{1-y}Sr_y)_xMnO_3$* , Phys. Rev. B **66**, 104416 (2002). [74](#)
- [158] K. Marumoto, K. Soda, S. Kuroda, and Y. Moritomo, *ESR studies of layered-perovskite manganites $R_{0.5}Sr_{1.5}MnO_4$ ($R=La,Nd$)*, J. Phys. Soc. Japan **72**, 582 (2003). [74](#)
- [159] J.-C. Bouloux, J.-L. Soubeyroux, A. Daouda, and G. Le Flem, *Proprietes magnetiques de la phase $Sr_{1.50}La_{0.50}MnO_4$* , Mat. Res. Bull. **16**, 855 (1981). [75](#)
- [160] I. V. Solovyev, *Charge ordering due to magnetic symmetry breaking*, Phys. Rev. Lett. **91**, 177201 (2003). [77](#)
- [161] L. Brey, *Phase diagram of half doped manganites*, Phys. Rev. B **71**, 174426 (2005). [77](#)
- [162] S.-W. Cheong, G. Aeppli, T. E. Mason, H. Mook, S. M. Hayden, P. C. Canfield, Z. Fisk, K. N. Clausen, and J. L. Martinez, *Incommensurate magnetic fluctuations in $La_{2-x}Sr_xCuO_4$* , Phys. Rev. Lett. **67**, 1791 (1991). [80](#)
- [163] H. A. Mook, P. C. Dai, S. M. Hayden, G. Aeppli, T. Perring, and F. Dogan, *Spin fluctuations in $YBa_2Cu_3O_{6.6}$* , Nature **395**, 580 (1998). [80](#)
- [164] J. M. Tranquada, P. Wochner, and D. J. Buttrey, *Spin dynamics in an ordered stripe phase*, Phys. Rev. Lett. **79**, 2133 (1997). [80](#)
- [165] P. Bourges, Y. Sidis, M. Braden, K. Nakajima, and J. M. Tranquada, *High-energy spin dynamics in $La_{1.69}Sr_{0.31}NiO_4$* , Phys. Rev. Lett. **90**, 147202 (2003). [80](#), [107](#)
- [166] P. G. Freeman, A. T. Boothroyd, D. Prabhakaran, C. D. Frost, M. Enderle, and A. Hiess, *Spin dynamics of half-doped $La_{3/2}Sr_{1/2}NiO_4$* , Phys. Rev. B **71**, 174412 (2005). [80](#)
- [167] K. Nakajima, K. Yamada, S. Hosoya, Y. Endoh, M. Greven, and R. Birgeneau, *Spin dynamics and spin correlations in the spin $S=1$ two-dimensional square-lattice Heisenberg antiferromagnet La_2NiO_4* , Z. Phys. B **96**, 479 (1995). [80](#)
- [168] W. Bao, J. D. Axe, C. H. Chen, and S.-W. Cheong, *Impact of charge ordering on magnetic correlations in perovskite $(Bi,Ca)MnO_3$* , Phys. Rev. Lett. **78**, 543 (1997). [82](#)
- [169] J. van den Brink, G. Khaliullin, and D. Khomskii, *Orbital Effects in Manganites*, in *Colossal Magnetoresistive Manganites*, edited by T. Chatterij, Kluwer Academic Publishers, Dordrecht-Boston-London, 2004. [82](#)
- [170] E. Dagotto, *Open questions in CMR manganites*, New J. Phys. **7**, 67 (2005). [82](#)

- [171] C. S. Hong, E. O. Chi, W. S. Kim, N. H. Hur, K. W. Lee, and C. H. Lee, *Magnetic properties and structural evolution in $Nd_{0.5}Sr_{1.5}MnO_4$* , Chem. Mater. **13**, 945 (2001). [83](#)
- [172] T. Kimura, K. Hatsuda, Y. Ueno, R. Kajimoto, H. Mochizuki, H. Yoshizawa, T. Nagai, Y. Matsui, A. Yamazaki, and Y. Tokura, *Charge-orbital ordering and ferromagnetic chains in single-layered manganite crystals*, Phys. Rev. B **65**, 020407 (2001). [83](#)
- [173] T. Nagai, T. Kimura, A. Yamazaki, T. Asaka, K. Kimoto, Y. Tokura, and Y. Matsui, *Transversely modulated crystal structure of charge-orbital ordered manganites $Nd_{1-x}Sr_{1+x}MnO_4$ ($x = 2/3, 3/4$)*, Phys. Rev. B **65**, 060405 (2002). [83](#)
- [174] W. Norimatsu and Y. Koyama, *Crystallographic features of the orbital-ordered, and charge-and-orbital-ordered states in $Sr_{2-x}Nd_xMnO_4$* , Phys. Rev. B **75**, 235121 (2007). [83](#)
- [175] T. Nagai, T. Kimura, A. Yamazaki, Y. Tomioka, K. Kimoto, Y. Tokura, and Y. Matsui, *Possible presence of a charge-orbital density wave in layered manganites $Nd_{1-x}Ca_{1+x}MnO_4$* , Phys. Rev. B **68**, 092405 (2003). [83](#), [105](#)
- [176] Sher Alam, A. T. M. N. Islam, T. Nagai, M. Xu, Javed Ahmad, Y. Matsui, and I. Tanaka, *Possible experimental signature of charge-orbital density waves in $Nd_{1-x}Ca_{1+x}MnO_4$: Heat capacity and magnetization study*, Phys. Rev. B **75**, 205134 (2007). [83](#)
- [177] M. Ibarra, R. Retoux, M. Hervieu, C. Autret, A. Maignan, C. Martin, and B. Raveau, *Charge-orbital ordering above room-temperature in the 2D $Pr_{1-x}Ca_{1+x}MnO_4$ manganites*, J. of Solid State Chem. **170**, 361 (2002). [83](#)
- [178] Y. S. Lee, T. Arima, S. Onoda, Y. Okimoto, Y. Tokunaga, R. Mathieu, X. Z. Yu, J. P. He, Y. Kaneko, Y. Matsui, N. Nagaosa, and Y. Tokura, *Correlation of electronic structure and ordered charge and orbital patterns for single-layered manganites in a wide hole-doping range ($0 \leq x \leq 1$)*, Phys. Rev. B **75**, 144407 (2007). [83](#)
- [179] X. Z. Yu, R. Mathieu, T. Arima, Y. Kaneko, J. P. He, M. Uchida, T. Asaka, T. Nagai, K. Kimoto, A. Asamitsu, Y. Matsui, and Y. Tokura, *Variation of charge/orbital ordering in layered manganite $Pr_{1-x}Ca_{1+x}MnO_4$ investigated by transmission electron microscopy*, Phys. Rev. B **75**, 174441 (2007). [83](#)
- [180] R. Mathieu, J. P. He, X. Z. Yu, Y. Kaneko, M. Uchida, Y. S. lee, T. Arima, A. Asamitsu, and Y. Tokura, *Coexistence of long-ranged charge and orbital order and spin-glass state in single-layered manganites with weak quenched disorder*, condmat/0701191 (2007). [83](#)
- [181] F. Anfuso, private communication. [98](#)

-
- [182] J. Zaanen and O. Gunnarsson, *Charged magnetic domain lines and the magnetism of high- T_c oxides*, Phys. Rev. B **40**, 7391 (1989). [103](#)
- [183] V. J. Emery, S. A. Kivelson, and H. Q. Lin, *Phase separation in the t - J model*, Phys. Rev. Lett. **64**, 475 (1990). [103](#)
- [184] J. M. Tranquada, B. J. Sternlieb, J. D. Axe, Y. Nakamura, and S. Uchida, *Evidence for stripe correlations of spins and holes in copper-oxide superconductors*, Nature **375**, 561 (1995). [103](#), [106](#)
- [185] J. M. Tranquada, D. J. Buttrey, and V. Sachan, *Incommensurate stripe order in $La_{2-x}Sr_xNiO_4$ with $x=0.225$* , Phys. Rev. B **54**, 12318 (1996). [103](#), [106](#)
- [186] B. O. Wells, Y. S. Lee, M. A. Kastner, R. J. Christianson, R. J. Birgeneau, K. Yamada, Y. Endoh, and G. Shirane, *Incommensurate spin fluctuations in high-transition temperature superconductors*, Science **277**, 1067 (1997). [103](#)
- [187] S. A. Kivelson, E. Fradkin, and V. J. Emery, *Electronic liquid-crystal phases of a doped Mott insulator*, Nature **393**, 550 (1998). [103](#)
- [188] J. Orenstein and A. J. Millis, *Advances in the physics of high-temperature superconductivity*, Science **288**, 468 (2000). [103](#)
- [189] J. M. Tranquada, D. J. Buttrey, V. Sachan, and J. E. Lorenzo, *Simultaneous ordering of holes and spins in $La_2NiO_{4.125}$* , Phys. Rev. Lett. **73**, 1003 (1994). [103](#)
- [190] H. Yoshizawa, T. Kakeshita, R. Kajimoto, T. Tanabe, T. Katsufuji, and Y. Tokura, *Stripe order at low temperatures in $La_{2-x}Sr_xNiO_4$ with $0.289 \lesssim x \lesssim 0.5$* , Phys. Rev. B **61**, R854 (2000). [103](#)
- [191] K. Yamada, C. H. Lee, K. Kurahashi, J. Wada, S. Wakimoto, S. Ueki, H. Kimura, Y. Endoh, S. Hosoya, G. Shirane, R. J. Birgeneau, M. Greven, M. A. Kastner, and Y. J. Kim, *Doping dependence of the spatially modulated dynamical spin correlations and the superconducting-transition temperature in $La_{2-x}Sr_xCuO_4$* , Phys. Rev. B **57**, 6165 (1998). [103](#)
- [192] M. Cwik, *Spin, Lattice and Charge Degrees of Freedom in Layered Cobaltates*, PhD thesis, University of Cologne, 2007. [103](#)
- [193] J. C. Loudon, S. Cox, A. J. Williams, J. P. Attfield, P. B. Littlewood, P. A. Midgley, and N. D. Mathur, *Weak charge-lattice coupling requires reinterpretation of stripes of charge order in $La_{1-x}Ca_xMnO_3$* , Phys. Rev. Lett. **94**, 097202 (2005). [103](#)
- [194] C. H. Chen, S.-W. Cheong, and H. Y. Hwang, *Charge-ordered stripes in $La_{1-x}Ca_xMnO_3$ with $x>0.5$ (invited)*, J. Appl. Phys. **81**, 4236 (1997). [103](#)

- [195] S. M. Hayden, H. A. Mook, P. Dai, T. G. Perring, and F. Doğan, *The structure of the high-energy spin excitations in a high-transition-temperature superconductor*, Nature **429**, 531 (2004). [107](#)
- [196] J. M. Tranquada, H. Woo, T. Perring, H. Goka, G. D. Gu, G. Xu, M. Fujita, and K. Yamada, *Quantum magnetic excitations from stripes in copper oxide superconductors*, Nature **429**, 534 (2004). [107](#)
- [197] A. T. Boothroyd, D. Prabhakaran, P. G. Freeman, S. J. S. Lister, M. Enderle, A. Hiess, and J. Kulda, *Spin dynamics in stripe-ordered $La_{5/3}Sr_{1/3}NiO_4$* , Phys. Rev. B **67**, 100407 (2003). [107](#)
- [198] R. H. Lyddane, R. G. Sachs, and E. Teller, *On the polar vibrations of alkali halides*, Phys. Rev. **59**, 673 (1941). [115](#)
- [199] V. G. Bar'yakhtar and I. Chapuis, *Quantum theory of oscillations in a ferromagnetic ferromagnet*, Sov. Phys. – Solid State **11**, 2628 (1970). [115](#), [135](#)
- [200] I. A. Akhiezer and L. N. Davydov, *Coupled electromagnetic spin waves in magnetically ordered ferroelectrics*, Sov. Phys. – Solid State **12**, 2563 (1971). [115](#), [135](#)
- [201] M. Fiebig, *Revival of the magnetoelectric effect*, Journal of Physics D: Applied Physics **38**, 123 (2005). [115](#), [116](#)
- [202] W. Eerenstein, N. D. Mathur, and J. F. Scott, *Multiferroic and magnetoelectric materials*, Nature **442**, 759 (2006). [115](#)
- [203] J. W. F. Brown, R. M. Hornreich, and S. Shtrikman, *Upper bound on the magnetoelectric susceptibility*, Phys. Rev. **168**, 574 (1968). [116](#)
- [204] H. Schmid, *Multiferroic magnetoelectrics*, Ferroelectrics **162**, 665 (1994). [116](#)
- [205] N. H. Hill, *Why are there so few magnetic ferroelectrics*, J. Phys. Chem. B **104**, 6694 (2000). [116](#)
- [206] D. I. Khosmkii, *Magnetism and ferroelectricity: Why do they so seldom coexist ?*, Bull. Am. Phys. Soc. C **21**, 2 (2001). [116](#)
- [207] E. F. Bertaut and M. Mercier, *Structure magnetique de $MnYO_3$* , Phys. Lett. **5**, 27 (1963). [116](#)
- [208] F. Kubel and H. Schmid, *Structure of a ferroelectric and ferroelastic monodomain crystal of the perovskite $BiFeO_3$* , Acta Crystallogr. B **46**, 698 (1990). [116](#)
- [209] M. Fiebig, T. Lottermoser, D. Frohlich, A. Goltsev, and R. Pisarev, *Observation of coupled magnetic and electric domains*, Nature **419**, 818 (2002). [116](#)

-
- [210] I. Sergienko and E. Dagotto, *Key role of Dzyaloshinskii-Moriya interaction in the multiferroic phenomena*, Phys. Rev. B **73**, 094434 (2005). [116](#), [120](#), [121](#)
- [211] T. Goto, T. Kimura, G. Lawes, A. Ramirez, and Y. Tokura, *Ferroelectricity and giant magnetocapacitance in perovskite rare-earth manganites*, Phys. Rev. Lett. **92**, 257201 (2004). [116](#), [119](#)
- [212] T. Kimura, G. Lawes, T. Goto, Y. Tokura, and A. Ramirez, *Magnetoelectric phase diagrams of orthorhombic $RMnO_3$ ($R = Gd, Tb, \text{ and } Dy$)*, Phys. Rev. B **71**, 224425 (2005). [116](#), [120](#), [143](#)
- [213] I. Kagomiya, K. Kohn, and T. Uchiyama, *Structure and ferroelectricity of RMn_2O_5* , Ferroelectrics **280**, 131 (2002). [116](#)
- [214] N. Hur, S. Park, P. Sharma, J. Ahn, S. Guha, and S.-W. Cheong, *Electric polarization reversal and memory in a multiferroic material induced by magnetic fields*, Nature **429**, 392 (2004). [116](#)
- [215] Y. Yamasaki, S. Miyasaka, Y. Kaneko, J.-P. He, T. Arima, and Y. Tokura, *Magnetic reversal of the ferroelectric polarization in a multiferroic spinel oxide*, Phys. Rev. Lett. **96**, 207204 (2006). [116](#)
- [216] G. Lawes, A. B. Harris, T. Kimura, N. Rogado, R. J. Cava, A. Aharony, O. Entin-Wohlman, T. Yildirim, M. Kenzelmann, C. Broholm, and A. P. Ramirez, *Magnetically driven ferroelectric order in $Ni_3V_2O_8$* , Phys. Rev. Lett. **95**, 087205 (2005). [116](#)
- [217] T. Masuda, A. Zheludev, A. Bush, M. Markina, and A. Vasiliev, *Competition between helimagnetism and commensurate quantum spin correlations in $LiCu_2O_2$* , Phys. Rev. Lett. **92**, 177201 (2004). [116](#)
- [218] S. Park, Y. J. Choi, C. L. Zhang, and S.-W. Cheong, *Ferroelectricity in an $S = 1/2$ chain cuprate*, Phys. Rev. Lett. **98**, 057601 (2007). [116](#)
- [219] T. Kimura, J. C. Lashley, and A. P. Ramirez, *Inversion symmetry breaking in the noncollinear magnet phase of triangular-lattice antiferromagnet $CuFeO_2$* , Phys. Rev. B **73**, 220401(R) (2006). [116](#)
- [220] O. Heyer, N. Hollmann, I. Klassen, S. Jodlauk, L. Bohaty, P. Becker, J. A. Mydosh, T. Lorenz, and D. Khomskii, *A new multiferroic material: $MnWO_4$* , J. Phys. – Condens. Matter **18**, L471 (2006). [116](#)
- [221] K. Taniguchi, N. Abe, T. Takenobu, Y. Iwasa, and T. Arima, *Ferroelectric polarization flop in a frustrated magnet $MnWO_4$ induced by a magnetic field*, Phys. Rev. Lett. **97**, 097203 (2006). [116](#)

- [222] M. Kenzelmann, A. Harris, S. Jonas, C. Broholm, J. Schefer, S. Kim, C. Zhang, S.-W. Cheong, O. Vajk, and J. Lynn, *Magnetic inversion symmetry breaking and ferroelectricity in $TbMnO_3$* , Phys. Rev. Lett. **95**, 087206 (2005). [116](#), [120](#), [121](#), [122](#), [131](#), [154](#), [157](#)
- [223] T. Arima, A. Tokunaga, T. Goto, H. Kimura, Y. Noda, and Y. Tokura, *Collinear-to-spiral spin transformation without changing modulation wavelength upon ferroelectric transition in $Tb_{1-x}Dy_xMnO_3$* , Phys. Rev. Lett. **96**, 097202 (2006). [116](#), [120](#), [123](#)
- [224] J. Blasco, C. Ritter, J. Garcia, J. de Teresa, J. Perez-Cacho, and M. Ibarra, *Structural and magnetic study of $Tb_{1-x}Ca_xMnO_3$ perovskites*, Phys. Rev. B **62**, 5609 (2000). [117](#), [118](#)
- [225] J. Alonso, M. Martínez-Lope, M. Casais, and M. Fernández-Díaz, *Evolution of the Jahn-Teller distortion of MnO_6 octahedra in $RMnO_3$ perovskites ($R = Pr, Nd, Dy, Tb, Ho, Er, Y$): A neutron diffraction study*, Inorg. Chem. **39**, 917 (2000). [117](#), [162](#)
- [226] R. D. Shannon, *Revised effective ionic radii and systematic studies of interatomic distances in halides and chalcogenides*, Acta Cryst. **A32**, 751 (1976). [118](#)
- [227] J. Rodríguez-Carvajal, M. Hennion, F. Moussa, A. Moudden, L. Pinsard, and A. Revcolevschi, *Neutron-diffraction study of the Jahn-Teller transition in stoichiometric $LaMnO_3$* , Phys. Rev. B **57**, R3189 (1998). [118](#), [162](#)
- [228] T. Kimura, S. Ishihara, H. Shintani, T. Arima, K. Takahashi, K. Ishizaka, and Y. Tokura, *Distorted perovskite with e_g^1 configuration as a frustrated spin system*, Phys. Rev. B **68**, 060403(R) (2003). [118](#), [119](#), [162](#), [164](#)
- [229] J.-S. Zhou and J. B. Goodenough, *Unusual evolution of the magnetic interaction versus structural distortions in $RMnO_3$ perovskites*, Phys. Rev. Lett. **96**, 247202 (2006). [118](#), [162](#), [163](#)
- [230] A. Muñoz, M. T. Casáis, J. A. Alonso, M. J. Martínez-Lope, J. L. Martínez, and M. T. Fernández-Díaz, *Complex magnetism and magnetic structures of the metastable $HoMnO_3$ perovskite*, Inorg. Chem. **40**, 1020 (2001). [119](#)
- [231] S. Quezel, F. Tcheou, J. Rossat-Mignoda, G. Quezel, and E. Roudaut, *Magnetic structure of the perovskite-like compound $TbMnO_3$* , Physica B **86-88**, 916 (1977). [119](#), [124](#)
- [232] R. Kajimoto, H. Yoshizawa, H. Shintani, T. Kimura, and Y. Tokura, *Magnetic structure of $TbMnO_3$ by neutron diffraction*, Phys. Rev. B **70**, 012401 (2004). [119](#), [122](#)
- [233] F. Jona and G. Shirane, *Ferroelectric Crystals*, Pergamon, New York, 1962. [119](#)

-
- [234] L. D. Landau and E. M. Lifschitz, *Elektrodynamik der Kontinua*, Akademie Verlag, Berlin, 1985. [119](#)
- [235] J. Baier, D. Meier, K. Berggold, J. Hemberger, A. Balbashov, J. Mydosh, and T. Lorenz, *Hysteresis effects in the phase diagram of multiferroic GdMnO₃*, Phys. Rev. B **73**, 100402(R) (2006). [120](#)
- [236] I. Dzyaloshinsky, *A thermodynamic theory of weak ferromagnetism of antiferromagnetics*, J. Phys. Chem. Solids **4**, 241 (1958). [121](#)
- [237] T. Moriya, *Anisotropic superexchange interaction and weak ferromagnetism*, Phys. Rev. **120**, 91 (1960). [121](#)
- [238] C. Jia, S. Onoda, N. Nagaosa, and J. H. Han, *Bond electronic polarization induced by spin*, Phys. Rev. B **74**, 224444 (2006). [121](#)
- [239] J. Hu, *Microscopic origin of magnetic ferroelectrics in nonlinear multiferroics*, condmat/0705.0955v1 (2007). [121](#)
- [240] T. Nagamiya, *Helical Spin Ordering - 1. Theory of Helical Spin Configurations*, in *Solid State Physics*, edited by F. Seitz, D. Turnbull, and H. Ehrenreich, Vol. 20, p. 305, Academic Press, New York, 1967. [123](#), [132](#), [160](#)
- [241] Y. Yamasaki, H. Sagayama, T. Goto, M. Matsuura, K. Hirota, T. Arima, and Y. Tokura, *Electric control of spin helicity in a magnetic ferroelectric*, Phys. Rev. Lett. **98**, 147204 (2007). [123](#)
- [242] T. Arima, T. Goto, Y. Yamasaki, S. Miyasaka, K. Ishii, M. Tsubota, T. Inami, Y. Murakami, and Y. Tokura, *Magnetic-field-induced transition in the lattice modulation of colossal magnetoelectric GdMnO₃ and TbMnO₃ compounds*, Phys. Rev. B **72**, 100102(R) (2005). [123](#), [146](#)
- [243] N. Aliouane, D. Argyriou, J. Stremper, I. Zegkinoglou, S. Landsgesell, and M. Zimmermann, *Field induced linear magneto-elastic coupling in multiferroic TbMnO₃*, Phys. Rev. B **73**, 020102 (2006). [123](#), [146](#)
- [244] T. Goto, Y. Yamasaki, H. Watanabe, T. Kimura, and Y. Tokura, *Anticorrelation between ferromagnetism and ferroelectricity in perovskite manganites*, Phys. Rev. B **72**, 220403(R) (2005). [124](#)
- [245] L. Noda, M. Akaki, T. Kikuchi, and H. Kuwahara, *Magnetic-field-induced switching between ferroelectric phases in orthorhombic-distortion-controlled RMnO₃*, J. Appl. Phys. **99**, 08S905 (2006). [124](#)
- [246] J. Hemberger, F. Schrettle, A. Pimenov, P. Lunkenheimer, V. Y. Ivanov, A. A. Mukhin, A. M. Balbashov, and A. Loidl, *Multiferroic phases of Eu_{1-x}Y_xMnO₃*, Phys. Rev. B **75**, 035118 (2007). [124](#)

- [247] R. Feyerherm, E. Dudzik, N. Aliouane, and D. N. Argyriou, *Commensurate Dy magnetic ordering associated with incommensurate lattice distortion in multiferroic DyMnO₃*, Phys. Rev. B **73**, 180401 (2006). [124](#)
- [248] O. Prokhnenko, R. Feyerherm, E. Dudzik, S. Landsgesell, N. Aliouane, L. C. Chapon, and D. N. Argyriou, *Enhanced ferroelectric polarization by induced Dy spin-order in multiferroic DyMnO₃*, Phys. Rev. Lett. **98**, 057206 (2007). [124](#)
- [249] R. Kajimoto, H. Mochizuki, H. Yoshizawa, H. Shintani, T. Kimura, and Y. Tokura, *R-Dependence of spin exchange interactions in RMnO₃ (R = rare-earth ions)*, J. Phys. Soc. Japan **74**, 2430 (2005). [125](#), [160](#), [161](#), [162](#)
- [250] U. Walter, *Treating crystal-field parameters in lower than cubic symmetries*, J. Phys. Chem. Solids **45**, 401 (1984). [125](#), [148](#)
- [251] Y. Yamada, G. Shirane, and A. Linz, *Study of critical fluctuations in BaTiO₃ by neutron scattering*, Phys. Rev. **177**, 848 (1969). [128](#)
- [252] Y. Yoshimori, *A new type of antiferromagnetic structure in the rutile crystal*, J. Phys. Soc. Japan **14**, 807 (1959). [132](#)
- [253] H. Katsura, A. V. Balatsky, and N. Nagaosa, *Dynamical magnetoelectric coupling in helical magnets*, Phys. Rev. Lett. **98**, 027203 (2007). [132](#), [134](#), [136](#), [152](#), [159](#), [170](#)
- [254] J. Goldstone, A. Salam, and S. Weinberg, *Broken symmetries*, Phys. Rev. **127**, 965 (1962). [134](#)
- [255] A. Pimenov, A. Mukhin, V. Ivanov, V. Travkin, A. Balbashov, and A. Loidl, *Possible evidence for electromagnons in multiferroic manganites*, Nature Physics **2**, 97 (2006). [134](#), [135](#), [143](#), [170](#), [173](#)
- [256] A. B. Sushkov, R. V. Aguilar, S. Park, S.-W. Cheong, and H. D. Drew, *Electromagnons in multiferroic YMn₂O₅ and TbMn₂O₅*, Phys. Rev. Lett. **98**, 027202 (2007). [135](#)
- [257] R. Valdés Aguilar, A. B. Sushkov, C. L. Zhang, Y.-J. Choi, S.-W. Cheong, and H. D. Drew, *Colossal magnon-phonon coupling in multiferroic Eu_{0.75}Y_{0.25}MnO₃*, condmat/0704.3632v1 (2007). [135](#)
- [258] V. G. Bar'yakhtar and I. Chapuis, *Phenomenological theory of a ferroelectric magnet*, Sov. Phys. – Solid State **10**, 2818 (1969). [135](#)
- [259] E. Fawcett, *Spin-density-wave antiferromagnetism in chromium*, Rev. Mod. Phys. **60**, 209 (1988). [140](#)
- [260] H. Hiraka, Y. Endoh, P. Böni, M. Fujita, K. Yamada, and G. Shirane, *Reinvestigation of magnetic excitations in the spin density wave of chromium*, Phys. Rev. B **67**, 064423 (2003). [140](#)

-
- [261] D. Meier, *Thermische Ausdehnung und Magnetostraktion multiferroischer Seltenerd-manganate*, Diploma Thesis, University of Cologne, 2006. [145](#), [147](#)
- [262] D. Meier, N. Aliouane, D. N. Argyriou, J. A. Mydosh, and T. Lorenz, *New features in the phase diagram of TbMnO₃*, New Journal of Physics **9**, 100 (2007). [145](#), [146](#), [147](#), [148](#)
- [263] D. N. Argyriou, N. Aliouane, J. Stremper, I. Zegkinoglou, B. Bohnenbuck, K. Habicht, and M. v. Zimmermann, *Melting of incommensurate-ferroelectric phase with magnetic field in multiferroic TbMnO₃*, Phys. Rev. B **75**, 020101 (2007). [146](#)
- [264] M. Mostovoy, private communication. [159](#)
- [265] N. W. Ashcroft and N. D. Mermin, *Solid State Physics*, Saunders College Publishing, New York, 1976. [161](#)
- [266] C. Boekema, F. van der Woude, and G. A. Sawatzky, *Covalency effects and hyperfine interactions in the rare-earth orthoferrites*, Int. J. Magn. **3**, 341 (1972). [162](#)
- [267] J.-S. Zhou and J. B. Goodenough, *Exchange interactions in the perovskites Ca_{1-x}Sr_xMnO₃ and RMnO₃ (R=La,Pr,Sm)*, Phys. Rev. B **68**, 054403 (2003). [162](#), [163](#)
- [268] J.-S. Zhou and J. B. Goodenough, *Orbital order-disorder transition in single-valent manganites*, Phys. Rev. B **68**, 144406 (2003). [162](#)
- [269] B. Dabrowski, S. Kolesnik, A. Baszczuk, O. Chmaissem, T. Maxwell, and J. Mais, *Structural, transport, and magnetic properties of RMnO₃ perovskites*, J. of Solid State Chem. **178**, 629 (2005). [162](#)
- [270] M. W. Kim, S. J. Moon, J. H. Jung, J. Yu, S. Parashar, P. Murugavel, J. H. Lee, and T. W. Noh, *Effect of orbital rotation and mixing on the optical properties of orthorhombic RMnO₃ (R = La, Pr, Nd, Gd, and Tb)*, Phys. Rev. Lett. **96**, 247205 (2006). [163](#)

Bibliography

List of Publications

I.) Publications including results of this thesis:

[senff05a] Crystal and magnetic structure of $\text{La}_{1-x}\text{Sr}_{1+x}\text{MnO}_4$: Role of the orbital degree of freedom

D. Senff, P. Reutler, M. Braden, O. Friedt, D. Bruns, A. Cousson, F. Bourée, M. Merz, B. Büchner, and A. Revcolevschi
Physical Review B **71**, 024425 (2005).

[senff06a] Spin-Wave Dispersion in Orbitally Ordered $\text{La}_{1/2}\text{Sr}_{3/2}\text{MnO}_4$

D. Senff, F. Krüger, S. Scheidl, M. Benomar, Y. Sidis, F. Demmel, and M. Braden
Physical Review Letters **96**, 257201 (2006).

[senff07a] Magnetic Excitations in Multiferroic TbMnO_3 : Evidence for a Hybridized Soft Mode

D. Senff, P. Link, K. Hradil, A. Hiess, L. P. Regnault, Y. Sidis, N. Aliouane, D. N. Argyriou, and M. Braden
Physical Review Letters **98**, 137206 (2007).

[senff07b] Mott-Hubbard versus charge-transfer behavior in LaSrMnO_4 studied via optical conductivity

A. Gössling, M. Haverkort, M. Benomar, T. Möller, D. Senff, M. Braden T. Lorenz, and M. Grüninger
accepted for publication in Physical Review B

[senff07c] Melting of magnetic correlations in charge-orbital ordered $\text{La}_{1/2}\text{Sr}_{3/2}\text{MnO}_4$: competition of ferro- and antiferromagnetic states

D. Senff, M. Benomar, M. Kriener, O. Schumann, T. Lorenz, Y. Sidis, K. Habicht, P. Link, and M. Braden
submitted to Physical Review B

[senff07d] Field Dependence of Magnetic Correlations through the Polarization Flop Transition in Multiferroic TbMnO_3 : Evidence for a Magnetic Memory Effect

D. Senff, P. Link, N. Aliouane, D. N. Argyriou, and M. Braden
submitted to Physical Review Letters

II.) Further publications and contributions to conferences:

1. Magnetic Heat Transport in R_2CuO_4 with $R = La, Pr, Nd, Sm, Eu,$ and Gd

K. Berggold, T. Lorenz, J. Baier, M. Kriener, D. Senff, H. Roth, A. Severing, H. Hartmann, A. Freimuth, S. Barilo, and F. Nakamura
Physical Review B **73**, 104430 (2006).

2. Thermal Conductivity of R_2CuO_4 , with $R = La, Pr$ and Gd

K. Berggold, T. Lorenz, J. Baier, M. Kriener, D. Senff, S. Barilo, and A. Freimuth
Physica B **378**, 1064 (2006).

3. Evidence for Multiple Phase Transitions in $La_{1-x}Ca_xCoO_3$

M. Kriener, M. Braden, D. Senff, O. Zabara and T. Lorenz
Journal of Magnetism and Magnetic Materials **310**, e187 (2006).

4. Magnetic Ordering in $La_{2-x}Sr_xCoO_4$ studied by Neutron Scattering: Evidence for Stripe Phases

M. Cwik, M. Benomar, D. Senff, T. Lorenz, Y. Sidis, K. Hradil, A. Hoser, and M. Braden
submitted to Physical Review Letters.

5. Contribution to conferences:

- Invited talk at the international workshop *Orbital 2007* in Stuttgart.
- Oral presentation at the *1st User Meeting of the FRM II* at the TU München, 2007.
- Several oral and poster presentations at the annual *DPG-Frühjahrstagung* in the years 2003-2007.
- Oral presentation at the *Frühjahrstagung 2006* of the German Crystallographic Society in Freiburg.
- Poster contribution at the joint conference on neutron and synchrotron scattering *SNI 2006* in Hamburg and at the annual meeting of the German Neutron-Scattering Society 2004 in Dresden.
- Presentations at the international workshops *Theoretical Magnetism 2004* in Abingdon/England and at the *Orbital 2006* in Berlin.

-
- Participation at the joint symposium of SFB 608 and Graduiertenkolleg 549 on *Functional Transition Metal Compounds & Multiferroics* in Köln, 2005, and at the international workshop of SFB 608 on *Strongly Correlated Transition Metal Compounds* in Köln, 2003.

List of Publications

Danksagung

Zum Schluss ist nun endlich Gelegenheit all denen zu danken, die mich im Laufe der Promotion begleitet und unterstützt haben, und ohne deren Hilfe und Zusammenarbeit diese Arbeit so nie entstanden wäre.

Besonders bedanken möchte ich mich bei meinem Doktorvater Prof. M. Braden, der mir diese Arbeit ermöglicht hat und dessen Intuition ich die Arbeit auf dem Gebiet der Manganate schulde. Neben den zahllosen Diskussionen über Streuquerschnitte, (Elektro-)Magnonen, Auflösungsellipsoide, Proposals und Veröffentlichungen werden mir vor allem die entspannten Abende während der gemeinsamen Messreisen in den Restaurants und Cafes von Paris, Grenoble und München in lebendiger Erinnerung bleiben. Vielen Dank Herr Braden für die großen Freiräume, die Sie mir seit dem Beginn der Diplomarbeit gelassen haben, Ihre Gelassenheit in all den stressigen Momenten, und Ihr stetes Vertrauen.

Den Mitgliedern der Prüfungskommission, Prof. M. Vojta, Prof. B. Büchner und Prof. L. Bohatý, danke ich für ihre Bereitschaft meine Arbeit zu lesen und die nötigen Gutachten zu erstellen.

Dr. D. N. Argyriou danke ich für die Einführung in die Physik der multiferroischen Manganate, die gute und enge Zusammenarbeit, die unterhaltsamen Diskussionen (nicht nur) über Spiralstrukturen und Zykloiden, die gelöste Atmosphäre während den gemeinsamen Messungen und für die Möglichkeit der Teilnahme an den beiden *Orbital*-Workshops in Berlin und Stuttgart.

Sämtliche Ergebnisse dieser Arbeit sind an den vier europäischen Neutronenzentren in Saclay, Grenoble, Berlin und München entstanden. Neben dem verlässlichen Neutronenfluss habe ich dabei vor allem von den bestens gepflegten Spektrometern, sowie dem persönlichen Engagement und der großen Erfahrung der jeweiligen Instrumentwissenschaftler, die mir rund um die Uhr mit Rat und Tat zur Seite standen und so manchen Unfall reparieren mussten, profitiert: At all experiments at the LLB, I have been supported by Yvan Sidis. Although he is probably the hardest working man in France, he always found some time to teach me all the tricks necessary to drive a TAS and to give a safe look on the data and their analysis. Thanks a lot Yvan, I truly enjoyed working at the LLB ! I further like to mention "Maître" Baroni for fixing numerous electronic problems and for many vivid discussions. They really helped improving my French vocabulary...

Als einer der ersten externen Nutzer der beiden TAS-Instrumente PANDA und

PUMA am FRM II in Garching war es mir eine Freude an der rasanten Entwicklung der beiden neuen Geräte teilnehmen zu dürfen. Bedanken möchte ich mich dafür insbesondere bei Klaudia Hradil und Peter Link, die mir vor, während und nach der Messung bei allen Problemen (nicht nur technischer Natur...) mit einem schier unermüdlichen Einsatz zur Seite standen, so dass ich den Leberkäs-Äquator immer wieder gerne in Richtung Süden überschritten habe.

An den diversen Messungen am ILL sind eine ganze Reihe unterschiedlicher Personen beteiligt gewesen, besondere Erwähnung verdienen an dieser Stelle aber vor allem Louis-Pierre Regnault – thank you very much Louis-Pierre for introducing me to the technique of polarized neutron scattering and for your patience upon explaining the various elements of the polarization matrix –, Arno Hiess für die gute Organisation, den sorgsam Aufbau des Cryopad-Setups am IN14 und die ganz besondere Aussicht auf Grenoble und das ILL, Wolfgang Schmidt für die hervorragenden Bedingungen und die relaxten Messzeiten am IN12 und Karin Schmalzl für das gemeinsame Grübeln über die unterschiedlichen Streuquerschnitte bei einer vollständigen Polarisationsanalyse.

Klaus Habicht vom HMI möchte ich für die große Unterstützung bei den Messungen am FLEX danken, die sich außer durch einen schnellen Umbau zwischen den unterschiedlichsten Probenumgebungen durch besonders freundliches Bahnpersonal und die Nähe zu Berlin ausgezeichnet haben.

Neben den Neutronenspektrometern sind vor allem die verwendeten große Einkristalle wesentlich für den Erfolg der einzelnen Messungen gewesen. Den beteiligten Kristallzüchtern bin ich daher zu besonderem Dank verpflichtet: Für ihren Ehrgeiz, ihre Ausdauer und ihre Bereitschaft mir ihre Kristalle schließlich anzuvertrauen (damit sie zunächst verstrahlt und anschließend für Jahre im Keller eines Reaktors eingebunkert werden...) bedanke ich mich bei Pascal, Nadir, Mohammed und Olaf. Meinem Studienfreund und langjährigen Büronachbarn Olaf gebührt weiterhin Dank für die Lösung unzähliger Computer- und Netzwerkprobleme, der Erschaffung des neuen Steuerprogramms unserer Röntgenapparaturen und des ungemein praktischen CLIP-Skriptes, das Ertragen diverser Wortspiele über Samba-Server und Tiki-Wikis (oder Moin-Moins...) und für das gemeinsame Erleben nächtlicher Fernsehübertragungen auf Bayern 3.

Im heimatlichen Institut in Köln haben in den vergangenen fünf Jahren alle Mitarbeiter auf die ein oder andere Art zu der guten Stimmung und dem fruchtbaren Arbeitsklima beigetragen, ein paar von ihnen möchte ich hier allerdings besonders erwähnen (ohne dabei all jene zu vergessen, die hier nicht namentlich erwähnt werden können): Harald Kierspel danke ich für seine Zusammenarbeit in allen Verwaltungsfragen und Andrea Severing für ihre Organisation des SFBs und die Bearbeitung einer Flut von Reisekostenabrechnungen. Bei Prof. D. Khomskii, Prof. M. Grüniger und Dr. T. Lorenz bedanke ich mich für eine Vielzahl von Gesprächen und Diskussionen über meine heißgeliebten Manganate.

Meinen Mitstreitern in der Neutronentruppe Thomas, Matthias, Wolf, Paul,

Alexander, Olaf, und Oliver danke ich für gemeinsames Orientieren, Heliumfüllen, Messen, Fitten, Warten und Rumlümmeln in den Reaktoren dieser Welt. Zusammen ist man eben doch weniger allein...! Besonders erwähnt sei dabei vor allem Paul, der mich nicht nur über die vollen 21 Semester bis zum gemeinsamen Doktorhut begleitet hat, sondern auch über verschlungene Pfade im reziproken Raum, über dunkle Felder und nächtliche Forschungszentren bis zum Saturn(e), in Pubs, Kneipen, Cafes, Pizzarien und Restaurants und durch die Abgründe unterschiedlicher Promotionsordnungen. Thomas möchte ich außerdem danken für eine Fahrt über die Alpen und die (natürlich) hoffnungslosen Konvertierungsversuche zur dunklen Seite des Glases.

Markus danke ich für die Messungen der spezifischen Wärme, für die Versorgung mit Getränken und für gemeinsame Heimwege auf die Seite des Rheins mit der schönsten Aussicht auf den Dom. Ina danke ich für ihre Mühen bei der Messung des elektrischen Widerstandes und für ihr Asyl für den kleinen Leo. Dem Laue-Team um Christina, Eva und Alexander vielen Dank für die Stunden vor und mit der Laue-Kamera. Jens danke ich für sein organisatorisches Geschick, Hilfestellungen bei L^AT_EX-Problemen, typographische Beratung und für einen sicheren Transport in Regensburg. Bei Kai bedanke ich mich für seine Hilfe mit dem Schnellmessstab, für eine Reihe von Korrekturen und für Prinzenrollen, und bei Jörg für die Messungen der thermischen Ausdehnung und für einen sehr aufschlussreichen Vortrag im Doktorandenseminar.

Stefan Scheidl und Frank Krüger möchte ich für ihre Zusammenarbeit und die Rechnungen auf dem Gebiet der halbdotierten Manganate danken, die, wenn ich sie selbst hätte durchführen müssen, das Ende meiner Doktorarbeit wohl um einiges verzögert hätten.

Den Mitarbeitern der mechanischen Werkstatt danke ich für ihre Hilfsbereitschaft, ihre Fingerfertigkeit und Erfahrung beim Anfertigen von Aluminiumdosen, ihre Geduld bei mehrmaligen spontanen Änderungswünschen und bei der Reparatur unseres Kryostaten. Beim Fuhrparkservice der Universität zu Köln möchte ich mich für die schicken blauen Autos und tausende Autobahnkilometer zwischen Köln, Paris, Grenoble, Mailand (!), München und Berlin bedanken.

Zum Abschluss möchte ich mich bei meiner Familie – bei meiner Mutter, meinen Großeltern Josephine und Justus, bei Ingrid, Alfred, Claudia, Kerstin und Michelle – bedanken, die mich das gesamte Studium über unterstützt hat: Vielen Dank für eure Unterstützung und euer Vertrauen in den letzten Jahren.

Meiner lieben Nicole, danke für alles. Danke für deine Liebe, deine Geduld, deinen Zuspruch, deinen Mut, deine Rücksicht und all die kleinen Aufmunterungen während des Schreibens.

Offizielle Erklärung

Ich versichere, dass ich die von mir vorgelegte Dissertation selbständig angefertigt, die benutzten Quellen und Hilfsmittel vollständig angegeben und die Stellen der Arbeit – einschließlich Tabellen, Karten und Abbildungen –, die anderen Werken im Wortlaut oder dem Sinn nach entnommen sind, in jedem Einzelfall als Entlehnung kenntlich gemacht habe; dass diese Dissertation noch keiner anderen Fakultät oder Universität zur Prüfung vorgelegen hat; dass sie – abgesehen von unten angegebenen Teilpublikationen – noch nicht veröffentlicht worden ist sowie, dass ich eine solche Veröffentlichung vor Abschluss des Promotionsverfahrens nicht vornehmen werde. Die Bestimmungen der Promotionsordnung sind mir bekannt. Die von mir vorgelegte Dissertation ist von Prof. Dr. M. Braden betreut worden.

Köln, den 11. September 2007

Daniel Senff

Kurzzusammenfassung

Der Schwerpunkt der vorliegenden Arbeit umfasst die Untersuchung des magnetischen Anregungsspektrums dreier unterschiedlicher Manganoxide mittels inelastischer Neutronenstreuung.

Die Eigenschaften von LaSrMnO_4 sind bestimmt durch das für Manganate typische komplexe Wechselspiel zwischen orbitalen und Ladungsfreiheitsgraden mit dem Gitter, und der Grundzustand von LaSrMnO_4 weist einige äußerst ungewöhnliche Eigenschaften auf. Die Analyse des magnetischen Anregungsspektrums legt einen inhomogenen Grundzustand nahe, in dem ferromagnetische orbitale Cluster oder Polaronen in einen antiferromagnetisch geordneten Hintergrund eingebettet sind.

Das dotierte System $\text{La}_{1/2}\text{Sr}_{3/2}\text{MnO}_4$ zeichnet sich durch eine sehr stabile ladungsgeordnete Phase aus, die zur Zeit in der Literatur kontrovers diskutiert wird. Auf Grundlage der beobachteten Spinwellendispersion finden wir eine exzellente Übereinstimmung mit einem klassischen Ansatz zur Beschreibung des geordneten Zustandes, während ein alternativer Zugang eindeutig ausgeschlossen werden kann. Der starke Unterschied zwischen ferro- und antiferromagnetischen Austauschenergien führt zu dem Schluss, dass der geordnete Zustand als eine schwache AFM-Kopplung stabiler FM-Ketten zu interpretieren ist. Diese Folgerung wird weiterhin belegt durch die thermische Entwicklung des geordneten Zustandes, der oberhalb des Néel-Übergangs mit einer ferromagnetischen Phase konkurriert, und durch die Dotierungsabhängigkeit, die ein stark unterschiedliches Verhalten im Bezug auf zusätzliche Elektronen oder Löcher aufweist.

Im Perowskit TbMnO_3 ist das Auftreten einer spontanen elektrischen Polarisation eng an eine komplexe magnetische Struktur gekoppelt. Durch eine genaue Analyse der verschiedenen magnetischen Anregungen können die mit dem ferroelektrischen Übergang korrelierten magnetischen Anregungen identifiziert werden, die auf Grund der starken magnetoelektrischen Kopplung als eine neue Art kollektiver Anregungen – stark gemischte Magnon-Phonon-Anregungen – zu interpretieren sind. Die detaillierte Untersuchung der Impuls-, Temperatur- und Feldabhängigkeit dieser Anregungen ist in Übereinstimmung mit verschiedenen Vorhersagen aktueller Theorien zur Erklärung der ungewöhnlich starken magnetoelektrischen Kopplung in der Familie multiferroischer Oxide.



Abstract

This thesis deals with magnetic excitations in three different Manganese oxides, single-layered LaSrMnO_4 , charge- and orbital-ordered $\text{La}_{1/2}\text{Sr}_{3/2}\text{MnO}_4$, and multiferroic TbMnO_3 , which are studied by means of inelastic neutron scattering.

The properties of the first system, LaSrMnO_4 , are governed by the complex interplay of orbital, spin, and lattice degrees of freedom typical for the physics of manganites. The magnetic low-temperature behavior is quite unusual, and the comprehensive analysis of the spin-wave spectrum of LaSrMnO_4 suggests a heterogenous ground state with ferromagnetic orbital polarons embedded in an antiferromagnetic background.

The doped system $\text{La}_{1/2}\text{Sr}_{3/2}\text{MnO}_4$ exhibits a stable charge- and orbital-ordered state, which today is discussed very controversially, as it is of great relevance for the colossal increase of electric conductivity at the metal-insulator transition in perovskite manganites. Analyzing the spin-wave dispersion of the ordered state, we find an excellent agreement with classical predictions by Goodenough and reject a recent alternative proposal. The different strength of the ferromagnetic and antiferromagnetic exchange in the CE-type ordering leads to the conclusion that the magnetic state has to be considered as a weak AFM coupling of stable FM elements. This thesis is further supported by the thermal evolution of the ordered state, revealing anisotropic correlations and the close competition of FM and AFM correlations above the Néel transition, as well as by the doping dependence of the charge- and orbital-ordered state, which is interpreted on the basis of a different response of the magnetic system with respect to additional electrons or holes.

In the orthorhombic perovskite TbMnO_3 the electric polarization is closely coupled to the magnetic degrees of freedom via a complex, non-collinear magnetic ordering. Precisely characterizing the different magnon excitations allows to identify all relevant modes of the ferroelectric phase, which for systems with strong electromagnetic coupling were predicted to contain a new type of collective excitations – strongly hybridized phonon-magnon vibrations – which have not been observed experimentally before. The temperature and momentum dependence, as well as the response of the different modes to an external magnetic field, is reported in detail, and the results strengthen recent theoretical concepts explaining the strong magnetoelectric coupling in the fascinating class of multiferroic oxides.